

Characterization of the Deformation Behaviour of Mould Slag Inclusions During Hot Rolling

Guilherme Melo

Master Dissertation

FEUP Supervisor: Prof. Fernando Jorge Lino Alves

Tata Steel Supervisor: Laurens-Jan Pille



Integrated Master in Mechanical Engineering

July 2019

Para os meus pais e para o Martim

Abstract

The present work aimed at furthering the characterization of the chemo-thermo-mechanical phenomena occurring during the hot-rolling of steel containing inclusions resulting from the mould slag in continuous casting.

To do so, artificial inclusions were embedded into powder metallurgy cylinders, which were fitted into steel slabs and rolled according to different schedules in a lab-scale hot strip mill. Different preparation conditions of the inclusions (fluorine and sodium content) and differences in the rolling process (soaking time, thickness reduction) ensured that several combinations of parameters were tested. The rolled inclusions were retrieved from the slabs in samples corresponding to longitudinal sections and characterized using optical and electron microscopy techniques.

Additionally, a finite element model of the lab-scale hot rolling process was developed to complement the interpretation of the results.

It was observed that a significant change in inclusion shape occurred between the rolling schedules with 2 and 3 passes. Evolutions in the relative plasticity index and aspect ratio of the inclusions were also displayed with varying depths within the slab and thickness reduction applied. No influence of the composition or soaking times was observed in the inclusion shape.

It was also concluded that the methodology used to produce variable F/Na contents resulted in different phases observed, where the poor F/Na inclusions presented both cuspidine and wollastonite as crystalline phases, while the rich F/Na displayed cuspidine as the single crystalline phase present.

Finally, it was observed that wollastonite was consistently found in elongated blocks in the rolling direction, whereas the cuspidine morphology changed significantly between globular and dendritic structures depending on the depth within the slab and additional phases present. For the most deformed inclusions, cuspidine also presented a change in morphology in the longitudinal direction, from a dendritic to a globular structure.

Caracterização da Deformação de Inclusões Provenientes de Fluxos de Cobertura Durante Laminagem a Quente

Resumo

O presente trabalho teve como objetivo aprofundar a caracterização dos fenómenos químico-termo-mecânicos ocorrentes durante o processo de laminagem a quente de aço com inclusões provenientes da escória criada pelos fluxos de cobertura no processo de vazamento contínuo.

Para tal, foram introduzidas inclusões artificiais em cilindros criados por pulverometalurgia, os quais foram inseridos em blocos de aço e sujeitos a diferentes sequências de laminagem a quente num laminador à escala laboratorial. A variação das condições de preparação das inclusões (relativamente ao conteúdo de sódio e flúor) e as diferenças no processo de laminagem (tempo de pré-aquecimento, redução de espessura) promoveram que diferentes combinações de parâmetros fossem testadas. As inclusões laminadas foram recuperadas dos blocos de aço em amostras correspondentes a secções longitudinais e caracterizadas usando microscopia ótica e eletrónica.

Adicionalmente, foi desenvolvido um modelo de elementos finitos do processo de laminagem a quente à escala laboratorial com o objetivo de auxiliar a interpretação dos resultados.

Foi observado que ocorreu uma alteração considerável na forma das inclusões entre as sequências de laminagem com 2 e 3 passagens. Foram também observadas evoluções do índice de plasticidade relativa e razão de aspeto das inclusões com a variação da profundidade no bloco de aço e redução de espessura aplicada. Não foi possível detetar influências da composição ou tempo de pré-aquecimento na forma final das inclusões.

Foi também concluído que a metodologia empregue para produzir duas variações do conteúdo de flúor e sódio resultou em fases diferentes observadas, sendo que as inclusões pobres em F/Na apresentaram cuspidine e wollastonite como fases cristalinas, enquanto que as inclusões ricas em flúor e sódio revelaram apenas cuspidine como a única fase cristalina presente.

Por fim, observou-se que a wollastonite foi consistentemente encontrada sob a forma de blocos alongados na direção de laminagem, enquanto que a cuspidine apresentou mudanças consideráveis na sua morfologia, entre estruturas globulares e dendríticas, dependendo da profundidade no bloco de aço e das restantes fases presentes. Nas inclusões mais deformadas, a cuspidine apresentou ainda uma alteração da sua morfologia na direção longitudinal, mudando de uma estrutura dendrítica para uma estrutura globular.

Acknowledgements

I would firstly like to thank Sido Sinnema for the opportunity provided for the realization of the internship in the CRC, which led to the present work.

Secondly, I would like to thank Laurens-Jan Pille, Wouter Tiekink and Fernando Jorge Lino Alves for the guidance provided in their supervision, without which the present work would not have been possible.

I would also like to thank James Small and Frank van der Does for all the help and expertise provided during the microscopy techniques used. Additionally, I would like to thank Enno Zinngrebe for the input provided for the chemical aspects of the present thesis.

Regarding the work conducted within the Innovation Centre at Tata Steel IJmuiden, I am especially thankful for the support, guidance and work environment provided by Edwin Swart as well as for the crucial help provided by Martin Sadhinoch during the development of the FE model. Moreover, I would like to thank Peter Gelten for the help provided regarding the material model used.

I would like to thank all remaining personnel in the Ceramics Research Centre and Innovation Centre at Tata Steel IJmuiden for the amicable and pleasant work environment provided during the internship.

I would like to thank the Faculty of Engineering of the University of Porto for the learning experience provided.

I would also like to express my gratitude to my parents, for the unconditional support and constant interest in my studies.

Finally, I would like to thank both Tata Steel and the Erasmus program for the financial support provided.

Contents

1	Introduction.....	1
1.1	Project Framing.....	1
1.2	The Clean Steel Project.....	1
1.3	Project Methodology.....	1
1.4	Structure.....	2
2	Bibliography Review.....	3
2.1	Final Products Defects.....	3
2.2	Inclusion Entrapment.....	4
2.3	Hot Rolling.....	7
2.4	Inclusion Characterization.....	11
2.4.1	Structure and Composition.....	11
2.4.2	Characteristics of Non Metallic Inclusions (NMI).....	15
2.5	Previous studies.....	19
2.5.1	Processes and Techniques.....	22
3	Materials and Methods.....	29
3.1	Slab Preparation.....	29
3.2	Sample Preparation.....	33
3.3	Testing.....	35
4	Results.....	37
4.1	Optical Microscopy.....	37
4.2	SEM.....	39
4.2.1	Inclusion Shape.....	40
4.2.2	Inclusion Composition and Phases.....	41
4.2.3	Phase Morphology.....	42
5	Modelling of the Hot Rolling Process.....	45
5.1	Finite Element Model.....	45
5.1.1	Material Properties.....	46
5.1.2	Interactions.....	49
5.1.3	Geometries and Mesh.....	52
5.1.4	Boundary and Initial Conditions.....	55
5.2	FE Results.....	56
6	Analysis and Discussion.....	67
6.1	Inclusion Shape.....	67
6.2	Inclusion Composition and Phases.....	80
6.3	Phase Morphology.....	82
7	Conclusions.....	93
8	Future Work.....	95
8.1	Plant Scale Trials.....	95
8.2	Slag Characterization Tests.....	96
	References.....	101
	APPENDIX A: Slab Dimensions.....	105
	APPENDIX B: Optical Microscopy Mosaics and Measurements.....	109
	APPENDIX C: Preliminary Analysis.....	113
	APPENDIX D: BSI Image Treatment.....	119
	APPENDIX E: EDS Measurement and Data Treatment Procedure.....	123

List of Symbols

- A - area of the inclusion's section
 a - contact length
 c - specific heat of the rolled material
 c_x - fitting coefficients of the Siciliano model
 $\dot{\epsilon}$ - strain rate
 ϵ - deformation strain
 E_1 - Young modulus of the cylinder in the Hertzian contact situation
 E_2 - Young modulus of the slab in the Hertzian contact situation
 E^* - combined Young modulus in the Hertzian contact situation
 F - applied force in the Hertzian contact situation
 f - composition-based factor in the Siciliano model
 FS - field strength
 \bar{h} - average convective heat transfer coefficient
 h_a - convection heat transfer coefficient
 h_c - contact conductance between the slab and the roll
 k - thermal conductivity of the rolled material
 k_{air} - conductivity of the air
 k_s - shear yield stress
 L - length of the slab
 L_i - initial slab length
 l_f - length of the inclusion after rolling
 L_n - normalized final slab length
 m - sticking friction factor
 MAR - maximum aspect ratio
 MFS - mean flow stress
 n - normal direction to the surface boundary during hot rolling
 NAR - normalized aspect ratio
 \overline{Nu}_L - average Nusselt number for $x=L$
 P - contact pressure
 p_{max} - maximum contact pressure
 Pr - Prandtl number for the air
 q - heat flux per unit area that crosses the surface from the slab to the roll
 q_f - rate of generated heat by friction on the contact surface during hot rolling
 Re_L - Reynolds number for $x=L$
 RPI - relative plasticity index
 r^{pl} - heat flux generated per unit of volume due to plastic deformation during hot rolling
 R_x - cooling rates applied in the slag characterization tests
 R_1 - radius of the cylinder in the Hertzian contact situation
 R_2 - radius of the slab in the Hertzian contact situation
 R^* - combined radius
 S - Stefan–Boltzmann constant
 SI - shape index of the inclusion
 T - temperature
 T_a - temperature of point a , in the slab

- T_b - temperature of point b , in the roll
 T_f - final slab thickness
 t_f^{\max} - maximum inclusion thickness after rolling
 t_f^{norm} - normalized inclusion thickness after rolling
 T_g - glass transition temperature
 T_i - initial slab thickness
 T_l - *liquidus* temperature
 T_{roll} - work-roll surface temperature
 T_{∞} - ambient temperature
 u - velocity component along x direction
 u_{∞} - relative speed of the air in relation to the slab
 v - velocity component along y direction
 w - velocity component along w direction
 \bar{W}_f - average final slab width
 W_i - initial slab width
 $[X]$ - fractions of each chemical element X in the Siciliano model
 x - rolling direction during hot rolling
 y - transverse direction during hot rolling
 z - thickness direction in during hot rolling
 α_R - mass proportional damping coefficient in the Rayleigh damping method
 β_R - stiffness proportional damping coefficient in the Rayleigh damping method
 Δv - relative tangential velocity between the slab and the roll
 $\bar{\epsilon}_i$ - average inclusion strain
 $\bar{\epsilon}_m$ - average steel strain
 $\dot{\boldsymbol{\epsilon}}^{pl}$ - strain rate vector
 η - fraction of friction heat transferred to the slab during hot rolling
 η_p - fraction of plastic work converted to heat
 λ - surface emissivity
 μ - coefficient of friction
 ν - dynamic viscosity of the air
 ν_1 - Poisson coefficient of the cylinder in the Hertzian contact situation
 ν_2 - Poisson coefficient of the slab in the Hertzian contact situation
 ζ - normalized contact length
 ρ - density of the rolled material
 $\boldsymbol{\sigma}$ - stress vector
 τ_c - critical shear stress value
 ϕ - heating rate

List of Abbreviations

BEI (or BSE) - back-scattering electron imaging
BF - blast furnace
BOF - basic oxygen furnace
BOP - basic oxygen process
BOS - basic oxygen steelmaking
CCT - continuous cooling transformation
CIP - carbonyl iron powder
EAF - electric arc furnaces
EDS - energy dispersive X-ray spectroscopy
ESEM - environmental scan electron microscopy
FE – finite elements
HIP - hot isostatic pressing
LVSEM - low voltage scan electron microscopy
NMI - non metallic inclusions
SEN - submerged entry nozzle
MP - mould powder
PM - powder metallurgy
PVD - physical vapour deposition
SEM - scan electron microscopy
TEM - transmission electron microscopy
TTT - time temperature transformation

List of Figures

Figure 1 - Example of the <i>Griffe Laminée</i> defect.....	3
Figure 2 - Example of the Split Flanges defect.....	4
Figure 3 - Schematic representation of the BOF and continuous casting process flow at Tata Steel IJmuiden	5
Figure 4 - Schematic representation of the continuous casting process.....	6
Figure 5 - Detail of the continuous casting process (left) and respective mould powder layers in the mould (right)	7
Figure 6 - The coefficient of friction as a function of velocity for two different steel grades.....	8
Figure 7 - The coefficient of friction as a function of thickness reduction for different temperatures.....	9
Figure 8 - Schematic representation of the neutral point and different slip regions	10
Figure 9 - Inhomogeneous deformation of material between rolls. Shaded areas are non-plastic regions.....	10
Figure 10 - SiO_4^{4-} tetrahedron (left) and a silicate network (right)	11
Figure 11 - Role of sodium and calcium oxides in modifying the silica network.....	12
Figure 12 - Phase diagram for the $\text{SiO}_2\text{-CaO-Na}_2\text{O}$ ternary system	14
Figure 13 - Phase diagram for the $\text{SiO}_2\text{-CaO-Na}_2\text{O-CaF}_2$ quaternary system	15
Figure 14 - Different types of inclusions in hot-rolled steel: (a) undeformed ‘hard’ inclusion, (b) brittle broken crystalline inclusion, (c) hard inclusion cluster (d) brittle–ductile multiphase complex inclusion and (e) ductile elongated inclusion. The scale in figures vary from few microns to tens of microns.....	16
Figure 15 - SEM picture of a multiphase Non Metallic Inclusion	17
Figure 16 - Measured and computed onset temperatures as a function of heating rate (ϕ) for peak 1 (cuspidine) during devitrification of mould slag A	18
Figure 17 - Temperature (yy axis) as a function of processing time (xx axis) for the different rolling stations (V1 through V6) at the centre of the slab (<i>kern</i> , red) and at the surface of the slab (<i>oppervlak</i> , blue).....	19
Figure 18 - Schematic drawing of the iron decomposition process	24
Figure 19 - Hot isostatic pressing system representation	25
Figure 20 - Different possible electron behaviour as a base for SEM image modes (left) and X-Ray emission mechanism as the base for the EDS mode (right).....	26
Figure 21 - Schematic representation of the production of the samples studied in the first stage. Indexed numbers indicate the slab numbers that result from the alternative processing routes, as can be consulted in Table 3-4.....	29
Figure 22 - Graphic representation of the (a) artificial inclusions, (b) PM cylinder with embedded artificial inclusions and (c) steel slab with shrink fitted PM cylinder	30
Figure 23 - SEM image of a mould powder particle after the first decarburization step.....	30

Figure 24 - Shaping step (left) and SEM image of the artificial inclusions after the shaping and final sieving steps (right)	31
Figure 25 - Powder metallurgy cylinders after HIP and machining (left, centre) and after cutting (right)	32
Figure 26 - Slabs 1 (lower left corner), 2 (lower right corner) and 3 (top) after hot rolling. PM cylinders visible in the centre of the slabs	33
Figure 27 - Struers Accutom-5 used in the sample cutting process	34
Figure 28 - Representation of the expected deformation of the rolled cylinders (not to scale)	34
Figure 29 - Struers PolyFast carbon-filled phenolic resin (left) and Struers Protonpress 10 (right) used in the sample mounting	34
Figure 30 - Struers Tegramin-30 used in the automated sample grinding and polishing steps	35
Figure 31 - Mosaic created with 50x optical microscopy images. Samples taken from the 85% reduction slabs	37
Figure 32 - Detail of sample from slab 8 (top) and 12 (bottom) created with 50x optical microscopy images. Relevant inclusions identified with capital letters above ...	38
Figure 33 - Detail of the sample from slab 2 created with 50x optical microscopy images. Boundary between the steel slab and the powder metallurgy cylinder highlighted	38
Figure 34 - Example of the results of the measurements conducted on the inclusions of slab 8 during optical microscopy	39
Figure 35 - Examples of individual BSI images, resulting from the SEM testing	39
Figure 36 - Example of the oval shape displayed in the 20% reduction inclusions. Example taken from slab 1, inclusion A. Rolling direction from left to right.....	40
Figure 37 - Example of the oval shape displayed in the 40% reduction inclusions. Example taken from slab 2, inclusion C. Rolling direction from left to right.....	40
Figure 38 - Example of the drop-like shape displayed in the 85% reduction inclusions. Examples taken from slab 8, inclusions A, B, C and D. The thin part of inclusions C and D is not fully displayed in the picture due to size restrictions. Rolling direction from left to right	40
Figure 39 - Example of the strain rate dependency of the elasto-plastic response of the slab material for a fixed temperature of 1200°C	47
Figure 40 - Example of the temperature dependency of the elasto-plastic response of the slab material for a fixed strain rate of 10 [s ⁻¹]	47
Figure 41 - Rolling force (left) and displacement curves of the strip (right) for different damping factors	48
Figure 42 - Work-roll partitioning (left) and mesh (right) used to reduce the number of elements	53
Figure 43 - Detail of the transition zones with triangular elements (left) and element size ratio between the roll and the strip (right)	53
Figure 44 - Schematic representation of the Hertzian contact situation.....	54

Figure 45 - Analytical and finite element solutions determined by Gillebaart (2011) for the pressure distribution throughout the contact length in the Hertzian contact problem	55
Figure 46 - Predicted temperature evolution at different slab depths (as a percentage of the initial slab thickness) during the one-rolling step, 40% thickness reduction, lab-scale hot rolling FE simulation.....	56
Figure 47 - Predicted temperature evolution at different slab depths (as a percentage of the initial slab thickness) during the single-step, lab-scale hot rolling FE simulations (20% and 40% thickness reduction).....	57
Figure 48 - Contact zones for the single-step, lab-scale hot rolling FE simulations (20% and 40% reduction)	57
Figure 49 - Heat transfer during hot rolling for the 40% reduction hot rolling simulations. Legend in [kW/m ²] units with lower bound set at 500 to highlight the conduction in the contact zone	58
Figure 50 - Temperature gradient during hot rolling for the 20% reduction hot rolling simulations. Legend in Kelvin [K] units with lower bound set at 1473 (=1200°C) to highlight only the temperature increase above the initial conditions.....	58
Figure 51 - Temperature gradient during hot rolling for the 40% reduction hot rolling simulations. Legend in Kelvin [K] units with lower bound set at 1473 (=1200°C) to highlight only the temperature increase above the initial conditions.....	59
Figure 52 - Predicted temperature evolution at different slab depths (10mm and 20mm correspond to 5% and 10% of the initial slab thickness, respectively) during the first rolling step (15% thickness reduction) of the plant-scale, hot rolling FE simulations conducted by Serajzadeh <i>et al.</i>	60
Figure 53 - Experimental surface temperature measurements at the entry (In) and exit (Out) of the lab-scale hot rolling mill for the single-pass, 20% reduction experiments.....	61
Figure 54 - Predicted temperature evolution at different slab depths (as a percentage of the initial slab thickness) during the two-rolling step, 60% thickness reduction, lab-scale hot rolling FE simulation.....	62
Figure 55 - Predicted temperature evolution at different slab depths (as a percentage of the initial slab thickness) during the three-rolling step, 85% thickness reduction, lab-scale hot rolling FE simulation. Measured surface temperature plotted for the slabs in the rolling trials	62
Figure 56 - Predicted and measured temperature variations during a 6-roughing stand, hot rolling process. FE model considering the thermo-mechanical-metallurgical response of a low-carbon steel.....	63
Figure 57 - Finite Element results (left) and experimental results (right) for the rolling force evolution throughout the single-pass, 20% reduction rolling schedule.....	64
Figure 58 - Finite Element results (left) and experimental results (right) for the rolling force evolution throughout the first pass in the 60% reduction rolling schedule	64

Figure 59 - Finite Element results (left) and experimental results (right) for the rolling force evolution throughout the second pass in the 60% reduction rolling schedule	65
Figure 60 - Relative displacements of a column of elements for the two single-pass hot rolling simulations (left) and for the 3-pass, 85% thickness reduction hot rolling simulation (right). Direction yy displayed as a percentual proportion to the final thickness to allow a comparison between the slabs	66
Figure 61 - Relation between the normalized and the maximum aspect ratios. Nomenclature of the subtitle indicates the slab number (1-16) and its respective thickness reduction (%), the F and Na content (Poor/Rich) and the soaking time (Low/High).....	68
Figure 62 - Influence of thickness reduction on the normalized aspect ratio of the inclusions	69
Figure 63 - Evolution of the standard deviation for the normalized aspect ratio measurements with thickness reduction	69
Figure 64 - Influence of depth on the maximum aspect ratio of the inclusions	70
Figure 65 - Influence of depth on the normalized aspect ratio of the 85% reduction inclusions	70
Figure 66 - Influence of depth on the final length of the 85% reduction inclusions.....	71
Figure 67 - Plastic equivalent strain after rolling for the 40% (left) and 85% (right) hot rolling simulations. Deformed slab profiles for each situation presented above each curve.....	71
Figure 68 - Influence of thickness reduction on the shape index of the inclusions.....	72
Figure 69 - Deformation of inclusions located in the centre of the modelled slab for a low reduction (light) multi-pass rolling scheme up to 20% thickness reduction (a) and for a higher reduction (high) multi-pass rolling scheme up to 42% thickness reduction (b).....	73
Figure 70 - Hard Al ₂ O ₃ inclusion behaviour during multi-pass cold rolling operations. Initial inclusion diameter of 20 μm	73
Figure 71 - Evolution of the relative plasticity index for inclusions located in the centre of the slab during the hot rolling process for the high reduction pass FE simulations conducted by Luo and Ståhlberg (2001)	74
Figure 72 - Evolution of the relative plasticity index with thickness reduction for the experimental data.....	75
Figure 73 - Relative plasticity index (indicated as “index”) evolution with the depth of the layer at which the inclusion is located (depth decreases for higher numbers) and the number of rolling passes	76
Figure 74 - Relative plasticity index evolution with the depth of the inclusion for the 60% thickness reduction inclusions	76
Figure 75 - Relative plasticity index evolution with the depth of the inclusion for the 85% thickness reduction inclusions	77
Figure 76 - Inclusion profile evolution for the last step of a 3-pass rolling schedule with the initial inclusion diameter	77

Figure 77 - Temperature profile in the middle of the slab at the end of the 1st rolling step (last stage of the 40% reduction rolling experiments) 2nd rolling step (last stage of the 60% reduction rolling experiments) and at the end of the 3rd rolling step (last stage of the 85% reduction rolling experiments)..... 78

Figure 78 - Average Relative Plasticity Index for the inclusions found in each slab. Slabs grouped by F and Na content (poor/rich) and soaking time (low/high) 79

Figure 79 - Average Maximum Aspect Ratio for the inclusions found in each slab. Slabs grouped by F and Na content (poor/rich) and soaking time (low/high) 79

Figure 80 - Section of the stitched BSI images for inclusion A found in the sample prepared from slab 1 at a depth of 3225 μ m (20% of the final slab thickness). Rolling direction from left to right 83

Figure 81 - Stitched BSI images for inclusions A (middle), B (right) and C (left) in the sample from slab 2. Inclusions organized (left to right) by increasing depth within the slab. Depths: inclusion C, 274 μ m (2% of the final slab thickness); inclusion A, 1736 μ m (14%) and inclusion B, 3136 μ m (26%)..... 84

Figure 82 - Temperature gradient during hot rolling for the 40% reduction hot rolling simulations. Legend in Kelvin [K] units with lower bound set at 1173 (= 900°C) to highlight only the slab temperature profile 85

Figure 83 - Path of elements chosen for plotting the temperature profile in the beginning of the contact zone, middle of the contact zone and end of the contact zone..... 85

Figure 84 - Temperature evolution with the depth within the slab for the 40% reduction hot rolling simulations conducted. Temperature profile taken in the beginning, middle and end of the contact zone. Depths of inclusions A, B and C from slab 2 marked on the curve. Only half the thickness is displayed (symmetry)..... 86

Figure 85 - Stitched BSI image section taken from inclusion A, slab 4 (top) and detail where the different phases are identified (bottom). Phases present are wollastonite (dark grey), cuspidine (light grey) and the remaining glassy phase (medium grey). Inclusion found at a depth of 1182 μ m (39% of the final slab thickness)..... 87

Figure 86 - Stitched BSI images for inclusion B of the sample from slab 6. Depth and length of the inclusion are 2194 μ m (18% of the final slab thickness) and 866 μ m respectively. Rolling direction from left to right..... 88

Figure 87 - BSI images taken from inclusion B, slab 6, highlighting the frozen transition zone between the glassy phase and the crystallized cuspidine 88

Figure 88 - BSI image “tail” sections from inclusions B (bottom) and D (top) found in the samples prepared from slab 8. Inclusions organized (top to bottom) by increasing depth within the slab. Depths: inclusion D, 606 μ m (20% of the final slab thickness) and inclusion B, 1412 μ m (47%). Rolling direction from left to right 89

Figure 89 - Temperature gradient during the last hot rolling pass for the 85% reduction hot rolling simulations. Legend in Kelvin [K] units with range set from 1173 to 1323 (=900°C to 1050°C) to highlight only the displayed slab zone temperature profile..... 89

Figure 90 - Temperature evolution with the depth within the slab for the third pass of the 85% reduction hot rolling simulations conducted. Temperature profile taken in the beginning, middle and end of the contact zone. Depths of inclusions A, B, C and D from slab 8 marked on the curve	90
Figure 91 - Detail from the Stitched BSI image from inclusion B, slab 8 where transition zone between the initial glassy structure, the following dendritic structure, the consequent broken dendrite zone and final globular structure is visible in a single image. A similar behaviour was observed for the remaining inclusions from the same sample, albeit more spread out through the inclusions, limiting its display	90
Figure 92 - BSI image of an inclusion taken from slab 7 (60% thickness reduction, rich Na/F content, low soaking time). Inclusion length of 1028 μ m. Rolling direction from left to right	91
Figure 93 - Powder metallurgy bar with visible layering.....	96
Figure 94 - Thermal cycles initially proposed for the different sample preparations	97
Figure 95 - Illustration of the CCT and TTT diagrams and corresponding approaches	97
Figure 96 - TTT diagram for slag A (Maldonado <i>et al.</i> , 2014), of similar composition to the MP-B slag	98
Figure 97 - Microstructures observed for different thermal cycles applied to the mould slag. BSE images	98
Figure 98 - Graphite crucible used by Pieter Put, 2012	99
Figure 99 - Example of a sample produced by Pieter Put, 2012	99
Figure 100 - Principles behind the proposed mechanical characterization test.....	100
Appendices	
Figure A1 - Steel slab before hot rolling. PM cylinder visible in the centre of the slab.....	105
Figure A2 - Steel slab after the 20% thickness reduction lab scale hot rolling scheme. PM cylinder visible in the centre of the slab. Example taken from slab 5	105
Figure A3 - Steel slab after the 40% thickness reduction lab scale hot rolling scheme. PM cylinder visible in the centre of the slab. Example taken from slab 2	106
Figure A4 - Steel slab after the 60% thickness reduction lab scale hot rolling scheme. PM cylinder visible in the centre of the slab. Example taken from slab 7	106
Figure A5 - Steel slab after the 85% thickness reduction lab scale hot rolling scheme. PM cylinder visible in the centre of the slab. Example taken from slab 12	106
Figure A6 - Schematic representation of the final shape of the rolled slabs and the considered final dimensions	107
Figure B1 - Mosaic of sample from slab 4 (a), 8 (b), and 16 (c) created with 50x optical microscopy images. Inclusions identified with capital letters above	109
Figure B2 - Mosaic of sample from slab 2 (a) and 6 (b) created with 50x optical microscopy images. Inclusions identified with capital letters below	109
Figure B3 - Mosaic of sample from slab 10 (a) and 14 (b) created with 50x optical microscopy images. Inclusions identified with capital letters above. It can be observed that an initial angling in the beginning of the rolling procedure resulted in a curved rolled slab	110

Figure B4 - Mosaic of sample from slab 1 created with 50x optical microscopy images. Inclusions identified with capital letters above	110
Figure B5 - Example of the length and maximum thickness measurements conducted on inclusion C of slab 2 during optical microscopy	111
Figure B6 - Example of the depth measurements conducted on inclusion C of slab 2 during optical microscopy	112
Figure B7 - Example of the area measurements conducted on inclusion A of slab 1 during optical microscopy	112
Figure C1 - Example of the analysis performed. Sample 4, Inclusion C, CaO evolution	113
Figure C2 - Compound and basicity evolutions for inclusion A, slab 4, displaying behaviour "A"	114
Figure C3 - Compound and basicity evolutions for inclusion C, slab 4, displaying behaviour "B"	114
Figure C4 - Compound and basicity evolutions for inclusion D, slab 4, displaying behaviour "B"	116
Figure C5 - Compound and basicity evolutions for inclusion D, slab 7, displaying behaviour "A"	117
Figure C6 - Compound and basicity evolutions for inclusion B, slab 15, displaying behaviour "A"	118
Figure C7 - Compound and basicity evolutions for inclusion C, slab 16, displaying a variation of behaviour "B" where CaO does not follow neither Na ₂ O nor F evolutions.....	118
Figure D1 - Examples of individual 4000x magnification BSI images taken from the 85% thickness reduction slabs, (a) inclusion A from slab 4, (b) inclusion A from slab 8, (c) inclusion B from slab 8, (d) inclusion C from slab 8, (e) inclusion D from slab 8, (f) inclusion A from slab 4	119
Figure D2 - Examples of individual 4000x magnification BSI images taken from the 40% thickness reduction slabs, (a) inclusion A from slab 2, (b) inclusion B from slab 2, (c) inclusion C from slab 2, (d) inclusion D from slab 2, (e) inclusion A from slab 6, (f) inclusion B from slab 6.....	119
Figure D3 - Examples of individual 4000x magnification BSI images taken from the 20% thickness reduction slab 1, inclusion A	120
Figure D4 - BSI images taken with Pathfinder automated capture mode. (a) Inaccurate alignment performed with the Pathfinder stitching feature, (b) images aligned manually and (c) images aligned with brightness and contrast correction. Example taken from slab 8, inclusion C.....	121
Figure E1 - Examples of the point measurements conducted. Images taken from sample 8, inclusion D.....	123
Figure E2 - Examples of the area measurements conducted. Images taken from sample 8, inclusion D.....	124
Figure E3 - Example of a point and corresponding overall area measurements (left and right respectively). Images taken from slab 8, inclusion A.....	125

Figure E4 - Example of the phase identification table created with the element composition of each measurement. Example taken from sample 8, inclusion B..... 126

List of Tables

Table 1 - Influences of the most common oxides in the viscosity, melting point and solidification point of the slag	13
Table 2 - Composition (wt%) of the mould powders (MP) used at Tata Steel.....	13
Table 3 - Schematic representation of NMI before and after deformation.....	16
Table 4 - Basicity and composition [wt%] of slag from mould powder A (Maldonado <i>et al.</i> , 2014) and difference to the slag from MP-B.....	18
Table 5 - Crystalline phases present in the inclusions for the different slabs examined	41
Table 6 - Average composition [at%] resulting from the EDS SEM measurements of the inclusions present in slab 1, with 20% reduction and low soaking time	41
Table 7 - Average composition [at%] resulting from the EDS SEM measurements of the inclusions present in slab 2, with 40% reduction and low soaking time	41
Table 8 - Average composition [at%] resulting from the EDS SEM measurements of the inclusions present in slab 4, with 85% reduction and low soaking time	42
Table 9 - Average composition [at%] resulting from the EDS SEM measurements of the inclusions present in slab 6, with 40% reduction and low soaking time	42
Table 10 - Average composition [at%] resulting from the EDS SEM measurements of the inclusions present in slab 8, with 85% reduction and low soaking time	42
Table 11 - Average composition of the original mould slag [at%].....	42
Table 12 - Chemical composition of the conventional low-carbon steel grade used. Values in [wt%]	47
Table 13 - Material characteristics for the roll and strip.....	48
Table 14 - Average composition [at%] resulting from the EDS SEM measurements conducted by Uittenbroek (2019) of the inclusions present in slab 3, with 60% reduction and low soaking time.....	80
Table 15 - Standard deviation of the results from the EDS SEM measurements of the composition of the inclusions present in slab 1, with 20% reduction and low soaking time.....	81
Table 16 - Standard deviation of the results from the EDS SEM measurements of the composition of the inclusions present in slab 2, with 40% reduction and low soaking time.....	81
Table 17 - Standard deviation of the results from the EDS SEM measurements of the composition of the inclusions present in slab 4, with 85% reduction and low soaking time.....	81
Table 18 - Standard deviation of the results from the EDS SEM measurements of the composition of the inclusions present in slab 6, with 40% reduction and low soaking time.....	82
Table 19 - Standard deviation of the results from the EDS SEM measurements of the composition of the inclusions present in slab 8, with 85% reduction and low soaking time.....	82

1 Introduction

1.1 Project Framing

The present dissertation was conducted in an internship within Tata Steel, in the Materials Engineering and Mathematical Modelling part of the Ironmaking, Steelmaking and Casting section of the Process Technology & Research portion of the R&D department, located in the CRC (Ceramics Research Centre) building of Tata Steel IJmuiden, Netherlands, in a partnership with the Mechanical Engineering Department of the Faculty of Engineering of the University of Porto, Portugal, as a Master Thesis Dissertation within the Production, Conception and Manufacturing option of the Integrated Masters in Mechanical Engineering.

1.2 The Clean Steel Project

Within Tata Steel, different final products presenting visual and mechanical defects have conducted researchers to try to understand the underlying phenomena behind it. It was not until the 8th International Conference on Clean Steel, Budapest, 2012 [1] where T. Hansén and M. Werke approached the subject of “Modelling and model validation of the deformation of macro inclusions during hot deformation” that the deformation behaviour of macro-inclusions during hot rolling started to be more heavily studied.

While these inclusions are impossible to fully eliminate, their size, shape and number should be kept below a maximum threshold value. In order to do so, the final aim of the Clean Steel Project is to have a better understanding of steel’s defects and defect mechanisms, to ultimately improve the overall quality of the steel produced.

It should be noted that the project at hand has had input from several different authors, and that the present dissertation is the continuation of the process being developed as a part of this project. Therefore, it is understandable that the starting point for the work presented is the consequence of the methodologies, conclusions and analysis made in previous works, which should be properly acknowledged.

1.3 Project Methodology

The present work was developed in an iterative way, where new procedures and directions were decided based on the results from the previous steps.

The first week was used to research the available bibliography and to get up to date with the advances made by previous interns and staff on the project, in order to get a better understanding of the subjects and principles at hand.

The following week was reserved to plan a study approach, determining details such as the number and parameters of the necessary samples, the equipment to use and the tests to perform,

based on the conclusions and preliminary analysis of the data from previous internships, and on the hypotheses proposed.

The following weeks were used to prepare the samples needed for the lab scale trial, as well as to conduct intermediate measurements. Afterwards, two weeks were used in testing and measurements using the already devised plan, followed by data treatment and result analysis.

During week 8 a progress report was conducted, and the first results evaluated. In light of the already available results and its analysis, the strategy to use in the project was revised. It was decided that, in order to fully understand the thermo-mechanical aspects of the results, a FE model would be required. To do so, the Innovation Centre at Tata Steel IJmuiden was contacted, and a new initiative to develop a 2D FE model of the lab-scale hot rolling process used in the experimental phase was created.

In the consecutive weeks, time was split between further testing and analysis on the prepared samples, and the creation and tuning of the FE model. It should be noted that the process of acquiring and testing/validating the material data and data-predicting models for the constitutive model took a significant amount of time.

The last two weeks were left to write the present dissertation, as well as to prepare the presentation of the project.

1.4 Structure

In the present dissertation, firstly, an introduction to the concepts approached is conducted. This introduction starts by contextualizing the defects that originated the project and their inclusions' origin and characterization. It is also presented a framing of the research conducted in the present thesis within the project previous to this dissertation, with a focus on the conclusions taken, and an exploration of the processes and techniques used.

Secondly, the materials and methodologies used in the manufacturing and preparation of the studied samples are presented, explaining the different processing routes and respective results.

Afterwards, the results of the conducted tests are presented. To justify and validate some of the results observed, a finite element model was created, and simulations were conducted. This stage is presented consecutively.

The following chapter regards the analysis of the results. An emphasis is made on the discussion and interpretation of the results obtained, and possible explanations and justifications are accordingly hypothesized.

Finally, the conclusions taken in the previous dissertation are properly identified, as well as the suggestions for future work.

2 Bibliography Review

2.1 Final Products Defects

As previously stated, the interest in studying inclusions and their behaviour comes primarily from the attempt to minimize the occurrence of the defects that these inclusions lead to. A particular case of inclusions is the one of Non Metallic Inclusions (or NMI for short), for which two of the major final defects on products are shown below.

It should be taken into account, however, that the presence of a Non Metallic Inclusion does not inherently lead to the presence of a defect, and that a specific inclusions tendency to cause a defect depends on the product being manufactured and on the process(es) used to get the final product [2].

a) *Griffe Laminée*

This defect, with an elongated, scratch-like appearance, is caused during hot rolling by an NMI situated at the surface of the slab (Figure 1). Despite being a visual defect, which does not induce a consequent alteration of the mechanical properties of the material, its undesirable visual and aesthetic properties lead it to be inconvenient, for example, in the automotive industry [2].

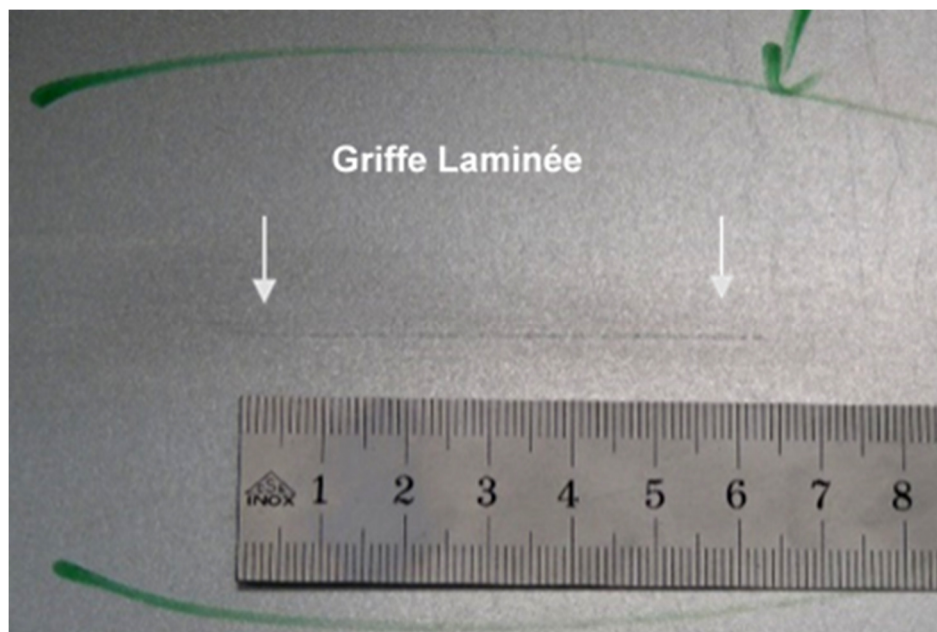


Figure 1 - Example of the *Griffe Laminée* defect [3].

b) *Split Flanges*

Unlike the previous one, this type of defect is due to an NMI much deeper in the material which induces an alteration of mechanical properties of the steel. It usually occurs in packaging steel and is a major inconvenience for the canning industry, for example (Figure 2) [2].

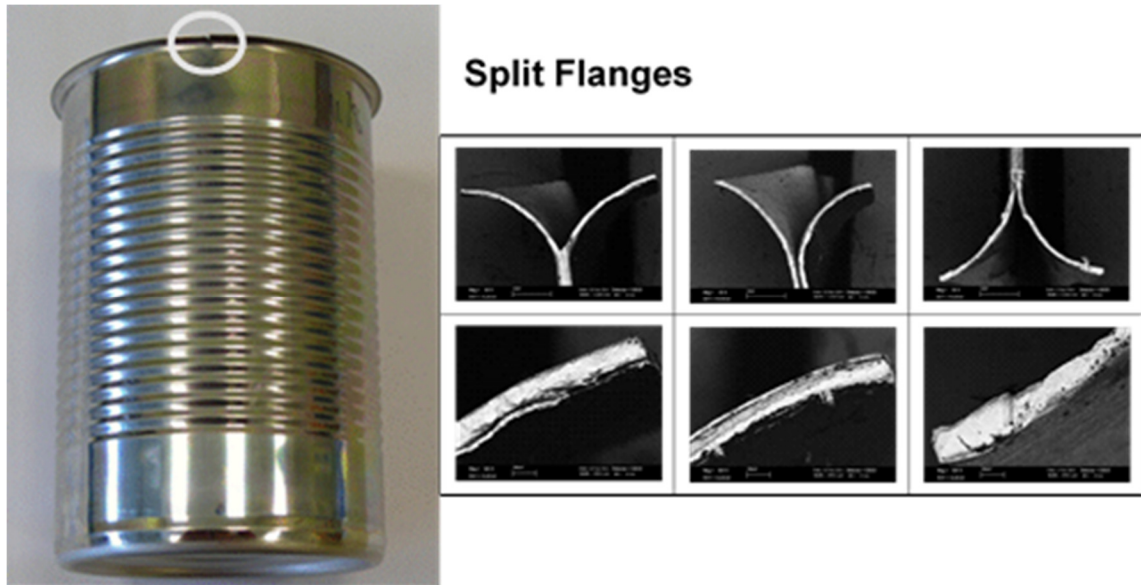


Figure 2 - Example of the Split Flanges defect [3].

2.2 Inclusion Entrapment

In order to understand the mechanisms behind these inclusions and consequent defects, one needs to understand their origins within the steelmaking process.

Firstly, in a general way, it can be considered that steel is produced through two types of processes: basic oxygen furnace - BOF (or different nomenclatures such as basic oxygen steelmaking – BOS and basic oxygen process – BOP) and electric arc furnaces (EAF). Moreover, it can also be considered that steel is mainly produced using two types of raw materials: hot metal (or pig iron), and steel scrap [4, 5].

In the BOF processes, only 25% of the raw materials is steel scrap, while approximately 75% of iron comes from the hot metal produced by blast furnace processes. On the other hand, the EAF process usually uses almost 100% of steel scrap, with some exceptions and additions (e.g. solid pig iron might be used as a purifying raw material and carbon source) [4].

Globally, as of 2014, the BOF processing route accounted for 66% of the total steel production, while the EAF route accounted for about 31%, with the remaining 3% being represented mainly by older processes [4].

It should be noted that the present work took place within Tata Steel IJmuiden, a steelmaking company that uses the BOF processing route with hot metal produced by the blast furnace (BF) process, for which the focus of the processing overview will be kept on this manufacturing route.

As can be expected, the main objective of blast furnace process is to produce hot metal with consistent quality for the BOF steelmaking process, which is achieved using iron ore as the iron-bearing raw material, coke and pulverized coal as reducing agents and heat source, and lime or limestone as the fluxing agents. This process is the main route to provide the raw

materials for the steelmaking industry, with over 93% of the total iron production from ores taking place via the BF process [4].

The hot metal (or pig iron) is then transformed into steel in converters. The basic idea of converter-using processes for steelmaking is to convert the carbon-rich liquid hot metal to the low-carbon steel. Among the different nomenclatures used (such as the aforementioned BOP, BOS and BOF), the common and distinguishing elements are *Basic*, which is referring to the basic furnace lining and slag, and *Oxygen*, used for the carbon oxidation, thus differing from older processes which used air [5]. The steel must then be converted into a usable semi-product. To that end, the liquid steel is usually cast and rolled [5].

At Tata Steel, steel slabs and sheets are produced using the continuous casting process (Figure 3), and then rolled into coils with different specifications.

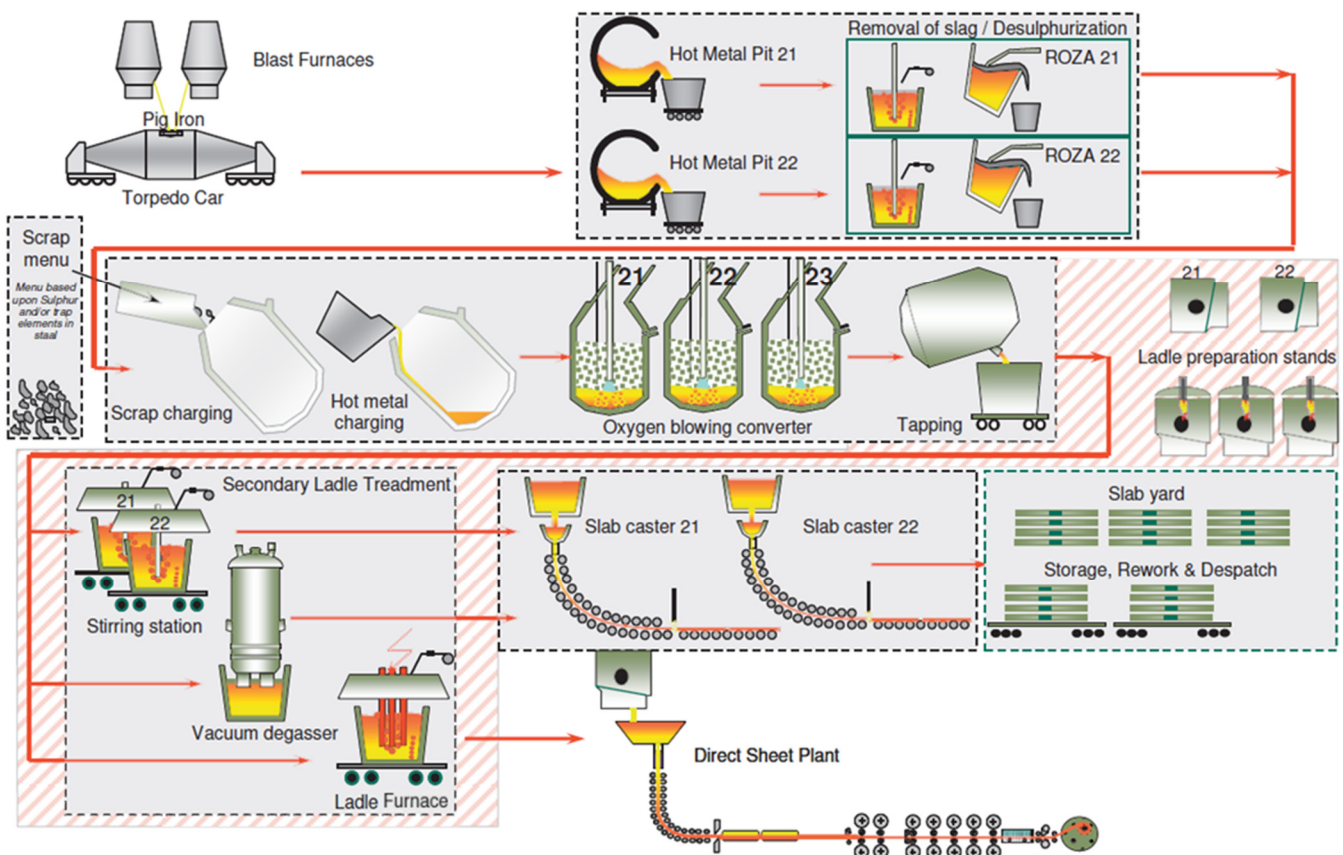


Figure 3 – Schematic representation of the BOF and continuous casting process flow at Tata Steel IJmuiden [6].

It is important to notice that the continuous casting method is the important linking process between steelmaking and rolling. Until the mid-1980s, the biggest casting method was the conventional ingot steel casting route, where individual moulds are filled with molten steel to produce steel ingots. Since then, however, the continuous casting process grew into the main methodology used (about 95% of the world's steel production), due to the benefits that it ensures when compared to the older ingot casting method in the field of steel quality (e.g. higher consistency levels of cleanliness and property values), as well as regarding energy efficiency and manpower [7, 8].

The principle behind the continuous casting method can be observed in Figure 4. Firstly, the liquid steel is transferred to the casting machine. When the nozzle at the bottom of the ladle is opened, the steel flows at a controlled rate into the tundish and from the tundish through a submerged entry nozzle (SEN) into the molten steel pool created within one or several moulds

[2, 7]. Since cooled moulds are used (usually water-cooled copper moulds), the first solidification takes place at the metal/mould interface resulting in a solidified shell with a liquid core. The thickness of this shell increases progressively, and it is sufficiently thick to support the liquid pool at the mould exit. It should be noted that the mould is subjected to an oscillatory motion so as to help prevent sticking. The solidification process continues below the mould, where the shell is further cooled by water spraying [7, 8]. At the machine end, the strand is cut off into slabs that will then be rolled [2, 7]. The resulting slab thickness is typically around 250 mm, and has been reduced to around 50 mm for “thin slab” processes [8].

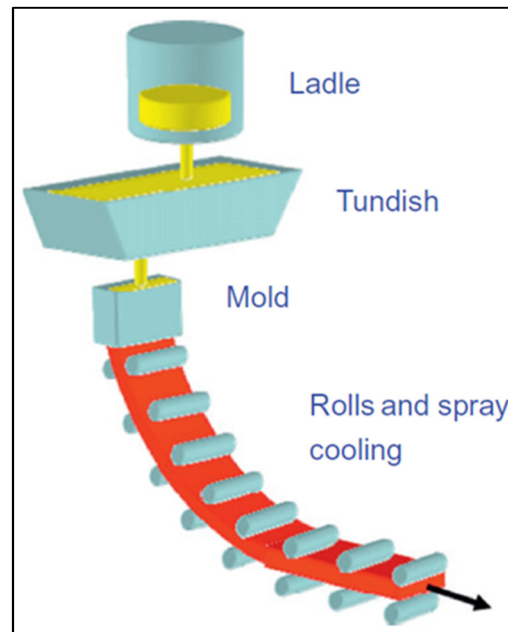


Figure 4 - Schematic representation of the continuous casting process [7].

Although steel cleanliness is significantly dictated by preceding operations, the casting itself influences the final result. It is during this stage that the inclusions studied in the present report are created, as explained hereafter.

During the casting process, a flux powder (also referred to as mould powder or casting powder) is added to the liquid steel pool. The reaction between the flux powder and the liquid metal forms several layers of flux, starting with a liquid flux layer (slag) directly in contact with the metal, followed by an intermediate quasi-sintered layer and finally the remaining powdered layer (Figure 5) [2, 6, 9].

The mould slag has specific desired functions in the steelmaking process. Firstly, it creates a protective layer from further oxidation of the steel; secondly, it infiltrates between the steel shell and the mould creating a thin slag film which solidifies into glassy and crystalline phases. The properties of this slag film dictate the main functions of strand lubrication and heat transfer between the steel and the mould, since the formation of crystals is favourable for a homogeneous and controlled heat transfer during casting, which is required in order to prevent the formation of surface cracks. Finally, the slag also promotes the absorption of inclusions present in the steel [2, 6].

However, some impurities get entrapped in the liquid flux layer and, as some droplets of liquid flux get entrapped in the molten steel by various phenomena (asymmetric flow of molten steel, droplets left in the ladle from the previous melt, etc.), these droplets are origins of NMI. These particles then nucleate and start to increase in size, leading to the studied inclusions [2, 6, 10].

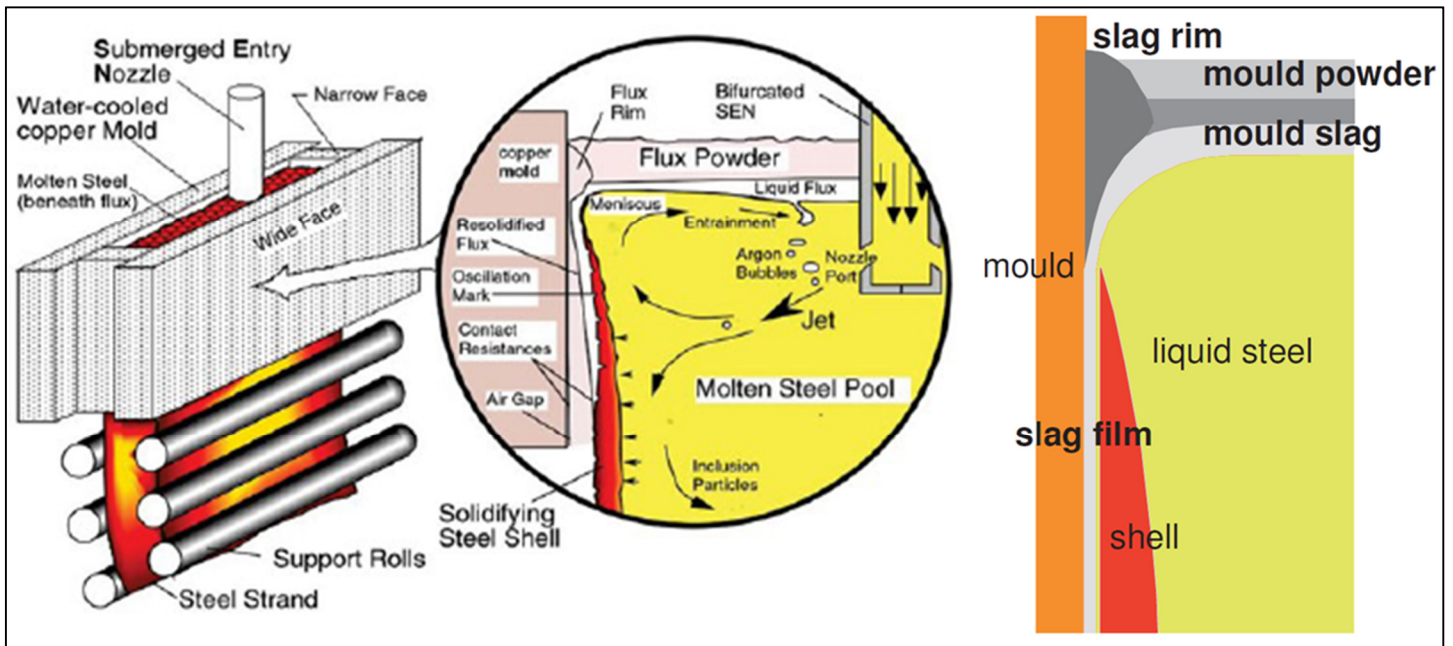


Figure 5 – Detail of the continuous casting process (left) [2] and respective mould powder layers in the mould (right) [6].

Other sources of inclusions during the process may occur (reoxidation via metal/air reactions, corrosion and chemical reaction with the refractory walls, etc.), but, given the defects at hand having been identified as caused by the NMI originated in the slag entrapment process, the focus of the present report will be kept on these [10].

It should also be noted that, as mentioned, the flux powder and consequent slag are intrinsic parts and perform desired functions in the process at hand. Therefore, the aim of the investigation is not focused on replacing or eliminating these components, but instead, on understanding the mechanisms that lead to Non Metallic Inclusions, consequent deformation and defect generation in the last stage in the semi-product manufacturing at hand, which is hot rolling.

Therefore, after re-heating to temperatures of $\approx 900-1200^{\circ}\text{C}$, the slabs are then progressively rolled down to the desired sheet thicknesses using a predefined rolling schedule and stored in coil form. Depending on the degree of thickness deformation occurring in each stand, the rolls can be divided into the initial “roughening” stands and the final “finishing” stands [8, 11]. The high temperatures achieved during the re-heating process cause the development of a thick layer of oxides, or scale which is removed in specialized de-scaling stands prior to the first rolling step [8]. Due to the attention given to the hot rolling process, especially during the modelling stage of the present work, an exploration of the mechanics and different aspects behind this process are presented followingly.

2.3 Hot Rolling

The hot rolling process, which in of itself is a subsection of the rolling processes umbrella, is, as would be expected, considerably complex to fully characterize. In the present section, instead of an extensive background along the broad scope of the different parameters present in the process, a more focused approach was used, taking into consideration the relevant aspects for the analysis of the experimental results and the parameters required for the modelling conducted.

Firstly, it will be considered that the law of constant volume is held throughout the process. Therefore, if a thickness reduction is required, the material will have to elongate either in the rolling direction or the transverse direction. Although the latter is possible for narrow bars and slabs, it is only relevant to consider that the main deformation for the problem at hand (in both the real life process and the experimental process conducted) is directed in the rolling direction, leading the slabs to elongate rather than enlarge (although with slight increases in width in the front and rear of the slab, a detail that is displayed for the lab scale process in Appendix A) [12].

Afterwards, it is important to mention that for hot rolling, the friction between the roll and the slab is the main driving mechanism behind the process. It is only with a high enough friction coefficient that the “roll bite” effect will happen, which is characterized by the gripping of the material by the roll and subsequent pulling into the rolling gap, and that the slab will ultimately be rolled [12, 13]. Besides the friction coefficient itself, this effect is governed by different aspects related to the friction phenomena (e.g. the entry angle between the slab and the roll). It is, therefore, of the utmost importance to characterize the friction behaviour during hot rolling [12, 13].

It should be noted that the friction coefficient during hot rolling is influenced by the chemical composition of the material being rolled [13]. This dependence can be observed in Figure 6, where the friction coefficient for a low carbon steel (AISI 1019) and a microalloyed steel (HSLA-Nb) are plotted against the rolling speed.

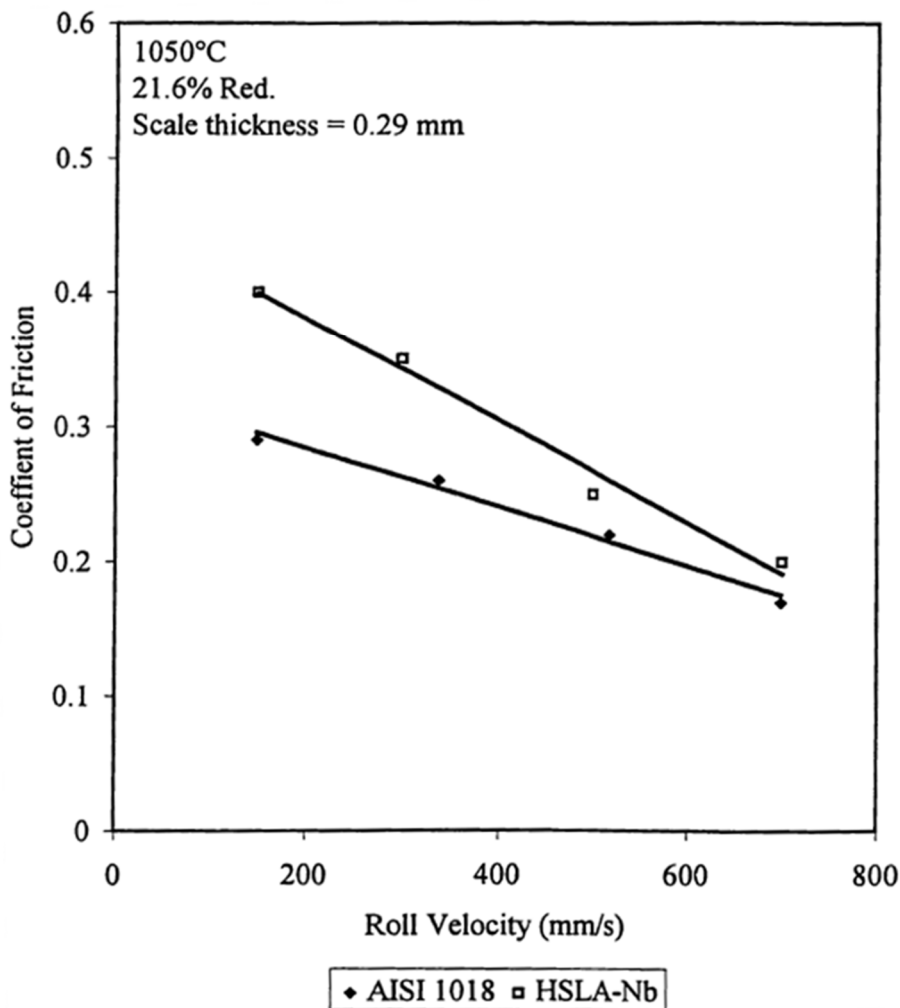


Figure 6 – The coefficient of friction as a function of velocity for two different steel grades [13].

As can be observed, not only is the friction coefficient lower for the low carbon steel grade, but it also decreases with increasing rolling speed for both steels, thus indicating yet another dependence [13].

Moreover, this parameter also depends on additional factors, some of which were studied in the experimental stages of the present work. An example of this dependence is represented in Figure 7, where the variation of the coefficient of friction with the thickness reduction is represented for several temperatures [13].

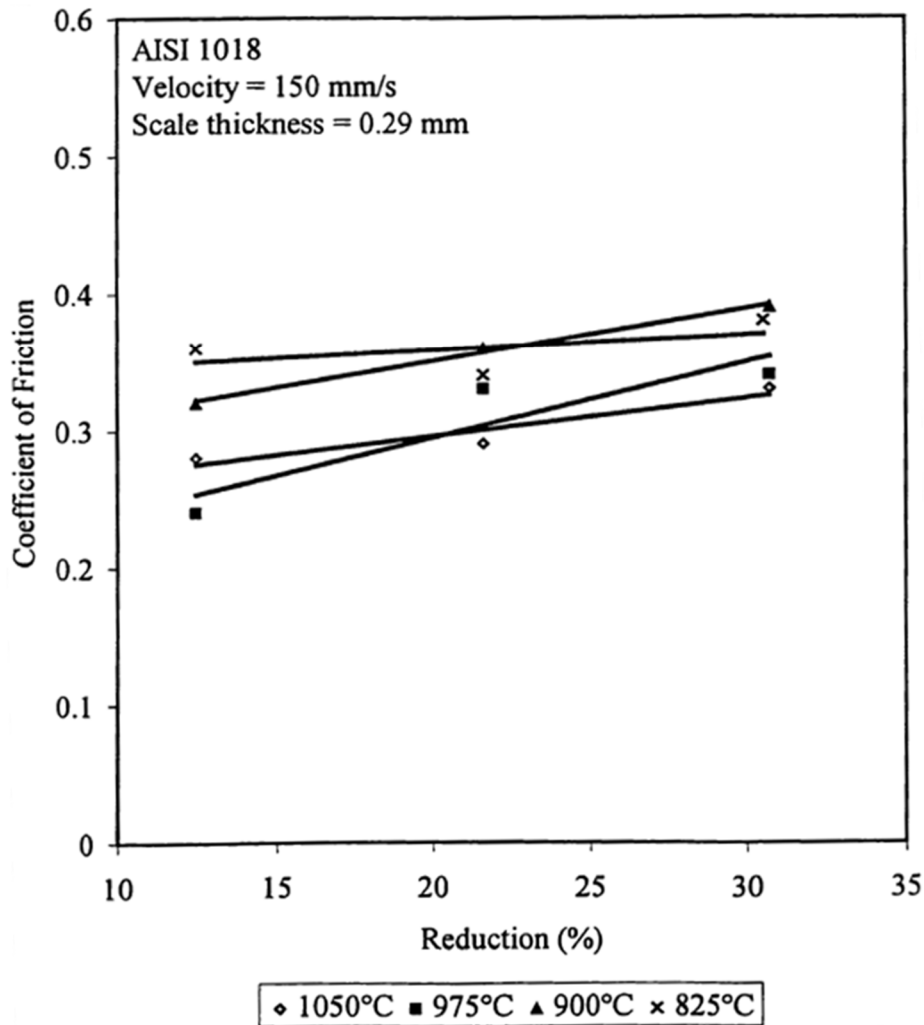


Figure 7 - The coefficient of friction as a function of thickness reduction for different temperatures [13].

As can be observed, the coefficient of friction decreases with the increase in temperature and is also expected to increase with increasing thickness reduction [13]. Since the friction coefficient plays a direct role in the rolling forces, the understanding of the evolution of this parameter can be a key aspect in interpreting the results in the present work

Besides the friction coefficient, it is relevant to refer the concept of the “neutral angle”. It is evident, considering the constant volume law, and considering that the deformation is mostly directed in the rolling direction, that the entry velocity of the roll is lower than the exit velocity of the roll. This means that it is somewhere within the contact length that a point exists where the velocity of the slab is equal to the component in the rolling direction of the tangential velocity of the roll, which results in a zone where the slab is subjected to a forward slip, and another where the slab is subjected to a backward slip, as represented in Figure 8 [12].

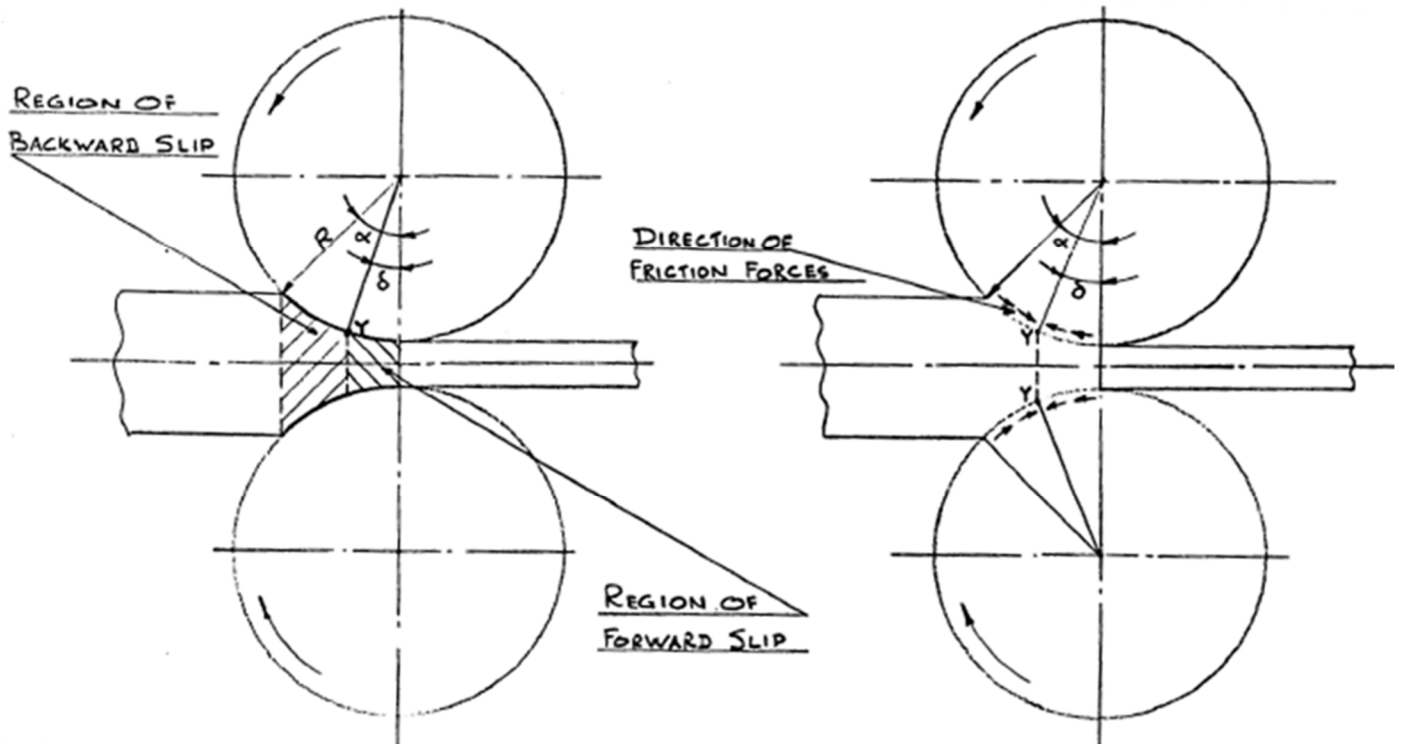


Figure 8 – Schematic representation of the neutral point and different slip regions [12].

It should be noticed that these slip phenomena are dependent on external factors, such as temperature and thickness reduction [12]. Moreover, the slip phenomena are not restricted to the surface. In fact, the existence of internal slip leads to the creation of an internal “neutral point”, where not only no slip occurs, but which leads to the creation of zones where no plastic deformation occurs [12]. This creates an “X” patterned region which is responsible for the plastic deformation at a given time in the contact zone, as can be observed in Figure 9 [12].

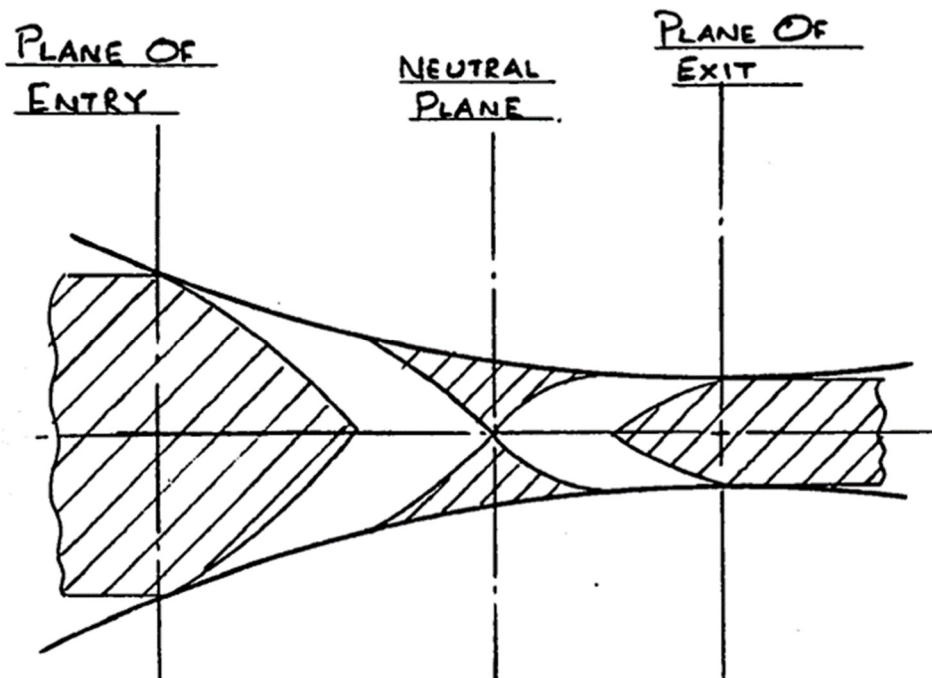


Figure 9 – Inhomogeneous deformation of material between rolls. Shaded areas are non-plastic regions [12].

With a sufficient amount of experimental data, the understanding of the rolling process and underlying mechanics could present itself to be critical in the analysis of the results of the present project, and therefore should not be dismissed. Moreover, since in the present work a FE model was developed, the phenomena presented can be used as a way to interpret the results obtained and possibly help validating the model.

2.4 Inclusion Characterization

To fully characterize the problem at hand, it is not only necessary to understand the manufacturing process in which it occurs but also the characteristics of the non-metallic inclusions whom ultimately generate it.

2.4.1 Structure and Composition

Since the flux powder is the origin of the slag that originates the inclusions at hand, it is firstly needed to explore its composition.

Given the high amount of silica, the structure of the mould slag can be simplified and described as a silicate network. The basic compound of these materials is the SiO_4^{4-} tetrahedron (SiO_4^{4-}): a structural unit with a silicon atom in the centre, surrounded by four oxygen atoms. This tetrahedron has a tendency to polymerise and to form networks as is the case of complex silicates or chains [6].

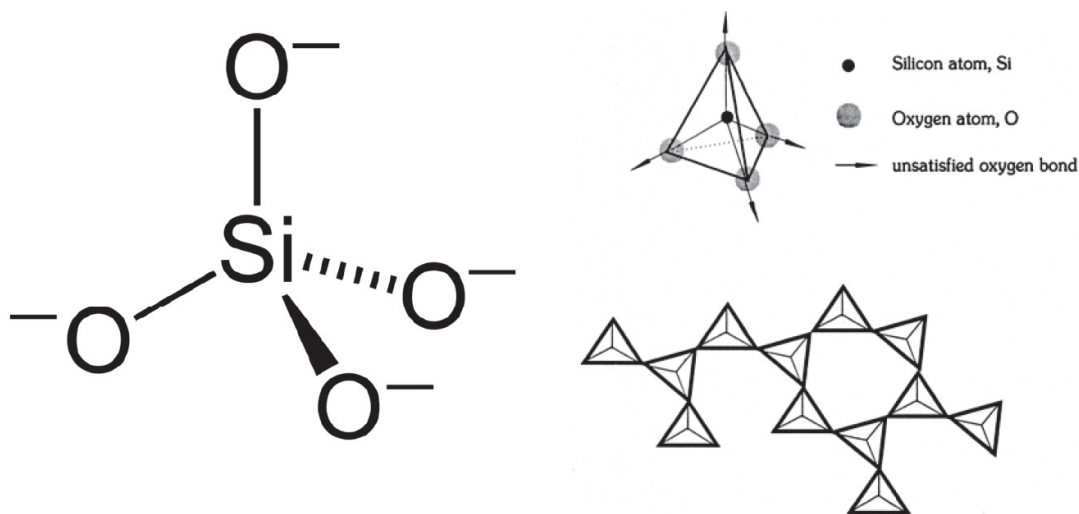


Figure 10 - SiO_4^{4-} tetrahedron (left) and a silicate network (right) [6].

This formation of networks is achieved by the complete saturation of the oxygen atoms with electrons, which can be obtained by another similar tetrahedron via oxygen bridges, in a structure defined chemically by $n(\text{SiO}_2)$. In general, these silicates have a high melting point and show a very high viscosity in the molten state [6].

Since in this structure the anion is oxygen, based on the network theory of Dietzel, cations can be classified as network-modifier, intermediate or network-former, which makes it possible to predict the effect of various cations on the silicate network [6]:

- network-modifiers: $FS \approx 0.1 - 0.4 [1/\text{\AA}^2]$
- network-formers: $FS \approx 1.5 - 2.0 [1/\text{\AA}^2]$
- intermediates: $FS \approx 0.5 - 1.0 [1/\text{\AA}^2]$.

where:

FS , is the field strength, dependent on the valence of the cation and on the ionic distance for oxides, therefore, on the radii of the ions in place.

As illustrated in Figure 11, the presence of a network-modifier like Na ($FS = 0.19 \text{ 1/\AA}^2$) or Ca, K, Li, Ba, Sr, Fe^{2+} , etc. will result in breaking of the oxygen bridges in the network. This leads to an increased mobility within the slag and, consequently, a decreased viscosity in the molten state and decreased melting point. As can also be seen in Figure 11, the divalent network-modifier ions like calcium and magnesium will break the network but still link the tetrahedra via ionic bonds. Since these ionic bonds are less rigid than the Si-O-Si bonds in the network, Ca and Mg still lower the viscosity and melting point, but less effectively. Additionally, Ca enhances the crystallisation tendency of mould slag [6].

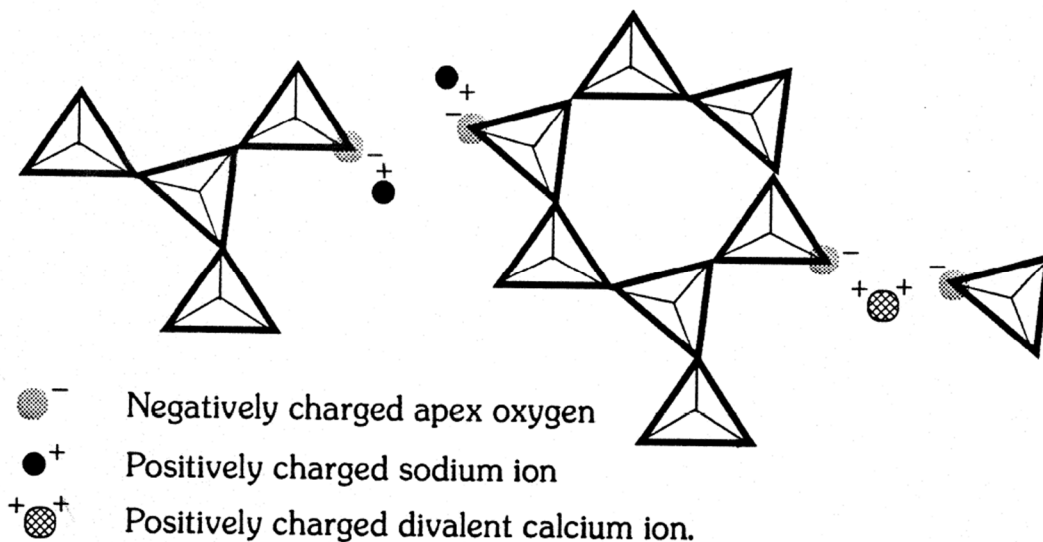


Figure 11 - Role of sodium and calcium oxides in modifying the silica network [6].

On the other hand, Mg, Fe^{3+} , Al and Ti are examples of intermediates and Si ($FS = 1.57 \text{ 1/\AA}^2$) and B are typical network-formers. Some elements such as Mn^{2+} can act both as network-modifier and as an intermediate, depending on the coordination number and ionic radius [6].

During the solidification of the mould slag, fluorine affects significantly the crystallisation performance, resulting in the crystal cuspidine ($\text{Ca}_4\text{Si}_2\text{F}_2\text{O}_7$) being characteristic of many slag compositions [14].

The effect of fluorine in mould slag, however, is a matter of research. One of the interpretations of its behaviour is that the single-valence fluorine ions will replace the oxygen within the silicate network, forming covalent Si-F bonds, leading to no further bonds being available. This causes the network to break up and reduces the viscosity of the slag. On the other hand, another description of the behaviour of fluorine is that it leads to the breaking of the network for acidic silicate slags but not for silicate networks in basic slags, for which the fluorine causes the formation of CaF_2 or stable Ca-F clusters that act as diluents [6].

The effects of sodium, calcium and fluorine in mould slag systems, including phase relations and slag crystallisation are particularly important in this field of study [6].

A summary table with the influences of the most common oxides in the viscosity, melting point and solidification point of the slag is presented in Table 1.

Table 1 - Influences of the most common oxides in the viscosity, melting point and solidification point of the slag [6].

component	viscosity	melting point	solidification point
SiO ₂	+	-	-
CaO	-	+	+
Al ₂ O ₃	+	+	-
Na ₂ O	-	-	-
F	-	-	+
MgO	-	-	-
TiO ₂	+/-	+	+
Fe ₂ O ₃	-	-	-
MnO	-	-	-
K ₂ O	-	-	-
Li ₂ O	-	-	-

+: increase -: decrease

At Tata Steel, three types of flux powder are used. Their compositions and the compositions of the resulting slags are presented in Table 2.

Table 2 - Composition (wt%) of the mould powders (MP) used at Tata Steel [2].

CaO/SiO ₂	<i>MP-A</i>		<i>MP-B</i>		<i>MP-C</i>	
	0.81		0.96		1.70	
	powder	slag	powder	slag	powder	slag
SiO ₂	32.8	37.3	33.6	38.3	24.6	27.7
CaO	26.5	30.1	32.2	36.7	41.7	47.0
MgO	1.2	1.4	0.8	0.9	0.5	0.6
Al ₂ O ₃	5.1	5.8	2.7	3.1	2.8	3.2
Na ₂ O	11.8	13.4	11.5	13.1	6.9	7.8
K ₂ O	0.8	0.9	0.4	0.5	0.2	0.2
Fe ₂ O ₃	1.6	1.8	0.3	0.3	1.6	1.8
F	9.1	10.4	8.0	9.1	10	11.3
C _{free}	4.4	0	3.9	0	5.8	0
CO ₂	7.7	0	8.5	0	5.5	0
C_{tot}	6.5	0	6.2	0	7.3	0

It should be noted that the mould powder mostly used at Tata Steel is the one referenced as MP-B, as well as that the flux referenced as MP-C is seldom used currently [2].

An evaluation of the slag can be done using the ratio between network-modifiers and network-formers. This ratio represents the concept of *basicity* and is widely used to characterize a mould powder or mould slag, as well as to predict its performance [6]. Therefore, the most common definition of the basicity for most of the slag compounds is the “V” ratio [15]:

$$\text{basicity} = \text{CaO [wt\%]} / \text{SiO}_2 \text{ [wt\%]} \quad (2.1)$$

This is the measure presented in the first line in Table 2 for each mould flux type. This definition can also be extended to encompass other compounds for some cases, such as Al_2O_3 and MgO , for example [6, 15]:

$$\text{basicity} = (\text{CaO} + \text{MgO}) / (\text{SiO}_2 + \text{Al}_2\text{O}_3) \quad (2.2)$$

With all components given in wt%.

Generally, lower values of basicity ($\text{CaO}/\text{SiO}_2 < 1.0$) result in the formation of a more glassy slag film and, therefore, improved lubrication and increased mould heat transfer. Higher values of basicity ($\text{CaO}/\text{SiO}_2 > 1.0$ for thin slab casting) result in a more crystalline and rigid slag film and, consequently, decreased values for mould heat transfer and strand lubrication. This leads to the need to find a balance in the mould flux composition such as to allow the control of mould heat transfer (crystalline slag) and the desired strand lubrication (glassy slag) [6].

Given the chemical composition of the slag, it is important to frame it within a system that encompasses all its phases. Ideally, this would be a SiO_2 - CaO - Na_2O - CaF_2 quaternary system, which is not recurrently used. It is, however, possible to find phase diagrams for the SiO_2 - CaO - Na_2O ternary system (as represented in Figure 12) or for the CaF_2 - Na_2O - SiO_2 ternary system in the Slag Atlas [15].

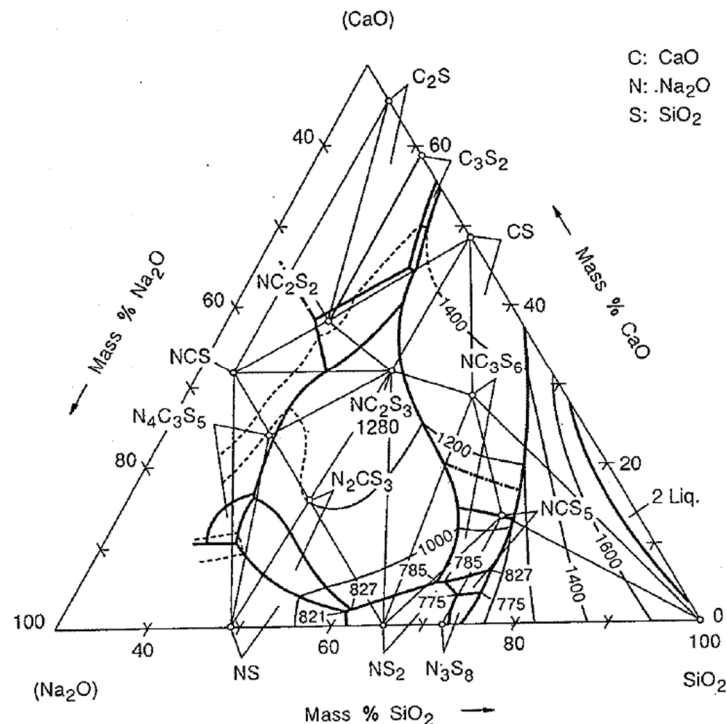


Figure 12 - Phase diagram for the SiO_2 - CaO - Na_2O ternary system [15].

Some thermochemical calculation software have also been extended for its application to mould fluxes, as is the case of FactSage, which reports being reliable for concentrations of up to 50

[at%] fluorine, and is able to calculate and generate the desired phase diagram, which can be observed in Figure 13 [16].

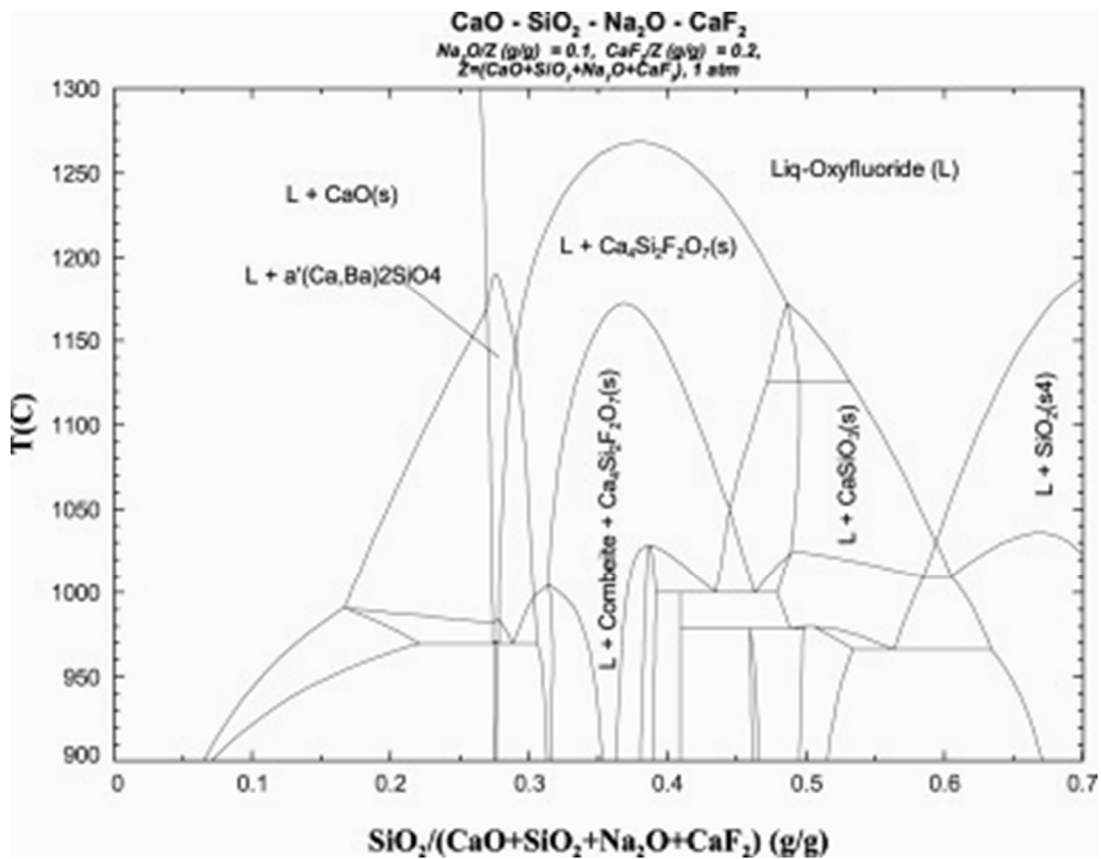


Figure 13 - Phase diagram for the SiO_2 -CaO- Na_2O - CaF_2 quaternary system [16].

2.4.2 Characteristics of Non Metallic Inclusions (NMI)

It has been established that, for steel, the amount and type of Non Metallic Inclusions influences different properties such as [17-20]:

- mechanical properties like strength and fatigue;
- ductile and brittle fracture;
- welding properties;
- machinability;
- surface polishing and finishing;
- corrosion behaviour.

Therefore, by understanding and controlling the composition, size, and distribution of these inclusions, the possibility of obtaining the desired steel properties is improved [17].

On the other hand, there are different types of Non Metallic Inclusions, differentiated by their chemical compositions and their crystallinity rate, which affect their mechanical behaviour and, inherently, the deformation behaviour during rolling [2, 17]. This differentiation in behaviour can be observed in Table 3. Moreover, examples of these inclusions for hot-rolled steel can be consulted in Figure 14.

Table 3 - Schematic representation of NMI before and after deformation [2].

Type of inclusion	Before and after rolling
a) A 'hard' inclusion	
b) A 'hard' crystalline inclusion broken	
c) A 'hard' inclusion cluster	
d) An inclusion composed of 'hard' crystals dispersed in a 'soft' matrix	
e) A 'soft' inclusion	

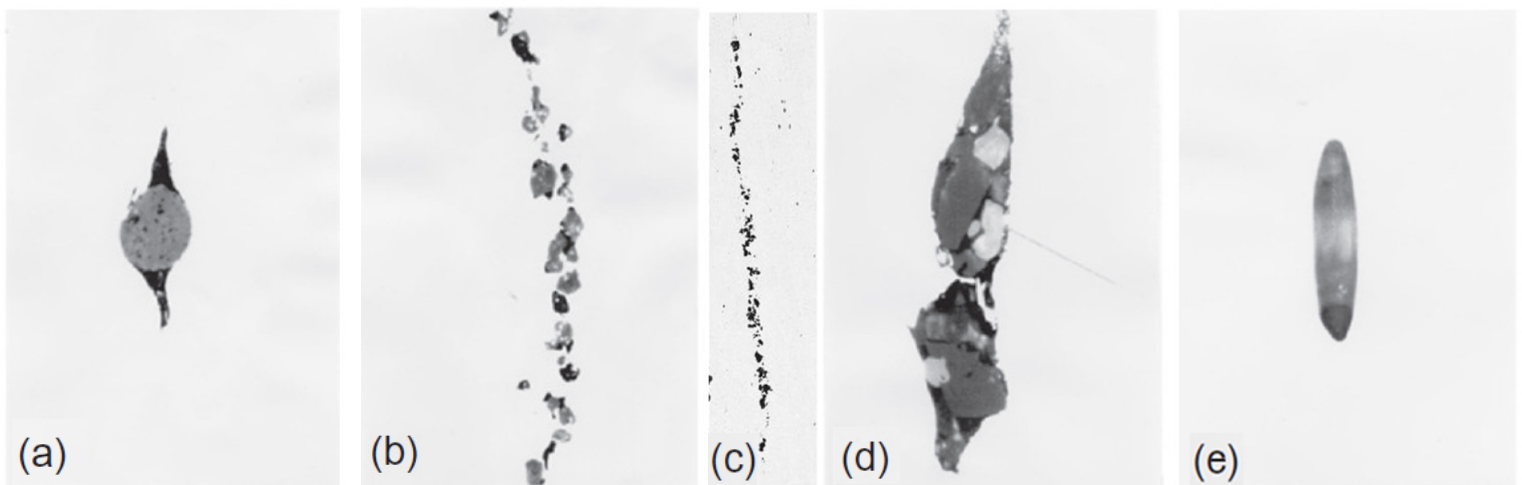


Figure 14 - Different types of inclusions in hot-rolled steel: (a) undeformed 'hard' inclusion, (b) brittle broken crystalline inclusion, (c) hard inclusion cluster (d) brittle-ductile multiphase complex inclusion and (e) ductile elongated inclusion. The scale in figures vary from few microns to tens of microns. Adapted from [17]. Inclusion (c) found in the plant trials conducted by Pille, 2016

As can be observed, the deformation behaviour of the NMI depends highly on the presence of "hard" compounds, which can be found in Al_2O_3 particles or clusters (found in (a) and (c), respectively), or crystalline structures (b), and on the presence of soft compounds, which can be found in MnS particles (e) or glassy phases [2].

It is to be noted, however, that combinations of these phases may, and do occur. In fact, a crystalline structure at high temperatures (1500°C) will be in a glassy form and behave as such. During cooling, this phase will begin to crystallize and before this process is fully complete will display a glassy matrix with crystals dispersed inside, with the behaviour observed in (d) [21].

Such is the case of the NMI at hand, which, while being rolled at 1000°C - 1200°C will display a type (d) behaviour, with the glassy phase being able to deform and the dispersed crystals (of usually Cuspidine or Wollastonite [9]) sustaining some deformation and/or breaking afterwards (Figure 15) [21]. Therefore, the overall deformation behaviour of the NMI depends highly on the crystalline/amorphous rate present at the rolling temperature, which in turn depends not only on the chemical composition but also on the cooling rate applied.

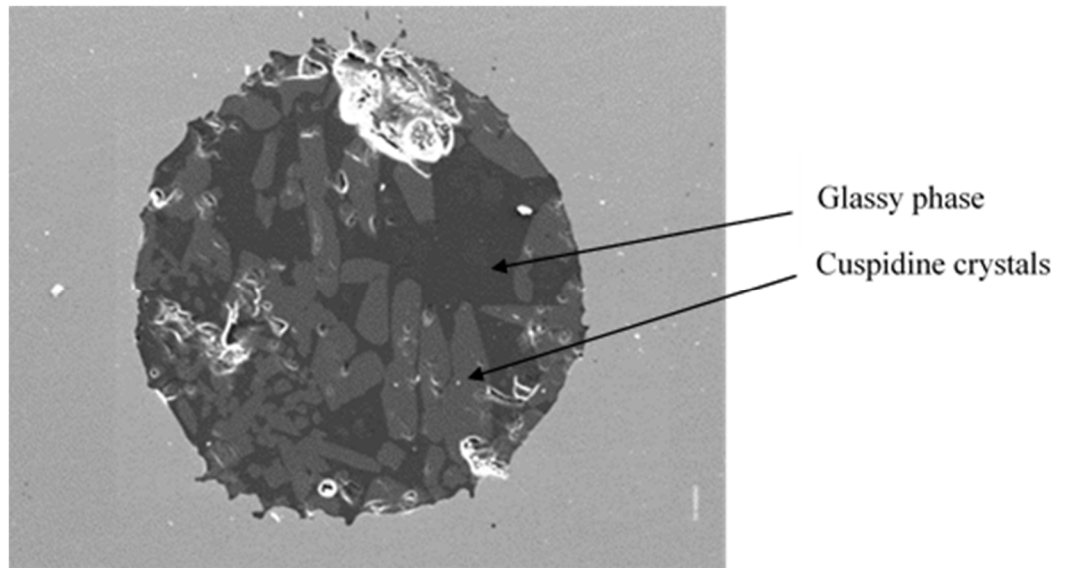


Figure 15 - SEM picture of a multiphase Non Metallic Inclusion [21].

This time-temperature dependant, semi-crystalline, structure found in the NMI leads to the conclusion that the study of the crystallization process of the slag is of the utmost importance to the study at hand. On this subject, it is firstly important to distinguish that the phenomenon of formation of crystals during cooling of liquid slag is classified as crystallization, and that the formation of crystals during heating of glass (which is formed by quenching liquid slag) may be classified as devitrification [22].

Given that the origin of the NMI at hand is the slag that is present in the mould and subsequently entrapped in the steel, the temperatures and temperature gradients during this phase should firstly be considered. In the commercial continuous casting process, the average cooling rates of the mould slag are of approximately -1200 to $-1500^{\circ}\text{C}/\text{min}$ with local cooling rates reaching -3000 to $-6000^{\circ}\text{C}/\text{min}$. Therefore, local cooling rates (especially near the mould wall) may be substantially higher than the lowest rate at which a melt can be cooled from T_l (*liquidus* temperature) to below T_g (glass transition temperature) without crystallizing, leading to the formation of an initial solid glass phase in the slag [22].

The temperature of the slag film on the mould side, however, is not as low as on the mould wall, ranging from 300°C to 500°C , which can lead to devitrification of the solid glass phase if it has enough time in the mould to re-heat. This may lead to a partially crystallized structure [22].

On the other hand, on the face of the slag film in contact with the steel, temperatures decrease from the steel *liquidus* temperature, at the top, to $\sim 1000^{\circ}\text{C}$ for thin slab casting or $\sim 1150^{\circ}\text{C}$ for conventional slabs. This thermal gradient and the consequent cooling rate often enable crystallization to happen in the liquid phase, leading to an overall slag structure that might contain a solid glass phase, a devitrified crystal phase and a crystallized phase in the mould [22].

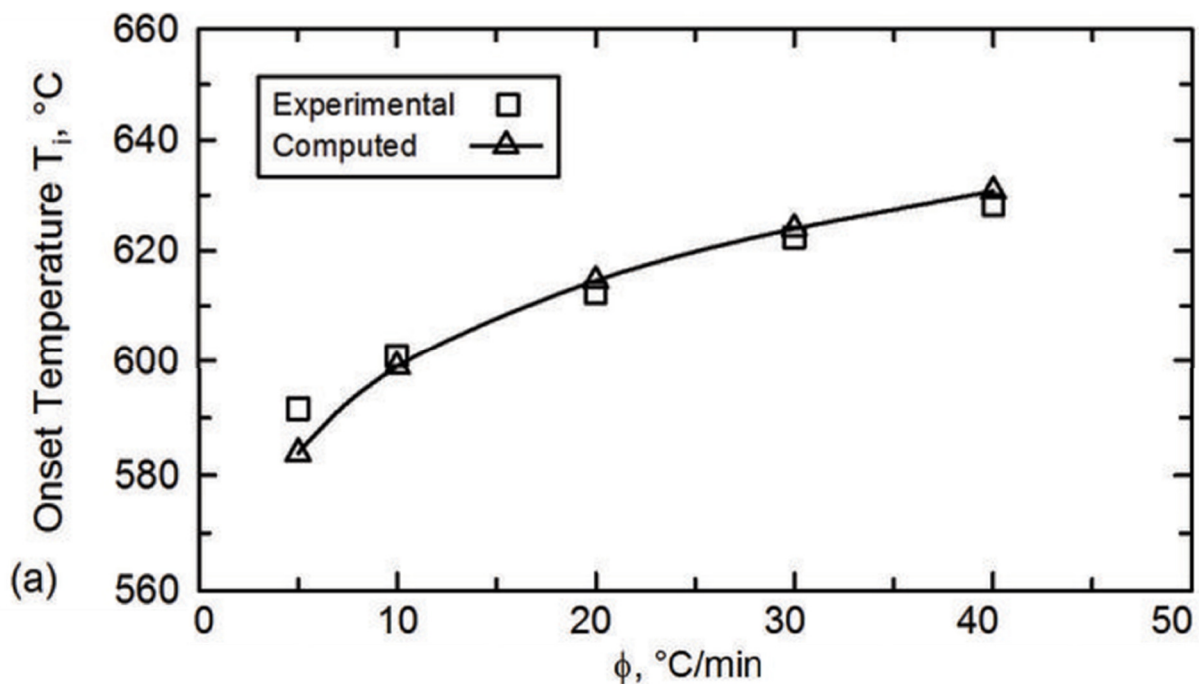
Research has been conducted in the matter of the devitrification and crystallisation phenomena for mould slags by Maldonado *et al.* (2014), leading to the estimation of TTT diagrams (presented in Section 8.2) for two different mould slags, one of which presents a similar composition to the one studied in the present thesis (with a maximum difference felt in the MgO content, which is higher by 2.92wt%), as presented in Table 4 [22].

Table 4 – Basicity and composition [wt%] of slag from mould powder A (Maldonado *et al.*, 2014) [22] and difference to the slag from MP-B.

Slag	Basicity	SiO ₂	CaO	MgO	Al ₂ O ₃	(Na ₂ O+K ₂ O)	MnO	F
A (Maldonado <i>et al.</i>)	0.94	37.0	34.8	3.8	3.3	13.6	-	7.6
Difference	0.02	0.55	1.18	2.92	0.26	0.27	0.00	1.32

During this research it has been established that two main peaks of phase transformation occur during devitrification, corresponding to the formation of cuspidine and combeite, a result that is also observed in the lab scale studies performed by previous interns in the project of this thesis (section 2.4). Only a main peak could be observed during crystallization, which should not be taken as an indicative that only one phase is present, since the number of peaks is not directly related to the number of phases [22].

The onset and maximum temperatures of these phases are also dependent on the heating and cooling rates, being that the higher the rate applied, the less time the material is at a given temperature range, leading to an increase in the start and end of transformation temperatures for devitrification, and to a decrease in the same temperatures for crystallization, as exemplified for the cuspidine peak during devitrification of mould slag A in Figure 16 [22].


 Figure 16 – Measured and computed onset temperatures as a function of heating rate (ϕ) for peak 1 (cuspidine) during devitrification of mould slag A [22].

This dependence on the heating/cooling difference and respective rates is not only applied in the entrapment phase of the inclusions during casting but also subsequently, during the rolling process. This phenomenon, however, is significantly different to define, due to the complex thermodynamics and temperature profiles felt during the rolling process, which can be observed in Figure 17 [23].

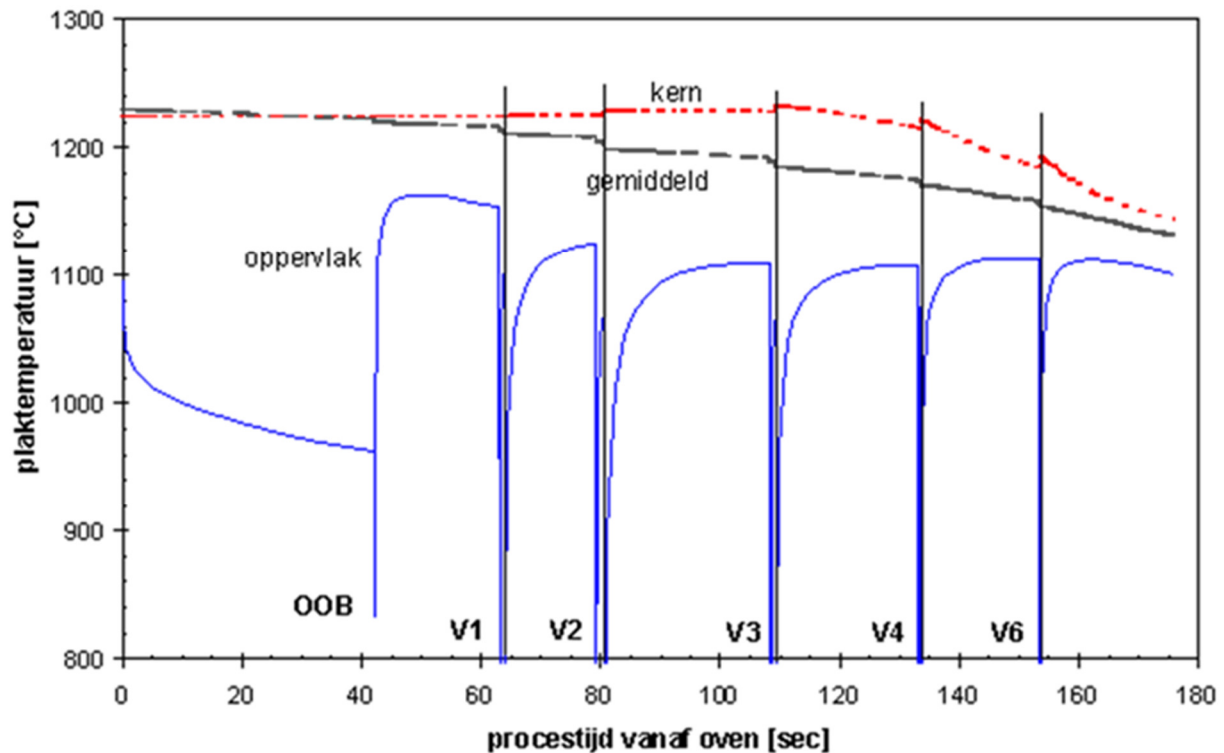


Figure 17 – Temperature (yy axis) as a function of processing time (xx axis) for the different rolling stations (V1 through V6) at the centre of the slab (*kern*, red) and at the surface of the slab (*oppervlak*, blue) [23].

As can be observed, the temperature profile (and consequent cooling/heating rates), specially at the surface of the slab, is not linear. At the start of the process there is an expected temperature gradient between the centre and the surface of the slab, with the centre temperature decreasing, due to the convection and radiation felt at the surface. Once the first roll, which is water-cooled, touches the slab there is a steep drop in surface temperature, which lasts a few seconds, the time that takes the slab to pass through the roll. Due to the relatively high thickness of the slab at this stage and the relatively high speed of the process, the centre temperature remains unchanged by the rolling process. Once the first rolling step is finished, it can be observed that the surface temperature rises. This is a result of the conduction felt between the centre and the surface of the slab, in an attempt to equilibrate the thermal gradient imposed in the process. These cooling and re-heating phenomena are repeated throughout the consecutive rolling steps, with the slight difference that, with the decrease in slab thickness, the centre temperature also begins to be affected during rolling, although only slightly, since the speed of the slab also increases from step to step, reducing the heat transfer time in each step.

As can be expected, the various temperatures, heating rates and cooling rates felt throughout the casting and rolling processes will lead to complex, composition-temperature-time dependant, microstructures of the resulting NMI, which will ultimately affect the final deformation behaviour during rolling.

2.5 Previous studies

As previously mentioned, the work developed during this internship is a continuation of the advances being done in Ceramic Research Centre of Tata Steel IJmuiden by both interns and staff. Therefore, an overview of the main procedures, findings and conclusions over the course of the project is of the utmost importance to understand the course taken.

- **Derk Doppenberg et al. (2014):** “*Evolution of macro-inclusions in steel during hot deformation - Development of model material*” [24]

The aim of the work developed in this first stage was the modelling of steel samples with inclusions placed at known locations, in order to study their deformation during hot rolling.

To do so, it was chosen the process of powder metallurgy with inclusions added at different depths. By alternating powder layers with different molybdenum content, an internal reference system was created, using the different visual properties (coloration) that this element provides after etching.

It was concluded that the chosen route led to viable samples, having, however, problems related to porosity and cracking between the different layers.

- **Luij George (2015):** “*Master Thesis - Deformation behavior of macro-inclusion during hot-rolling of steel*” [25]

In this stage it was intended to devise a methodology by which it could be possible to understand the deformation behaviour of inclusions.

Experimentally, the sample preparation route developed in the previous stage was used, followed by the rolling of the samples, Non Destructive Evaluation (using radiography) and Analysis (Image and Microstructure).

It was concluded that this methodology was viable and that the processing parameters should be optimized in order to obtain the best possible results.

- **Avinash Kandalam et al. (2016):** “*Modelling and Validation of Deformation Behaviour of Macro Inclusions during Hot and Cold Rolling*” [26]

This stage in the project was aimed at studying the deformation behaviour of hard Al_2O_3 particles, MP-B slag particles and soft, low melting point, Borax particles.

It was concluded that the average deformation for the MP-B particles is independent from the depth at which they are located, although standard deviation is lower for particles located near the centre of the slab. These particles also displayed a behaviour in which they fragment and form a line after some rolling passes.

It was also validated that the alumina particles don't deform but start to break after some rolling passes.

Finally, it was observed that the Borax inclusions tend to flow through the pores in the material, highlighting that the porosity obtained from the powder metallurgy process is a major problem in the experimental validation.

- **Imad Khlifi (2016):** “*Study of the deformation behaviour of macro-inclusions during hot rolling*” [27]

With this work it was possible to identify the role of temperature and heating/cooling rates in the deformation behaviour of the inclusions, and to establish its influence on chemical composition of mould slag and the degree of crystallinity, along with the nature of the formed crystals.

Furthermore, the liquid state inclusion content at the rolling temperature was concluded to be of critical importance to the longitudinal and transverse deformation observed.

This conclusions regarding chemical composition and crystallization would later on be echoed throughout most of the further reports, eventually taking a bigger role than inclusion depth within the slab.

- **Laurens-Jan Pille (2016):** “*Clean Steel Project - A study of the deformation behaviour of macro-inclusions during hot deformation at plant conditions*” [23]

The main goal of this phase was translating the lab testing into real full-sized slabs. Various cylindrical samples were produced and embedded into a real-size steel slab, which was hot rolled in 12 steps with a thickness reduction of 98.9%.

The samples were then retrieved from the slab and studied.

The results obtained from this full-scale experiment were concluded to be in accordance with the lab experiments, thus validating the methodology used, and resulting in a process that can be applied in further studies.

- **Bernadeta Karnasiewicz (2017):** “*Evaluation and Characterization of the In-house Produced Artificial NMI Inclusions*” [28]

It was during this stage that it was identified that the inclusions studied in the experiments did not accurately represent the real slag inclusions that lead to the undesired defects.

Among the differences observed are incontrollable amounts of Al/Al₂O₃, incorporation of alloying elements (Al, Mn) into the system, dispersion of the mould slag into the residual porosity of the steel matrix and, most significantly, the (almost complete) loss of Na and F during the processing route. This resulted in a considerable difference in the morphology and behaviour from the real inclusions, which rendered the results insufficient to fulfil the aim of the project.

A new processing methodology that allowed the inclusions to maintain their Na and F contents was therefore suggested, which included stages of decarburization, homogenization, and crushing to the right size.

- **Karim Geussous et al. (2017):** “*Investigation on chemical composition of macro-inclusions and its influence on deformation behavior during hot rolling*” [29]

In this stage, the processing methodology proposed by Karnasiewicz (2017) [28] was used, and the resulting samples were studied after rolling.

It was concluded that although the Na and F loss was considerably minimized, the inclusion's liquid phase was still prone to infiltrate in the porosity present in the samples, influencing the inclusion's deformation behaviour, and rendering it impossible to highlight the effect of the amount of Na/F compounds.

In order to overcome the porosity and the remaining loss of Na/F, a different sample preparation process using Hot Isostatic Pressing (HIP) was suggested.

- **Thomas Meyneng et al. (2017):** “*Characterisation of the deformation of macro inclusions in slabs during hot deformation pilot trials*” [21]

This stage of the study started by still using the powder metallurgy route to obtain the samples. This led to the same phenomenon previously observed, where the liquid glassy phase infiltrates in the porosity of the samples. It was, however, concluded that among the remaining crystallite phases present, small crystals tend to deform easier than large ones.

It was also during this study that the first samples using the suggested HIP were created and preliminarily observed. They were concluded to be representative of real slag compounds (the loss of Na/F was minimized) and of real steel structure (the density achieved reached values of 98% instead of the earlier 80-85%).

- **Corentine le Bihan et al. (2018):** “*Characterization (e.g. SEM, microscopy techniques) of the deformation of macro-inclusions in slabs during hot deformation pilot trials*” [2]

During this stage, the composition and morphology of the samples produced in 2016, during Laurens-Jan Pille’s internship (2016) [23] were analysed.

It was discovered that instead of the crystals of cuspidine ($\text{Ca}_4\text{Si}_2\text{F}_2\text{O}_7$) and combeite ($\text{Na}_2\text{Ca}_2\text{Si}_3\text{O}_9$) surrounded by a glassy phase that were expected, 100% pure crystals of wollastonite (CaSiO_3) were found in the samples with slag inclusions from MP-B and MP-A mould powders and 2CaO-SiO_2 and rankinite ($\text{Ca}_3\text{Si}_2\text{O}_7$) for the MP-C mould powder. This was concluded to be a consequence of the loss of F and Na, still present in the processing used in the 2016 stage which originated these samples. This rendered the results not to be representative of the real problem at hand.

- **Lennard Uittenbroek (2019):** “*Characterisation of Macro-inclusions in Steel after Deformation by Hot Rolling*” [9]

This stage used the samples produced with HIP as the final sintering stage, which were press-fitted into slabs of 100x80x20mm, submitted to an isothermal stage, hot rolled to different thicknesses and studied using optical and SEM microscopy techniques. The inclusion production was organized in a way that inclusions with both a high and a low Na and F content were obtained. The effects of Na and F content, thickness reduction and isothermal stage time were studied.

It was once again verified that the usage of HIP results with samples with inclusions that resemble real mould slag Na and F concentrations in a steel matrix with considerably reduced porosity. However, it was also noticed that the F content was high, even for the supposedly low F inclusions, revealing a possible flaw in the processing phase. The phases observed in the inclusions consisted of cuspidine, wollastonite, glass and a yet unidentified dendritic phase (in the Na/F-rich samples with higher isothermal times).

The deformed inclusions did not present crushed clusters, indicating that they were in a mostly liquid state during rolling. However, the inclusions in the 85% reduction samples not only exhibited a significantly higher deformation but also appeared to have developed a “drop-like” shape in the rolling direction, displaying a thicker zone in the “tail” direction of the slab and a thinner zone in the “head” direction of the slab.

It was not possible to observe a difference in the morphology and geometry of the inclusions observed with the depth in the slab, a difference that is known to be present at full scale. This indicated a need to upscale this study to verify if these differences can be identified.

2.5.1 Processes and Techniques

In order to fully understand the processes and methodologies mentioned in this overview and used throughout the present work, a brief contextualization of some of these items will be presented in the following sections.

Powder Metallurgy

In the experimental stage of the present work, powder metallurgy was behind some of the procedures used, leading to a brief introduction of this process hereafter.

Powder metallurgy (PM) is the technology that allows to produce metallic components from powders instead of the classical routes [30]. Besides being applied to materials that are not accessible or cannot achieve the properties required by other routes (e.g. WC-Co hardmetal), this process also offers economical manufacturing of complex-shaped parts in large numbers (e.g. automotive camshaft belt pulleys) [30].

This is something that is also applied for ferrous powder metallurgy products. In fact, the group of sintered steel components is the largest group of PM products (regarding weight) due to the geometric complexity and precision required, combined with large production volumes. In this case, the production route is usually composed of phases of pressing and sintering, resulting in parts that are not fully dense, as mentioned in the project overview [30].

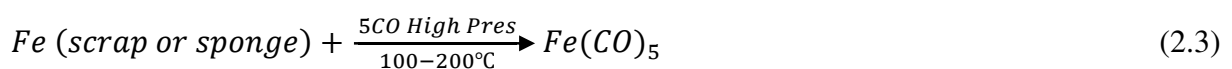
It should be mentioned that several techniques can be used to further extend the application of powder metallurgy technology (Metal Injection Moulding, Spray Forming or even Selective Laser Sintering/Melting are examples of extensions of Powder Metallurgy processes), but, since the present work will be using parts produced by the traditional pressing and sintering process (with an additional HIP phase, to be explained afterwards), the focus will be maintained in this type of processing technique [30, 31].

In this case, the process starts with the phases of powder production and preparation. Various methods can be used for powder production [32]:

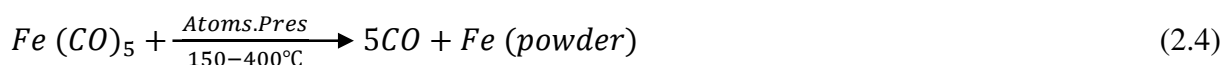
- *atomization*, which can be used for any metal or alloy system that can be melted;
- *chemical reduction*, which consists in the production of sponge iron from scale or iron oxides;
- *mechanical crushing*, which is mainly used for brittle materials (e.g. antimony and beryllium);
- *electrolysis*, mainly used for deposition of high purity powders.

The atomization and reduction processes are the most widely used in large scale production, while mechanical crushing and electrolysis are used mainly small quantities of specialty materials [32].

The chemical reduction (also known as decomposition) process is often regarded as the best process to achieve high purity powders. In this method, the compound of a metal is broken down so that the metal forms in a particle form [33]. Some iron powders, including the one used in the present project, are produced commercially by decomposition of their carbonyls (coordination complexes of metals with carbon monoxide ligands) which, when mixed with an inert gas, lead to decomposition away from the walls of the vessel and spherical particles with an onionskin-layer structure are produced [33]. A schematic representation of this type of process is shown in Figure 18. The reactions involved in the formation and decomposition of the iron carbonyl can be observed hereafter [33]:



and:



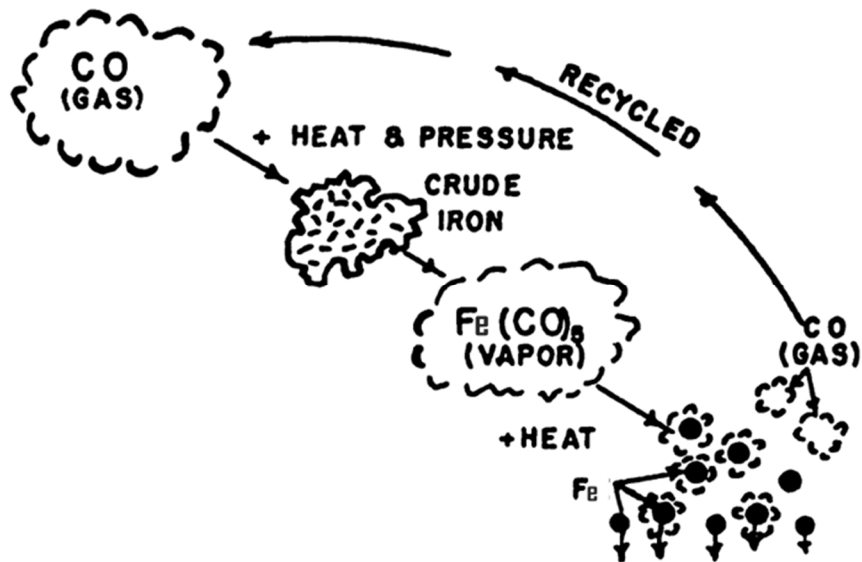


Figure 18 - Schematic drawing of the iron decomposition process. Adapted from [33].

Subsequently, the preparation of the produced powders usually consists of classification, blending and preliminary processing.

During classification, powders (of different sized particles), are divided into fractions of different coarseness. To do so, the equipment used is a combination of various sieves or screens, with sizes and materials adapted to the powder at hand and desired size [34]. In the blending stage, powders with different chemical compositions and alloying elements are mixed to form a charge with the required composition and consequent physical properties [34].

During preliminary processing, the physical properties of the powders (e.g. compressibility) are tuned to the desired specification via thermal or mechanical processes [34].

The process of introducing binding agents consists of soaking the powder mixture in a solvent and binder solution, stirring it thoroughly. Afterwards, the mixture is dried in order to remove the solvent and sieved or passed through a strainer to avoid even the smallest of lumps, which can cause defects during pressing [34].

The next main stage of the process consists of forming of the mixed powder into a compact via pressing. As expected, the equipment used in this stage usually consists of hydraulic or crank presses, with single or double action [35]. It is important to notice that after this stage, the strength of the "green" compacts must be sufficiently great to withstand the handling and any operations performed prior to sintering, with the risk of cracks developing in the product which will be kept in the final component [35, 36].

Other considerations should also be made in this stage. For example, the compressibility of powders is influenced by their preliminary treatment. When powders are pre-treated in ball mills their apparent density raises and they suffer work hardening. This demands increased pressures for compacts of low density, with the influence of work-hardening decreasing with increasing density of compact, reaching a stage, for high density compacts, where the initial work-hardening of the powders is of no importance due to the high pressures required during pressing (the pressing itself is a source of work-hardening) [35].

Preliminary heat treatment also has a considerable influence on the properties of powders since it removes work hardening and affects the apparent density of the powder (decreasing with low-temperature annealing or increasing with high-temperature annealing) resulting in changes in the pressure required for high-density compacts [35].

The last step in the powder metallurgy process is the sintering of the compact to enhance integrity and strength. This process step involves heating of the material, usually in a protective atmosphere, to a lower temperature than the melting point of the basic ingredient in the charge. In some cases, a minor constituent may form a liquid phase during sintering; such cases are described as liquid phase sintering [37].

Hot Isostatic Pressing (HIP)

Another process used along with powder metallurgy during the experimental procedure, and which requires a brief explanation, is the HIP process.

The basis for the Hot Isostatic Pressing method is the application of pressure and temperature simultaneously. Its particularity, however, is that the pressure application is made through an isostatic medium, which results in it being transmitted to the material with a constant intensity in all directions. HIP can be used directly on powders, or, as happens in this case, pre-sintered parts [38].

Due to the high temperatures at which the pressure is applied, an inert, noble gas heavy enough to transmit the pressure is required. Therefore, the gas usually selected to do so is Argon, which could transmit the pressure at temperatures higher than 2000°C [38].

Different advantages can be obtained when using HIP: firstly, despite being a high temperature process, because the combined effect of pressure and temperature improves the sintering efficiency, the temperature of the process can be significantly lower than conventional sintering temperatures, thus resulting in smaller grain sizes and more importantly, minimizing the loss of volatile elements such as Na and F, critical to this study [2]; secondly, due to the pressure being isostatically applied, the final product is isotropic in all properties; and finally, as mentioned, the maximum density can be nearly achieved, with residual porosity so small and rounded that it is not detrimental to the mechanical properties of the material [38].

In summary, with HIP one can obtain a material close to the real, bulk processing one, with a high control of the chemical composition (minimizing the loss of Na and F), close to the maximum density, isotropic properties, and good control of the microstructure with small grains [38]. A schematic representation of a typical HIP equipment can be observed in Figure 19.

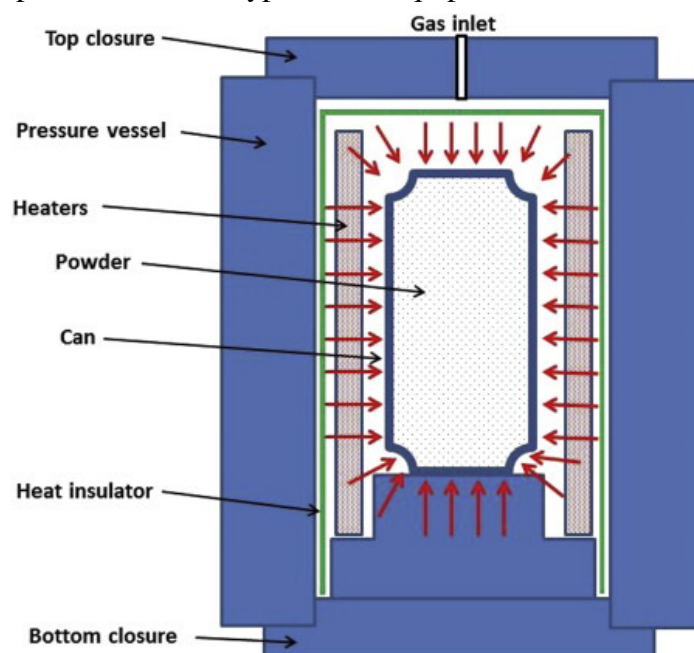


Figure 19 - Hot isostatic pressing system representation [38].

Scanning Electron Microscopy (SEM)

As mentioned in the overview, the use of Scan Electron Microscopy (SEM) has been, and will continue to be throughout this report, detrimental to the analysis of the deformed inclusion being studied. Therefore, an introduction to this technique and its variants should be explained.

Firstly, it is relevant to contextualize the electron microscopy technique in relation to the optical microscopy techniques. To do so, one needs to look no further than the resolution and its inherent principles.

In optical microscopy, resolution is dependent on the physical phenomena of light. Therefore, it is limited by the mechanics that dictate optics, particularly refraction, before interference occurs. Since for visible light the wavelength varies between 400 to 800nm, the resulting maximum resolution is limited to approximately $0.2\mu\text{m}$ [39].

On the other hand, since electron microscopy does not use light, the wavelength is not limited to its physical properties. Instead, variable wavelengths can be obtained as a function of the frequency and energy of the electron beam used [39].

Since for SEM the energies used correspond to acceleration voltages of approximately 100V to 30kV, the resolution obtained can reach values of 3.5 - 1nm, reaching values of $\sim 0.5\text{nm}$ in the best cases [39]. It is therefore possible to distinguish a whole different window of usage for SEM when compared to optical microscopy.

Secondly, it is important to mention that among the SEM umbrella, several functioning modes can be used, each with its own different working principle behind. Some of these modes are inherent to the process at hand, and other may require additional equipment to compliment the basic SEM functionalities. Concerning the first type, its basis consists of the phenomena that occur when the primary electron beam hits the sample surface and the incident electrons are able to interact with the nuclei of the atoms. A representation of the different possible behaviours observed can be consulted in Figure 20 (left).

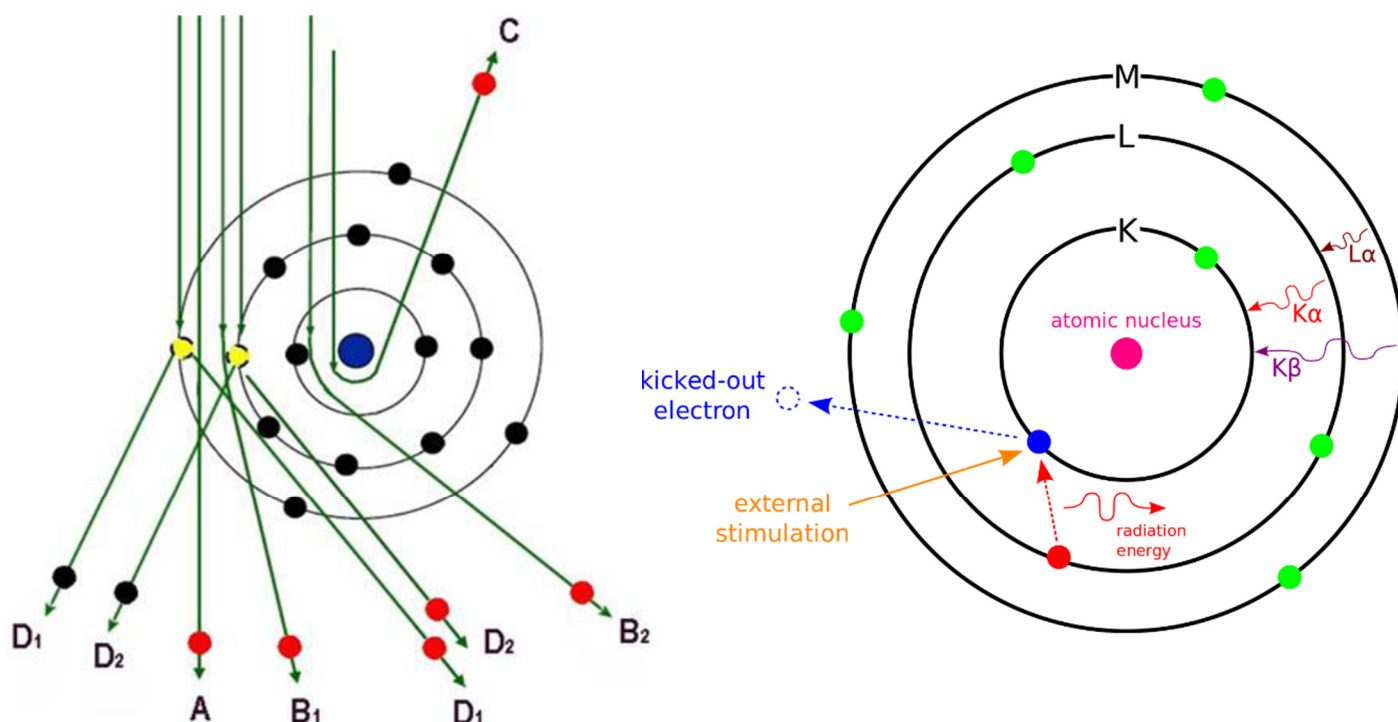


Figure 20 - Different possible electron behaviour as a base for SEM image modes (left) [39] and X-Ray emission mechanism as the base for the EDS mode (right) [9].

During past stages of this project, as well as during the present report, two techniques will be presented: Back-Scattering Electron Imaging (BEI or BSE) mode and Energy Dispersive X-ray Spectroscopy (EDS) mode.

During BSE, a contrast image is created with backscattered electrons. These are the results of the interaction marked with the letter C in Figure 20 (left). This interaction will deviate the electron's trajectory and is often described as high angle elastic interaction. The deviated electron can re-emerge from the sample surface and be detected with a backscattering electron detector [9, 39].

In this mode, the fact that elements that have a higher atomic number (and thus weight) deflect the incident electrons more strongly than the lighter elements can be explored, creating a grey-tone, contrast image based on phase and composition, where the presence of heavier elements (e.g. iron) will create brighter areas (more backscattered electrons) than lighter elements (e.g. silicon) [9, 39].

The other mode used in the present dissertation is EDS. This method takes advantage of the phenomena described with the letter D in Figure 20 (left). As can be observed in Figure 20 (right), when a primary electron collides with the material's electrons, these are taken out of their orbits. If this occurs at the valence orbit, the material will simply be ionized. However, if this occurs at a lower energy orbit, an electron from a higher energy orbit will replace it, releasing the excess energy in the process in the form of radiation X, which can be detected and measured. Since the energy differences between the different energy states are unique for each element, measuring the energy of the detected X-rays leads to the chemical composition analysis of the sample (in a certain point or area of the image) [9, 39].

Finally, the preparation and conditioning of the samples should also be explained. Opposite to optical microscopy and Transmission Electron Microscopy (TEM), the thickness of the sample in SEM does not have to be reduced. It does, however, have to be electrically conductive. This is due to the bombardment of the surface with electrons, which, if the sample is not conductive, leads to negative charge build-up in the surface which in turn might affect, deviate, or in some extreme cases fully reverse the electron beam, rendering the results unreliable [39].

To assure this property, the sample's surface must be coated with a thin layer of a conductive material via sputtering or vacuum deposition. In this project's case (in which the non-conductive inclusions might influence the results) a carbon coating is applied via Physical Vapour Deposition (PVD), where the carbon condenses on the sample's surface. Due to its low atomic number, carbon readings and measurements are often discarded, and doesn't considerably influence the measurements [9, 39].

Other concerns on the preparation of SEM samples regard the liquid content present, which can be surpassed with the usage of different modes (i.e. LVSEM or/and ESEM) and does not present any problem to the metallic samples being observed [39].

3 Materials and Methods

The experimental study conducted in the present work concerned the further analysis of the rolled slabs resulting from the lab-scale milling trial conducted in October of 2018 in the Ceramics Research Centre at Tata Steel IJmuiden. These slabs were already prepared, some in the pre-rolling state and some in a post-rolling state with reductions of 20, 40, 60 and 85% of the initial thickness. A total of 8 samples was already prepared from the 60% and 85% slabs.

3.1 Slab Preparation

Although the preparation of the slabs was not conducted in the present study, it is no less detrimental to the interpretation of the results obtained and should, therefore, be explained. To do so, firstly, a schematic representation of the procedure used to prepare the slabs that served as the base material for the samples studied in this phase can be observed in Figure 21, along with a graphic representation of the intermediate stage products in Figure 22. The process will be explained in detail followingly.

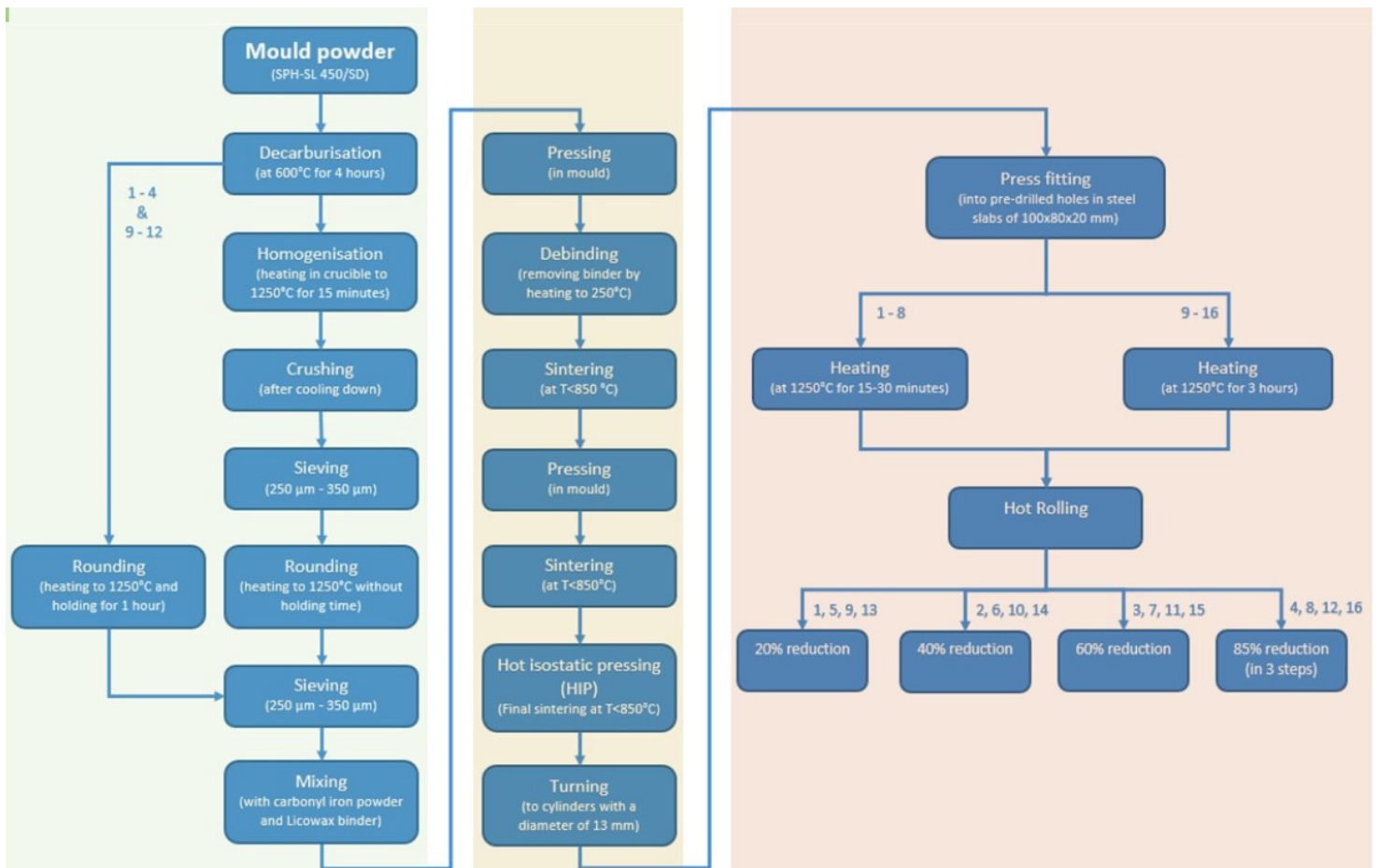


Figure 21 – Schematic representation of the production of the samples studied in the first stage. Indexed numbers indicate the slab numbers that result from the alternative processing routes, as can be consulted in Table 3-4 [9].

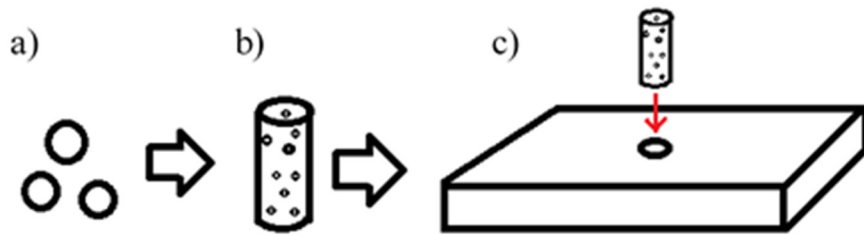


Figure 22 – Graphic representation of the (a) artificial inclusions, (b) PM cylinder with embedded artificial inclusions and (c) steel slab with shrink fitted PM cylinder.

As can be observed, the overall production of the samples can be divided in 3 main groups, organized in columns in Figure 21: the production of the inclusions, the production of the powdered metallurgy cylinders, and the final production of the slabs followed by hot rolling.

The production of the inclusions was conducted in a fashion that intended to have two different types of inclusions: Na/F rich inclusions and Na/F poor inclusions. To do so, the methodology being used before Karnasiewicz's (2017) work was followed to achieve the Na/F poor inclusions (since it was concluded that this method resulted in the volatilization of these elements) [28]. On the other hand, the methodology suggested by Karnasiewicz and first implemented during Geussous' research (2017) was used to obtain the Na/F rich inclusions (since it was concluded that this method minimized the loss of Na and F) [29].

The mould powder used as a base for the inclusions was the aforementioned MP-B, with the composition observed in Table 2, since this type of mould powder is the one most often used during the continuous casting operations at Tata Steel IJmuiden.

The first step for the inclusion production consisted of the decarburization of the powder, by heating it up to 600°C and holding an isothermal stage at this temperature for 4 hours. After this step, the particles were differentiated into groups that resulted in either Na/F rich or poor inclusions (Figure 23).

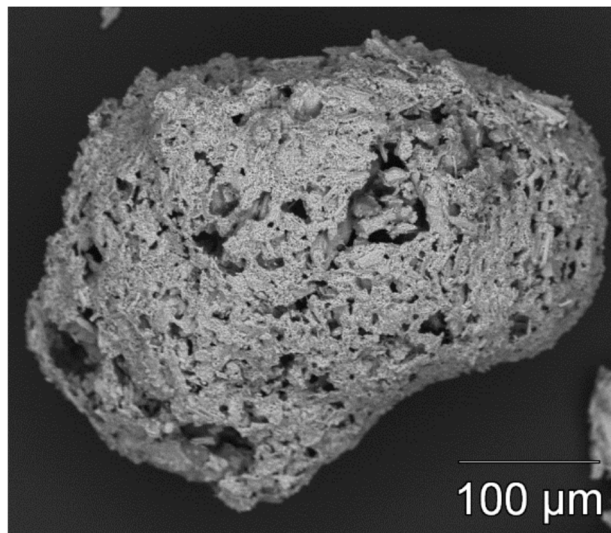


Figure 23 – SEM image of a mould powder particle after the first decarburization step [23].

For the Na/F rich inclusions, one part of the powder was poured into a graphite crucible which was heated to 1250°C. Once this temperature was reached, the powder had fully molten and the crucible was removed from the furnace, leading to a fast solidification below the evaporation point of Na and F (which is approximately 850°C), minimizing element loss and leaving no time for the material separate into layers with different compositions, resulting in a homogeneous material.

Afterwards, the material was removed from the crucible and crushed to small pieces, which were sieved in order to obtain particles with a size between 250 μm and 350 μm (inclusions in this size range have shown to be the main contribution to the studied defects [9]).

In order to achieve the round shape that the real inclusions tend to have, the particles were dispersed on a graphite plate and heated to 1250 $^{\circ}\text{C}$. Due to the surface tension between the now molten slag and the graphite, the particles form spheres, leading to inclusions with a shape, size and composition that resembles real mould slag inclusions (Figure 24).

For the Na/F poor inclusions, the mould powder was directly rounded on the graphite plate, by heating it to 1250 $^{\circ}\text{C}$ and holding this temperature for one hour. During this time, it is expected that the Na and F evaporate, leading to particles that, when measured during the studies performed by Karnasiewicz (2017), reached 0% F and Na [28]. After the rounding steps, a final sieving stage was performed, to discard any particles outside the size range of 250-350 μm .

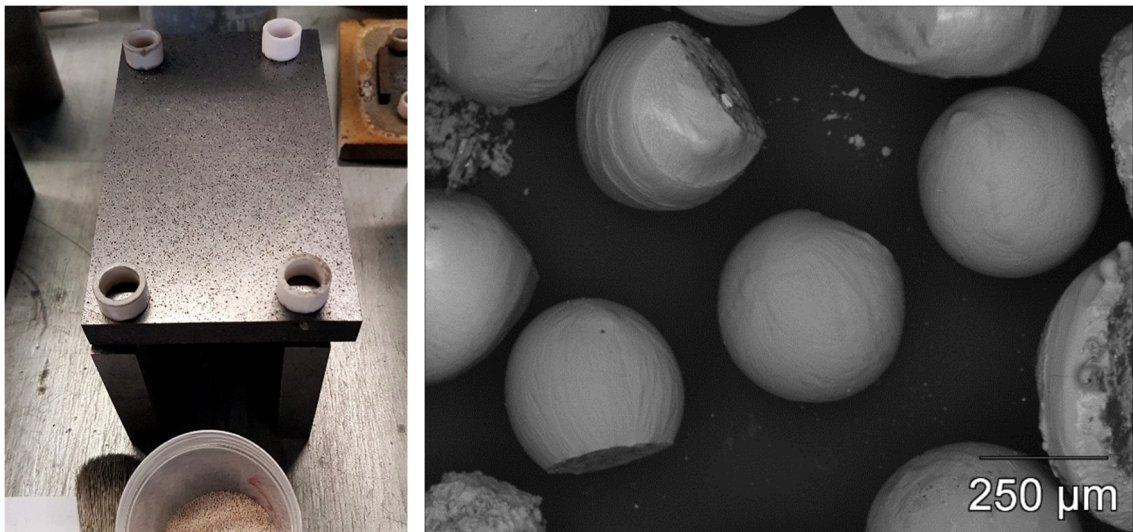


Figure 24 – Shaping step (left) and SEM image of the artificial inclusions after the shaping and final sieving steps (right) [23].

The second stage of the procedure concerns the preparation of the powder metallurgy cylinders containing the inclusions. To do so, firstly, CIP-CC (Carbonyl Iron Powder) was mixed with a binder (Licowax) and pressed into a bar. The artificial inclusions were introduced in these bars, randomly distributed. The samples were slowly heated to 250 $^{\circ}\text{C}$ to remove the Licowax binder and then sintered in a furnace, using two sintering stages at 800 $^{\circ}\text{C}$, a temperature which is inferior to the Na and F evaporation points ($\approx 850^{\circ}\text{C}$), to minimize the loss of these elements.

It should be noted that the chosen temperature of 800 $^{\circ}\text{C}$ also avoided the steel transformation from the *bcc* structure of ferrite to the *fcc* structure of austenite and consequent expansion, which would counteract the pressing process. It was reported that the final density registered was of $\approx 100\%$ that of non-PM steel.

An intermediate pressing step was used to uniformly reduce the porosity to a density $\geq 96\%$, in order to close all porosity and allow the bars to be submitted to final a HIP stage at an equally low temperature and a reported pressure of $\approx 80\text{MPa}$.

Due to equipment restrictions, the entirety of this second stage, regarding the production of the PM cylinders was conducted in the Aachen University (RWTH) in Germany [2].

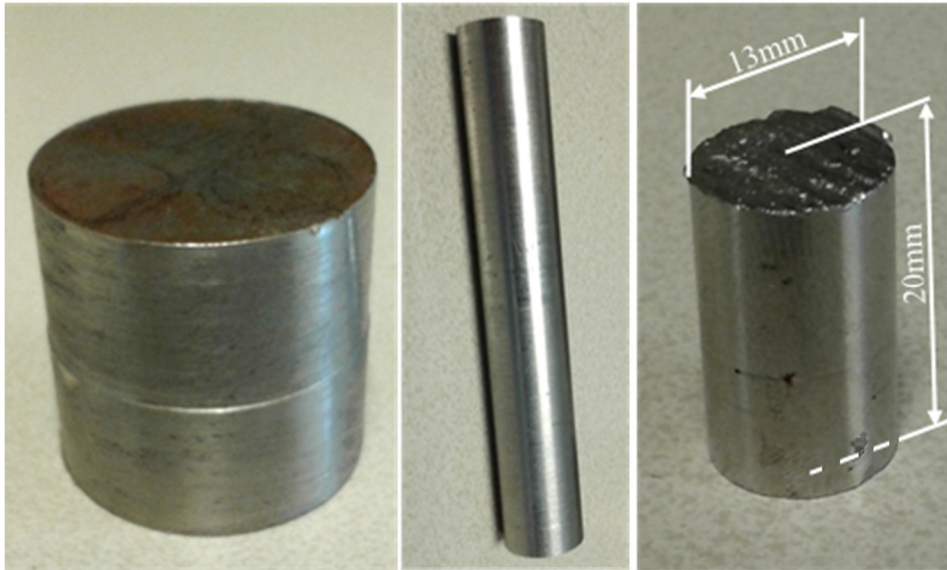


Figure 25 – Powder metallurgy cylinders after HIP and machining (left, centre) and after cutting (right).

The last stages of the process, regarding the insertion of the PM cylinders in the steel slabs and consequent hot rolling, were once again conducted at Tata Steel IJmuiden.

Firstly, the cylinders received from Aachen University were machined and cut into smaller cylinders with a diameter of 13mm and a length of 20mm (Figure 25). Afterwards, these cylinders were press-fitted into holes in 100x80x20mm conventional low-carbon steel slabs and machined in order to get a clean, flat surface without marks between the steel in the powder metallurgy cylinders and the steel in the slabs. Finally, the resulting samples were submitted to a pre-heating isothermal stage (also referred to as “soaking”) at 1250°C for either 15-30 minutes (in accordance with previous lab trials) or 3 hours (representing plant conditions) depending on the sample, and subsequently hot rolled with a rolling speed of 45mm/s to different thickness reductions [9]. A summary of the different slabs produced for the lab scale trials and respective differences can be observed in Table 3 and Table 4 along with a picture of the final slabs (1, 2 and 3) after rolling (Figure 26).

Table 3 – Summary of the low soaking time slabs produced for the lab scale trials.

<i>Slab</i>	<i>1</i>	<i>2</i>	<i>3</i>	<i>4</i>	<i>5</i>	<i>6</i>	<i>7</i>	<i>8</i>
Soaking time [min]	15-30	15-30	15-30	15-30	15-30	15-30	15-30	15-30
Na/F content	poor	poor	poor	poor	rich	rich	rich	rich
Thickness reduction [%]	20	40	60	85	20	40	60	85
Final Thickness [mm]	16	12	8	3	16	12	8	3
Rolling steps	1	1	2	3	1	1	2	3

Table 4 – Summary of the high soaking time slabs produced for the lab scale trials.

<i>Slab</i>	<i>9</i>	<i>10</i>	<i>11</i>	<i>12</i>	<i>13</i>	<i>14</i>	<i>15</i>	<i>16</i>
Soaking time [min]	180	180	180	180	180	180	180	180
Na/F content	poor	poor	poor	poor	rich	rich	rich	rich
Thickness reduction [%]	20	40	60	85	20	40	60	85
Final Thickness [mm]	16	12	8	3	16	12	8	3
Rolling steps	1	1	2	3	1	1	2	3



Figure 26 – Slabs 1 (lower left corner), 2 (lower right corner) and 3 (top) after hot rolling. PM cylinders visible in the centre of the slabs.

Additional pictures (with dimensions displayed) of the slabs before and after rolling are presented in Appendix A.

Among the samples already produced and rolled, the slabs with a thickness reduction of 20% (slab 1) and 40% (2, 6, 10 and 14) were studied in the present report, along with new samples taken from the slabs with a thickness reduction of 85% (4, 8, 12 and 16). Further analysis on the samples already studied by Uittenbroek (2019) was also conducted, in order to validate and/or extend the conclusions taken in the previous work and during the present study [9].

3.2 Sample Preparation

In order to allow the study of the inclusions, samples were prepared from the produced slabs.

Firstly, rough cuts were made with an angle grinder in order to remove the bulk of the material surrounding the now deformed powder metallurgy cylinders containing the inclusions. This step was performed in the 60% and 85% reduction slabs, for which the resulting length after rolling did not allow the appropriate handling for the next steps.

Subsequently, cross-section cuts were made on the powder metallurgy cylinder zones. Since the inclusions were expected to be elongated in the rolling direction, in order to increase the chance of finding the inclusions easily, a cross-section perpendicular to this direction (also mentioned in previous research documents as RD section) was made. These cuts were made using a liquid-cooled Struers Discotom 50 equipped with a 300x2x32mm Struers 30A30 alumina disc. In the longitudinal direction (also referred to as TD cross-sections), to prevent an excessive material loss, the cutting procedure was conducted in a Struers Accutom-5 (Figure 27) using a silicon carbide cutting disc with a thickness of 0.5mm.

A total of 7 samples resulting only from longitudinal cross-sections was studied in the present work, to observe the rolling direction behaviour along with the through-thickness behaviour.

It is important to notice that the cutting process needs to take into consideration the fact that the cylinders are deformed non-linearly due to the velocity differences experienced in the slab surface and centre, as well as due to the acceleration in the rolling direction, caused by the constant volume of material getting thinner (and not significantly wider). This causes a deformation in the rolling direction with a varying magnitude across the slab's thickness, resulting in a wavy and oddly deformed cylinder (Figure 28) [9]. Therefore, a cut might miss the cylinder. In such cases, a new offset cut needs to be made.



Figure 27 – Struers Accutom-5 used in the sample cutting process.



Figure 28 – Representation of the expected deformation of the rolled cylinders (not to scale) [9].

The cut samples were then embedded in a Struers PolyFast carbon-filled phenolic resin (Figure 29, left) using a Struers Protonpress 10 (Figure 29, right). The choice of a carbon filled resin aims at obtaining an electrically conductive sample, a characteristic that, as previously mentioned, is required for SEM samples.



Figure 29 - Struers PolyFast carbon-filled phenolic resin (left) and Struers Protonpress 10 (right) used in the sample mounting.

Subsequently, in order to allow a clear view of the inclusions, the samples were grinded and polished using a Struers Tegramin-30 (Figure 30). For the grinding sequence, the equipment used resin-bonded diamond discs (Struers MD-Piano) with grits of 100-120, 1200, 2000 and 4000 consecutively. The polishing was conducted with a woven acetate disk (Struers MD-DAC) accompanied with a self-lubricating polycrystalline diamond suspension of 3 μ m granulometry. The automated polishing step was sometimes followed by a manual stage with the same granulometry to remove imperfections, if these appeared.

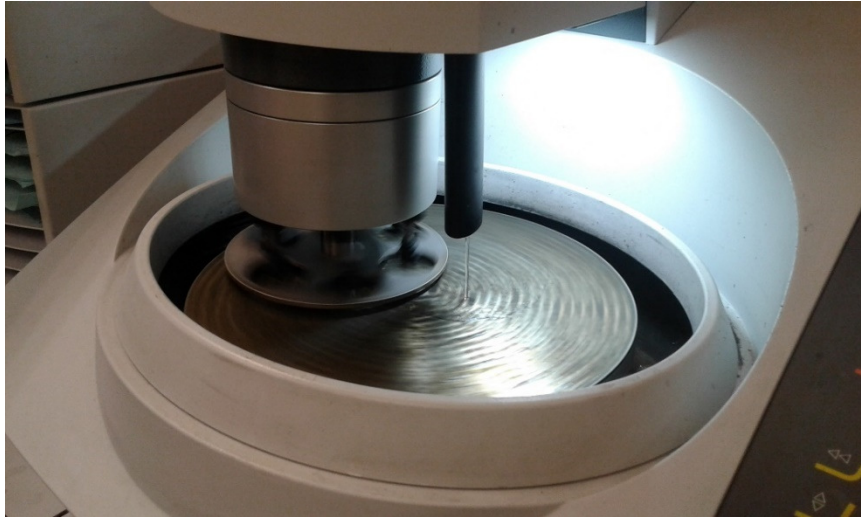


Figure 30 - Struers Tegramin-30 used in the automated sample grinding and polishing steps.

By the end of the polishing step the samples were prepared for optical microscopy. However, an additional step was carried out in order to make them suitable for SEM, due to the non-conductive properties of the Non Metallic Inclusions, consisting of depositing a 6nm layer of carbon on the sample's surface via PVD, using a Cressington Carbon Coater 208 Carbon.

3.3 Testing

Firstly, in order to identify the inclusions visible in the samples' surface, a "mosaic" was created using optical microscopy by stitching several 50x magnification images together. To do so, a Zeiss Axio Imager Z1 optical microscope (equipped with a Zeiss ECEpiplan-NEOFLUAR 5x/0,13 HD DIC 1156 - 514 objective) was used along with AxioVision software. The rolled inclusions, clearly visible on the mosaic created, were then identified and numbered so that, using a print-out, they could be easily found during SEM testing.

Measurements of the inclusions' length, thickness and depth within the slab were also conducted during optical microscopy testing, following the methodology properly explained in Appendix B.

For the SEM stage, a JEOL JSM-5900LV SEM using high vacuum conditions and an acceleration voltage of 15kV was used in combination with Pathfinder software. The BEI mode was used to take images of the identified inclusions with the several phases highlighted due to composition differences. An automated capture function in grid mode with a 4000x magnification was used for this step. The several pictures of each inclusion were later on stitched together manually to allow its global visualization, for which an overlap of 10% in the grid capture was selected.

EDS mode was used to determine the composition throughout each inclusion, which was conducted via point (local values) and area (average values) measurements. Within the several area measurements conducted, two modes were used: polygonal area, mainly used for large areas composed primarily of a single phase; and a composition-based area (selected using the magic wand tool in Pathfinder), used for smaller areas where two or more phases are present in significant amounts, which would lead an overall polygonal measurement not to have the same relevance due to the differences in composition observed.

Examples and descriptions of how the SEM/EDS measurements were carried are given in Appendix E.

4 Results

4.1 Optical Microscopy

An example of a full mosaic obtained for the new samples taken from slabs 4, 8, 12 and 16 (Table 3 and Table 4) can be observed in Figure 31 (from bottom to top, respectively). Additional mosaics are presented in Appendix B.

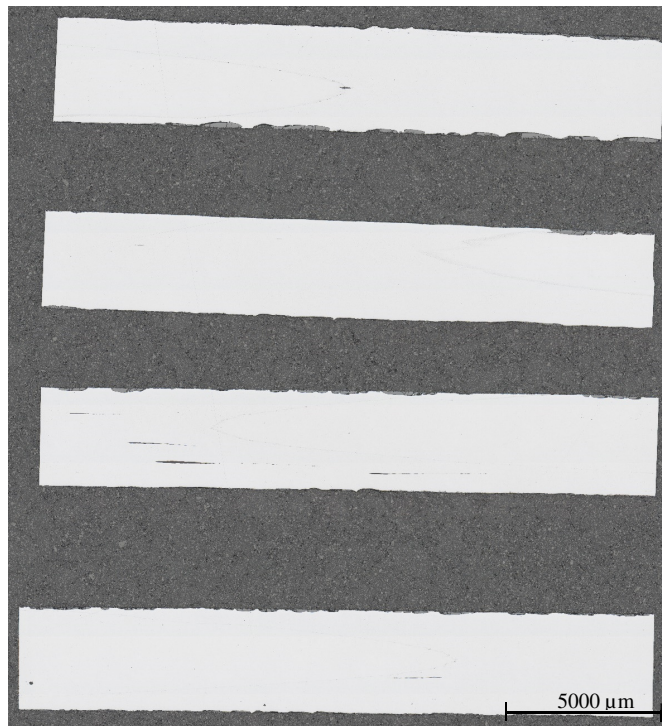


Figure 31 – Mosaic created with 50x optical microscopy images. Samples taken from the 85% reduction slabs. As can be observed, the surfaces obtained in the samples display visible inclusions (shown in detail in Figure 32).

However, it is also possible to observe that not every slab resulted in samples with visible or relevant inclusions, as is the case of the surface of the sample from slab 12, as can be observed in Figure 32 (bottom), where the inclusions observed were determined as not resulting from the introduced mould powder.

In other cases (slab 16, bottom of Figure 31), inclusions of smaller dimensions and not displaying the same shape were found, indicating that the sample cut might have passed through its extremity, not allowing a clear visualization of the length of the inclusions. In such cases, the sample was re-polished in order to find new inclusions.

An additional phenomenon can be observed in Figure 31 and Figure 32, where a thin, deformed oxide layer separates the slab steel from the powder metallurgy steel, as can be observed in detail in Figure 33.

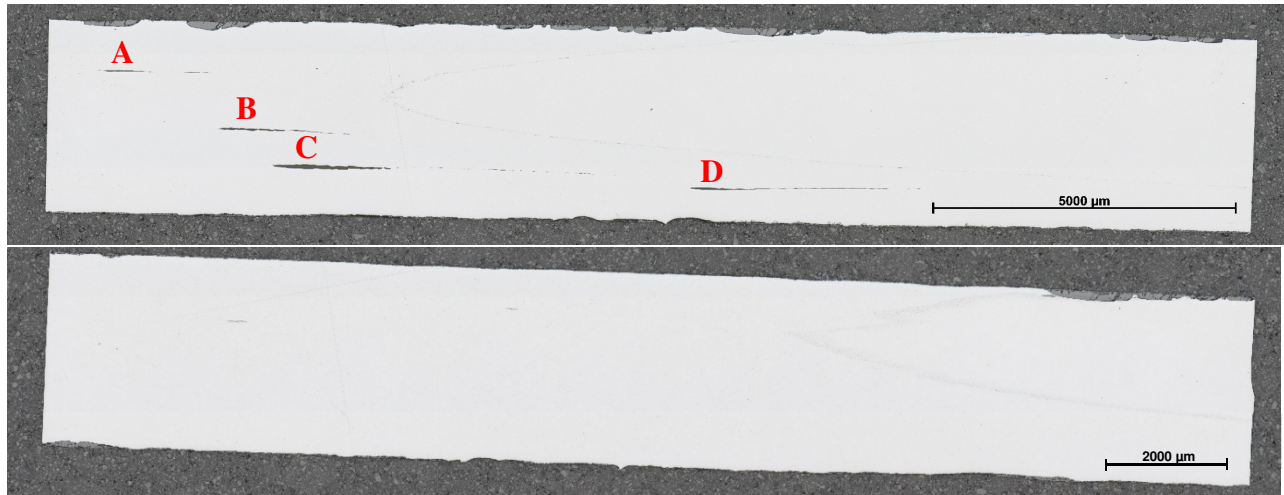


Figure 32 – Detail of sample from slab 8 (top) and 12 (bottom) created with 50x optical microscopy images. Relevant inclusions identified with capital letters above.



Figure 33 – Detail of the sample from slab 2 created with 50x optical microscopy images. Boundary between the steel slab and the powder metallurgy cylinder highlighted.

Moreover, the results of the measurements conducted during optical microscopy were properly registered for analysis. An example of an image capture of the result of the measurements conducted on the sample from slab 8 can be observed in Figure 34.

A total of 27 inclusions were analysed in optical microscopy, taken from slabs 1, 2, 4, 6, 8, 10, 11, and 16. Additional testing was conducted on the 30 inclusions from slabs 3, 4, 5, 7, 8, 11 and 16 found in the samples studied by Uittenbroek (2019) [9].

It should be noted that despite several different samples being prepared from slab 12, no inclusions were found in the longitudinal cuts. This might indicate that the cylinder region was lost during cutting or grinding, due to the thinning behaviour of the cylinders represented in Figure 28.

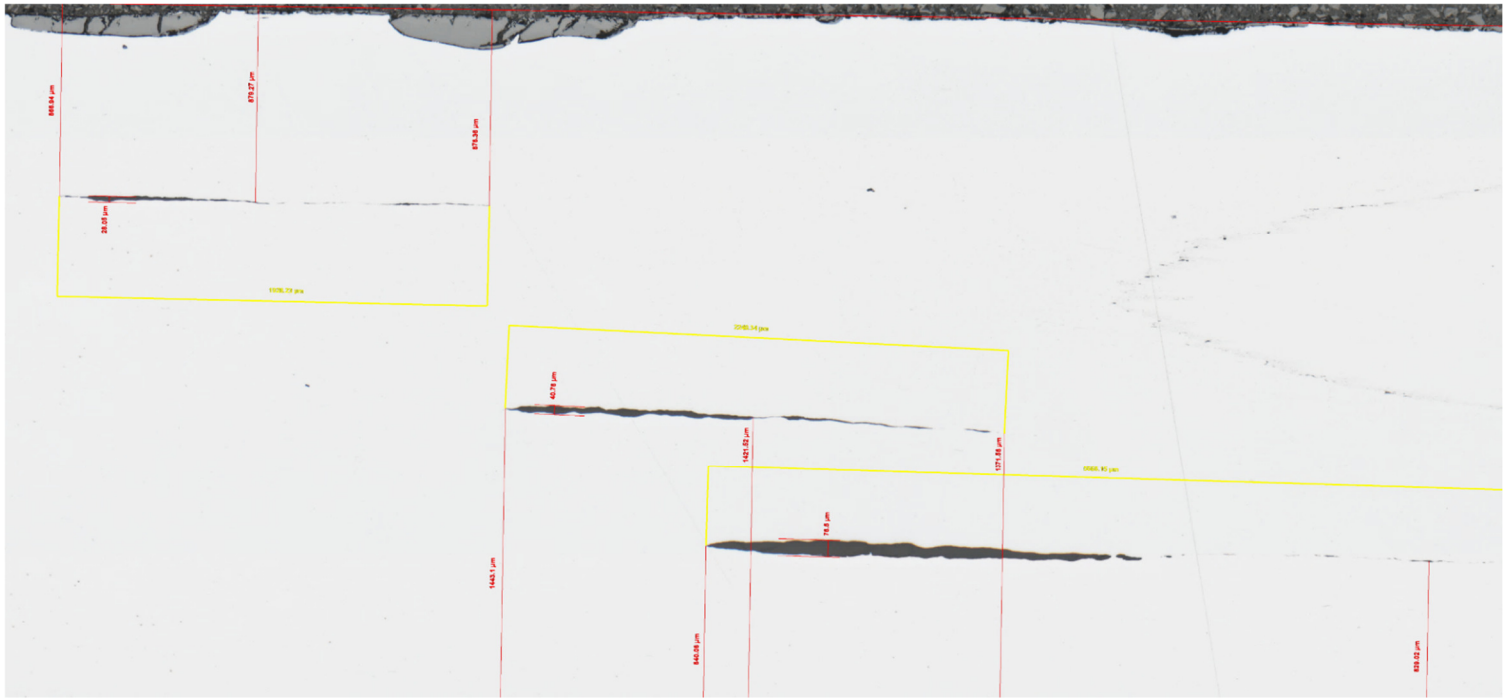


Figure 34 – Example of the results of the measurements conducted on the inclusions of slab 8 during optical microscopy.

4.2 SEM

Secondly, the SEM results are presented. These are divided into two sets of raw data: the automated BSI images taken with 4000x magnification for each inclusion, and the EDS measurements (both point and area), imported into separate worksheets per inclusion. A total of 13 inclusions were studied, taken from the low soaking time slabs with 20% thickness reduction (slab 1), 40% thickness reduction (slabs 2 and 6) and 85% thickness reduction (slabs 4 and 8).

Examples of the individual BSI images can be observed in Figure 35, where the resolution chosen easily allows for the visualization of the details in the microstructure and respective morphology.

Additional examples of high-resolution BSI images are presented in Appendix D.

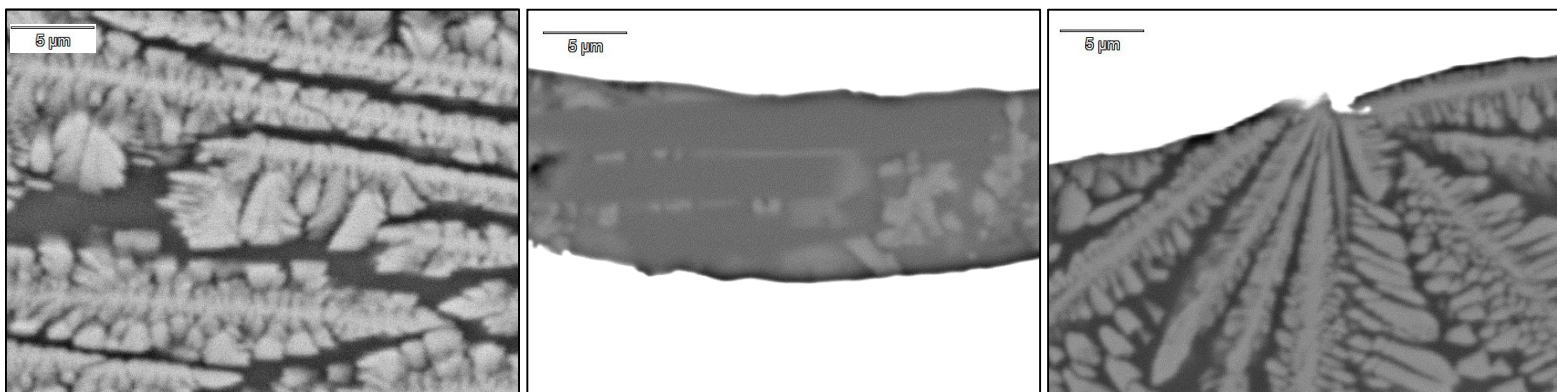


Figure 35 – Examples of individual BSI images, resulting from the SEM testing.

In order to allow its usage for an overall morphology and microstructure analysis, these images were then grouped and stitched by inclusion, taking into consideration that the image capture method used in the Pathfinder software performs an automatic brightness and contrast correction for each picture based on its greyscale levels, resulting in different combinations of these parameters from picture to picture, a phenomenon that had to be corrected manually

during stitching. A more detailed explanation and exemplification of the stitching process can be consulted in Appendix D.

The EDS measurement results were then treated, and the phase corresponding to each measurement identified. Due to the massive data to analyse, an algorithm was developed to identify the phases present in the inclusions based on the measurements and on the stoichiometric compositions of the most common phases in mould slag inclusions.

The EDS measurement and data processing methodology used is further explained in Appendix D.

4.2.1 Inclusion Shape

The overall shape of the inclusions varied significantly with the increase in thickness reduction.

As can be observed in Figure 36 and Figure 37, the inclusions in the 20% and 40% thickness reduction slabs display a quasi-oval shape, whereas the inclusions in the 85% thickness reduction slabs display a characteristic drop-like shape, with a thicker part in the tail zone, a thinning behaviour in the rolling direction, and a thin, elongated part in the head zone of the inclusion (Figure 38).

On the other hand, it can also be observed that the 40% reduction inclusions do not present any discontinuities throughout their length, while the 85% reduction inclusions occasionally display breaks, both in the tail and head areas, although more frequently in the thinner, head zone.

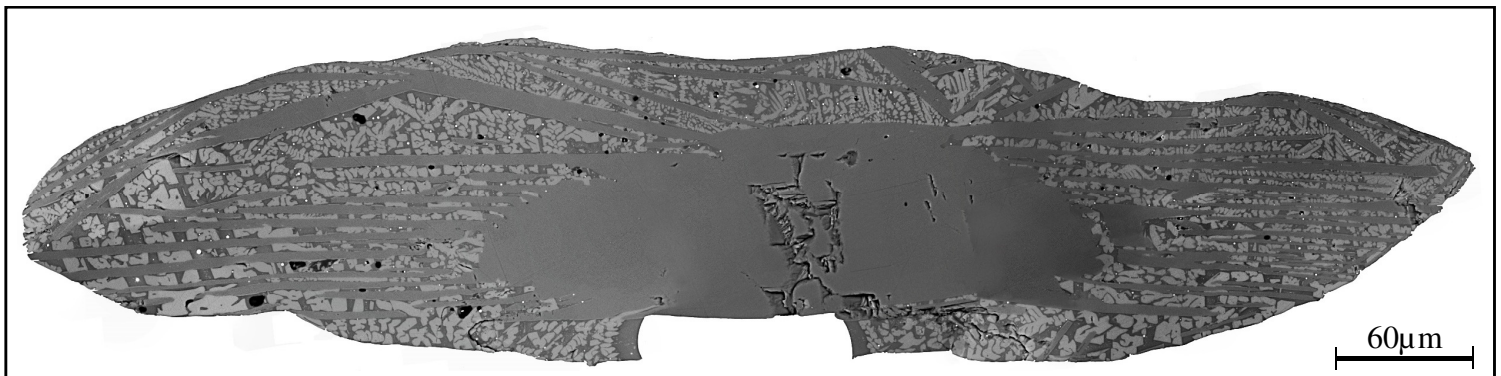


Figure 36 - Example of the oval shape displayed in the 20% reduction inclusions. Example taken from slab 1, inclusion A. Rolling direction from left to right.

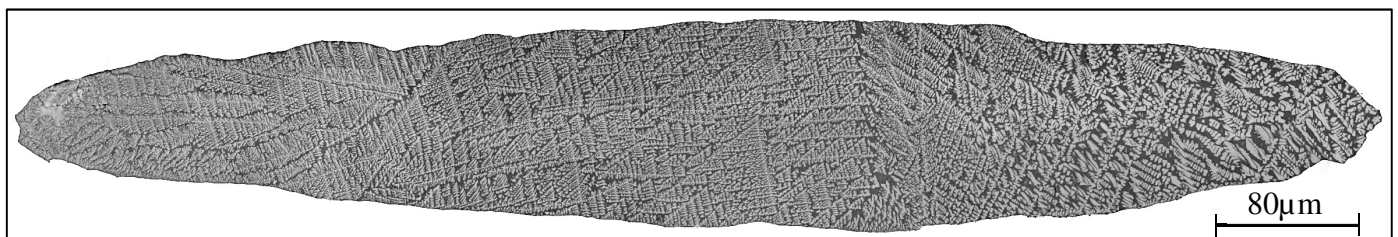


Figure 37 – Example of the oval shape displayed in the 40% reduction inclusions. Example taken from slab 2, inclusion C. Rolling direction from left to right.

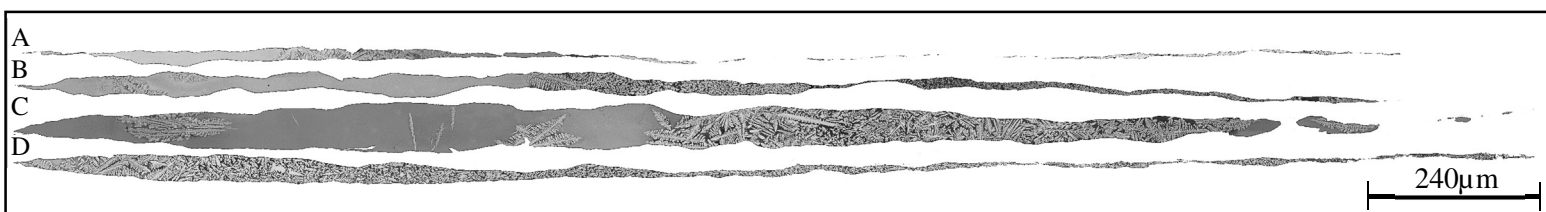


Figure 38 – Example of the drop-like shape displayed in the 85% reduction inclusions. Examples taken from slab 8, inclusions A, B, C and D. The thin part of inclusions C and D is not fully displayed in the picture due to size restrictions. Rolling direction from left to right.

4.2.2 Inclusion Composition and Phases

The composition of the inclusions, and most noticeably the present crystalline phases, varied significantly between the Na and F rich and poor inclusions, as can be observed in Table 5.

Table 5 – Crystalline phases present in the inclusions for the different slabs examined.

Slabs	Na/F Content	Soaking Time	Crystalline Phases	
			Cuspidine	Wollastonite
1/2/4	Poor	Low	Yes	Yes/No/Yes
6/8	Rich	Low	Yes	No

It should be noted that, as previously mentioned, the analysis of the phases crystallized in the final inclusions does not relate directly the final composition of the inclusions, since it does not take into account the multiple possible phases seemingly indistinguishable in the amorphous, glassy form. Therefore, a more detailed, case-by-case presentation of the results of the inclusion's composition is hereafter presented.

Fluorine and Sodium Poor Samples

As mentioned in Table 5, the phases present in the F and Na poor inclusions include cuspidine and wollastonite in a crystalline form, as well as glassy phases with different compositions.

In the low soaking time samples studied, the average compositions of the inclusions found in the slabs produced with a 20%, 40% and 85% thickness reduction are presented in Table 6, Table 7 and Table 8.

These compositions were obtained from the average atomic contents resulting from the EDS measurements (both point and area measurements were used).

The displayed oxygen content does not result from a direct measurement, but instead is calculated from the basic compound calculations, corrected to include CaF₂, as displayed in Appendix C.

Table 6 – Average composition [at%] resulting from the EDS SEM measurements of the inclusions present in slab 1, with 20% reduction and low soaking time.

	Average Composition [at%] - Slab 1 (20% reduction)									
	O	Ca	Si	F	Na	Al	Mg	K	Fe	Other
Cuspidine	48.83	24.21	14.07	11.11	0.28	0.47	0.29	0.00	0.54	<0.21
Glass	58.74	11.39	17.40	0.97	2.32	4.86	1.15	0.02	2.82	<0.32
Wollastonite	59.97	18.79	19.65	0.01	0.14	0.39	0.28	0.01	0.54	<0.22

Table 7 – Average composition [at%] resulting from the EDS SEM measurements of the inclusions present in slab 2, with 40% reduction and low soaking time.

	Average Composition [at%] - Slab 2 (40% reduction)									
	O	Ca	Si	F	Na	Al	Mg	K	Fe	Other
Cuspidine	48.95	22.74	13.96	11.09	0.61	1.61	0.29	0.01	0.67	<0.08
Glass	58.16	10.92	15.96	1.42	2.65	7.51	0.90	0.04	2.34	<0.10

Table 8 – Average composition [at%] resulting from the EDS SEM measurements of the inclusions present in slab 4, with 85% reduction and low soaking time.

	<i>Average Composition [at%] - Slab 4 (85% reduction)</i>									
	O	Ca	Si	F	Na	Al	Mg	K	Fe	Other
Cuspidine	49.53	20.15	14.27	10.31	1.47	1.87	0.71	0.02	1.56	<0.10
Glass	56.81	10.95	15.28	1.35	3.88	4.48	1.96	0.06	5.07	<0.18
Wollastonite	59.27	18.06	18.80	0.28	0.70	0.93	0.47	0.01	1.39	<0.08

Fluorine and Sodium Rich Samples

The phases present in the F and Na rich inclusions mainly include cuspidine in a crystalline form, as well as glassy phases with different compositions. The average compositions of the inclusions found in the slabs produced with a 40% and 85% thickness reduction are presented in Table 9 and Table 10.

Table 9 – Average composition [at%] resulting from the EDS SEM measurements of the inclusions present in slab 6, with 40% reduction and low soaking time.

	<i>Average Composition [at%] - Slab 6 (40% reduction)</i>									
	O	Ca	Si	F	Na	Al	Mg	K	Fe	Other
Cuspidine	50.81	19.59	14.91	8.43	3.04	1.42	0.28	0.04	1.21	<0.26
Glass	56.19	9.45	17.23	1.86	7.23	2.58	0.84	0.13	4.00	<0.48

Table 10 – Average composition [at%] resulting from the EDS SEM measurements of the inclusions present in slab 8, with 85% reduction and low soaking time.

	<i>Average Composition [at%] - Slab 8 (85% reduction)</i>									
	O	Ca	Si	F	Na	Al	Mg	K	Fe	Other
Cuspidine	47.40	21.17	14.16	12.49	2.31	0.94	0.21	0.03	1.18	<0.10
Glass	53.02	10.65	15.85	4.92	7.58	2.54	0.60	0.13	4.48	<0.22

As can be observed, for all samples, while the crystallized phases present a composition closer to their stoichiometric one, the original mould slag composition (Table 11) is situated somewhere between the glass composition and the crystallized phase composition, displaying the decomposition that happens during crystallization.

Table 11 – Average composition of the original mould slag [at%].

	<i>Average Composition [at%] – Original Mould Slag</i>									
	O	Ca	Si	F	Na	Al	Mg	K	Fe	Other
Mould Slag	46.90	15.17	14.77	11.10	9.80	1.41	0.52	0.25	0.09	

It can already be observed that, besides the lower F and Na content (which, even for the “rich” samples did not reach the desired original mould slag values) and the exceptional peak in Al for the inclusions in the sample from slab 2, the main difference observed between the original composition and the inclusion composition is the Fe content, which is significantly higher than the original value. A more detailed analysis and possible interpretation of the composition results will be further explored in Chapter 6.

4.2.3 Phase Morphology

The morphology of the crystalline phases present in the studied inclusions varied greatly from inclusion to inclusion, ranging from fine dendritic structures, which can already be seen in the

cuspidine structures (light) presented in the example given in Figure 35 (left), to coarse structures, such as the ones observed for the wollastonite blocks (dark) present in the example given in Figure 35 (centre) or the coarse cuspidine structures (light) present throughout Figure 36.

Besides varying from slab to slab, the phase morphology of the crystalline phases also presented variation between the different inclusions of the same slab, and even presented changes within the same inclusion for some cases.

Therefore, in Chapter 6, an analysis of these variations and possible justifications for the different behaviours found will be presented in detail.

5 Modelling of the Hot Rolling Process

In order to validate and allow a better understanding of the results obtained in the experimental part of the project, a finite element model of the lab-scale hot rolling process was developed using the software Abaqus CAE. A plane strain model was used in coordination with a macroscale constitutional model to predict the strain and temperature profiles in the slabs as well as its evolution in the hot rolling process. The final goal of this part is to investigate the need for a multi-scale approach, where the output from the macro-scale model can be adapted into a mesoscale model of a steel matrix with the embedded inclusions, and consecutively to a microscale model of the inclusion deformation process. This stage was conducted in a collaborative project with the Knowledge Group (Plasticity and Tribology) in the Innovation Centre (IC) at Tata Steel IJmuiden.

The developed model will be used for the analysis of the influence of the process conditions on the temperature and strain profiles of the slabs during the hot rolling process. The simulations conducted aim at reproducing the experimental part of the present research, where slabs containing artificial inclusions are used to study their deformation behaviour. The modelling results are validated based on the measured roll forces, surface temperatures at the start and end of the rolling process and deformation of the rolled material.

It should be noted that, as previously mentioned, friction conditions between roll and strip on the slip path are of the utmost importance, as they cause different velocities through the thickness of the slab, a phenomenon that might play an important role in the deformation of the inclusions. On the other hand, the heat transfer mechanisms present during the process are also of significant relevance, as they directly affect the temperature profiles and, therefore, cooling rates suffered by the inclusions, which in turn will ultimately affect the microstructure found in the final rolled inclusions and possibly their behaviour during rolling.

In this chapter a description of the finite element model will first be given in Section 5.1. In Section 5.2 the numerical results of the simulations are presented and discussed. The joint analysis of the experimental results combined with the FE model results will be conducted in Chapter 6.

5.1 Finite Element Model

Due to the fact that the increase in width of the strip during the process is significantly smaller in comparison with the other two dimensions, it is assumed that a plane strain condition is valid. This allows the reduction of the problem to a 2-dimensional plane strain problem, thus simplifying the model by a significant amount and reducing considerably the computational effort.

Furthermore, the rolling process was considered to be symmetric, causing only one roll and half the strip thickness to be modelled, thus reducing the computational effort even further. This approximation, however, which is fairly accurate for the automated plant scale rolling processes, does not take into consideration some practical aspects of the more manual lab scale rolling process, which might lead to some minor discrepancies in the results, as will be explored

in the results section. Another factor that was simplified in the modelling was the thin oxide layer formed immediately after descaling, which should affect both the thermal (e.g. contact conductance) and the mechanical (e.g. friction coefficient) aspects of the process.

Due to its fully coupled thermo-mechanical character, as well as due to the considerably high deformation inherent to the hot rolling process, dynamic, temperature-displacement, explicit steps were used in model, leading to the usage of the explicit solver of ABAQUS to simulate the rolling process.

In the developed macro-scale model, the rolls were considered as strictly elastic bodies with temperature as a degree of freedom. The slab, however, was assumed to be deformable with temperature and strain rate dependent plastic behaviour properties. The macro-scale model was used to simulate both single- and multi-pass hot rolling, considering that the inclusions present are affected but do not affect the overall rolling process, and therefore do not need to be incorporated in the model.

5.1.1 Material Properties

The accuracy of the model will significantly depend on the material properties used, which should take into consideration that different requirements for the roll and for the slab.

Firstly, to be able to reproduce the behaviour of the roll, an isotropic elastic material was used, being assumed that no plastic deformation takes place in the roll, since a plastically deformed roll would result in significant problems in the real hot rolling process.

The slab, however, will experience plastic deformation, since this is the ultimate goal of the process itself. Therefore, an isotropic elasto-plastic material was chosen to represent its behaviour. The plastic behaviour of the slab was considered as variable with the temperature and strain rate applied. Therefore, as applied by Gelten and Pattabhiraman (2019), a modified version of the Siciliano predictive model (which is an extension of the extensively used Misaka model) was used to describe the plastic behaviour of the material during the hot rolling process, as a function of temperature and strain rate, as represented in Eq.(5.1) [40-42]:

$$MFS = f \cdot 9.8 \cdot \exp\left(0.126 - 1.75 \cdot [C] + 0.594 \cdot [C]^2 + \frac{2851+2968 \cdot [C] - 1120 \cdot [C]^2}{T}\right) \cdot eps^{c_{eps}} \cdot epa^{c_{epa}} \quad (5.1)$$

and:

$$f = c_0 + c_{Mn} \cdot [Mn] + c_{Nb} \cdot [Nb] + c_{Cr} \cdot [Cr] + c_{Mo} \cdot [Mo] + c_{Al} \cdot [Al] + c_{Si} \cdot [Si] + c_B \cdot [B] \quad (5.2)$$

where:

MFS, is the mean flow stress [MPa];

f, is a composition-based factor;

eps, is the deformation strain;

epa is the strain rate [s^{-1}];

c_x , are the fitting coefficients;

[X], are the fractions of each chemical element X in [wt%], except for B, which is in [ppm];

T, is the temperature [K].

It should be noted that the effects of the residual strain between rolling steps were dismissed.

The fitting coefficients (c_x) used in the model were optimized by Gelten and Pattabhiraman (2019) for the hot strip mill at Tata Steel IJmuiden and, therefore, should present some error when describing the lab scale process at hand in the present work. Due to confidentiality issues the exact values cannot be shown in the present thesis. In further research within the project, a new optimization of the fitting coefficients would be helpful for continuing to tune the developed model [40]. The chemical composition of the conventional low-carbon steel grade used for the lab scale trials was acquired from measurements conducted in the coils rolled in

2019 at Tata Steel IJmuiden and used for the predictive model and can be observed in Table 12.

Table 12 – Chemical composition of the conventional low-carbon steel grade used. Values in [wt%].

Element	C	Mn	Si	P	S	Cr	Mo	Al	V	Cu	Ni	N
Content [wt%]	0.042	0.210	0.001	0.012	0.013	0.024	0.002	0.047	0.001	0.014	0.023	0.004

Following the described model, an example of the influence of the strain rate on the predicted response for a fixed temperature of 1200°C (corresponding to the initial conditions) is shown in Figure 39.

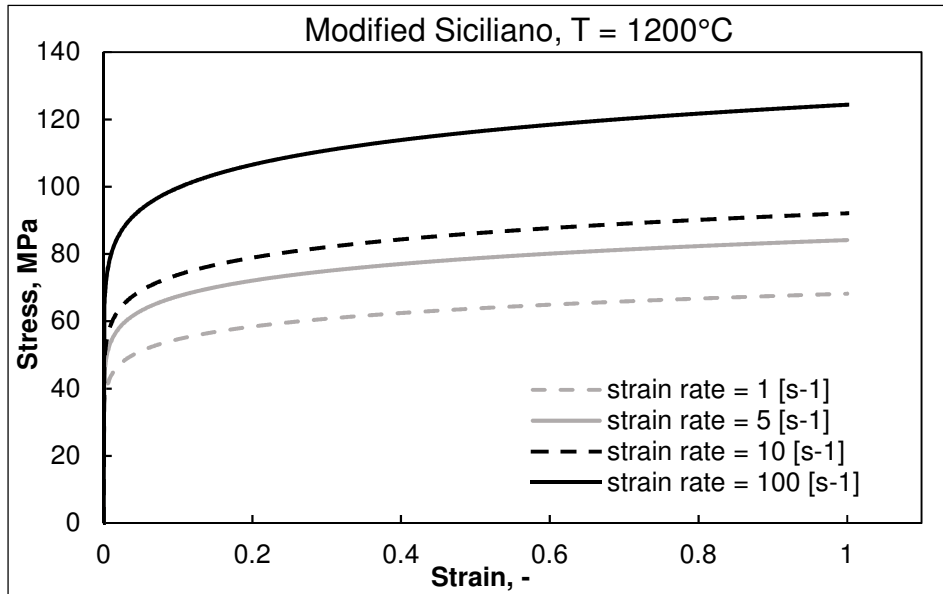


Figure 39 – Example of the strain rate dependency of the elasto-plastic response of the slab material for a fixed temperature of 1200°C.

On the other hand, an example of the temperature influence for a fixed strain rate of 10 s⁻¹ is shown in Figure 40.

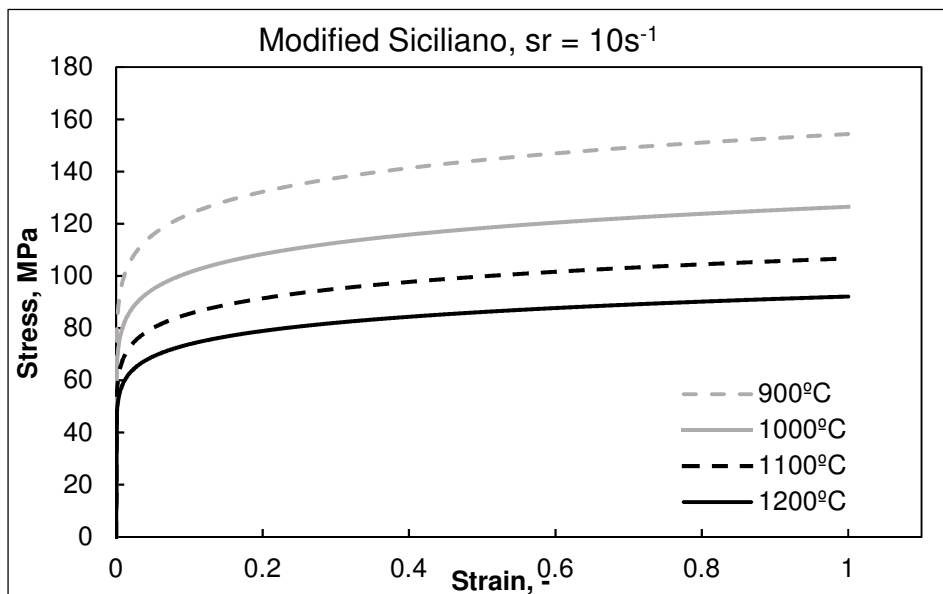


Figure 40 – Example of the temperature dependency of the elasto-plastic response of the slab material for a fixed strain rate of 10 [s⁻¹].

Moreover, as defined by Nioi *et al.* (2019) [43], the thermal conductivity of the slab material was fixed to 60 [W·K⁻¹·m⁻¹], the linear thermal expansion coefficient of the material was fixed

to $10.8 \cdot 10^{-6} \text{ [K}^{-1}\text{]}$, the emissivity of the material surface was fixed to 0.81 and the specific heat of the material was fixed to $490 \text{ [J} \cdot \text{kg}^{-1} \cdot \text{K}^{-1}\text{]}$.

For the material used in the roll, the material properties used were the ones defined by Gillebaart (2011), for the temper rolling process, conducted in the same lab-scale mill used in the present work. Therefore, a thermal conductivity of $60 \text{ [W} \cdot \text{K}^{-1} \cdot \text{m}^{-1}\text{]}$, a linear thermal expansion coefficient of $10.8 \cdot 10^{-6} \text{ [K}^{-1}\text{]}$ and a specific heat of $490 \text{ [J} \cdot \text{kg}^{-1} \cdot \text{K}^{-1}\text{]}$ were used [44].

An overview of additional material properties for both the roll and the slab materials can be consulted in Table 13.

Table 13 - Material characteristics for the roll and strip.

	<i>Roll material</i>	<i>Slab material</i>
Density [kg/m^3]	7850	7850
Young's modulus [GPa]	230	210
Poisson's ratio [-]	0.3	0.3
Plasticity	No	Yes

It should be noted that at the start of the simulation the strip and roll are disconnected, and that at some point they will have to make contact, resulting in the two parts bumping into each other. In a model without any concern for this phenomenon, the contact would result in an oscillation in the model that would propagate, thus providing an oscillating result that would not correspond to the real process conditions. To address this, Gillebaart (2011) resorted to damping in a model developed for the temper rolling process. However, when applying damping, it should be considered that it should not significantly affect the results of the simulation, other than removing the undesired oscillation. Therefore, Gillebaart (2011) conducted an analysis where a number of different damping methods and quantities were used with its results compared to the undamped model, reaching the conclusion that material damping was the most suitable approach to the problem. This approach uses the Rayleigh damping method and is described with the factors α_R and β_R , describing the amount of mass proportional damping and stiffness proportional damping, respectively. Usually, it is considered that mass proportional damping is mostly suitable for low frequency behaviour and stiffness proportional damping for high frequency behaviour. Therefore, in the rolling process it was concluded that the influence of the mass proportional damping was negligible, but the stiffness proportional damping had a considerable influence on the results [44]. Gillebaart (2011) analysed different values for the β_R factor in order to reach a value that led to sufficient damping of the oscillations, but still an accurate result when compared to the undamped model, as can be observed in Figure 41 [44].

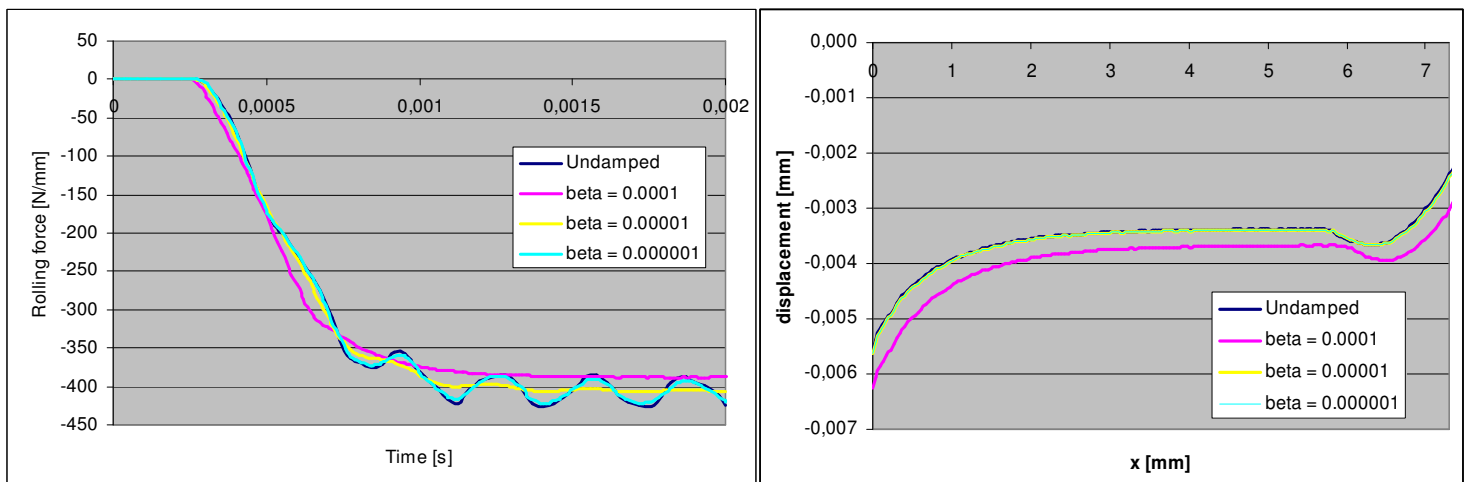


Figure 41 - Rolling force (left) and displacement curves of the strip (right) for different damping factors [44].

It was concluded from this analysis that the most suitable value for β_R for the rolling process being simulated was 0.00001 (yellow line), for which the oscillations are damped, while the displacement curve is very close to the undamped result. In the present work it was assumed that the same value would be suitable for the rolling process at hand, and therefore the same value was applied for all conducted simulations.

5.1.2 Interactions

The thermo-mechanical contact between the roll and the slab is the main factor in the hot rolling process and has significant influence on the results obtained. In the deformation zone, the volumetric heat caused by the deformation and the heat generation due to friction at the contact regions with the work-rolls should be considered in the thermal problem. Therefore, the general heat conduction equation, regarding the imposed velocity field, may be expressed by [11]:

$$\frac{\partial}{\partial x} \left(k \frac{\partial T}{\partial x} \right) + \frac{\partial}{\partial y} \left(k \frac{\partial T}{\partial y} \right) + \frac{\partial}{\partial z} \left(k \frac{\partial T}{\partial z} \right) + \dot{Q} = \rho c \frac{\partial T}{\partial t} + \rho c u \frac{\partial T}{\partial x} + \rho c v \frac{\partial T}{\partial y} + \rho c w \frac{\partial T}{\partial z} \quad (5.3)$$

where:

- x, y, and z, are the rolling direction, transverse direction, and thickness direction respectively;
- k, is the thermal conductivity of the rolled material;
- u, v, and w, are the velocity components along x, y, and z directions, respectively.

Furthermore, the thermal boundary conditions can be expressed as [11]:

$$-k \frac{\partial T}{\partial n} = h_c (T - T_{roll}) - q_f - r^{pl} \quad (5.4)$$

where:

- q_f , is the rate of generated heat by friction on the contact surface;
- r^{pl} , is the heat flux generated per unit of volume due to plastic deformation;
- n, is the normal direction to the surface boundary;
- h_c , is the contact conductance;
- T_{roll} , is the work-roll surface temperature;

These phenomena were implemented in the model separating the different mechanisms in three main factors.

Firstly, conductance between the two contacting surfaces was introduced as a contact property, as described by Eq.(5.5):

$$q = h_c \cdot (T_a - T_b) \quad (5.5)$$

where:

- T_a and T_b , are the temperatures of point a and b , belonging to the slab and roll respectively;
- q , is the heat flux per unit area that crosses the surface from point a to point b ;

The contact conductance was fixed to 20 [kW·m⁻²·K⁻¹] as used by Nioi *et al.* (2019) in the modelling of the deformation of surface defects during hot rolling [43], which was defined considering the oxide layer, according to the formulas provided in the extensive research on oxide scale behaviour during rolling carried out by Krzyzanowski *et al.* (2010) [45].

Secondly, the friction interaction between the roll and the slab was simulated using the same methodology used by Nioi *et al.* (2019) [43], which considered the isotropic Coulomb and stick-slip friction model (Lenard, 1990) [46], for which it was assumed that sliding at the contacting surfaces occurs when the equivalent shear stress at a contact point exceeds the critical shear

stress value defined by the coefficient of friction and the contact pressure, as can be consulted in Eq.(5.6):

$$\tau_c = \mu \cdot p \quad (5.6)$$

where:

- τ_c , is the critical shear stress value;
- μ , is the coefficient of friction;
- p , is the contact pressure.

Among the different parameters involved in the contact, one of the most important parameters involved is the aforementioned friction coefficient, since it drives the slab through the rolls. Since the modelled lab scale hot rolling process is a dry process, for which the friction coefficient between the roll and slab can be in the range of 0.1 to 0.3 [13, 44], in this model, a coefficient of friction of 0.25 was applied. This value was the result of several simulation attempts, where the minimum value which ensured the start of the rolling process by friction alone (corresponding to the real situation) was determined.

As defined by Nioi *et al.* (2019), it was also assumed that 90% of the frictional work is converted to heat that is equally transferred to the slab and the roll at the contact point (and therefore, an index of 0.5 was applied for the fraction of heat that is transferred to the slave surface, i.e. slab) [43]. This phenomenon was implemented as a heat generation type of interaction property and can be expressed by [11]:

$$q_f = \eta \cdot m \cdot k_s \cdot \Delta v \quad (5.7)$$

where:

- η , is the fraction of friction heat transferred to the slab ($\eta = 0.9 \cdot 0.5 = 0.45$);
- m , is the sticking friction factor;
- k_s , is the shear yield stress;
- Δv , is the relative tangential velocity between the slab and the roll.

Additionally, according to Shangwu *et al.* (2001) [47], it was assumed that 95% of the mechanical work is converted to thermal energy resulting in added heat flux to the rolled slab, implemented according to Eq.(5.8):

$$-r^{pl} = \eta_p \cdot \sigma : \dot{\epsilon}^{pl} \quad (5.8)$$

where:

- η_p , is the fraction of plastic work converted to heat ($\eta_p = 0.95$);
- σ and $\dot{\epsilon}^{pl}$, are the stress and strain rate vectors, respectively.

The normal contact behaviour is also important in this simulation, since to get an accurate result there should be as little penetrations as possible. A hard contact method was therefore used between the roll and slab.

Furthermore, the contact between the roll surface and the surface of the slab was defined using a surface-to-surface discretization method, since this will give a more accurate pressure distribution at the contact interfaces compared to the alternative node-to-surface contact [44].

The remaining interactions modelled concern the remaining heat transfer mechanisms occurring during the process. In a plant scale process, initially, the material is heated in a preheating furnace up to the hot rolling temperature and then, before starting the first rolling pass or during the interval between two successive stands, the metal is cooled by convection and radiation in the air. Furthermore, in the descaling section(s), the metal is subjected to high-pressure water jets to remove the oxide layer from the surface of the slab. However, in the lab

scale process being modelled, the descaling is conducted manually via hammering, a process which was not modelled, and which does not present such a significance to the heat transfer mechanisms as the automated water jet descaling found in full scale applications. To determine temperature distribution throughout the slab in the zones exposed to the air during the process, the governing heat conduction nonsteady-state equation in a Eulerian framework associated with appropriate boundary and initial conditions equation can be used [11]:

$$\frac{\partial}{\partial x} \left(k \frac{\partial T}{\partial x} \right) + \frac{\partial}{\partial y} \left(k \frac{\partial T}{\partial y} \right) + \frac{\partial}{\partial z} \left(k \frac{\partial T}{\partial z} \right) = \rho c \frac{\partial T}{\partial t} + \rho c u \frac{\partial T}{\partial x} \quad (5.9)$$

where:

- ρ , is the density of the rolled material;
- c , is the specific heat of the rolled material;

The thermal boundary conditions for cooling in the air should consider the convective and radiative heat transfer between the slab and the environment, and can be expressed as [11]:

$$-k \frac{\partial T}{\partial n} = h_a (T - T_\infty) + S \lambda (T^4 - T_\infty^4) \quad (5.10)$$

where:

- h_a , is the convection heat transfer coefficient;
- T_∞ , is the ambient temperature;
- S , is the Stefan–Boltzmann constant;
- λ , is the emissivity of the surface.

The convection heat transfer coefficient was calculated considering a laminar, incompressible flow without heat dissipation and without pressure gradients, for dry air at an ambient temperature of 20°C, calculated by [48]:

$$Re_L = \frac{u_\infty \cdot L}{\nu} \quad (5.11)$$

$$\overline{Nu}_L = 0.664 Re_L^{\frac{1}{2}} \cdot Pr^{\frac{1}{3}} \quad (5.12)$$

and:

$$\bar{h} = \frac{\overline{Nu}_L \cdot k_{air}}{L} \quad \text{for: } Pr > 0.6 \quad \text{and} \quad Re_L < 5 \times 10^5 \quad (5.13)$$

where:

- Re_L , is the Reynolds number for $x=L$;
- u_∞ , is the relative speed of the air in relation to the slab ($u_\infty = u$, assuming that the air is still);
- L , is the length of the slab;
- ν , is the dynamic viscosity of the air;
- \overline{Nu}_L , is the average Nusselt number for $x=L$;
- Pr , is the Prandtl number for the air;
- k_{air} , is the conductivity of the air;
- \bar{h} , is the average convective heat transfer coefficient.

It should be noted that all properties for the air were considered constant and corresponding to 20°C.

It should also be kept in mind that the problem at hand was reduced to a 2-dimensional, plain strain process, thus allowing the simplification of the heat transfer mechanisms by disregarding the transverse direction. Therefore, the boundary conditions were applied in a way as to provide results corresponding to the middle longitudinal cross section of the roll and slab, allowing the

visualization of the temperature, stress and strain profiles through the thickness direction in the central section of the slab.

5.1.3 Geometries and Mesh

The roll and the half slab were modelled with the dimensions corresponding to those found in real life lab conditions. The rolling gap was adjusted to obtain the desired 20% and 40% reductions for the 1 step rolling experiments (corresponding to slabs 1, 2, 5, 6, 9, 10, 13 and 14). For the 2-rolling step slabs (3, 7, 11 and 15) and for the 3-rolling step slabs (4, 8, 12 and 16), additional rolls were modelled and positioned next to each other.

Extra steps and boundary conditions were applied in such a way as to reproduce the time interval between rolling passes observed in real life, using video data from the lab experiments as a reference.

Since the roll and the slab have considerably different dimensions, the meshing strategy became of the utmost importance to the computational time.

The thickness of half of the slab is 10 mm and to get an accurate description of the stresses in the strip it was decided that at least 10 elements would be needed through the thickness direction, as shown by Gillebaart (2011) [44]. This decision directly influences the mesh size on the roll, since the parts are in contact with each other, and considering that, to get a proper result for the stress distribution in the roll, a sufficient number of elements are needed along the contact zone between the roll and slab. A ratio of approximately 4-1 between the size of the elements in the roll and the size of the elements in the slab was selected for the contact.

However, it would be inefficient, due to the added computational complexity, to mesh the whole roll uniformly with such small elements, since only a small portion of these will ultimately contact with the slab surface, corresponding to the outmost elements, radially. Therefore, the roll was meshed in a way that the mesh size is increasingly smaller outwards, in the radial direction.

On the other hand, with this strategy alone, there is still a large section of the roll that does not contact with the slab (the contact is conducted in less than a full rotation of the roll) and is meshed with small elements, thus reducing the computational efficiency of the model by not contributing significantly to the results of the simulation. To address this problem, the section that contacts the slab should be meshed finely while the rest of the roll is meshed relatively coarse. Due to the mismatch of the meshes in these two sections, the roll could not be modelled as a single part, leading it to be modelled as two separate parts, connected with tie-constraints, which ensures that the nodes of the slave surface will remain connected to the master surface at all times [44].

Additionally, the angle of the finely meshed section could be varied to optimize the computational time. A number of simulations were run to define the best possible contact angle, resulting in a finely meshed section of $\approx 100^\circ$, $\approx 200^\circ$ and 360° for the first, second and third rolling passes respectively.

The resulting meshing system of the roll can be observed in Figure 42.

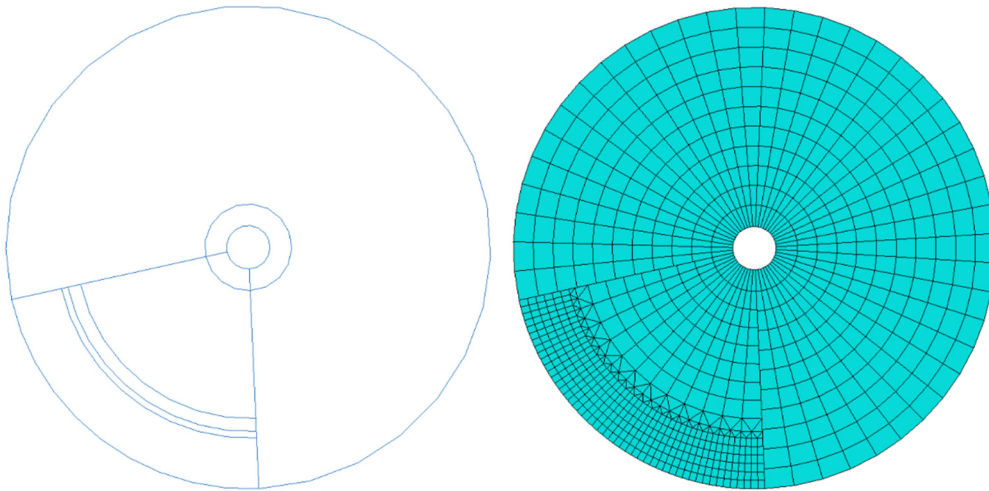


Figure 42 - Work-roll partitioning (left) and mesh (right) used to reduce the number of elements.

The radial transition in mesh size was achieved using zones with triangular elements that double the number of elements in the circumferential direction leading to the desired element ratio between the roll and the slab, as can be observed in detail in Figure 43.

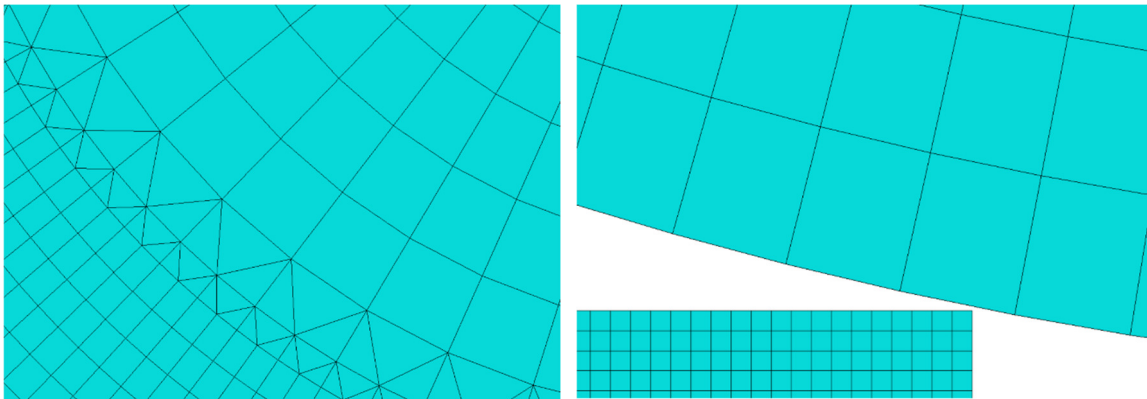


Figure 43 – Detail of the transition zones with triangular elements (left) and element size ratio between the roll and the strip (right).

Reduced integration, 4-node, plain strain thermally coupled quadrilateral, bilinear displacement and temperature elements with hourglass control (CPE4RT) were used to mesh the slab. 18 elements were used through the half-thickness, a choice that had in mind the linear geometric order of the chosen elements, which required an increase in element number to maintain the accuracy pretended. This resulted in elements with a size of $\approx 556\mu\text{m}$.

For the roll, reduced integration, 4-node, plain strain thermally coupled quadrilateral, bilinear displacement and temperature elements with hourglass control (CPE4RT) were used, as well as 3-node plain strain thermally coupled triangle, linear displacement and temperature elements (CPE3T) for the triangular transition zones.

The reduced integration was selected to avoid the shear locking effect due to an excessive deformation in the elements that might occur with fully integrated elements in contact situations [43, 44]. However, when reduced integration is used the elements might exhibit zero-energy deformation modes, an effect called hourglassing that requires the chosen elements to also have hourglass control to withstand these non-physical deformations. The triangular elements used do not exhibit shear locking, excluding the need for reduced integration [44].

An additional phenomenon called volumetric locking, which causes the mesh to behave stiffer than normal, should be taken into account when formulating the meshing for the model. To check if this phenomenon is present, the Hertzian contact situation (represented in Figure 44) is simulated and compared with analytical expressions defined by Konter (2005) [44, 49].

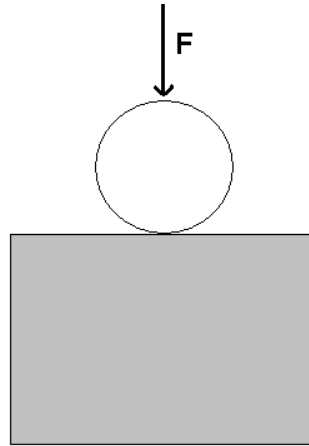


Figure 44 – Schematic representation of the Hertzian contact situation [44].

The analytical functions for the maximum contact pressure and for the contact length can be derived from the Hertzian contact theory, by Eq.(5.14) and Eq.(5.15) respectively [44]:

$$p_{max} = \sqrt{\frac{F \cdot E^*}{2\pi R^*}} \quad (5.14)$$

$$a = \sqrt{\frac{8 \cdot F \cdot R^*}{\pi E^*}} \quad (5.15)$$

where:

- p_{max} , is the maximum contact pressure;
- a , is the contact length;
- F , is the applied force;
- E^* , is the combined Young modulus of the parts;
- R^* , is the combined radii of the parts;

The combined Young's modulus and radii of the cylinder and slab can be determined by Eq.(5.16) and Eq.(5.17) respectively [44]:

$$E^* = \frac{2 \cdot E_1 \cdot E_2}{E_2(1-\nu_1^2) + E_1(1-\nu_2^2)} \quad (5.16)$$

$$R^* = \lim_{R_2 \rightarrow \infty} \frac{R_1 \cdot R_2}{R_1 + R_2} = R_1 \quad (5.17)$$

where:

- E_1 and E_2 , are the Young modulus of the cylinder and the slab, respectively;
- ν_1 and ν_2 , are the Poisson coefficients of the cylinder and the slab, respectively;
- R_1 and R_2 , are the radii of the cylinder and the slab, respectively ($R_2 = \infty$);

The complete pressure distribution can then be plotted using Eq.(5.18) [44]:

$$p = p_{max} \sqrt{1 - \xi^2} \quad (5.18)$$

where:

- ξ , is the normalized contact length ($\xi = x/a$).

The volumetric locking check was conducted by Gillebaart (2011) for the same element type as the one used in the present work (minus the temperature degrees of freedom, which do not affect locking). The analytical and finite element solutions for the pressure distribution throughout the contact length for said verification are shown in Figure 45 [44].

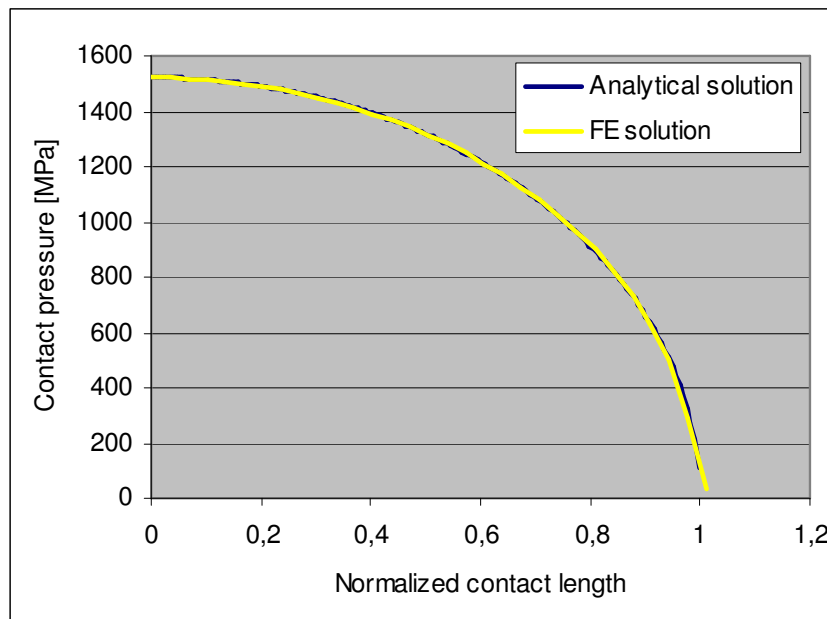


Figure 45 - Analytical and finite element solutions determined by Gillebaart (2011) for the pressure distribution throughout the contact length in the Hertzian contact problem [44].

As can be observed, the maximum pressure and the contact length are significantly similar for the FE solution compared to the analytical one, thus leading to the conclusion that volumetric locking is not an issue in the finite element model created.

5.1.4 Boundary and Initial Conditions

To properly constrain the roll, the inner ring is made into a rigid body with a rigid body constraint, as shown by Gillebaart (2011) and Swart (2013) [44, 50]. This rigid body has a reference point in the centre of the roll, where the boundary conditions are applied. A predefined field corresponding to an initial rotational velocity of 4.036rad/s is applied in this point, corresponding to the translational velocity of 0.45m/s applied to the slab in order to replicate the test conditions of the experimental stage. The matching velocities assure that the slab will go along smoothly with the surface of the roll. To ensure the smooth start of the rotational motion, the rest of the roll is given an equal initial rotational velocity as well, applied as a boundary condition. As already mentioned, a symmetry plane was also applied as a boundary condition to model the half-width of the slab, in order to reduce the computational effort of the simulation.

Since the model is thermo-mechanically coupled, initial predefined fields corresponding to the temperatures of 20°C and 1200°C were also applied to the roll and slab respectively, to replicate the test conditions.

Another factor to consider for the initial setup of the system was the location of the slab with respect to the roll. From several attempts it became clear that it is significantly beneficial to have no initial penetration or contact between the two parts, since this would force the solver to initially take very small steps to establish the relatively large contact area occurring immediately. If the slab is disconnected from the roll, the contact is gradually established, and the solver can use larger steps, thus reducing the computational time.

Finally, in order to reduce the computational effort when simulating the time between steps for the multi-step rolling schedules, the slab was modelled as being still, while keeping the thermal exchange mechanisms active (even convection). The time in between steps was averaged from the video footage from the lab scale rolling trials conducted for each thickness reduction schedule. However, due to the mismatch in times between the rolling pass steps and the transition steps from one pass to another (each rolling pass takes less than 0.6s to complete, while the slab waits 3-5s in between two consecutive passes), the simulation of these long waiting periods would still be too slow if no additional care was employed in the model. Therefore, in order to further reduce the computational time, mass scaling was applied uniformly to the whole model, only in between rolling passes. It should be noted that, in the steps where mass scaling was employed, the slab was standing still, and only thermal exchange occurred. Since mass scaling does not affect the thermal solution response in a fully coupled thermal-stress analysis [51], this resulted in an unaltered simulation solution.

5.2 FE Results

The results of the FE simulation conducted for the four different rolling schedules modelled are presented followingly. When possible, comparisons will be drawn with the experimental data available from the lab-scale hot rolling trials conducted at Tata Steel IJmuiden and from which the present work's samples were obtain, as well as with available literature.

Starting with the temperature evolutions during the process, the plotted results for different depths from the 40% reduction, single-step rolling schedule simulated is presented in Figure 46.

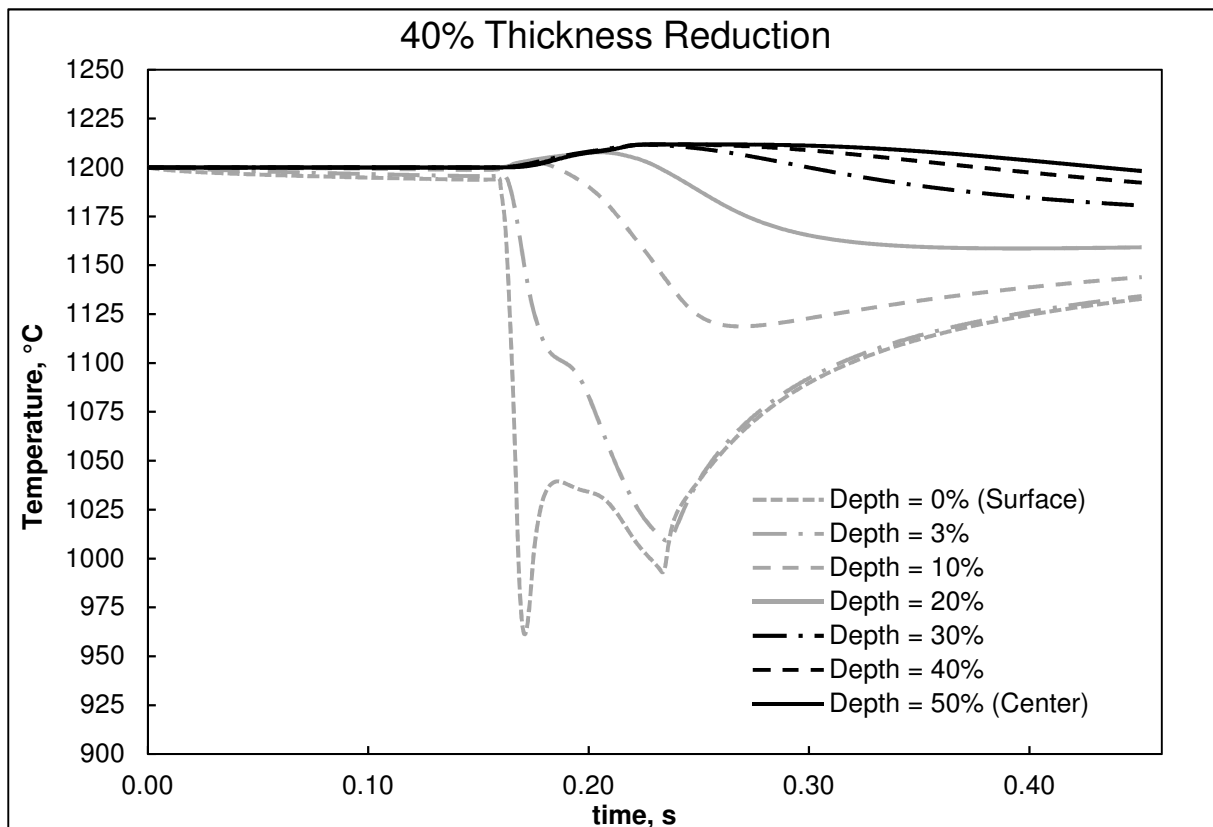


Figure 46 – Predicted temperature evolution at different slab depths (as a percentage of the initial slab thickness) during the one-rolling step, 40% thickness reduction, lab-scale hot rolling FE simulation.

It can be firstly be concluded that the predicted evolution is in accordance with the plant scale process evolution presented in Figure 17, where the surface temperature drops extensively during each rolling pass and re-heats from the centre, while the central temperature rises slightly during rolling due to the frictional work and plastic deformation converted into heat and cools

down afterwards due to the continuing heat exchange with the environment. Additionally, a comparison can be drawn between the two different thickness reductions simulated, as represented in Figure 47.

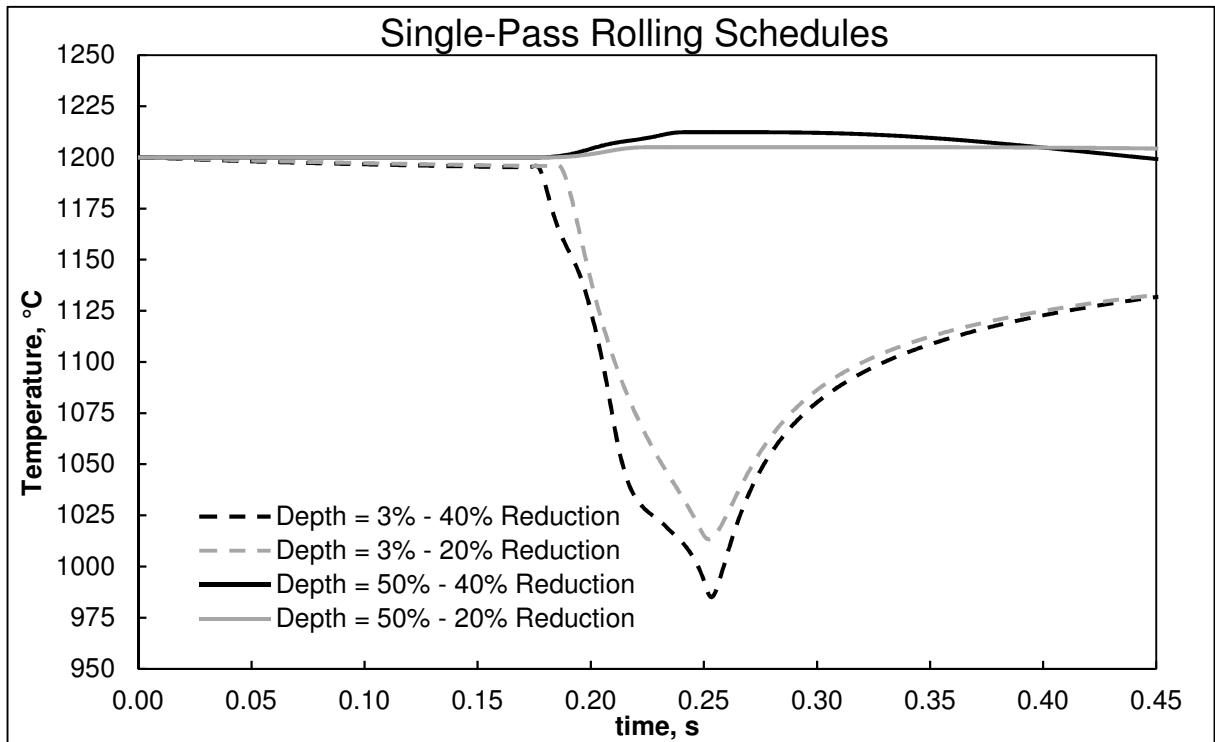


Figure 47 – Predicted temperature evolution at different slab depths (as a percentage of the initial slab thickness) during the single-step, lab-scale hot rolling FE simulations (20% and 40% thickness reduction).

As can be observed, the increase in thickness reduction is predicted to have a significant impact in the temperature evolutions felt during rolling. For higher thickness reductions, it is expected that the overall thermal gradient occurring between the slab’s most superficial layers and the slab’s central layers will increase as well, with a difference of $\approx 50^{\circ}\text{C}$ being felt at 3% of the slabs depth (the available value closer to the lowest registered inclusion’s depth in the experimental stage of the present work) and a difference of $\approx 10^{\circ}\text{C}$ registered at the slab centre. Although seemingly counterintuitive that the ultimately thinnest slab will experience the highest thermal gradient, this phenomenon is easily justifiable. Firstly, regarding the superficial temperature, it should be noted that the 40% reduction rolling results in a considerably higher contact length, as can be observed in Figure 48.

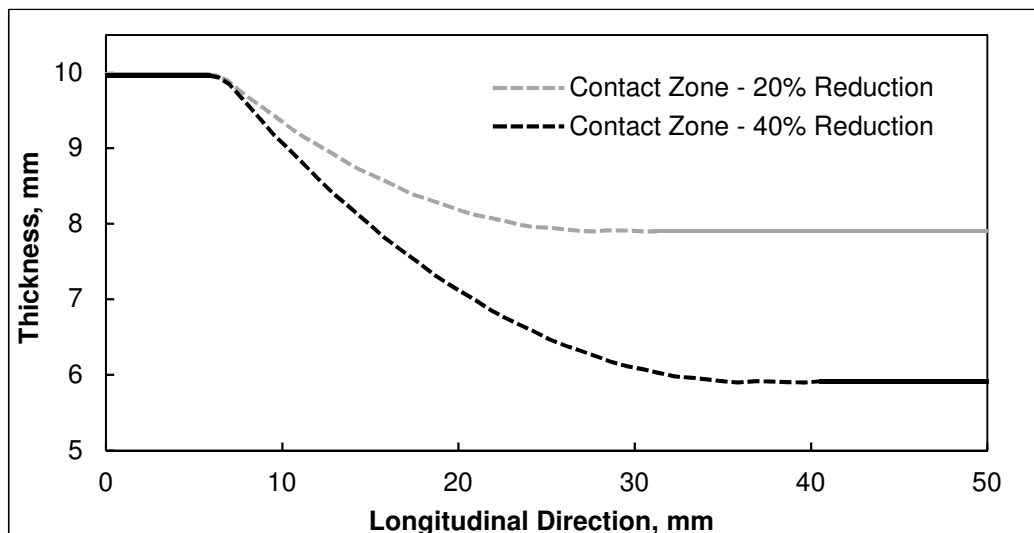


Figure 48 – Contact zones for the single-step, lab-scale hot rolling FE simulations (20% and 40% reduction).

Since the conduction between the slab and the roll is the most influencing thermal exchange phenomenon affecting the slab during rolling (Figure 49), it is expected that the increase in contact length will potentialize this phenomenon and result in lower surface and surface-adjacent temperatures.

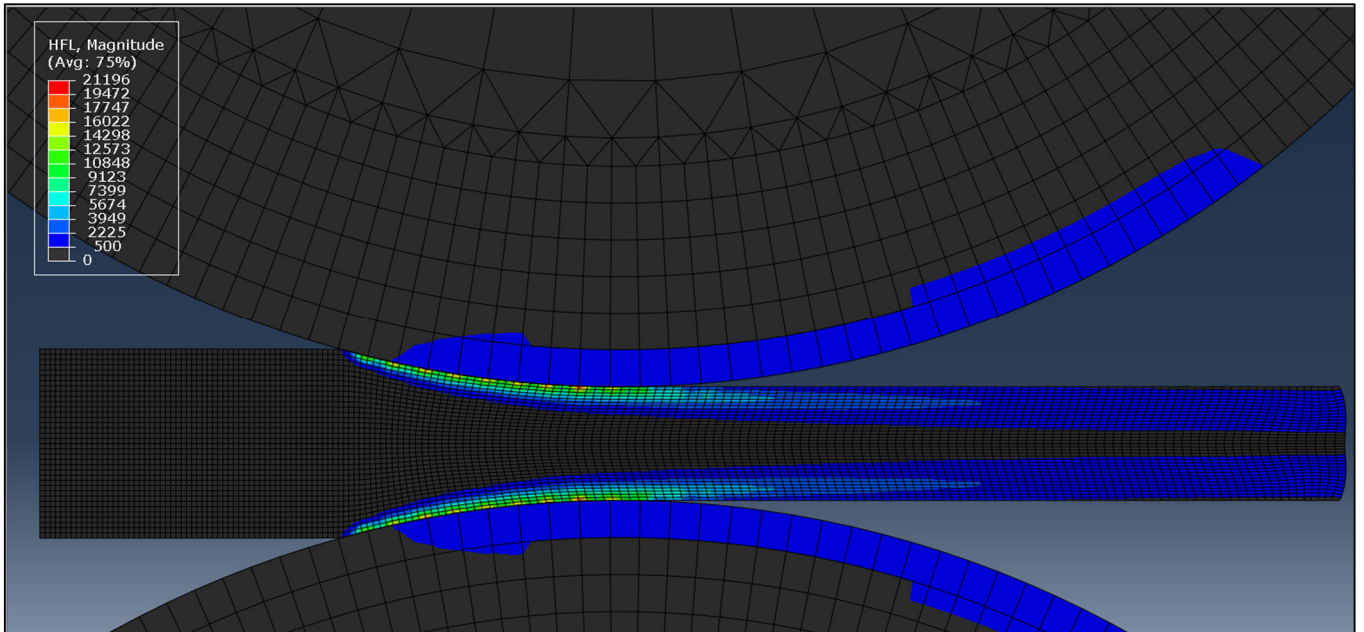


Figure 49 – Heat transfer during hot rolling for the 40% reduction hot rolling simulations. Legend in [kW/m²] units with lower bound set at 500 to highlight the conduction in the contact zone.

On the other hand, since the increase in temperature observed in the centre of the slab is resultant from the frictional work and the plastic deformation converted into heat during rolling, with the increase of the deformation suffered in the slab during rolling, it is also expected that the centre of the slab will also increase its temperature, reflecting these phenomena. This can be observed in Figure 50 and Figure 51.

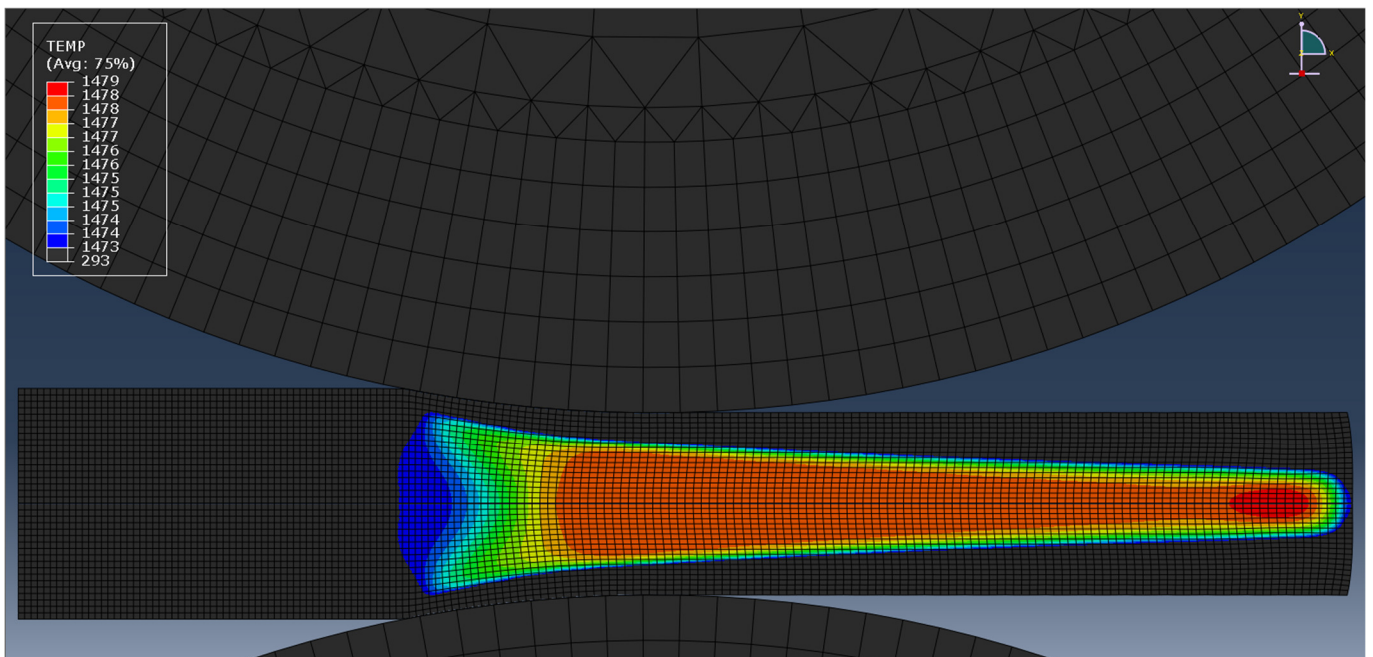


Figure 50 – Temperature gradient during hot rolling for the 20% reduction hot rolling simulations. Legend in Kelvin [K] units with lower bound set at 1473 (=1200°C) to highlight only the temperature increase above the initial conditions.

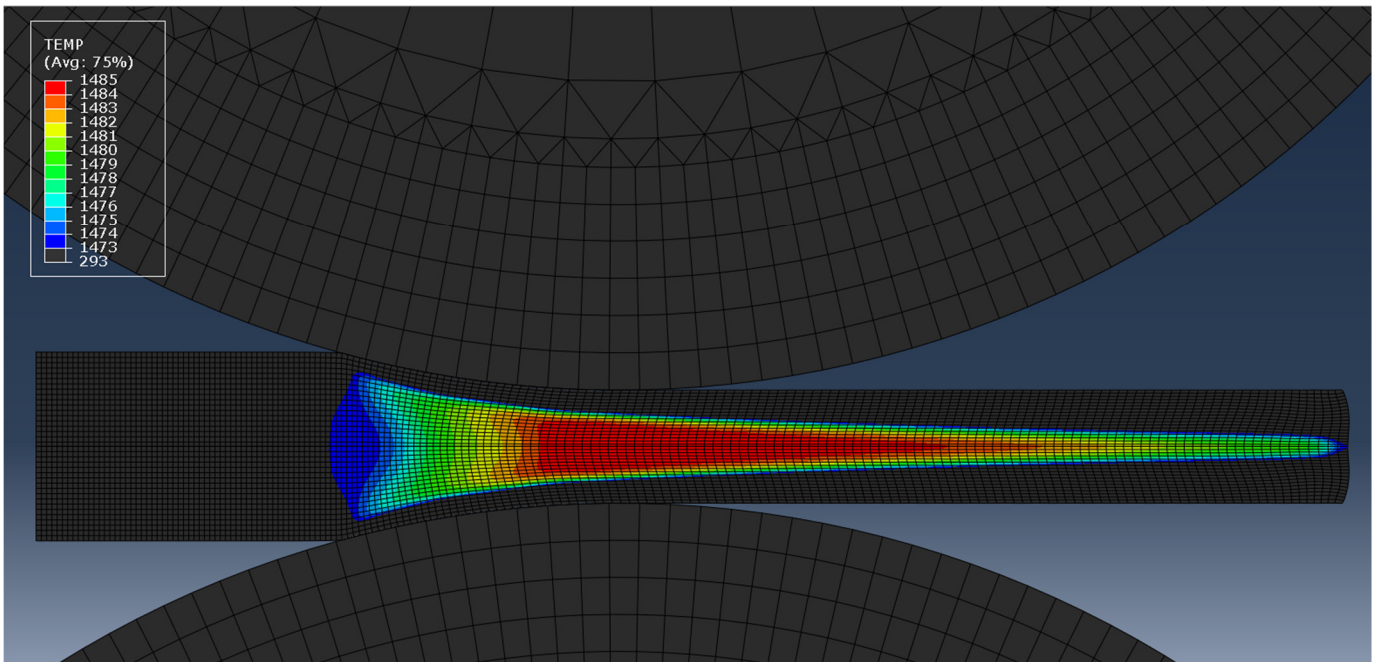


Figure 51 – Temperature gradient during hot rolling for the 40% reduction hot rolling simulations. Legend in Kelvin [K] units with lower bound set at 1473 (=1200°C) to highlight only the temperature increase above the initial conditions.

As can be observed, while the 20% reduction slabs experienced an increase in temperature that reached 6°C above the initial modelled temperature, the 40% reduction slab reached 13°C above its initial temperature, thus also aiding in the creation of a higher maximum temperature gradient in the slab.

Moreover, in Figure 47 it can also be observed that the temperature in the centre of the slab for the 40% reduction simulation eventually drops below that of the 20% reduction slab. This is most likely explained by the final lower thickness of the slab, which results in a higher cooling rate and ultimately in a lower temperature, even in the centre of the slab.

Since the temperature gradients (and consequent cooling and heating rates) play a role in the final inclusion's microstructure, the understanding of these influences is important for the interpretation of the results.

On the other hand, a comparison for the single pass schedules can be made with different (and more complex) FE models. Such is the case of the model developed by Serajzadeh *et al.* (2002) where a 6-roughing stand hot rolling process with a maximum of 31% thickness reduction in a single step is modelled along with the recovery and recrystallization of hot deformed austenite considering structural heterogeneity [52]. In Figure 52, the temperature evolution for the first rolling stand in the Serajzadeh *et al.* (2002) FE model can be observed [52]. It should be noted that, in this model, the pre-heating temperature simulated corresponds to 1270°C, a higher temperature than the one used in the present work [52]. Additionally, the model has the first rolling stand after a descaling stand (simulating the real-scale process) where additional heat exchange occurs [52]. Therefore, the initial temperature profile does not correspond to the quasi-uniform found in the simulations conducted in the present work. Moreover, it should be considered that the first rolling stand in the Serajzadeh *et al.* (2002) FE model leads to a 15% thickness deformation, a value that is lower than the minimum value simulated in the present work [52].

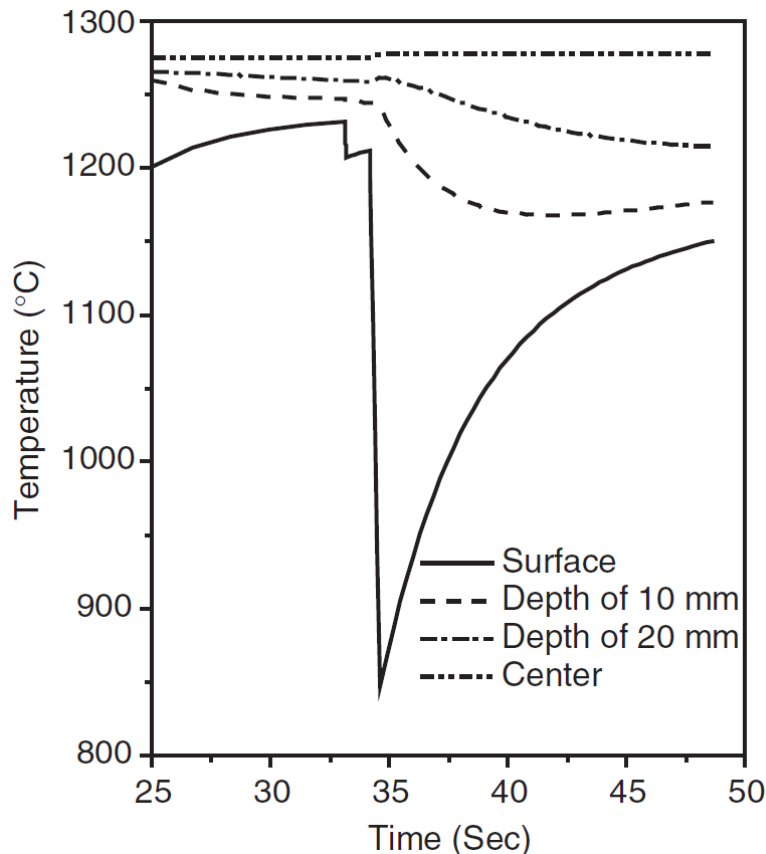


Figure 52 – Predicted temperature evolution at different slab depths (10mm and 20mm correspond to 5% and 10% of the initial slab thickness, respectively) during the first rolling step (15% thickness reduction) of the plant-scale, hot rolling FE simulations conducted by Serajzadeh *et al.* [52].

As can be observed, the results registered by the Serajzadeh *et al.* (2002) FE model present a similar evolution to the ones found in the present work's FE model, although with a higher temperature gradient than the one found in the 40% reduction simulation conducted, which contradicts the conclusion that higher thickness reductions result in higher temperature gradients. However, this can be explained by the fact that the plant-scale process modelled by Serajzadeh *et al.* (2002) uses steel slabs with an initial thickness of 200mm, 10x higher than the one used in the lab-scale process at hand, and rolls with a 1093mm diameter, while the ones used in the present work have only 223mm [52]. Since the thermal response is a function of the slab and roll dimensions, it is understandable that the different contact lengths resulting from the different sizes of the processes and the different heat exchange resulting from the different slab dimensions will ultimately result in different values for temperatures and respective variations, invalidating yet another direct comparison.

Furthermore, the predicted temperatures can also be compared with the experimental results from the lab-scale hot-rolling trials. However, it should be noted that the temperature during the rolling trials was measured in a fixed point in space at the entrance and exit of the lab-scale mill. Therefore, while there is no information about the real temperature evolution during rolling, since the slab was placed under the entry temperature sensor before rolling there is information about the cooling that the surface of the slabs experienced on this initial phase, as well as information about the exit surface temperature. It should be kept in mind that the experimental process was conducted manually, and therefore the slabs passed under the exit sensor at different times, which resulted in different exit temperature values (depending on the time that the slab had to re-heat from the centre), which complicates the comparison with the FE results.

An example of the entry and exit surface temperatures for a single rolling step is presented in Figure 53, for the 20% thickness reduction experiments.

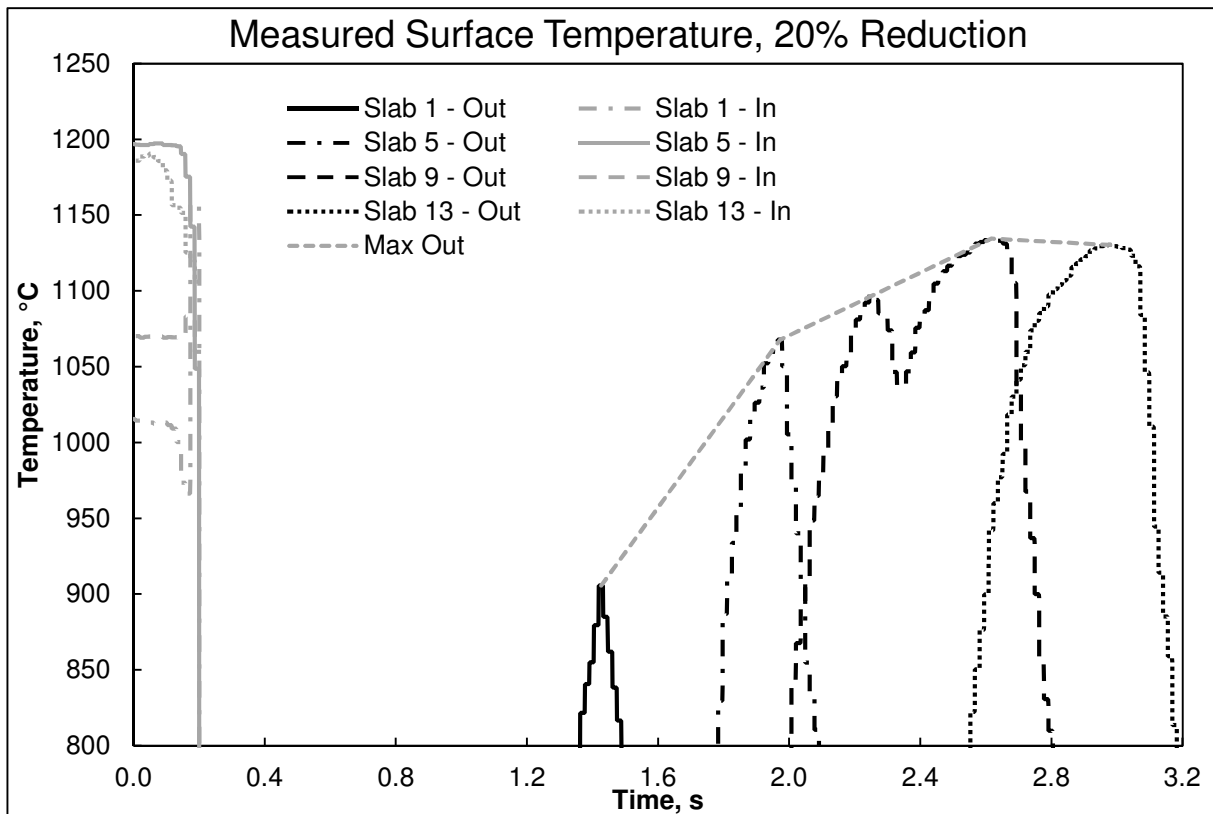


Figure 53 - Experimental surface temperature measurements at the entry (In) and exit (Out) of the lab-scale hot rolling mill for the single-pass, 20% reduction experiments.

As can be observed, the entry temperature varies significantly between experiments. This fact can be explained by the waiting time before rolling, which, since the slab is placed on a steel table, results in a significant heat loss before the process begins. While not explored in the present work, further simulations could evaluate the difference that this initial temperature variance has on the temperature evolutions and profiles during the rolling process so as to aid in the interpretation of experimental results. Moreover, despite the different times at which the exit temperature was measured (the ≈ 1.5 s difference between slab 1 and slab 13 is understandable for a manual process such as the experiments conducted, but makes a significant difference in the measured results), the re-heating phenomenon followed by further cooling can still be observed if a joint analysis of the different slab results is conducted, taking in consideration that the evolution of the maximum exit surface temperatures at different times should indicate the overall behaviour after rolling, as presented by the 'Max Out' curve in Figure 49.

Regarding the temperature evolution for the multi-pass rolling schedules, the plotted results for different depths from the 60% reduction, 2-pass and 85%, 3-pass rolling schedules simulated are presented in presented in Figure 54 and Figure 55.

The measured surface temperature results from the lab-scale milling trials on the 85% reduction schedule are also displayed on Figure 55. To do so, the average entry temperature and peak exit temperature were plotted against time, synchronized with the simulation by the initial time of each rolling step, to compensate the time variations between experiments. This synchronization, while possibly introducing new errors, is assumed not to be significantly disruptive, since the only thing that is altered is the time in between rolling passes, in which the heat exchange was extensively lower than during each pass.

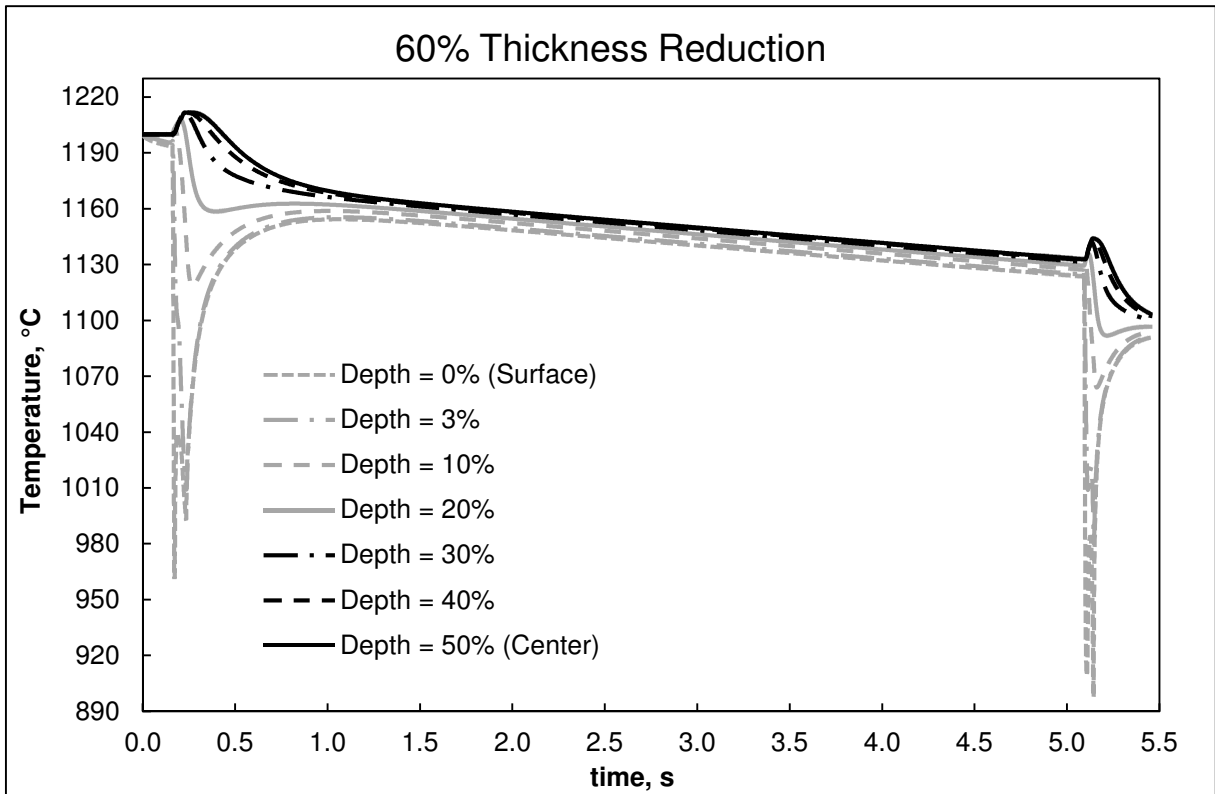


Figure 54 – Predicted temperature evolution at different slab depths (as a percentage of the initial slab thickness) during the two-rolling step, 60% thickness reduction, lab-scale hot rolling FE simulation.

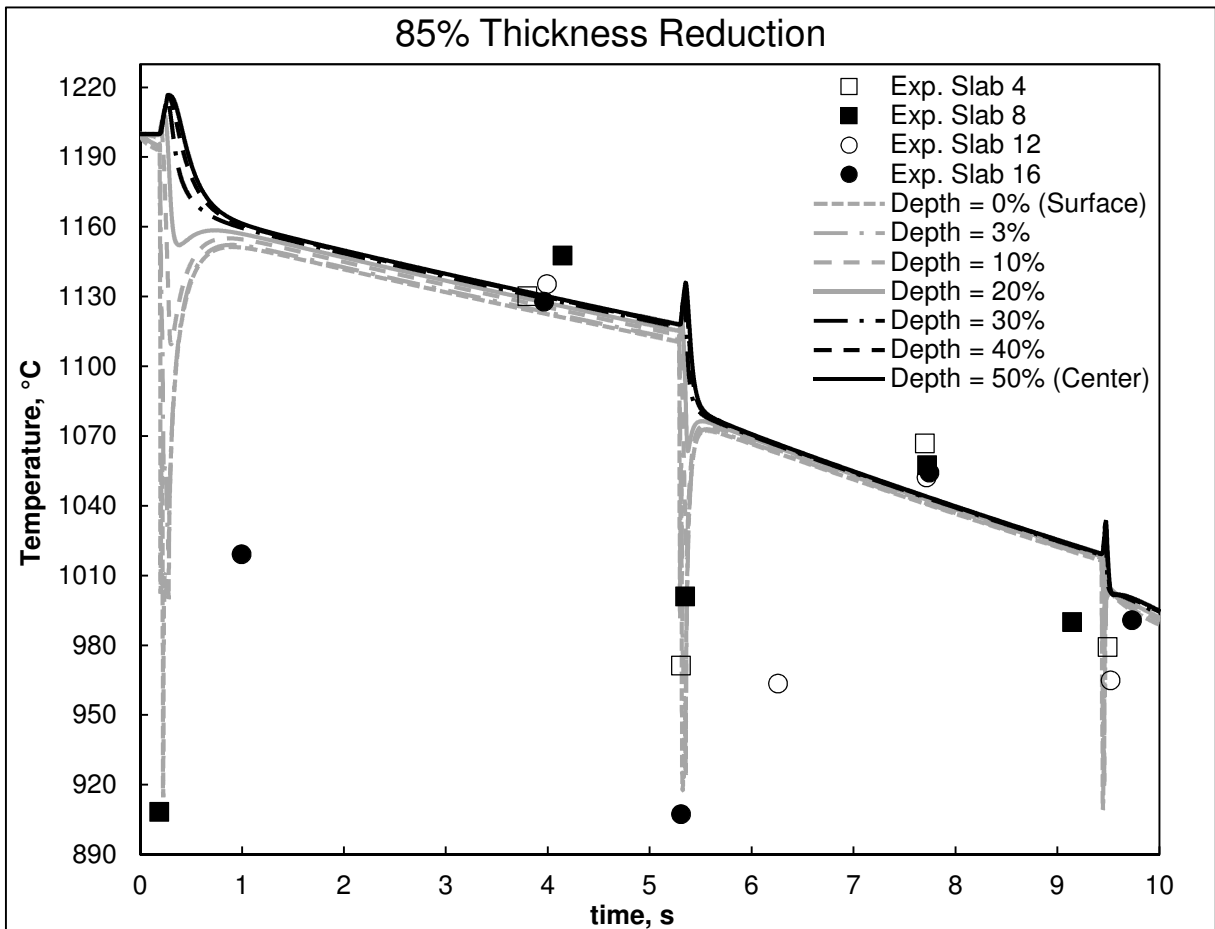


Figure 55 – Predicted temperature evolution at different slab depths (as a percentage of the initial slab thickness) during the three-rolling step, 85% thickness reduction, lab-scale hot rolling FE simulation. Measured surface temperature plotted for the slabs in the rolling trials.

It can be observed that the model presents a good approximation of the measured temperature results, although predicting a considerably faster surface re-heating effect than the experimental measurements. Moreover, the predicted evolutions are also in accordance with those found in the literature for other FE models, such as the one developed by Serajzadeh *et al.* (2002), as can be observed in Figure 56 [11, 52].

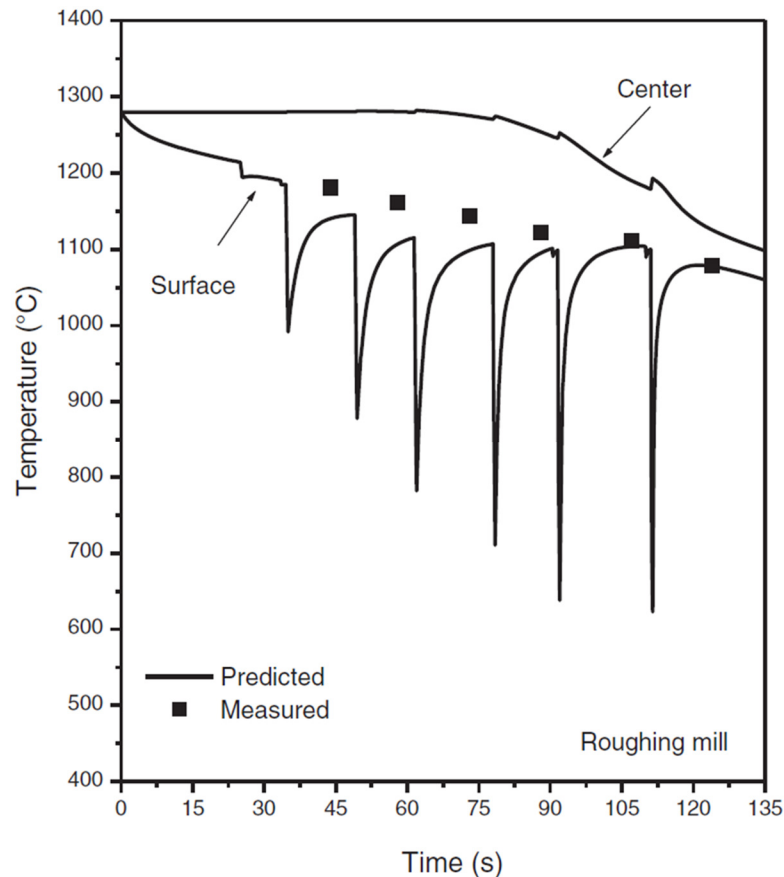


Figure 56 – Predicted and measured temperature variations during a 6-roughing stand, hot rolling process [11]. FE model considering the thermo-mechanical-metallurgical response of a low-carbon steel [52].

However, although displaying a similar evolution to the more advanced models, the developed FE model could be further tuned so as to take into account the specific metallurgical response in the lab scale process. It should be kept in mind that the coefficients in the modified Siciliano predictive model used for the material characterization were tuned for the real-scale hot strip mill at Tata Steel IJmuiden, and that in the present work the inter-stand recrystallization phenomena were dismissed.

Moreover, it is also important to notice that a direct comparison between the FE model presented by Serajzadeh *et al.* (2002) and the FE model developed in the present work is not possible, since the present work used fewer rolling steps with considerably higher deformations per step [52]. A simulation of a rolling schedule equivalent to the one used by Serajzadeh *et al.* (2002) could be of significant importance for further work regarding the tuning of the model at hand [52].

Furthermore, despite not being the main objective of the developed model, the rolling force results are important to validate the simulated process. Therefore, when considering the rolling forces, the FE simulations were compared with the measured results from the lab-scale hot rolling trials, obtained with loading cells on both bearings of the non-adjustable axis of the lab-scale hot strip mill.

For the single pass, 20% reduction process, this comparison can be consulted in Figure 57.

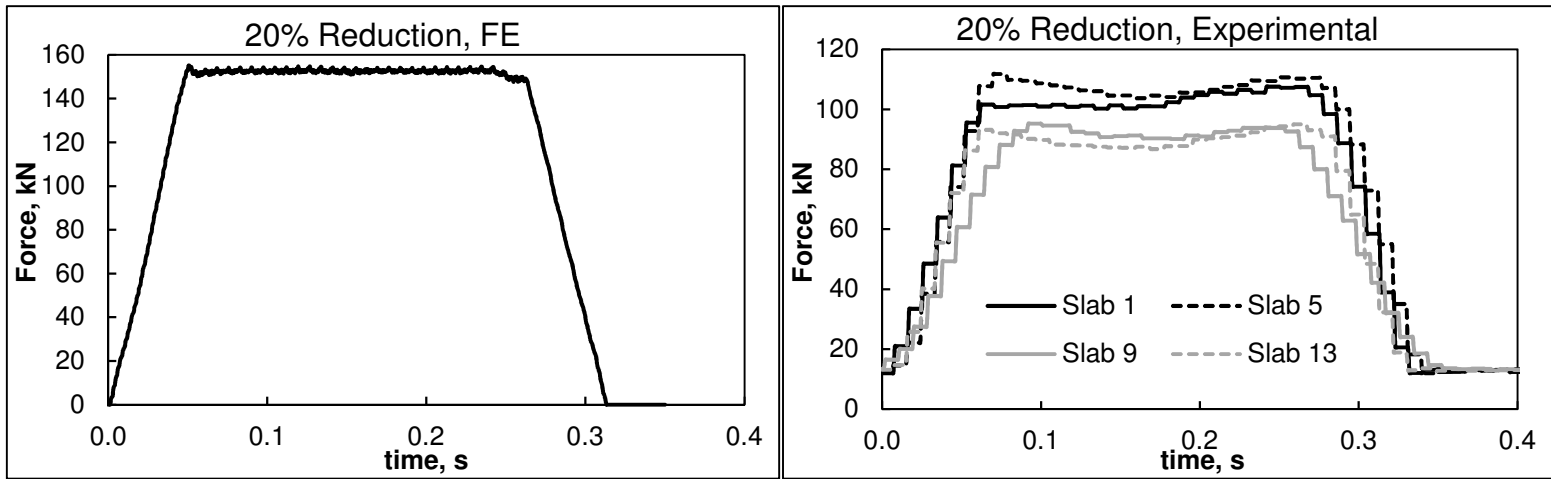


Figure 57 – Finite Element results (left) and experimental results (right) for the rolling force evolution throughout the single-pass, 20% reduction rolling schedule.

As can be observed, it is firstly noticeable that the measured force results display an offset of $\approx 10\text{kN}$. This is a result of the weight of the frame, axis and rolls, constantly present in the measurements. This offset, however, was chosen not to be corrected, since this weight will ultimately apply a force during rolling, aiding the process. Secondly, it can be observed that the measured results are considerably lower than the predicted ones ($\approx 40\text{kN}$). This difference can begin to be explained by the friction coefficient used, one of the main contributors for the final rolling force value. In the FE model, it was considered that a fixed friction coefficient of 0.25 would be appropriate, an estimation that can be confirmed consulting Figure 6. However, as displayed in Figure 7, this parameter is also expected to present a variation with temperature. Since the process starts at higher temperatures than that of 1050°C , for which the coefficient of friction for a 20% thickness reduction process would be ≈ 0.25 , a lower value would be more suitable. However, as could be observed by the temperature profiles, the surface temperature presents a considerably variable and non-uniform evolution, thus leading to the conclusion that in order to more accurately ascertain the rolling forces, further tuning of the model could focus on implementing a temperature-dependent friction coefficient. Additionally, it can be confirmed that the predicted rolling time is in accordance with the measured results, validating this aspect of the developed model. Finally, it can also be observed that the experimental data presents a high variation between the several experiments conducted ($\approx 20\text{kN}$) a factor that will be explored in detail followingly, when evaluating the rolling forces in the 2-passes, 60% reduction rolling schedule (equivalent to the first and only pass in the 40% rolling schedule) in Figure 58 and Figure 59.

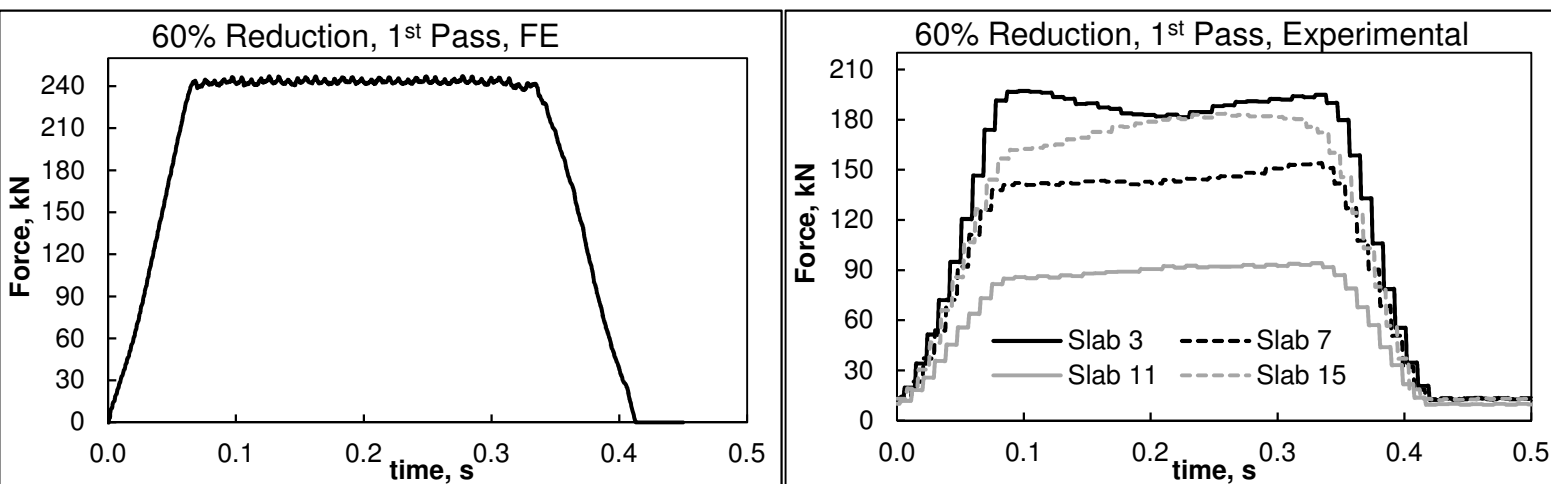


Figure 58 – Finite Element results (left) and experimental results (right) for the rolling force evolution throughout the first pass in the 60% reduction rolling schedule.

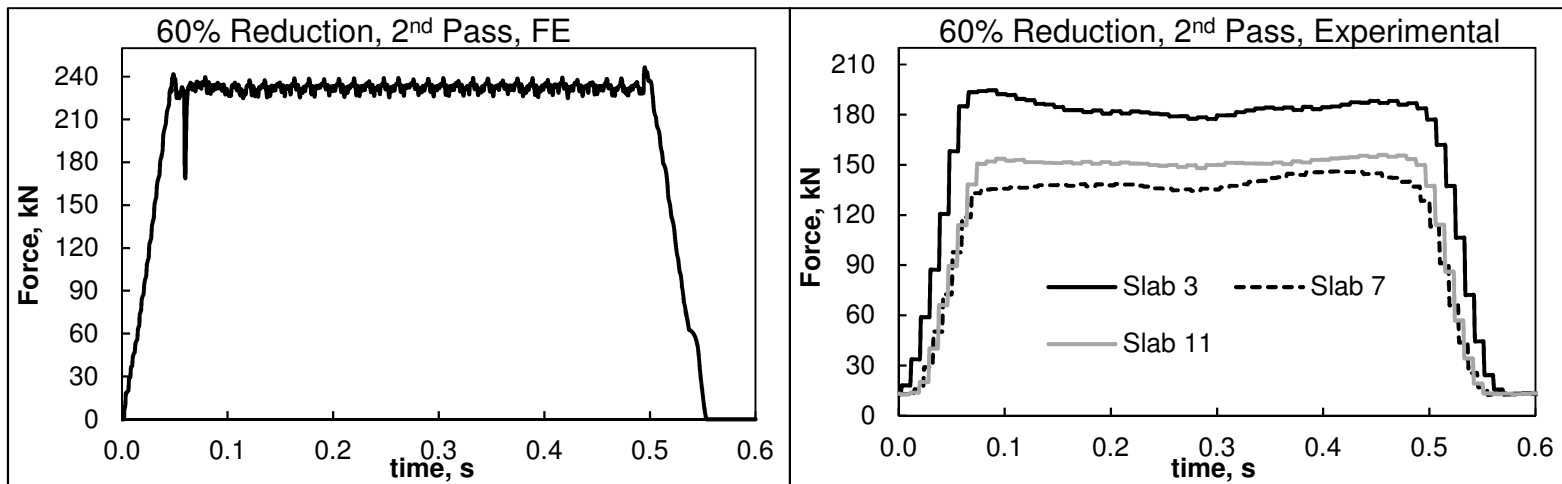


Figure 59 – Finite Element results (left) and experimental results (right) for the rolling force evolution throughout the second pass in the 60% reduction rolling schedule.

Once again, as observed for the 20% rolling passes, the simulated rolling time coincides with the measured results. However, the experimental results present a considerably high variance between different slabs, with a higher difference between the higher and lower values than the difference between the FE results and the higher measured result, a phenomenon that is more pronounced than what was observed for the 20% reduction experiments. It can also be observed that the lowest measured results in the first pass (equivalent to a 40% reduction) present a rolling force that is inferior to all of the 20% reduction experimental results, something that indicates the unreliability of the experimental data set. To ascertain the reason behind this variance in the force measurements, the video footage of the lab-scale experiments was analysed, and it could be observed that the slabs were sometimes pulled during the milling process. This factor affects the force results to a significant degree (the pulling of the slab reduces considerably the force necessary to “push” the slab naturally via rolling), creating experimental results that not only display different values based on the pulling force but also an overall lower rolling force than that of the simulated, not pulled, rolling schedules in the FE model.

An additional reason behind the force difference between the measured and simulated results could come from the material properties. Instead of being derived from experimental tests, the stress-strain curves for the slab material were determined using the aforementioned Siciliano model, optimized for the real-scale hot strip mill and not for the lab-scale hot strip mill. Further tuning of the coefficients used in the predictive model could result in force results that more accurately describe the process at hand. Furthermore, the friction coefficient also varies with the thickness reduction applied by the rolls (Figure 7). This fact leads to the conclusion that in future work, the adaptation of the friction coefficient to the deformation applied in each step would present more accurate results.

Finally, in order to confirm the deformed profile of the PM cylinders inserted in the slabs during the experimental stages of the process, the deformation of a column of elements along the slab depth was evaluated. In Figure 60 (left), the resulting deformed profiles at the end of the process are displayed for the conducted single-pass hot-rolling simulations, where it can be concluded that the same behaviour displayed in detail in Figure 33 and represented schematically in Figure 28 is seen in the FE results. However, upon comparison of the displacements along the xx axis between the FE results and the real PM cylinder separation lines (e.g. Figure B2 in Appendix B), it can also be observed that the magnitude of the deformation is less severe for the FE simulations (e.g. the deformed profile for the 40% reduction slabs presents a maximum displacement of 1.4mm in the rolling direction for the FE simulations, while it presents a maximum magnitude of ≈ 3 mm for the real PM cylinders).

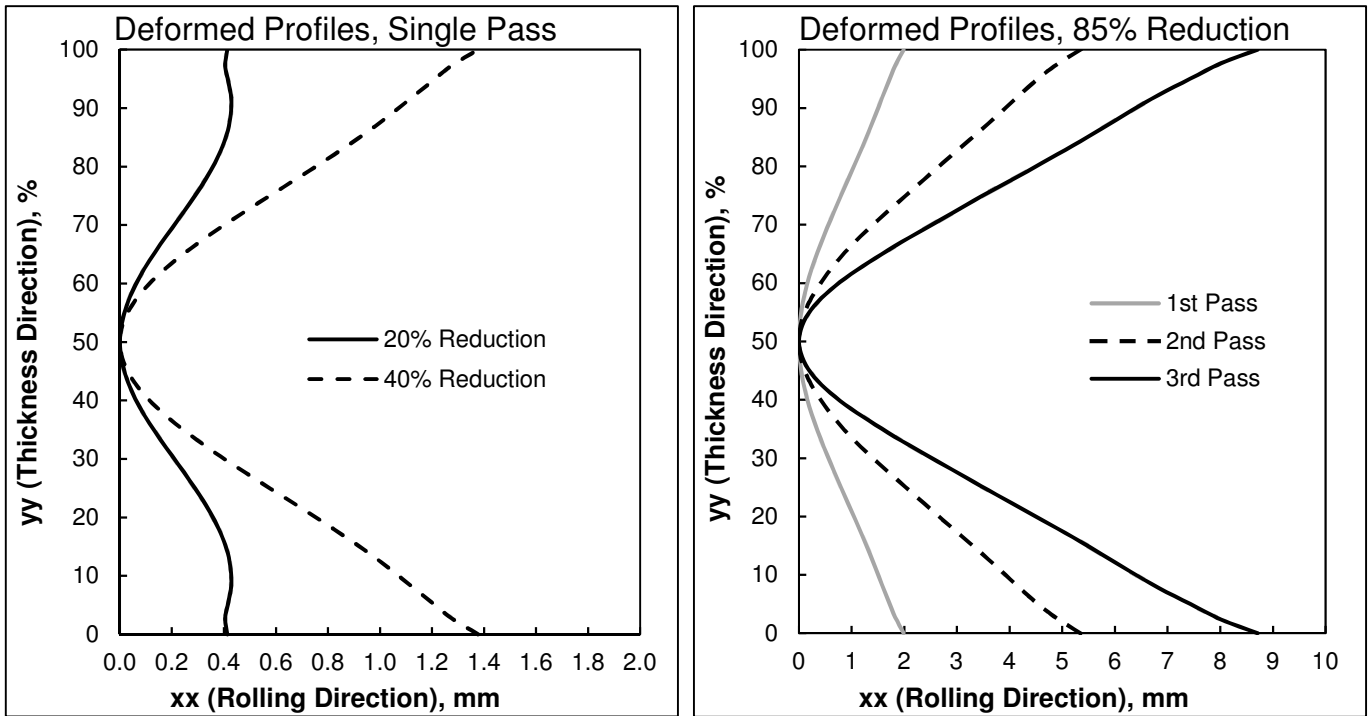


Figure 60 – Relative displacements of a column of elements for the two single-pass hot rolling simulations (left) and for the 3-pass, 85% thickness reduction hot rolling simulation (right). Direction yy displayed as a percentual proportion to the final thickness to allow a comparison between the slabs.

This fact might be explained by two main factors: firstly, the cuts observed in the optical microscopy images of the slabs where this behaviour is observed do not correspond to the exact central section of the slab, since there are several millimetres of material loss during cutting, grinding and polishing to find inclusions, which, since the cylinders present a non-linear deformation (Figure 28), leads to more deformed profiles away from the centre of the slab; secondly, the deformed profiles in the FE results are perfectly mirrored along the yy direction, while the real results tend to be unevenly deformed (e.g. Figure B3 in Appendix B), resulting in a higher maximum deformation being concentrated in one of the sides.

Additionally, the resulting profiles for the 3-pass, 85% thickness reduction hot-rolling simulations are displayed in Figure 60 (right) for the end of each rolling pass, displaying the evolution that this behaviour has with the increase in the number of steps, and ultimately representing the deformed shape that could be seen in the 85% reduction slabs' PM cylinders (e.g. Figure 32 and Figure B1 in Appendix B).

6 Analysis and Discussion

The analysis of the results obtained from the experiments conducted is hereafter presented, accompanied by a comparison between the experimental and the simulated results, as well as by a discussion of the similarities and differences observed. Additionally, a preliminary analysis was also conducted with the results from the work developed by Uittenbroek (2019), which was intended to evaluate the compositional variations in the inclusions and its possible identifiable behaviours in the longitudinal direction [9]. While interesting, this analysis was not carried out with the present work's results due to time restrictions. Therefore, in order not to disrupt the flow of thought and information in the present thesis, this analysis is presented in Appendix C.

6.1 Inclusion Shape

The analysis of the inclusions' shape was conducted based on the optical microscopy measurements of length, thickness, depth and area of the inclusions. Data from the inclusions found in the 60% and 85% reduction samples studied by Uittenbroek (2019) was included in the analysis in order to allow a full representation of the shape evolutions with the increase in thickness reduction, as well as to complete the data sets obtained in the present work [9].

It should be noted that given that the experimental procedure used to observe the inclusions has an inherent tendency to produce geometry data with high variance, due to the fact that is impossible to determine if all inclusions found were cut equally and the same section was observed (it was defined that sections corresponding to longitudinal cuts through the middle plane of the inclusion were the desired standard). Therefore, in order to allow a considerably valid analysis of the shape of the inclusions, a high number of inclusions is necessary to produce a statistically relevant data set.

Moreover, to avoid any unnecessary deviations from the overall behaviour, the exclusion of the inclusions that were undoubtedly observed in longitudinal cuts corresponding to offsets to the middle plane of the inclusion was conducted. Out of the 57 inclusions available in the joint data between the present work and the study conducted by Uittenbroek (2019), 13 inclusions were deemed unfit for geometric analysis and therefore excluded [9].

The geometry of the observed inclusions was evaluated based on ratios. Firstly, two different aspect ratios were defined: the maximum aspect ratio and the normalized aspect ratio. The maximum aspect ratio (used by Uittenbroek, 2019 [9]), represents the relation between the maximum thickness of the deformed inclusion, measured as specified in Appendix B, and the final length of the inclusion, as can be observed in Eq.(6.1):

$$MAR = \frac{t_f^{max}}{l_f} \quad (6.1)$$

where:

MAR, is the maximum aspect ratio;

t_f^{max} , is the maximum thickness of the inclusion after rolling;

l_f , is the length of the inclusion after rolling.

The normalized aspect ratio (used by Meyneng *et al.*, 2017 [21]) aims at correcting the fact that, as could be observed in Figure 37, and Figure 38, the inclusion's shape changes from an oval shape to a drop-like shape with the increase in thickness reduction, thus rendering the maximum thickness a poor measure of the behaviour of the inclusion, since the majority of the inclusions has a significantly lower overall thickness than the maximum registered. Therefore, the normalized aspect ratio defines the thickness of the inclusion as a virtual thickness, equivalent to that of a perfect ellipse with area and length equal to those measured for the inclusion, as can be consulted in Eq.(6.2) and Eq.(6.3):

$$NAR = \frac{t_f^{norm}}{l_f} \quad (6.2)$$

and:

$$t_f^{norm} = \frac{A}{\pi \cdot l_f} \quad (6.3)$$

where:

NAR, is the normalized aspect ratio.

t_f^{norm} , is the normalized thickness after rolling;

A, is the area of the inclusion's section.

The relation between these two parameters for the measured inclusions can be consulted in Figure 61.

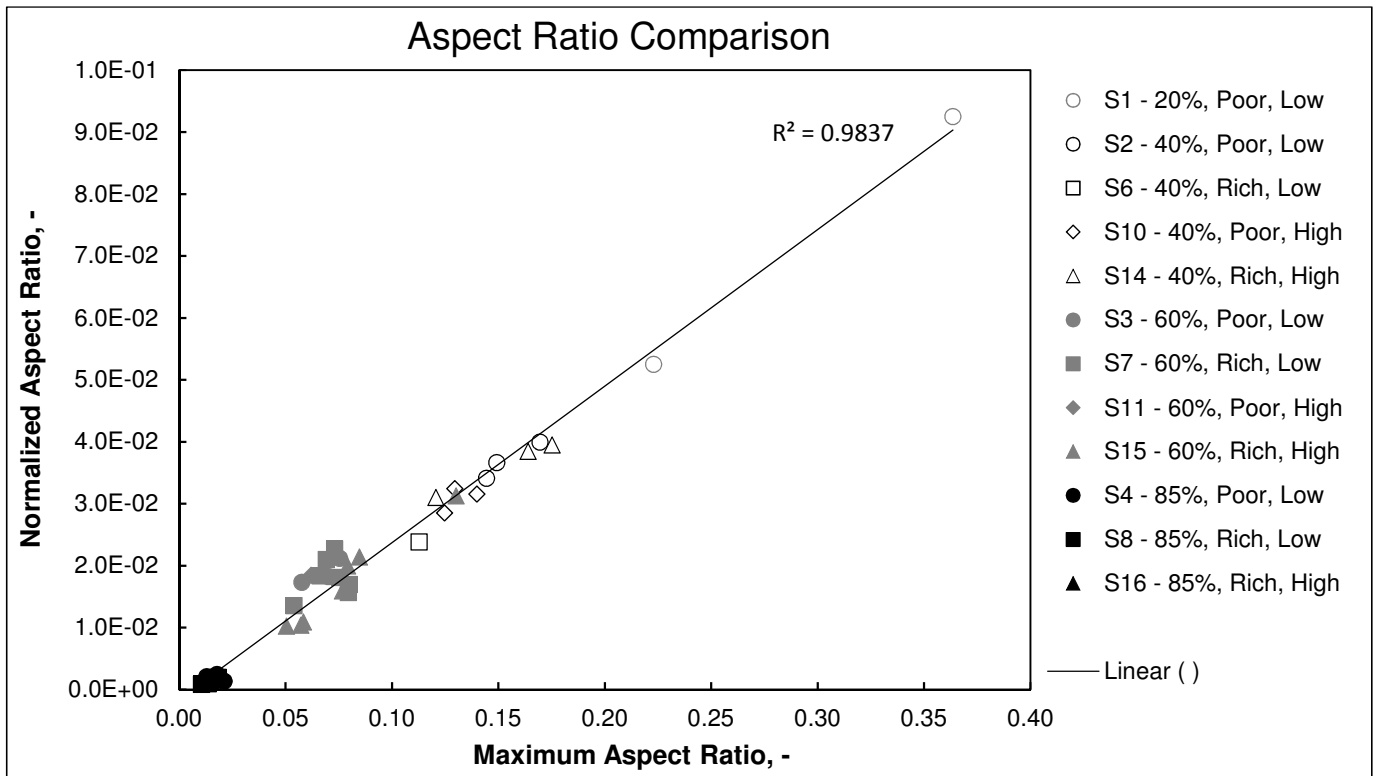


Figure 61 – Relation between the normalized and the maximum aspect ratios. Nomenclature of the subtitle indicates the slab number (1-16) and its respective thickness reduction (%), the F and Na content (Poor/Rich) and the soaking time (Low/High).

As can be observed, these two parameters present a strong correlation, which, since the normalized aspect ratio is based only on the area and length measurements, points towards the possibility of predicting the final maximum thickness of a given inclusion based only on these two parameters.

Moreover, the evolution of the normalized aspect ratio for the different thickness reductions can be found in Figure 62.

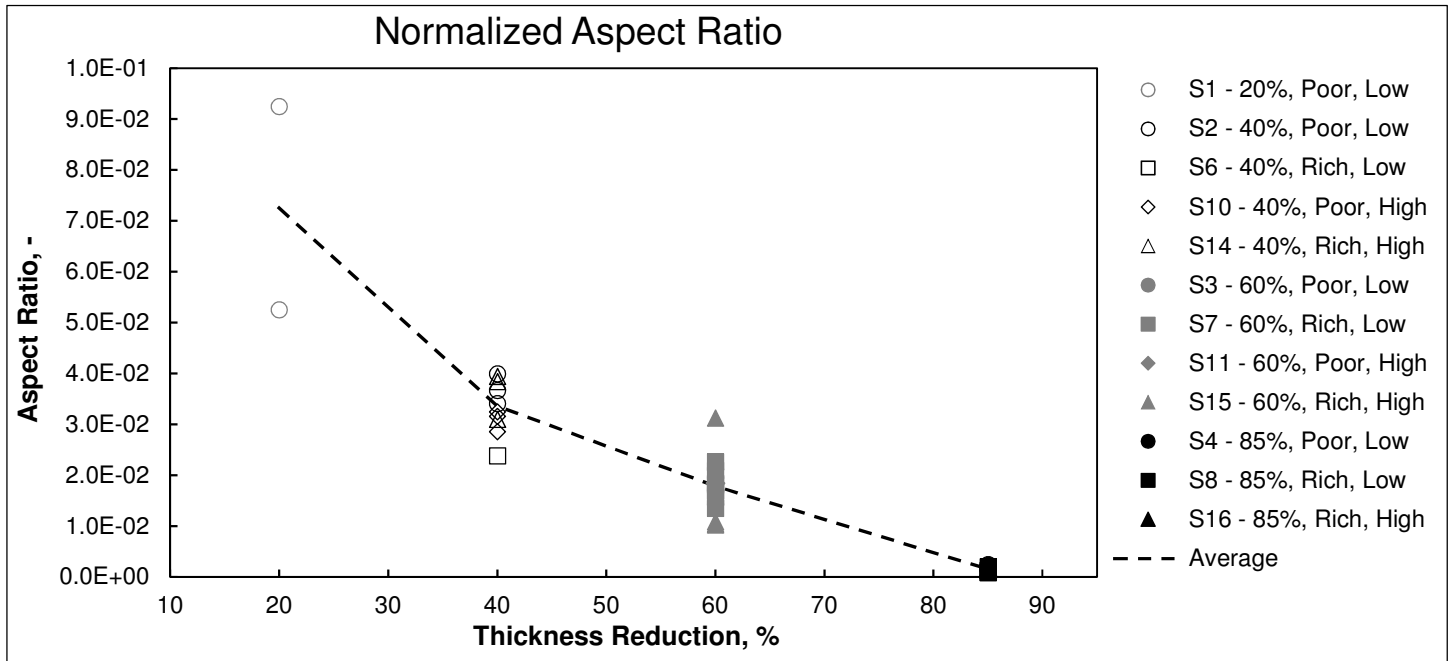


Figure 62 – Influence of thickness reduction on the normalized aspect ratio of the inclusions.

As expected, the increase in thickness reduction results in longer and thinner inclusions, represented by a lower aspect ratio (both maximum and normalized). However, it is also interesting to observe that not only does the aspect ratio reduce with the increase in thickness reduction, but it also stabilizes, as can be observed in Figure 63, where the standard deviation of the normalized aspect ratio is plotted against the thickness reduction.

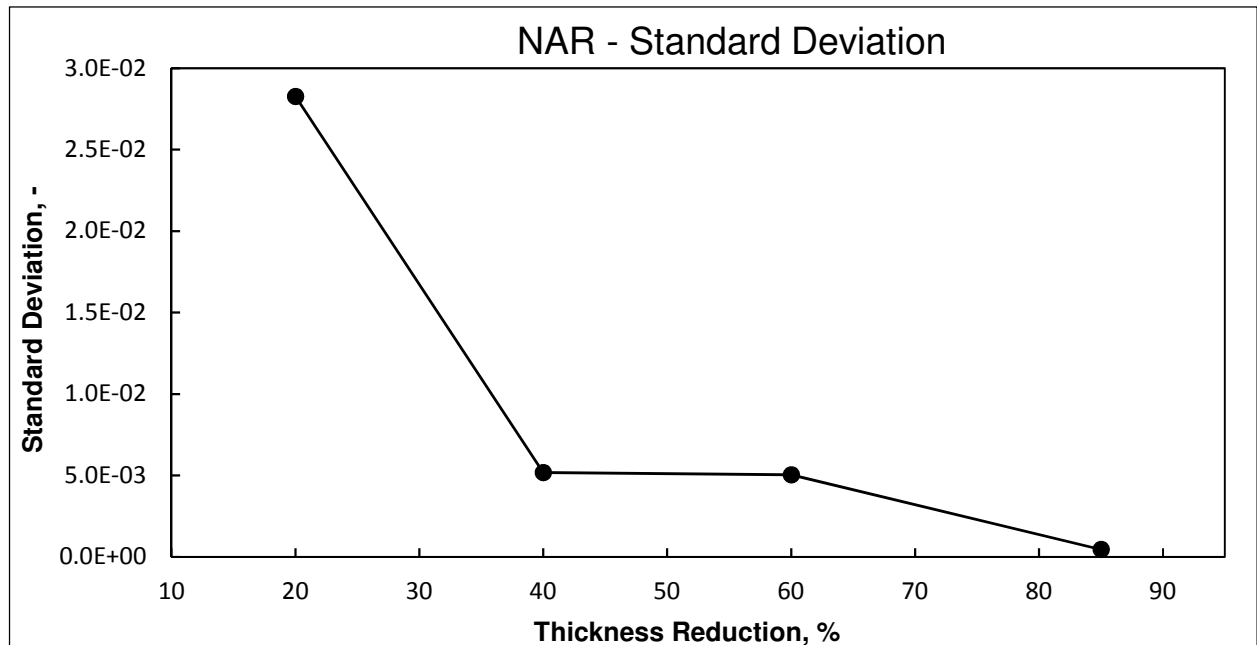


Figure 63 – Evolution of the standard deviation for the normalized aspect ratio measurements with thickness reduction.

Additionally, the influence of the depth on the final aspect ratio of said inclusion was also analysed, as can be observed in Figure 64, where depth is defined the fraction (in percentage) of the final slab thickness at which the inclusion was found.

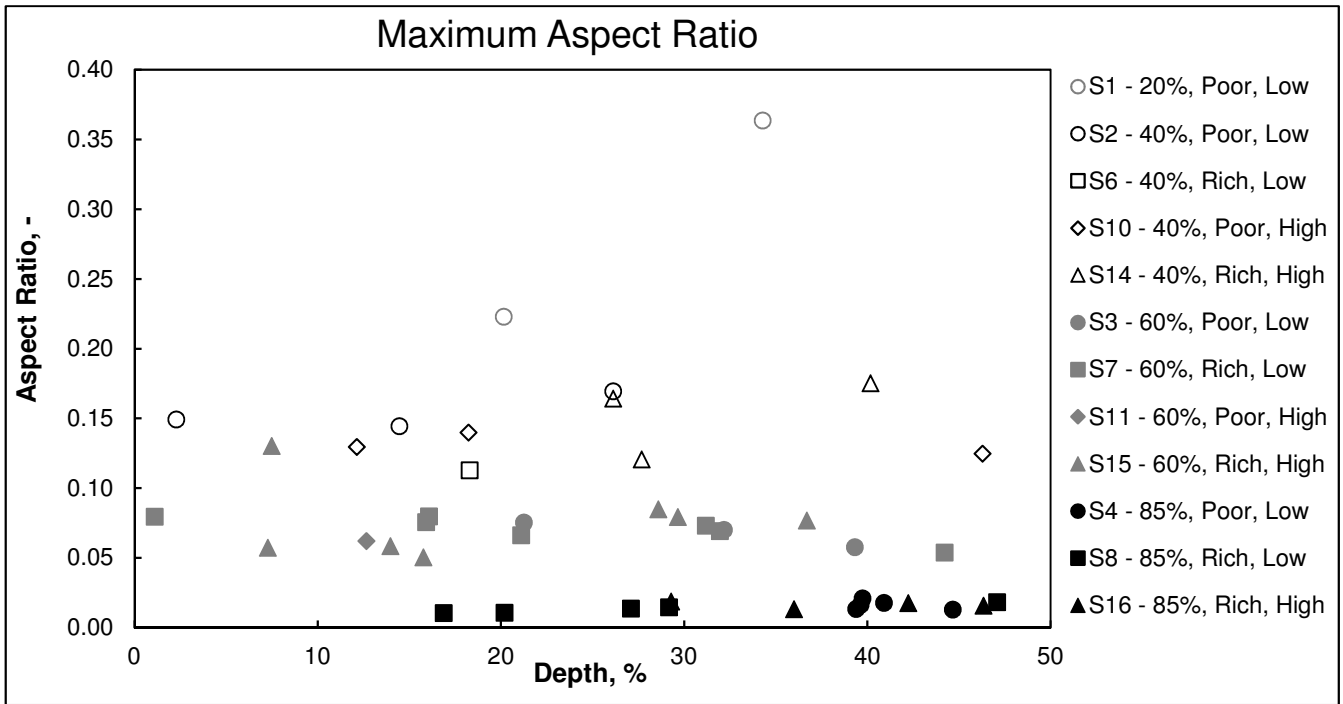


Figure 64 – Influence of depth on the maximum aspect ratio of the inclusions.

Consulting Figure 64, it could initially be determined that no definite influence is observable between depth and aspect ratio. However, although true for the 20% (for which the low number of inclusions does not allow conclusions to be taken), 40% and 60% thickness reductions, this reasoning might not be accurate for the 85% reduction inclusions where, upon closer observation, an increase in aspect ratio seems to be observable with the increase in depth, a behaviour that is present for both aspect ratios evaluated, as can be observed in Figure 65, this time only for the 85% reduction inclusions and for the normalized aspect ratio.

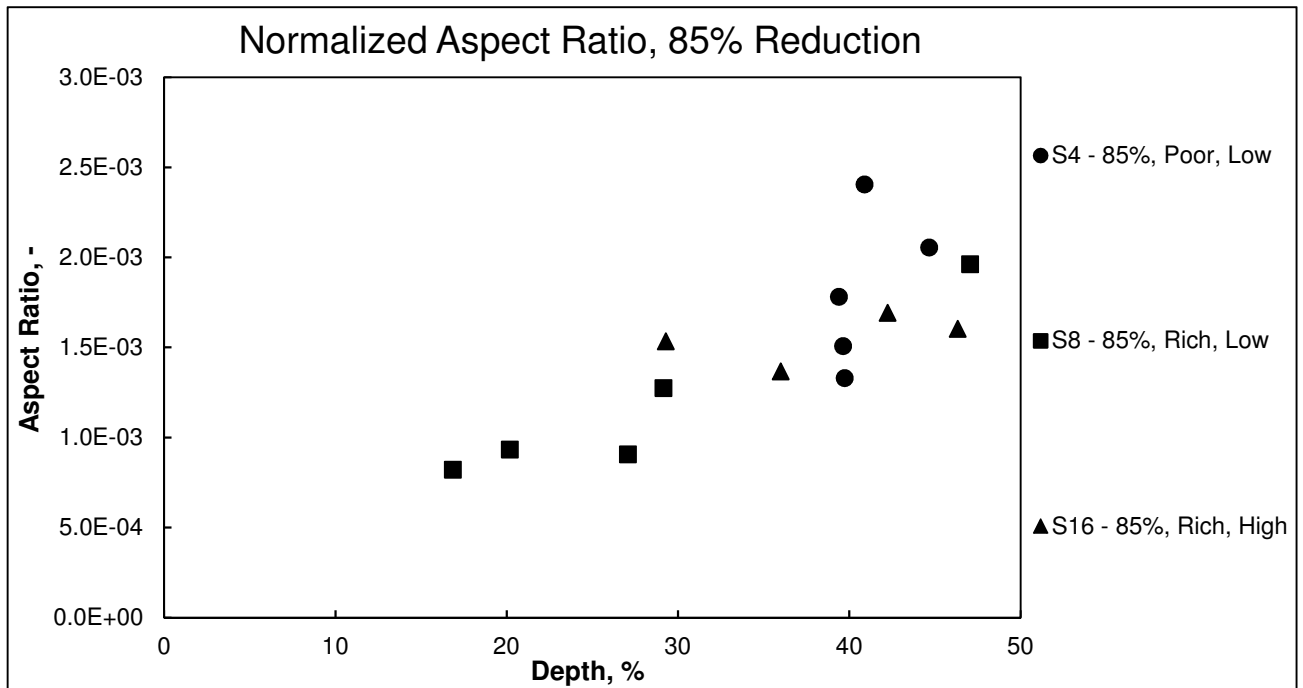


Figure 65 – Influence of depth on the normalized aspect ratio of the 85% reduction inclusions.

Being true for both the normalized aspect ratio as well as for the maximum aspect ratio, the underlying cause for this increase can be identified as the decrease in inclusion length with the increase in depth, as represented in Figure 66.

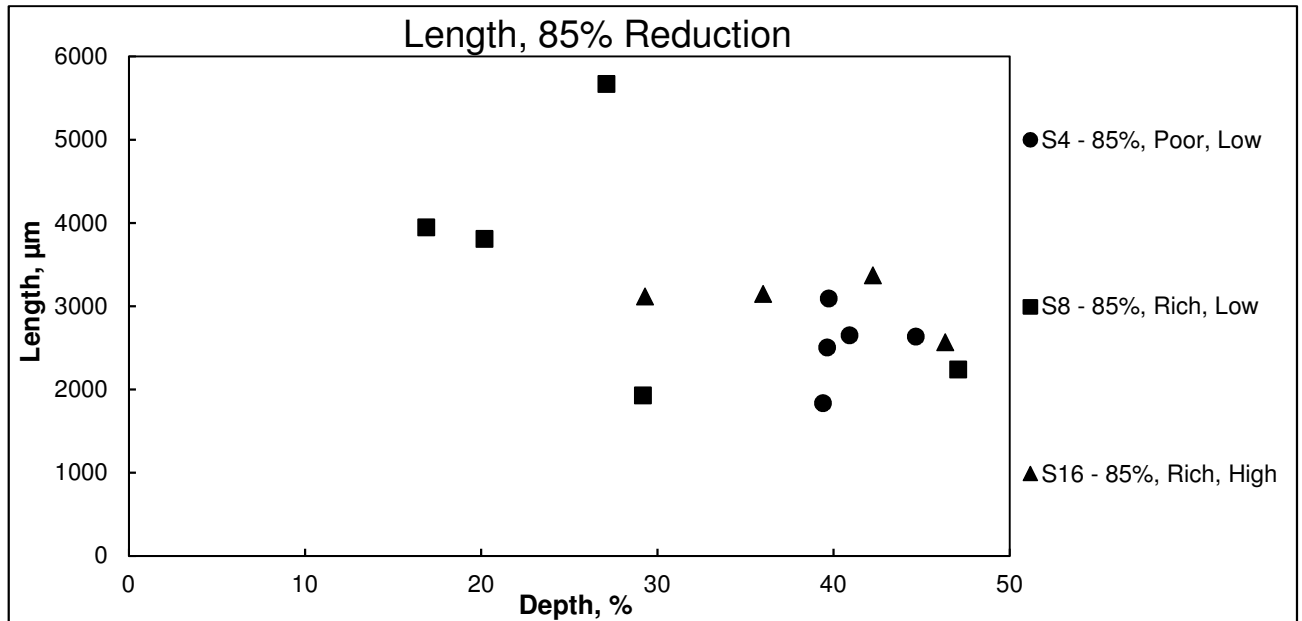


Figure 66 – Influence of depth on the final length of the 85% reduction inclusions.

The reason why this behaviour is found in the 85% reduction inclusions but not for lower thickness reductions might be attributed to the higher strain gradients after rolling between the surface and the centre of the slab where the inclusions are located, as represented in Figure 67 for the 40% and 85% reduction hot rolling simulations, along with respective the rolled profiles.

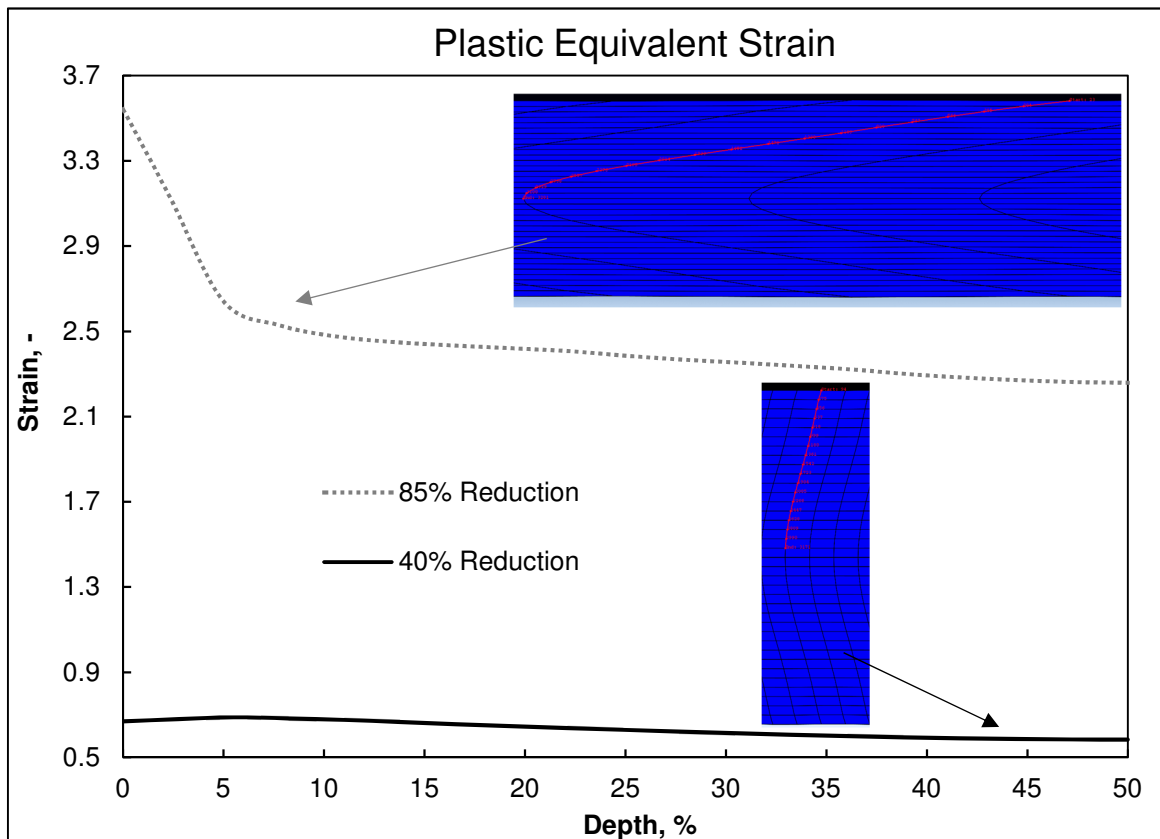


Figure 67 – Plastic equivalent strain after rolling for the 40% (left) and 85% (right) hot rolling simulations. Deformed slab profiles for each situation presented above each curve.

Despite these clear differences, one would expect at least a slight influence of the strain gradient in the through-thickness direction on the final length of the inclusion for the lower deformation slabs. The fact that this is not found points towards a considerable change in behaviour between the 60% and the 85% reduction slabs.

This could already be verified visually in Figure 37 and Figure 38 by the change from the quasi-oval shape found for the 20%, 40% and 60% thickness reductions to the elongated drop-like shape of the 85% reduction inclusions. This fact warrants a way of evaluating the changes between shape types.

To do so, a shape index was defined as the ratio between the area of a given inclusion and the area of a reference shape, which was chosen to be a perfect ellipse with the maximum thickness and length of said inclusion, as represented in Eq.(6.4):

$$SI = \frac{A}{\pi \cdot l_f \cdot t_f^{max}} \cdot 100 \quad (6.4)$$

where:

SI, is the shape index of the inclusion [%].

This index indicates how close the shape of the inclusions is to that of a perfect ellipse. However, it should be noted that since no inclusion is close to be a perfect ellipse, the index should be interpreted purely as a comparative measurement in between inclusions. The criterion for the choice of the reference shape was that it was simple, somewhat similar to the inclusion's shape and with geometry measurements easy to define.

The evolution of the inclusions' shape index with the thickness reduction can be observed in Figure 68.

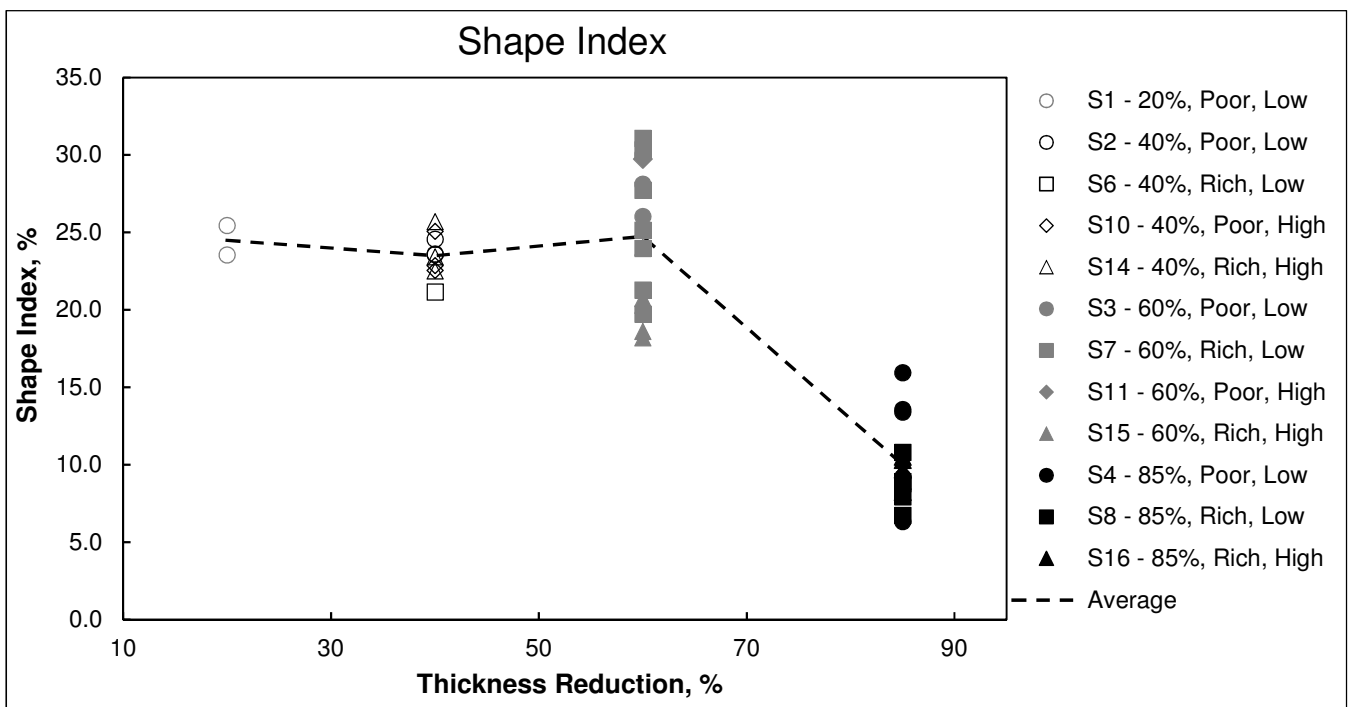


Figure 68 – Influence of thickness reduction on the shape index of the inclusions.

As can be observed, the shape index remains relatively constant for the three lower thickness reductions, indicating that while the shape of the inclusions might change (decrease in aspect ratio), its shape type remains the same, although with a considerable variance for the 60% reduction inclusions. Between the 60% and the 85% reductions, however, it can be observed that not only did the aspect ratio decrease, but the shape index also decreased significantly, representing the change from the oval shape to the drop-like shape. Therefore, it is possible to identify visually a threshold in inclusion behaviour between the 60% reduction and the 85% reduction slabs, as well as it is possible to quantify this change in order to validate the visual analysis.

The development of a FE micro-model or a FE meso-model could lead to understand the causes for these two different shapes observed. However, since the modelling conducted in the present work did not reach the meso- or micro-scale, an analysis of the literature is required.

Luo and Ståhlberg (2001) studied the inclusion behaviour in hot rolling using a developed rigid-viscoplastic FE code, based on a mesomechanical approach. In this study, the modelled inclusion flow stress was expressed as a linear viscous relation with the applied strain rate, and therefore produced results closer to the soft inclusion behaviour presented in Table 3 (e) and Figure 14 (e) where the inclusion deforms uniformly into a quasi-oval shape as can be observed in Figure 69 [53].

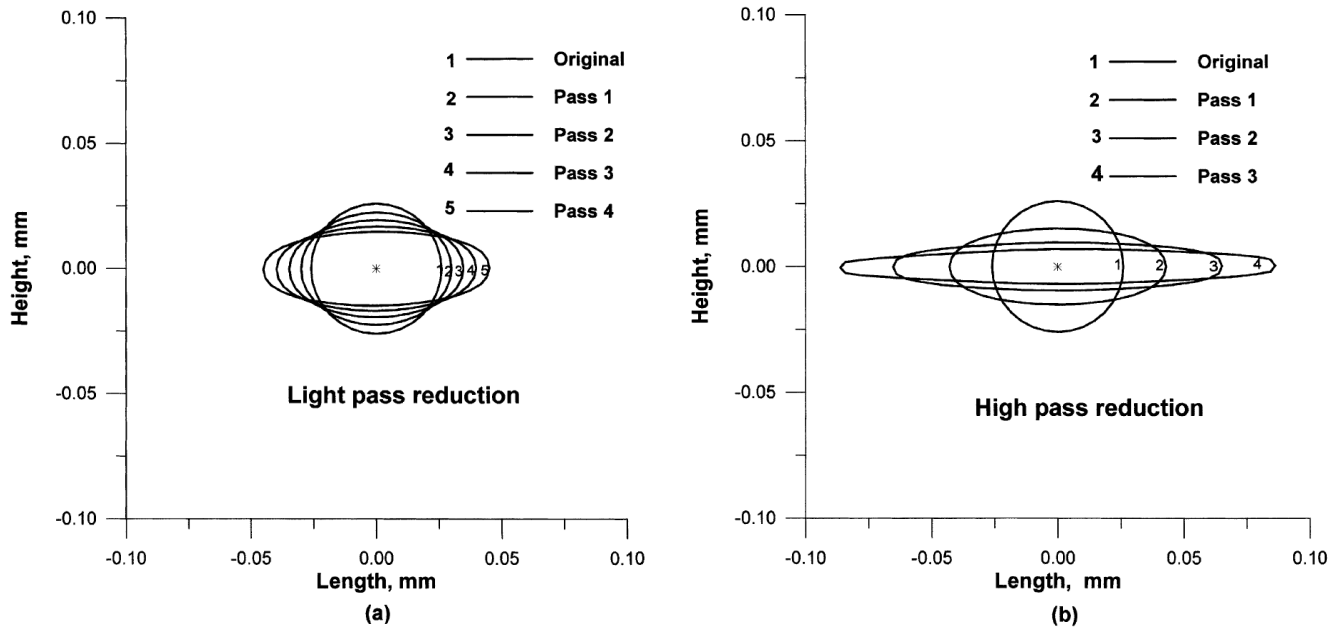


Figure 69 – Deformation of inclusions located in the centre of the modelled slab for a low reduction (light) multi-pass rolling scheme up to 20% thickness reduction (a) and for a higher reduction (high) multi-pass rolling scheme up to 42% thickness reduction (b) [53].

As can be observed, despite the significantly different initial inclusion size not allowing a direct comparison with the experimental results of the present work, the shape changing behaviour observed is relatively close to the one observed for the inclusions found in the 20% and 40% thickness reduction slabs, where a uniform, quasi-symmetrical shape is obtained. However, it can also be observed that the model did not reproduce the asymmetrical drop-like shape behaviour found for the 85% reduction slabs.

On the other hand, Yu *et al.* (2008) studied the deformation of hard Al_2O_3 inclusions during cold rolling using a mesoscale FE and updating geometric method on the platform of LS-DYNA [54]. While seemingly irrelevant for the present work, where the process at hand is hot rolling and the inclusions are silicates, the results produced by this method did in fact predict the asymmetrical drop-like shape found in the experimental stages of the present work, as can be observed in Figure 70.

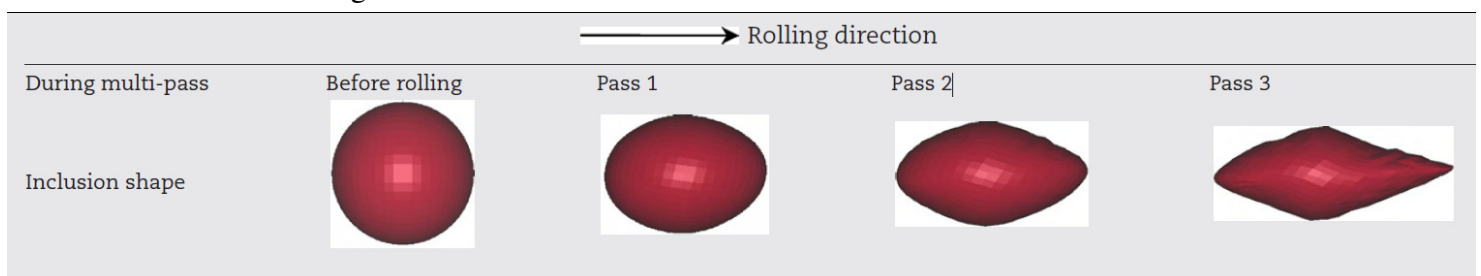


Figure 70 – Hard Al_2O_3 inclusion behaviour during multi-pass cold rolling operations. Initial inclusion diameter of 20 μm . Adapted from [54].

As can be observed, for multi-pass operations, the model predicts an increasingly asymmetrical deformation in the front and rear of the inclusion, a behaviour that is also found in multi-pass hot-rolled silicate inclusions studied.

In order to interpret these differences, one needs to take into account that the hot-rolling mesoscale model does not study the effects of thickness reductions higher than 42% and does so with small thickness reduction steps (4 steps to achieve 42% thickness reduction) when compared with the work at hand (40% thickness reduction achieved in a single step), not allowing direct comparisons to be made.

Moreover, the inclusion size in both models is significantly inferior to the one used in the experimental stage of the present work. However, one can compare the main adimensional index studied by Luo and Ståhlberg (2001) in order to contextualize the results observed. For that, the relative plasticity index between the inclusions and the steel, defining the ratio between the inclusion deformation and the steel deformation, was calculated for all of the studied inclusions as presented in Eq.(6.5) [53]:

$$RPI = \frac{\bar{\varepsilon}_i}{\bar{\varepsilon}_m} \quad (6.5)$$

where:

- RPI, is the relative plasticity index (usually presented with the nomenclature ν , which was dropped in the present thesis to avoid confusion with different parameters)
- $\bar{\varepsilon}_i$, is the average inclusion strain;
- $\bar{\varepsilon}_m$, is the average steel strain.

It should be noted that, when defined according to Malkiewicz and Rudnik (1963), the relative plasticity index used the average effective strains of the inclusion and steel, whereas in the study conducted Luo and Ståhlberg (2001) a local deformation index using the average strain was used instead. For the experimental data available the overall strain was used, since, not resulting from FE simulations, local values were not available [53, 55]. The calculation of the overall strain for the steel matrix took into account a normalized final length for the slabs, whose calculation is presented in Appendix A.

The influence of the number of rolling steps in the relative plasticity index according to Luo and Ståhlberg (2001) for “high” reduction steps (closer to the ones used in the experimental stage) can be observed in Figure 71 [53].

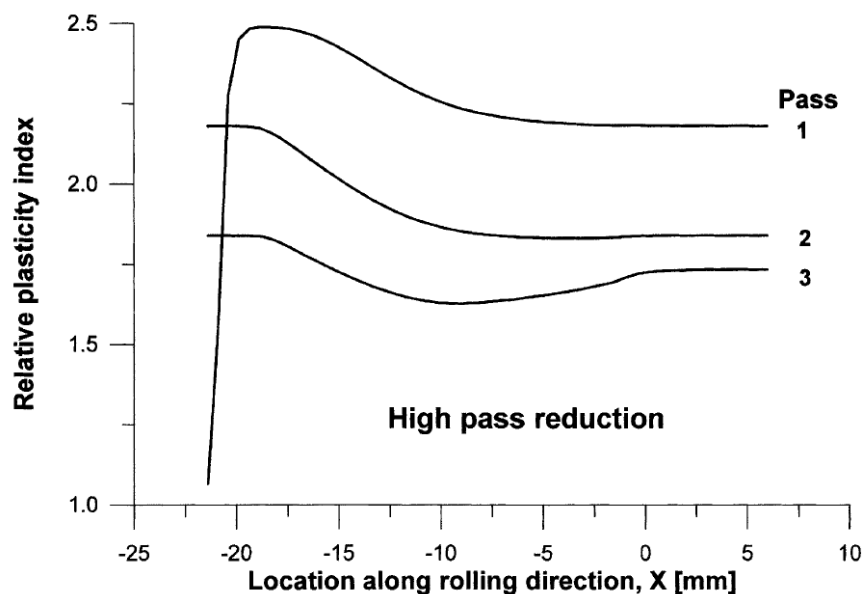


Figure 71 – Evolution of the relative plasticity index for inclusions located in the centre of the slab during the hot rolling process for the high reduction pass FE simulations conducted by Luo and Ståhlberg (2001) [53].

As can be observed, a decrease in the final relative plasticity index is expected with the increase in the number of rolling steps. For the experimental data, the relative plasticity index evolution with the increase in thickness reduction (which should present an evolution similar to the increase in rolling steps) is displayed in Figure 72.

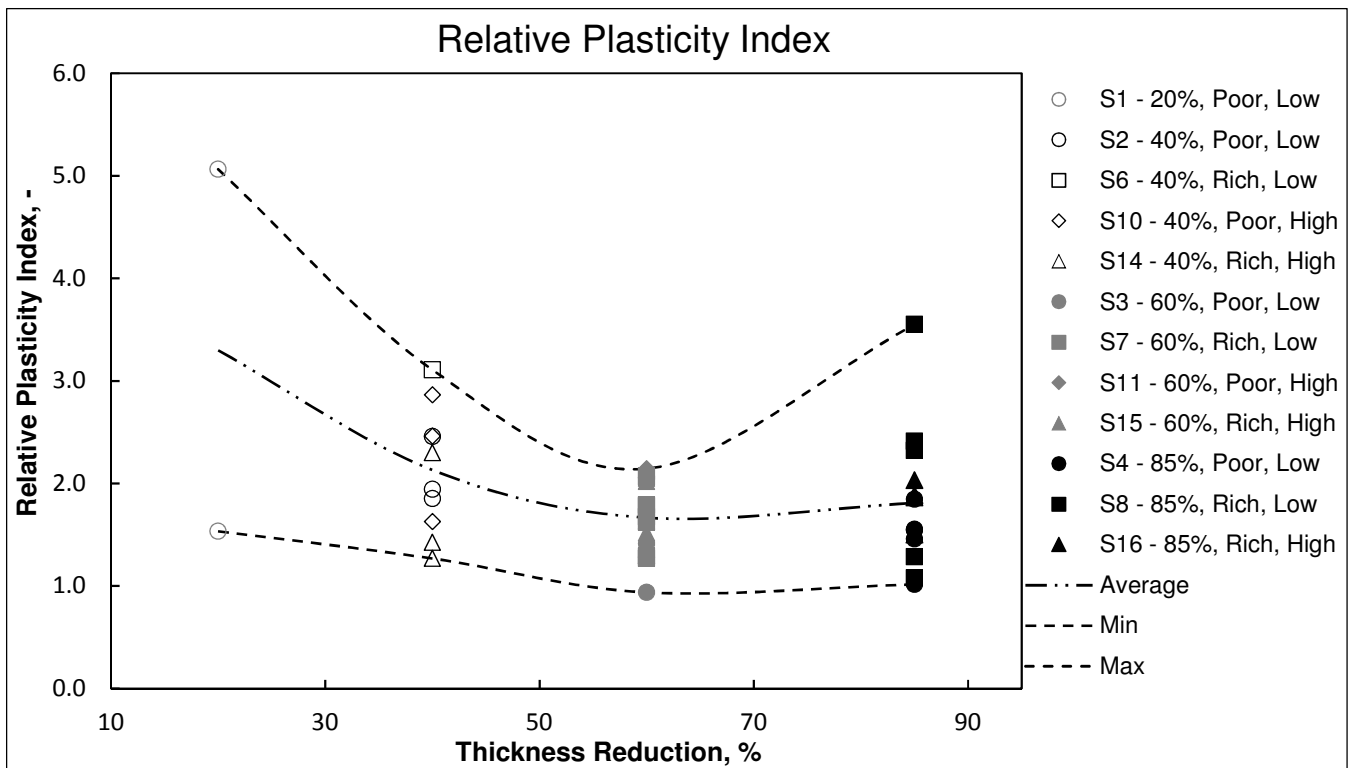


Figure 72 – Evolution of the relative plasticity index with thickness reduction for the experimental data.

As can be observed, the behaviour reported by Luo and Ståhlberg (2001) for reductions up to 42% is also found in the experimental data up to 60% thickness reduction [53]. However, for the 85% reduction, a stabilization of this index is found, with an increase in the maximum value (which, being the result of a single inclusion, should not be considered as a definite behaviour without further verification).

This change in trend from the 60% reduction inclusions to the 85% reduction inclusions further establishes that a threshold for the inclusion deformation behaviour exists between these two reductions. The low number of inclusions for the 20% reduction slabs should be also considered when drawing conclusions from the results, indicating that further testing to validate the analysis is necessary.

On the other hand, Luo and Ståhlberg (2001) predict that, with the increase in the number of rolling steps (and therefore of thickness reduction), the evolution of the relative plasticity index with depth changes from somewhat constant to displaying a decrease with the increase in depth.

This behaviour can be observed in Figure 73, where the layer number evolves with the decrease in depth (layer 1 is located in the centre, layer 6 is located on the surface) [53].

For the experimental results, the relative plasticity index evolution with depth can be observed for the 60% (2 rolling steps) reduction inclusions and for the 85% (3 rolling steps) reduction inclusions in Figure 74 and Figure 75.

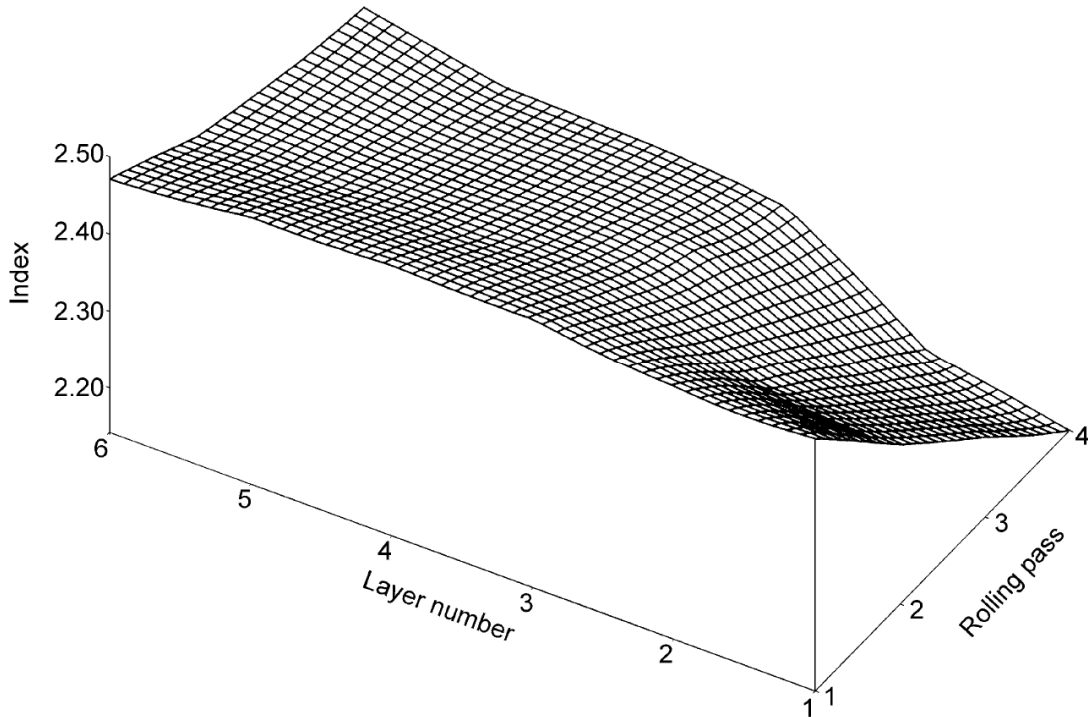


Figure 73 – Relative plasticity index (indicated as “index”) evolution with the depth of the layer at which the inclusion is located (depth decreases for higher numbers) and the number of rolling passes [53].

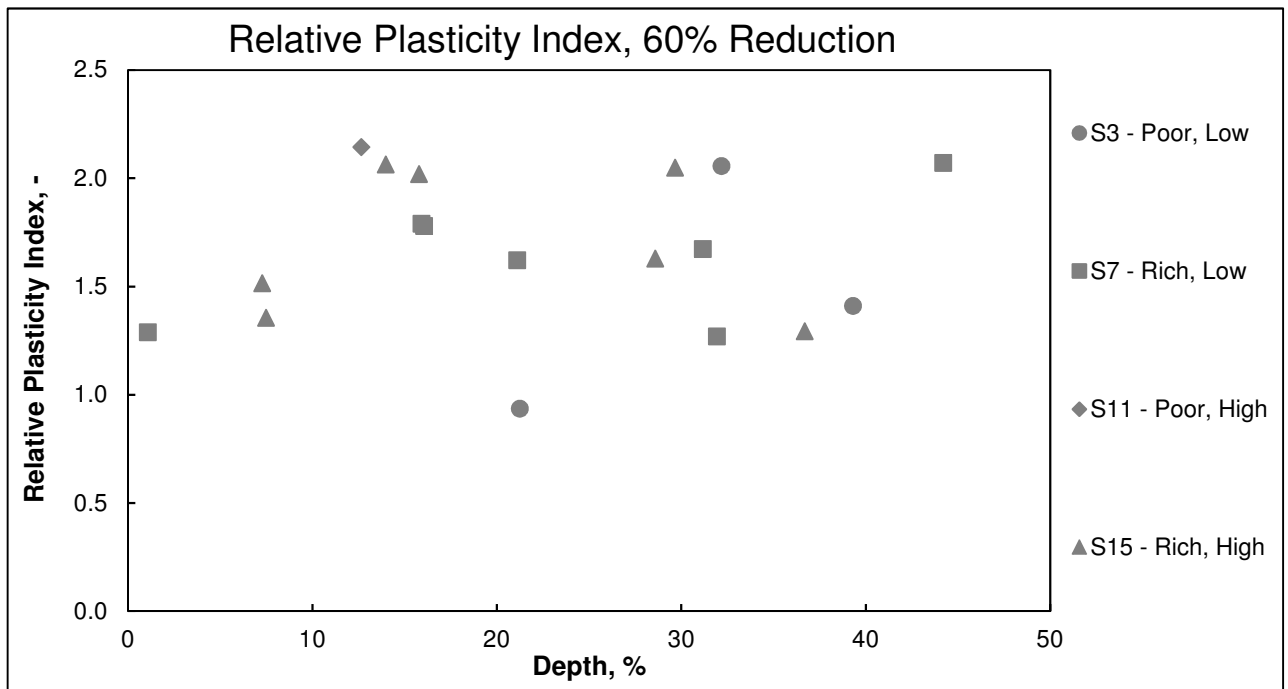


Figure 74 – Relative plasticity index evolution with the depth of the inclusion for the 60% thickness reduction inclusions.

As can be observed, although difficult to attribute a definite evolution due to the high variance in the results, there seems to be possible to identify a decrease in the relative plasticity index for the 85% reduction inclusions (Figure 75) which was not present in the 60% reduction inclusions (Figure 74). If confirmed, this behaviour is not only in accordance to the FE results expected by Luo and Ståhlberg (2001) but also strengthens the hypothesis that a threshold is to be found between these two thickness reductions.

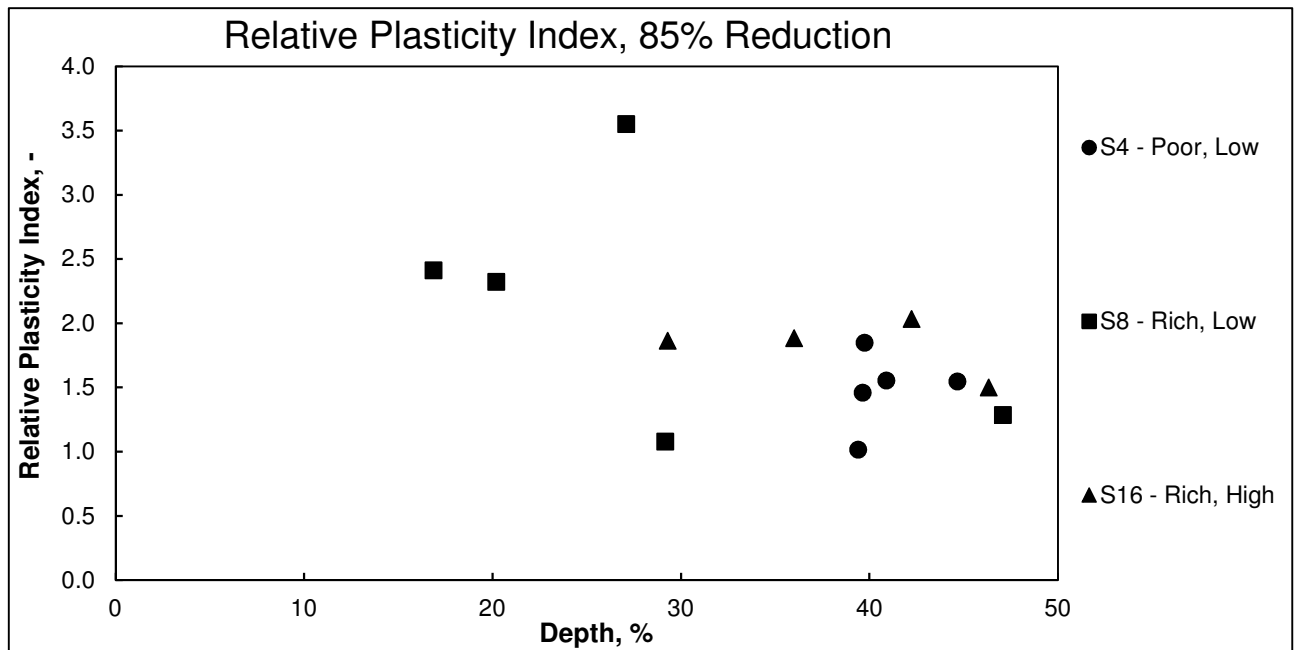


Figure 75 – Relative plasticity index evolution with the depth of the inclusion for the 85% thickness reduction inclusions.

Additionally, for the cold rolling FE model, despite not defining an adimensional measurement, Yu *et al.* (2008) do establish a relation between the deformation difference from the rear to the front of the inclusion and the size of the inclusion, where the asymmetrical behaviour is expected to increase with the increase in initial inclusion diameter (Figure 76) [54].

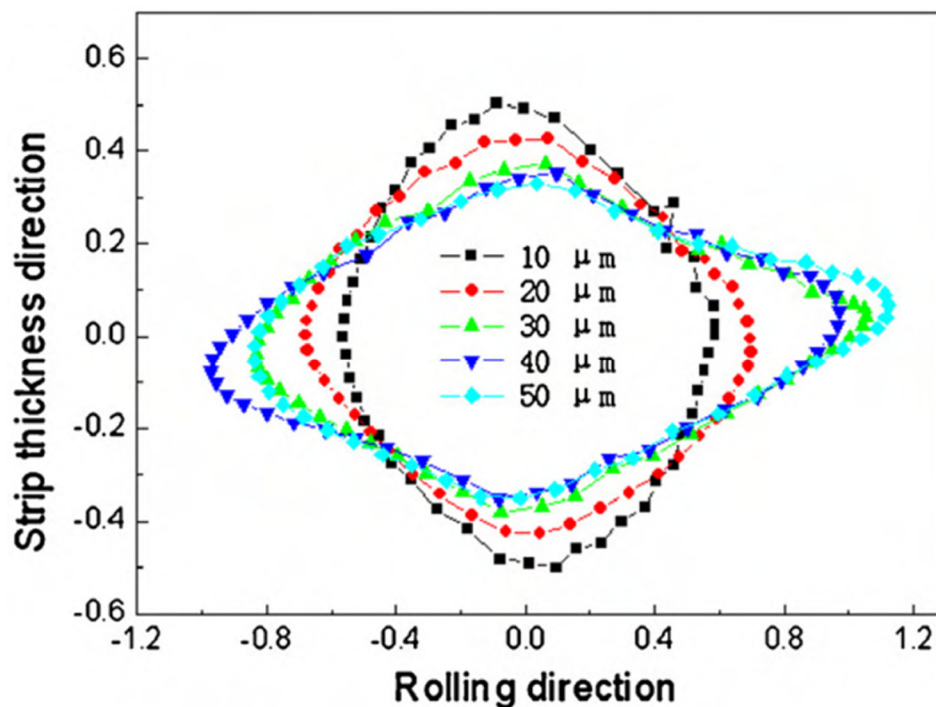


Figure 76 - Inclusion profile evolution for the last step of a 3-pass rolling schedule with the initial inclusion diameter [54].

This evolution can be one of the aspects used to explain the significantly more asymmetrical behaviour found in the 85% reduction inclusions studied in the present work, which were produced with an initial diameter 6x higher than the maximum one studied by Yu *et al.* (2008), and therefore display a significantly higher deformation difference from the front to the rear [54].

The joint analysis of the inclusion shape behaviour for the experimental results seems to indicate that the inclusion follows a behaviour similar to the one characterized by Luo and Ståhlberg (2001) (for soft inclusions during hot rolling), but changes to a behaviour closer to the one characterized by Yu *et al.* (2008) (for hard inclusions during cold rolling) in the inclusions subjected to the 3-step, 85% thickness reduction schedule.

One possible justification for this change in behaviour lies in the fact that the temperature difference in the 3rd rolling step is significantly lower than the one in the 2nd rolling step, and that the inclusion solidifies to a substantially higher degree for this last step, becoming hard enough to change its behaviour.

To illustrate this difference, the temperature profile in the middle of the slab at the end of the 1st rolling step (last stage of the 40% reduction rolling experiments), 2nd rolling step (last stage of the 60% reduction rolling experiments) and at the end of the 3rd rolling step (last stage of the 85% reduction rolling experiments) is displayed in Figure 77.

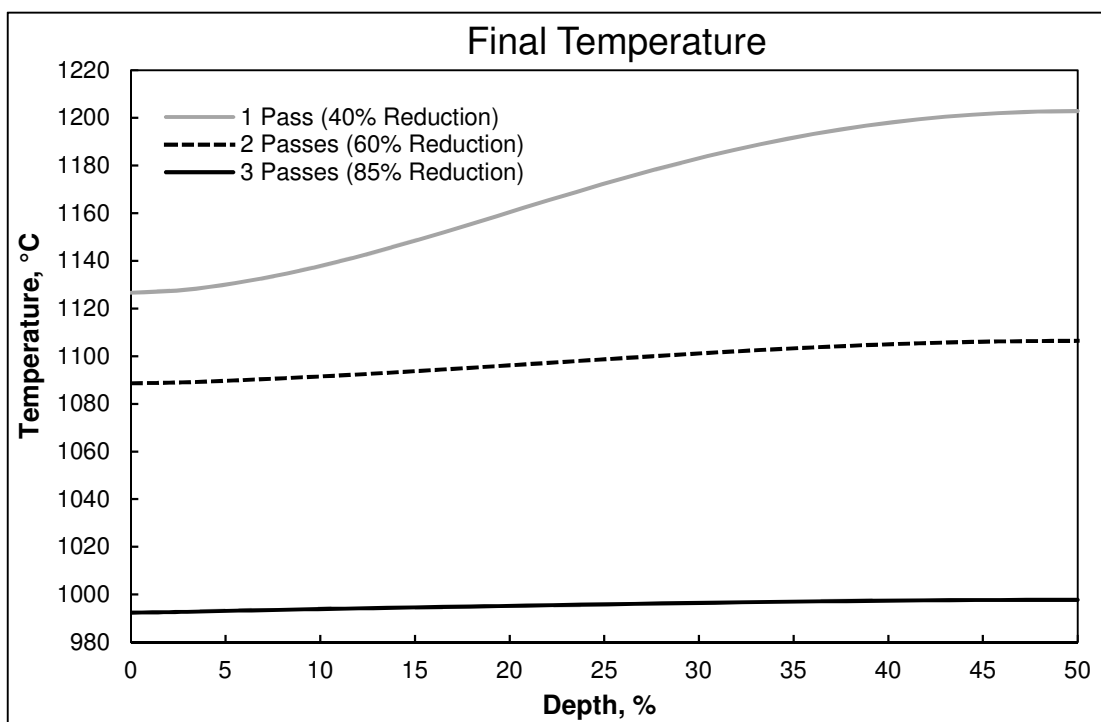


Figure 77 - Temperature profile in the middle of the slab at the end of the 1st rolling step (last stage of the 40% reduction rolling experiments) 2nd rolling step (last stage of the 60% reduction rolling experiments) and at the end of the 3rd rolling step (last stage of the 85% reduction rolling experiments).

Finally, it should also be noted that no discernible evolutions for the relative plasticity index or for the aspect ratios were determined with the Na/F content or the soaking time difference (Figure 78 and Figure 79 respectively). This conclusion, on the one hand, might derive from the fact that only two levels were studied for these parameters (poor/rich Na and F content; low/high soaking time) but that, on the other hand, could indicate that no major influence exists in the deformation behaviour of the inclusions with the variation of these processes. The fact that, as will be explained in the following section, the difference in F between the two desired levels is lower than what was desired, along with the fact that a lower number of high soaking time inclusions was studied might also have been influencing the results.

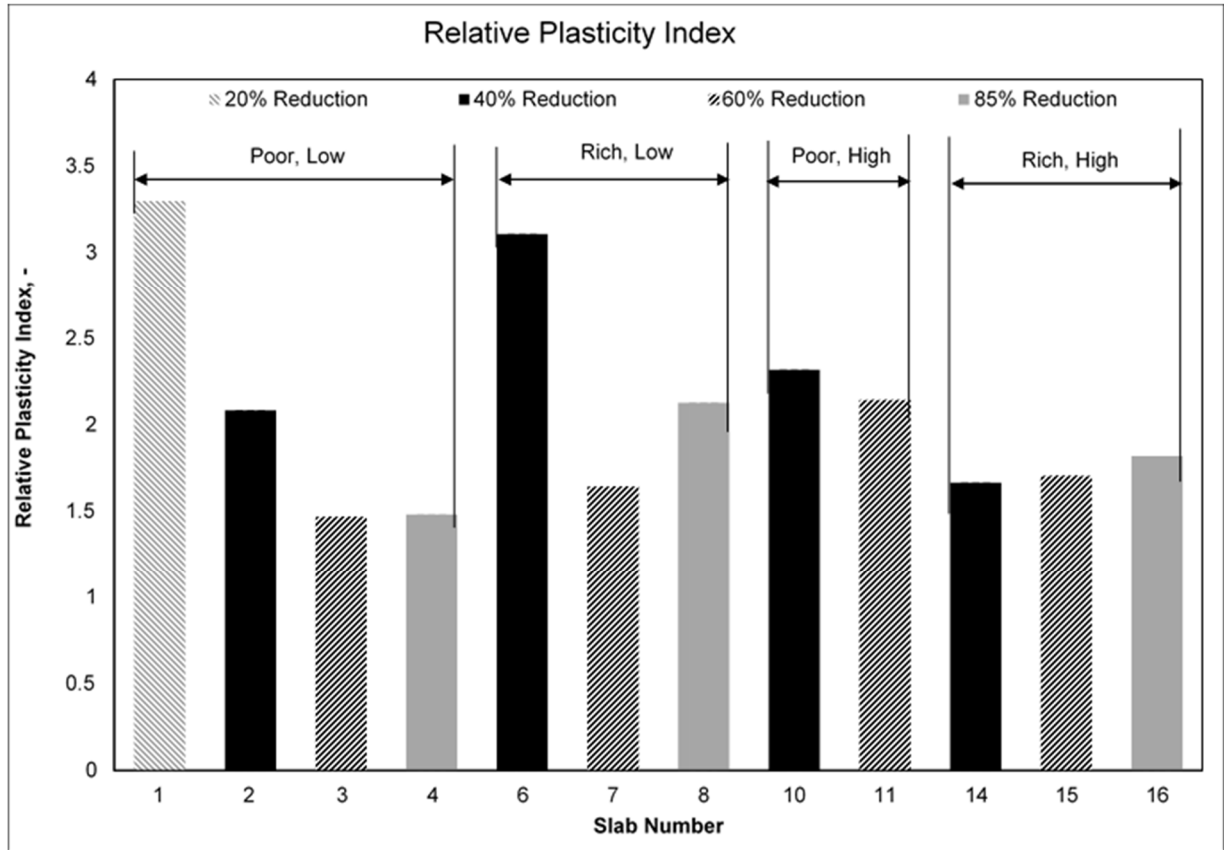


Figure 78 – Average Relative Plasticity Index for the inclusions found in each slab. Slabs grouped by F and Na content (poor/rich) and soaking time (low/high).

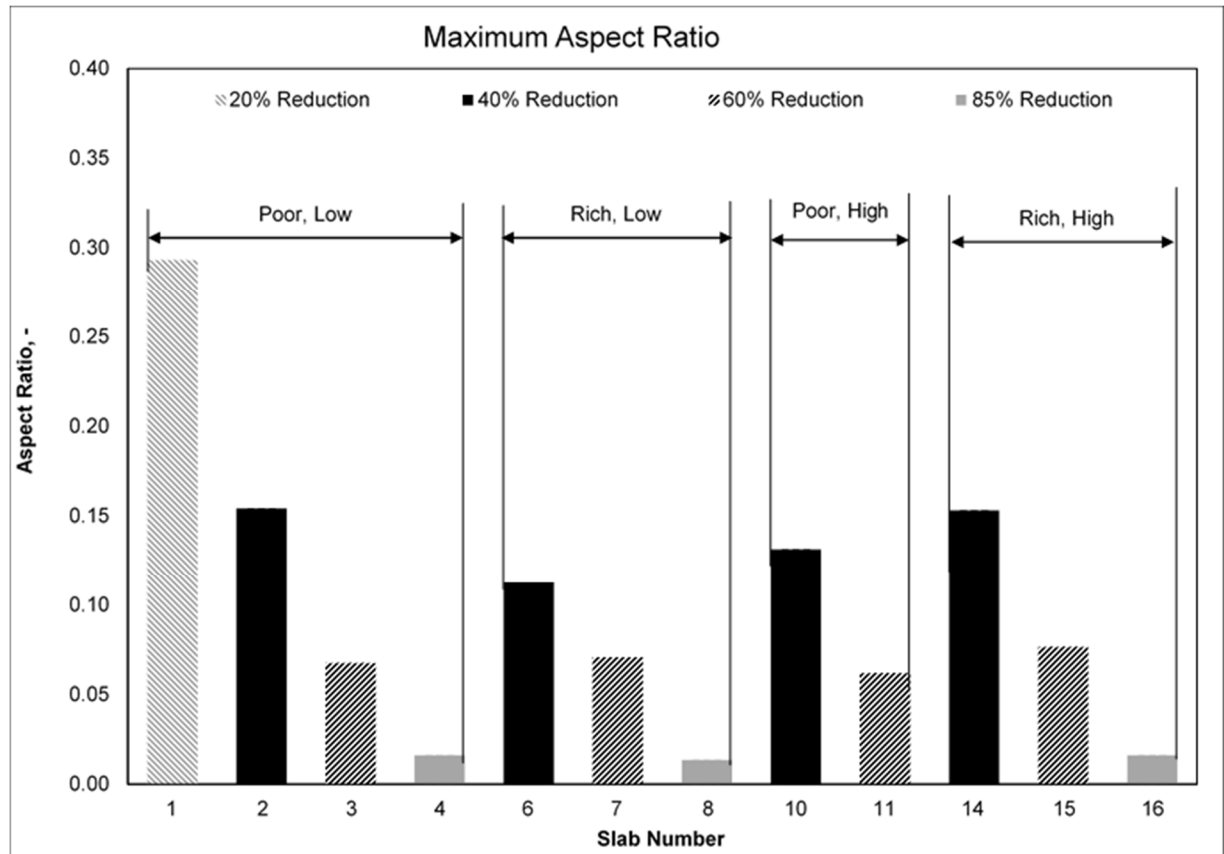


Figure 79 – Average Maximum Aspect Ratio for the inclusions found in each slab. Slabs grouped by F and Na content (poor/rich) and soaking time (low/high).

6.2 Inclusion Composition and Phases

As could be observed in Table 5, firstly, the crystalline phases observed are in accordance with the results of the analysis conducted by Uittenbroek (2019), with cuspidine and wollastonite being the main distinguishable phases present in the examined samples [9].

Regarding the sodium and fluorine content of the artificial inclusions, it can firstly be observed that while the two processing routes chosen to achieve the poor and rich inclusions did indeed produce low Na inclusions and high Na inclusions, it did not influence significantly the fluorine content in the 40% reduction inclusions (as can be observed by comparing both samples' fluorine content in the glassy phase). The reason for this phenomenon could not be identified in the present thesis, but intermediate chemical composition measurements in between each experimental procedure step could allow the cause to be identified in future works.

On the other hand, it can be observed by analysing the overview of the crystalline phases that the Na and F contents did indeed play a major role in the microstructure of the final inclusions. The inclusions with a low Na and F content revealed a tendency to include wollastonite in the final composition, a behaviour that might be justified by the lack of fluorine to form the alternative cuspidine, leading to the crystallization of CaSiO_3 , composed by elements which were predominant in the mould slag composition. In the Na and F rich inclusions, however, the F content was apparently high enough for cuspidine ($\text{Ca}_4\text{Si}_2\text{F}_2\text{O}_7$) to be formed as the main crystalline phase throughout the inclusions.

Fluorine and Sodium Poor Samples

Firstly, it should be noted that the results observed in the sample taken from sample 4 are in accordance to those found for the similar 85% reduction samples studied by Uittenbroek (2019). Furthermore, the results from the sample taken from slab 3 (60% thickness reduction and equal remaining conditions) by Uittenbroek (2019) can be compared with those found in the presented samples, as can be consulted in Table 14 [9].

Table 14 – Average composition [at%] resulting from the EDS SEM measurements conducted by Uittenbroek (2019) of the inclusions present in slab 3, with 60% reduction and low soaking time [9].

	<i>Average Composition [at%] – Slab 3 (60% Reduction)</i>									
	O	Ca	Si	F	Na	Al	Mg	K	Fe	Other
Cuspidine	46.23	24.98	13.60	14.10	0.22	0.16	0.15	0.00	0.49	<0.07
Glass	52.75	11.62	12.57	6.30	3.09	7.71	0.67	0.04	5.11	<0.14
Wollastonite	59.74	17.85	19.23	0.01	0.55	0.98	0.46	0.00	1.10	<0.08

As can be observed, the individual phase compositions resemble those found in this work's studied samples, while the glass composition resembles that of the inclusions in slab 2, which is especially noticeable in the unexplained high aluminium content. Moreover, it can also be observed a more elevated iron content in the measurements, a factor that can be caused by the selection of measurement points close to the inclusion's interface with the steel, something that is considerably easy to happen, especially at lower magnifications such as the one used by Uittenbroek (2019) corresponding to 700x to 1000x instead of the 4000x used in the present work. Moreover, Uittenbroek (2019) conducted a vastly inferior number of measurements, a factor that, given the human factor that plays a role in the measurement point selection process, will influence the statistical results of the measurements [9]. Additionally, the undesired high fluorine content is also present in the supposedly low F inclusions, showing an even more pronounced behaviour than what was found for the inclusions in slab 2, with 40% reduction.

Furthermore, as can be observed, despite an overview of the phases showing that wollastonite is to be found in the Na and F poor samples, in fact this phase was not found in the slabs for all

of the thickness reductions. In slab 2, submitted to a 40% thickness reduction and a low soaking time, there was no wollastonite found in a crystalline form (for any of the inclusions studied), but instead cuspidine accompanied by glassy phases. These glassy phases presented several compositions, some of which were considerably close to the wollastonite stoichiometric composition but presented an amorphous structure and a relatively high compositional variation from point to point. While this is most likely an effect of the undesired higher F content in the inclusions, it also points to the necessity of studying the spread of the data for the conducted measurements, something that is presented in the form of the standard deviations of the measurements, without oxygen (which is calculated) in Table 15, Table 16 and Table 17.

Table 15 – Standard deviation of the results from the EDS SEM measurements of the composition of the inclusions present in slab 1, with 20% reduction and low soaking time.

	<i>Standard Deviation - Slab 1 (20% reduction)</i>								
	Ca	Si	F	Na	Al	Mg	K	Fe	Other
Cuspidine	2.22	1.57	1.59	0.44	0.84	0.29	0.01	0.65	<0.06
Glass	5.72	1.85	2.75	0.62	2.16	0.55	0.06	1.67	<0.46
Wollastonite	2.48	1.15	0.18	0.58	1.19	0.38	0.02	1.08	<0.13

Table 16 – Standard deviation of the results from the EDS SEM measurements of the composition of the inclusions present in slab 2, with 40% reduction and low soaking time.

	<i>Standard Deviation - Slab 2 (40% reduction)</i>								
	Ca	Si	F	Na	Al	Mg	K	Fe	Other
Cuspidine	3.84	1.95	3.91	0.89	2.95	0.30	0.03	1.10	<0.06
Glass	4.96	4.45	3.01	1.60	4.98	0.68	0.13	1.80	<0.09

Table 17 – Standard deviation of the results from the EDS SEM measurements of the composition of the inclusions present in slab 4, with 85% reduction and low soaking time.

	<i>Standard Deviation - Slab 4 (85% reduction)</i>								
	Ca	Si	F	Na	Al	Mg	K	Fe	Other
Cuspidine	2.42	2.54	2.96	0.84	1.16	0.36	0.05	1.66	<0.05
Glass	3.40	3.11	3.27	2.03	2.30	1.11	0.09	3.32	<0.08
Wollastonite	5.14	4.19	1.80	2.09	2.57	0.84	0.05	2.63	<0.06

As can be observed, it is no surprise that, among the phase measurements, the glass standard deviation presents some of the higher values, a fact that can be explained by the different phases that are indistinguishable within the glassy component of the inclusions.

Furthermore, there is a higher value and variance in the glassy phases' Fe content in the 85% reduction inclusions when compared to the lower reduction ones. This might be explained by the fact that the thinner shape displayed in these inclusions leads to a higher number of measurements close to the interface with the steel, affecting the measurement results.

Fluorine and Sodium Rich Samples

The composition results taken from the F/Na rich samples firstly confirm that the processing route used to obtain fluorine and sodium levels closer to the original mould powder (in order to more accurately represent the real mould slag inclusions) was relatively successful, resulting in inclusions with cuspidine as the only crystallized phase, as well as glassy phases with a significantly higher Na content. The varying fluorine contents in the glassy phase might reflect the degree of cuspidine crystallization between the two thickness reductions, which might also be a result of the low number of inclusions studied for the 40% reduction slab (only one

inclusion was found) leading to erroneous conclusions based on an exceptional case. Further testing on samples from slab 6 would be required in order to validate this behaviour as a definite evolution between the two rolling schemes.

As conducted for the F/Na poor samples, the standard deviation of the composition measurements conducted for the F and Na rich, low soaking time inclusions can be observed in Table 18 and Table 19.

Table 18 – Standard deviation of the results from the EDS SEM measurements of the composition of the inclusions present in slab 6, with 40% reduction and low soaking time.

	<i>Standard Deviation - Slab 6 (40% reduction)</i>								
	Ca	Si	F	Na	Al	Mg	K	Fe	Other
Cuspidine	1.77	1.08	1.71	1.07	0.51	0.10	0.04	0.82	<0.08
Glass	9.20	5.67	5.51	3.90	1.73	0.83	0.12	4.09	<0.17

Table 19 – Standard deviation of the results from the EDS SEM measurements of the composition of the inclusions present in slab 8, with 85% reduction and low soaking time.

	<i>Standard Deviation - Slab 8 (85% reduction)</i>								
	Ca	Si	F	Na	Al	Mg	K	Fe	Other
Cuspidine	3.10	1.76	1.97	1.94	1.01	0.14	0.06	1.95	<0.05
Glass	7.29	6.80	5.78	3.98	2.15	0.48	0.12	5.51	<0.10

In these samples it is once again clearly visible that the cuspidine measurements present a significantly inferior variation when compared to the glassy phase measurements, possibly indicating that this phase was in a stable, fully crystallized form once the sample cooled.

Finally, it is also important to analyse the considerably high difference in the Fe content observed between the original mould powder composition and the inclusion composition. This difference is possibly justified by an interaction of the inclusions with the surrounding PM cylinder steel (which is almost completely composed of iron) during the processing stages. This could have happened during the powder metallurgy phase (relatively high pressure and temperatures during pressing, sintering and most noticeably during HIP), during the isothermal stage at high temperature, during the rolling itself (high pressures at high temperatures) or as a combination of all possible factors. If, during further research, the influence of the iron content in the inclusion is found to be important for the rolling behaviour, the determination of exactly when, how and why this increase in Fe occurs might become a critical aspect to determine.

6.3 Phase Morphology

An additional attention was given to the phase morphology, in order to analyse its variation in the longitudinal direction, as well as in the through-thickness direction.

Fluorine and Sodium Poor Samples

Starting with the lower reduction slabs, the overall microstructure of a 20% thickness reduction inclusion can be observed in Figure 80, where it can be confirmed that both wollastonite and cuspidine are found as the main crystalline phases.

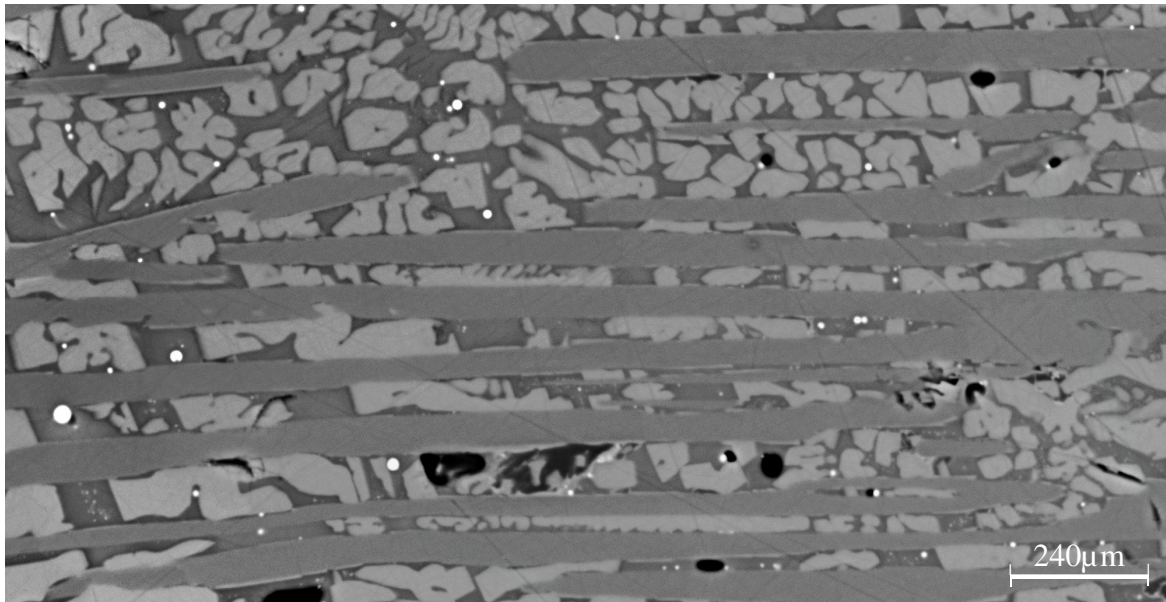


Figure 80 – Section of the stitched BSI images for inclusion A found in the sample prepared from slab 1 at a depth of 3225 μm (20% of the final slab thickness). Rolling direction from left to right.

As can be observed, in the present inclusion wollastonite is mainly found organized in thin blocks oriented in the rolling direction, whereas cuspidine is found in a globular form between the wollastonite blocks, indicating that it was subjected to a cooling rate low enough to grant time for cuspidine to achieve a lower energy state.

This result is in accordance to what was found by Uittenbroek (2019) for different samples taken from the 85% slab with the same processing conditions, indicating that the wollastonite behaviour might not be considerably dependant on the deformation applied to the slab within the range tested [9].

Regarding directional evolutions, no discernible behaviour could be found in the rolling direction, except that wollastonite seems to be concentrated in the centre of the inclusion. Additionally, no distinct behaviour could be observed in the through-thickness direction for the inclusions subjected to this thickness reduction, which, since only two inclusions were studied in SEM, might not indicate a trend. An additional number of inclusions should be explored in further research to fully characterize the existence or non-existence of directional evolutions in this inclusion type.

For the 40% reduction experiments, although the resulting inclusions do not display a noticeable morphology variation in the longitudinal direction, due to the different depths at which the several inclusions identified in slab 2 were found, one can firstly distinguish the variation of the crystalline phase morphology in the through-thickness direction. This difference can be observed in Figure 81, where besides being indicated the absolute depth at which the inclusions were found, this measure is also displayed as a fraction of the total final slab thickness, in percentage.

As can be observed, with the decrease in depth within the slab, the crystalline morphology of the inclusions evolves into a fine structure. This difference can easily be justified by the increasing cooling rate acting on the slab closer to the surface. Moreover, the difference in phase morphology is specially accentuated for inclusion C, which was found extremely close to the surface. This heightened difference can be explained by the significantly higher cooling rates caused by the contact with the rolls during rolling.

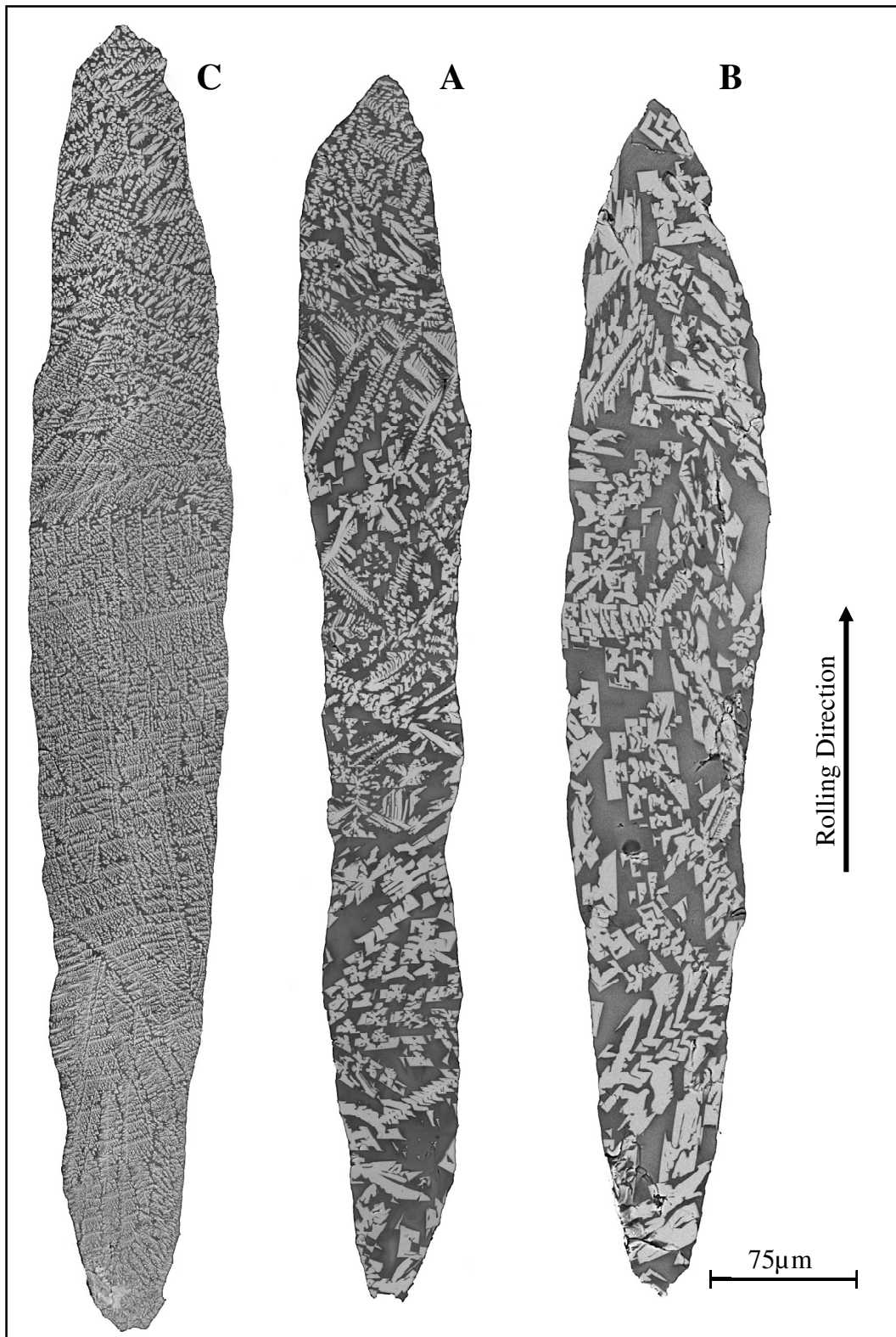


Figure 81 – Stitched BSI images for inclusions A (middle), B (right) and C (left) in the sample from slab 2. Inclusions organized (left to right) by increasing depth within the slab. Depths: inclusion C, 274 μm (2% of the final slab thickness); inclusion A, 1736 μm (14%) and inclusion B, 3136 μm (26%).

This justification can also be verified by the hot rolling simulations conducted, as can be observed in Figure 82.

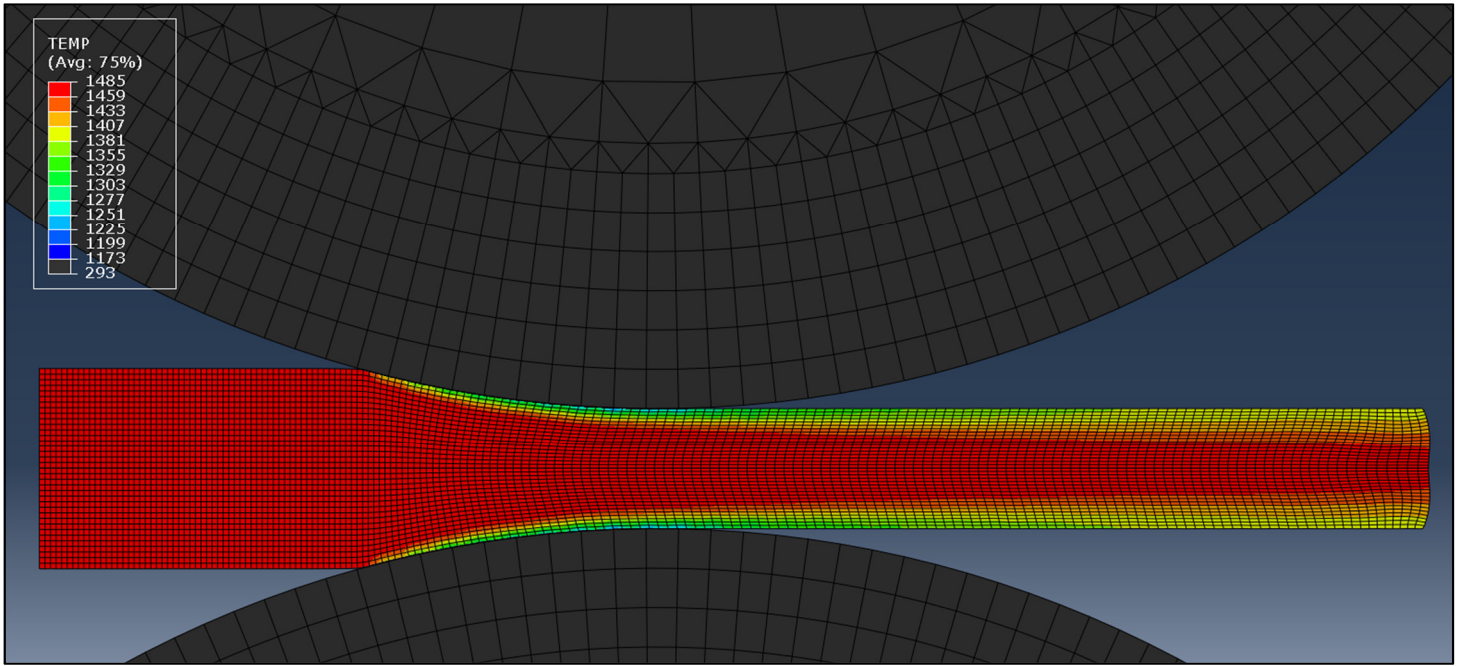


Figure 82 – Temperature gradient during hot rolling for the 40% reduction hot rolling simulations. Legend in Kelvin [K] units with lower bound set at 1173 (= 900°C) to highlight only the slab temperature profile.

As can be observed, the temperature throughout the thickness direction is noticeably lower for the initial depths, increasing more gradually for zones closer to the centre of the slab.

This evolution can be further explored in Figure 84, where the temperature resulting from the 40% reduction hot rolling simulations was plotted against the thickness (for a column of elements in the undeformed slab, along the contact zone, Figure 83).

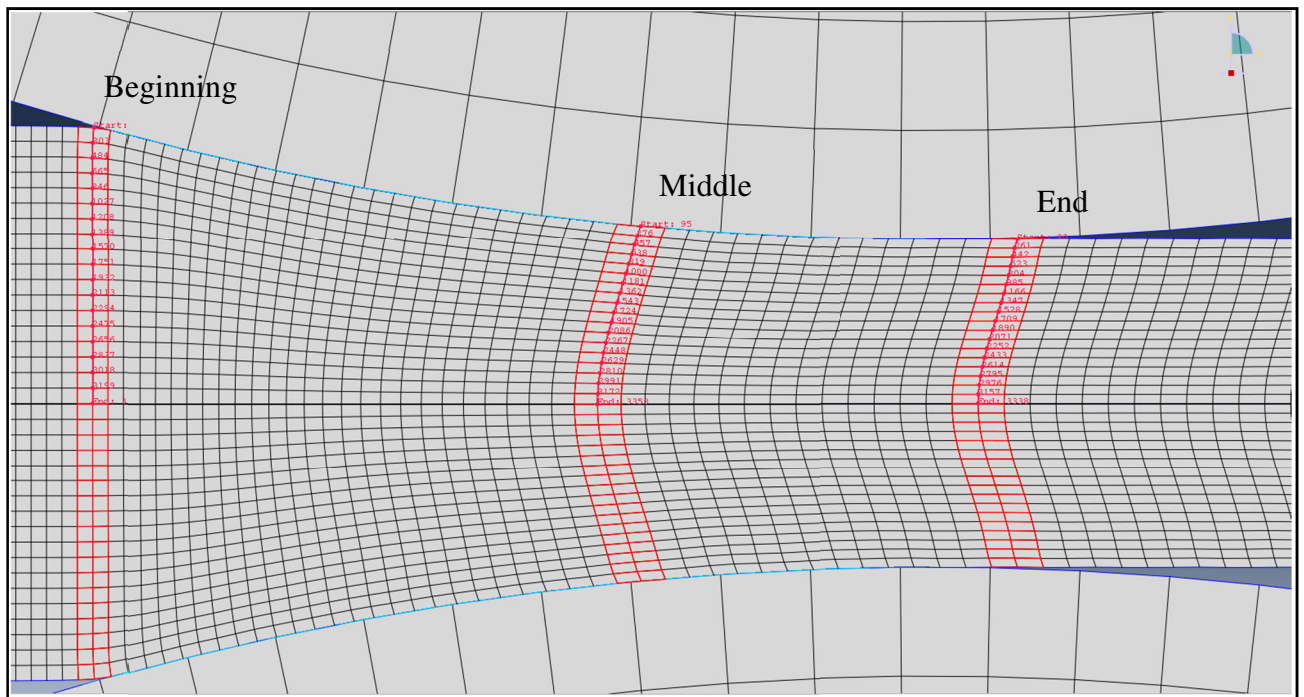


Figure 83 – Path of elements chosen for plotting the temperature profile in the beginning of the contact zone, middle of the contact zone and end of the contact zone.

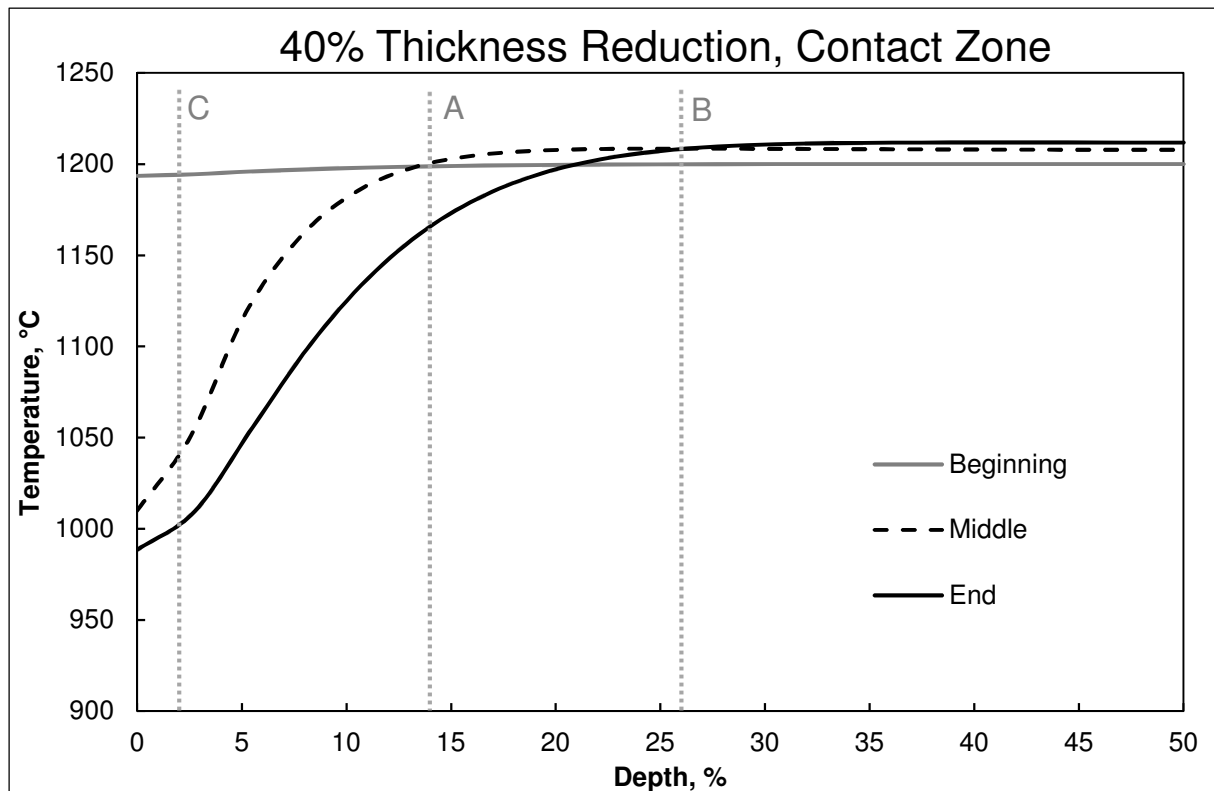


Figure 84 – Temperature evolution with the depth within the slab for the 40% reduction hot rolling simulations conducted. Temperature profile taken in the beginning, middle and end of the contact zone. Depths of inclusions A, B and C from slab 2 marked on the curve. Only half the thickness is displayed (symmetry).

As can be observed, according to the FE model results, it can be expected that, as an overall evolution, inclusion C experienced a $\approx 200^{\circ}\text{C}$ temperature decrease, which may have led to a considerably fast crystallization during cooling below the $\approx 1200^{\circ}\text{C}$ melting point for the mould slag particles. Inclusion A was exposed to a more moderate $\approx 50^{\circ}\text{C}$ temperature decrease, which may have led to a slight fast crystallization during rolling followed by the remaining crystallization on the cooling stand. Inclusion B maintained the same approximate temperature throughout the contact zone (with a slight temperature increase), which, being around the melting point, could indicate that this inclusion crystallized only after rolling, and therefore, considerably slowly.

It is then clearly seen that despite being fairly equally spaced in the thickness direction, the studied inclusions were subjected to a temperature profile that did not reflect linearly the position within the slab, thus resulting in a phase morphology that presented a significantly higher difference from inclusion A to C than from inclusion B to A. However, it should be kept in mind that, in the cooling stand, the most superficial layers of the slab and respective inclusions are being re-heated by the centre of the slab, possibly partially devitrifying part of the crystalline phases formed during rolling.

Exploring the 85% reduction inclusions, the fact that only one inclusion was found for slab 4 limits the analysis. The morphology of this inclusion's phases is, however, complex enough to warrant interpretation.

In a similar fashion to what was found in Slab 1, the parameter combination applied to slab 4 ensured that two main crystalline phases are present: wollastonite and cuspidine. The morphology of these phases did not present a distinct evolution in the rolling direction, and therefore can be represented by a section of the overall inclusion, as can be observed in Figure 85.

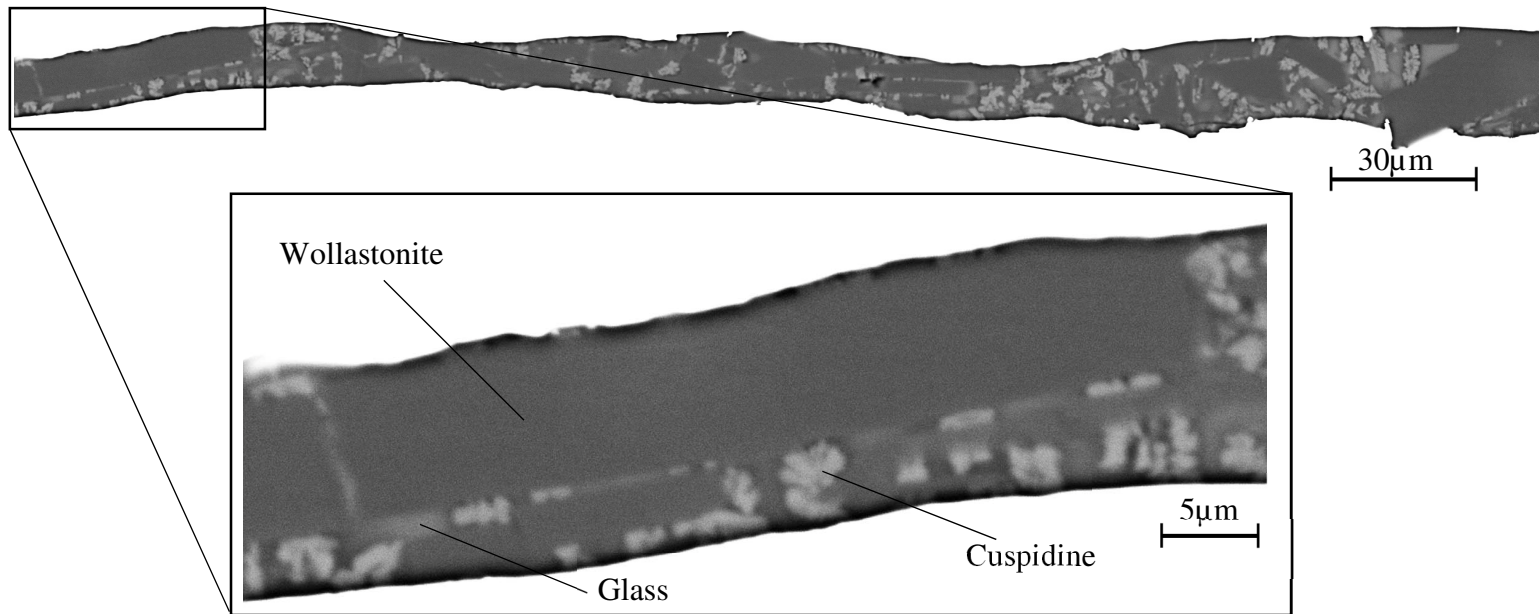


Figure 85 – Stacked BSI image section taken from inclusion A, slab 4 (top) and detail where the different phases are identified (bottom). Phases present are wollastonite (dark grey), cuspidine (light grey) and the remaining glassy phase (medium grey). Inclusion found at a depth of 1182µm (39% of the final slab thickness).

Firstly, it should be noted that the microstructure present in the analysed inclusion is in accordance with those of the inclusions studied by Uittenbroek (2019) for different samples taken from the same slab (slab 4), thus validating that the analysis further conducted will not be based on an exceptional case [9]. On the other hand, all of the inclusions studied by Uittenbroek (2019) were found at approximately the same depth as the one studied in the present work, not allowing the analysis of the through-thickness behaviour for these slab preparation conditions [9].

As can be observed, the inclusions resulting from a low Na and F content and subjected to a low soaking time are expected to develop relatively large blocks of wollastonite along with small cuspidine structures. Once again, the wollastonite is found mainly oriented in the rolling direction, a behaviour that possibly indicates that either (a) the phase is more easily deformable or (b) the phase was in the crystallization (or devitrification) process while being rolled, and cooled due to the extreme heat transfer occurring in this stage, maintaining the deformed shape it acquired. Cuspidine, on the other hand, presents a fine structure, organized in what appears to be small quasi-dendritic zones, seemingly nucleating in between the wollastonite blocks, possibly indicating that it crystallized after wollastonite.

Fluorine and Sodium Rich Samples

In the low soaking time, F/Na rich samples studied, which presented only cuspidine as the main crystalline phase, it is firstly important to mention that only one full inclusion (labelled B) and one partial inclusion (labelled A, smaller, very likely resulting from a cut offset from the central section of the inclusion) were found in sample 6. Since this 40% reduction sample's inclusions also did not display any clear phase morphology variation behaviour in the rolling direction (Figure 86), the low number of inclusions limited the analysis in the remaining, through-thickness, direction.



Figure 86 – Stitched BSI images for inclusion B of the sample from slab 6. Depth and length of the inclusion are $2194\mu\text{m}$ (18% of the final slab thickness) and $866\mu\text{m}$ respectively. Rolling direction from left to right.

The cuspidine morphology in this inclusion, however, is different to that of the cuspidine found in the inclusions observed in the samples from slab 2, when properly considering that the depth at which it was found can be placed between inclusion A and B of slab 2. Instead of large cuspidine blocks, this inclusion presents a more uniform, smaller and quasi-dendritic morphology, a fully glassy zone in the middle of the inclusion, and what seem to be dendritic-type structure nucleation points in the interface with the steel matrix. On the other hand, it is fairly visible in this inclusion that the transformation from a glassy amorphous phase into the crystallized cuspidine was interrupted during cooling, as can be observed in Figure 87, which might indicate that the melting point of these inclusions was lower than that of the low Na and F inclusions, which would be in accordance to the influences presented on Table 1, where it can be observed that F and Na are expected to lower the melting point. Although these differences might point to a significant composition influence on the phase morphology and possibly mechanical behaviour, it should be noted that only one full inclusion was studied for these slab preparation conditions, indicating that further research should be conducted to validate the proposed hypothesis.

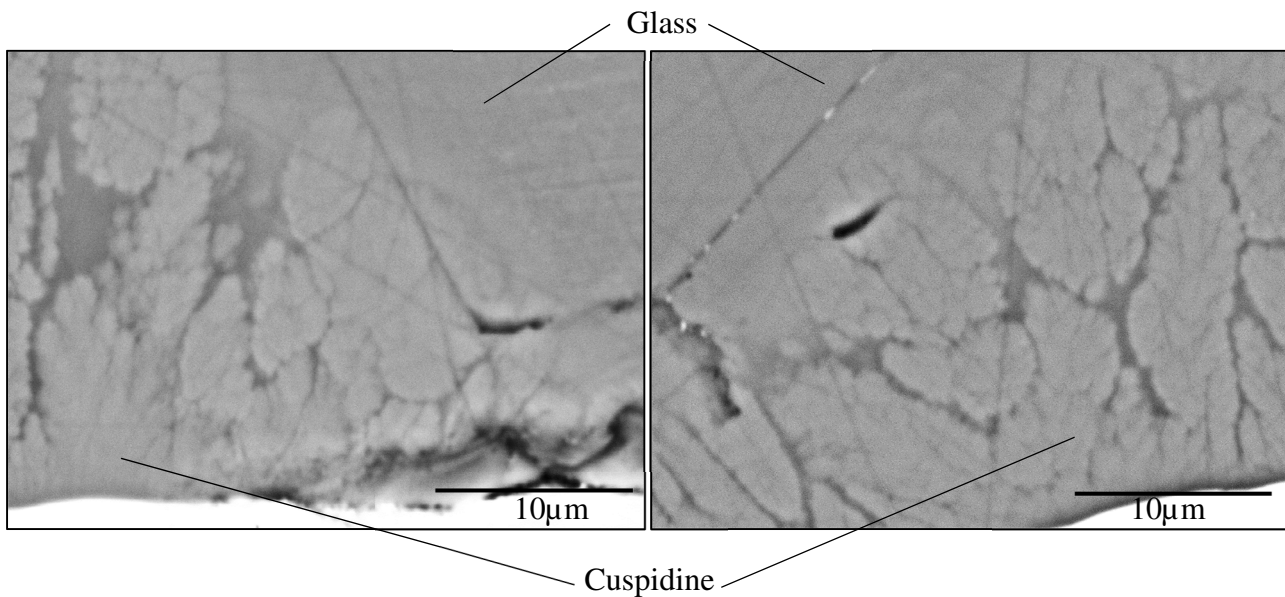


Figure 87 – BSI images taken from inclusion B, slab 6, highlighting the frozen transition zone between the glassy phase and the crystallized cuspidine.

On the other hand, for the 85% reduction samples in the same conditions, the number of inclusions found was sufficient to allow both rolling direction and through-thickness direction analysis of the phase's morphology.

Beginning with the through-thickness direction, differences were observed between the most superficial inclusion found and the remaining, deeper inclusions, as can be observed in Figure 88.

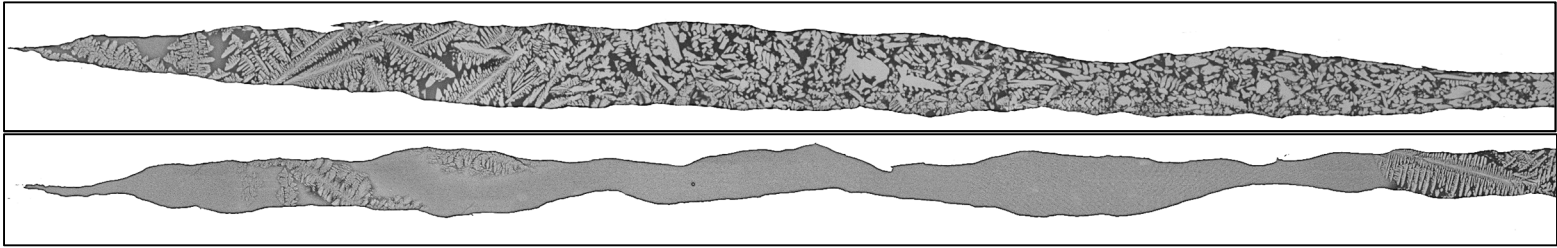


Figure 88 – BSI image “tail” sections from inclusions B (bottom) and D (top) found in the samples prepared from slab 8. Inclusions organized (top to bottom) by increasing depth within the slab. Depths: inclusion D, 606 μm (20% of the final slab thickness) and inclusion B, 1412 μm (47%). Rolling direction from left to right.

Observing Figure 88, it is fairly noticeable that the thicker section of the rolled inclusions (corresponding to the “tail” direction in the slab) presents a fully crystallized, dendritic structure for inclusion D, found a lower depth within the slab whereas for inclusion B, found deeper in the slab it presents a mostly glassy structure changing to a dendritic structure further along the rolling direction. What is also interesting, however, is that inclusion A and C present a behaviour similar to inclusion B, being found at an intermediate depth, but considerably closer to that of inclusion D than that of inclusion B (A - 875 μm , and C - 813 μm).

Once again, this non-linearity on the morphologic response might be explained by the non-linear temperature profile in the slab during rolling (Figure 89), as can also be observed by the plotted temperature response with the depth (Figure 90), determined in a similar fashion as the one described for Figure 84 in Figure 83.

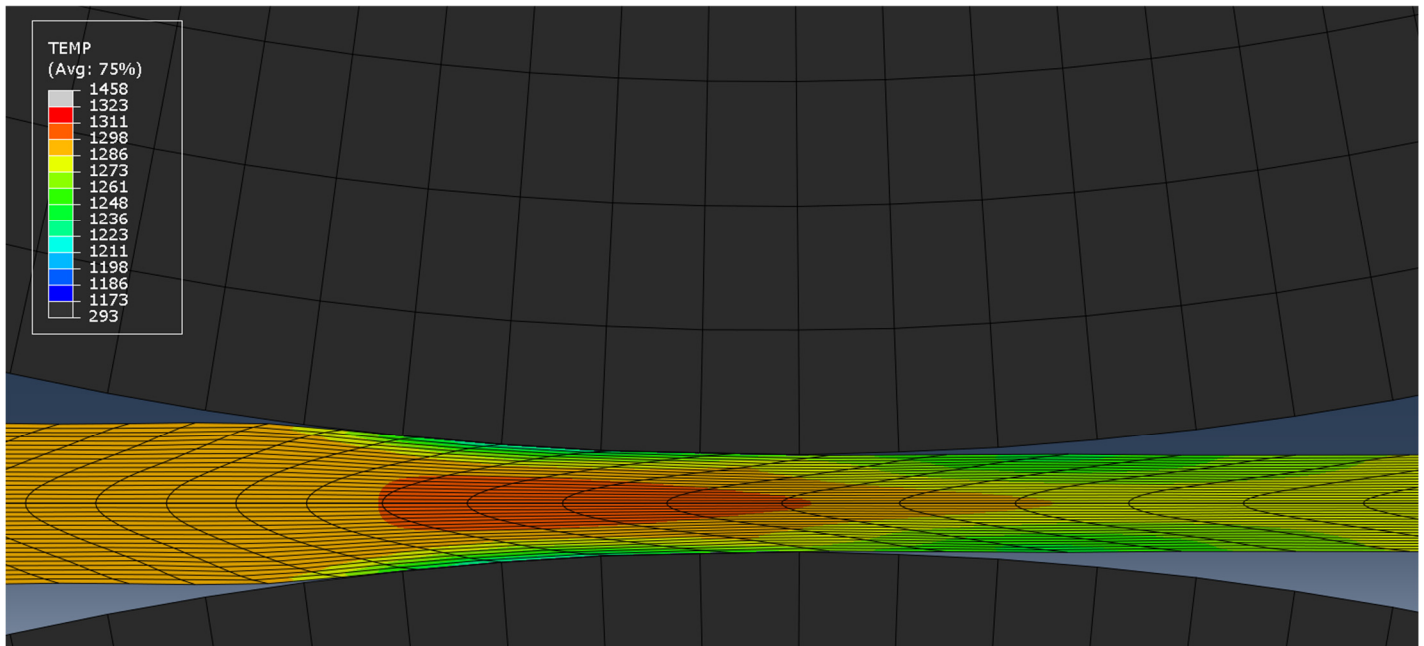


Figure 89 – Temperature gradient during the last hot rolling pass for the 85% reduction hot rolling simulations. Legend in Kelvin [K] units with range set from 1173 to 1323 ($\approx 900^{\circ}\text{C}$ to 1050°C) to highlight only the displayed slab zone temperature profile.

It can be observed that even the $\approx 200\mu\text{m}$ difference between the depth of inclusion D and inclusions A/C is sufficient to obtain a different thermal response in the slab, and therefore a different response in the phase morphology. Further analysis on the influence of cooling rates and thermal gradients on the crystallization response of cuspidine dendrites might support this observation.

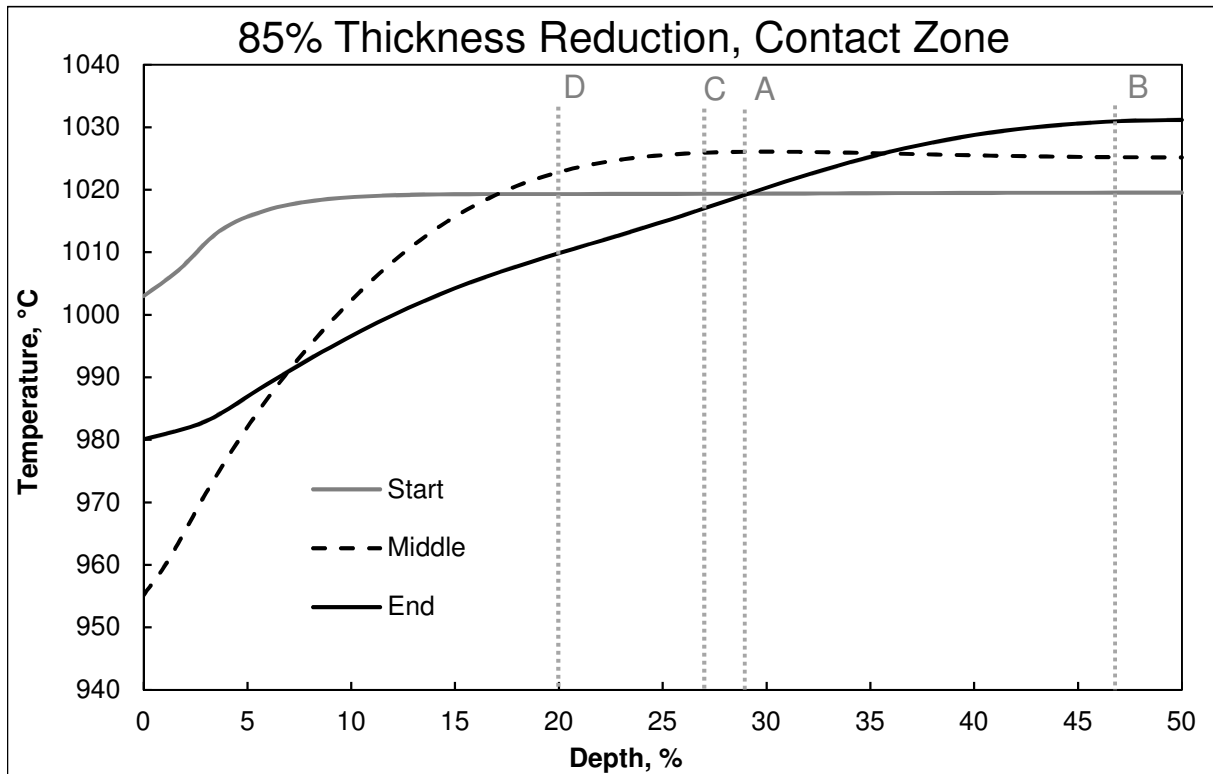


Figure 90 – Temperature evolution with the depth within the slab for the third pass of the 85% reduction hot rolling simulations conducted. Temperature profile taken in the beginning, middle and end of the contact zone. Depths of inclusions A, B, C and D from slab 8 marked on the curve.

Furthermore, although the crystallized cuspidine structures in the “tail” were defined as dendritic, it can be observed that, for all inclusions, this dendritic structure appears to be broken in the rolling direction, resulting in a globular structure closer to the “head” section, as can be observed in detail in Figure 91.

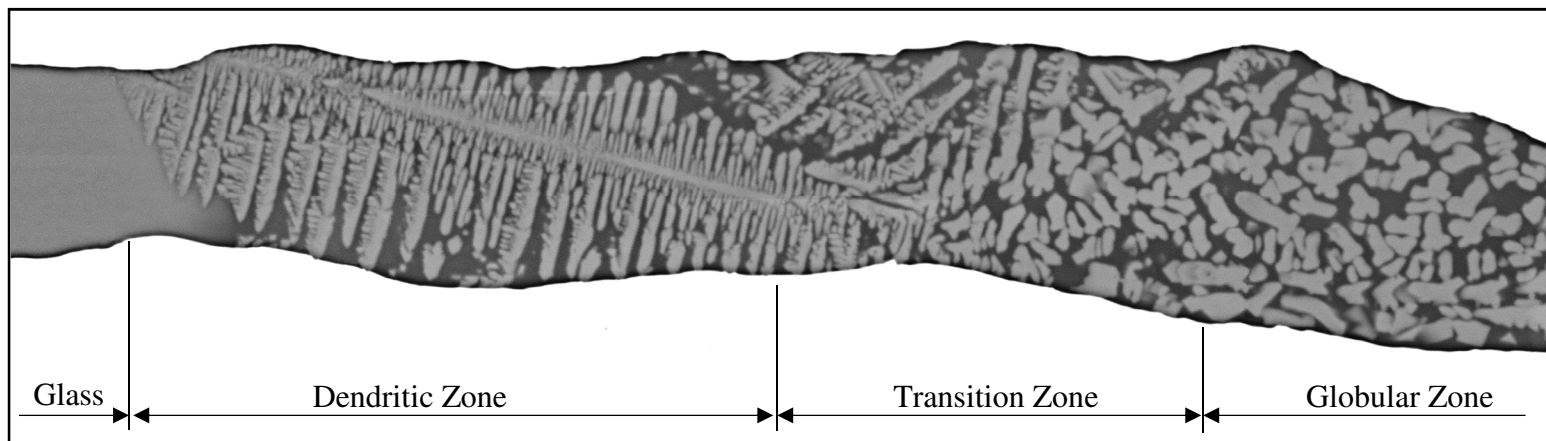


Figure 91 – Detail from the Stitched BSI image from inclusion B, slab 8 where transition zone between the initial glassy structure, the following dendritic structure, the consequent broken dendrite zone and final globular structure is visible in a single image. A similar behaviour was observed for the remaining inclusions from the same sample, albeit more spread out through the inclusions, limiting its display.

This phenomenon of the breaking of dendrites possibly presents some information about the cooling suffered by the inclusions during rolling. Firstly, the fact that a glassy structure is concentrated in the “tail” end of the inclusion might be justified by the squeezing of the amorphous content either in the liquid or semi-solid state during the last rolling pass. Moreover, the fact that a dendritic microstructure was broken indicates that it already existed during rolling, and therefore had to be formed either before or while the rolling process occurred. On the other hand, the fact that only a partial fraction of dendrites was broken and globulized

indicates that the behaviour during rolling is changing, that the properties of the inclusion are not constant in the longitudinal direction, or that, as already presented in the shape analysis, the strain suffered in the “tail” end and the “head” end of the inclusion are different. The most probable conclusion is that all hypotheses are true, but further research would be needed to confirm this, and if so, to determine the weight of each of the phenomena in the final result.

This behaviour hypothesis is further validated by the microstructure observed in the 60% reduction samples by Uittenbroek (2019), which presented similar microstructure, with the same dendrite breaking phenomenon near the front end of the inclusion (“head” direction) along the longitudinal direction (Figure 92) [9].

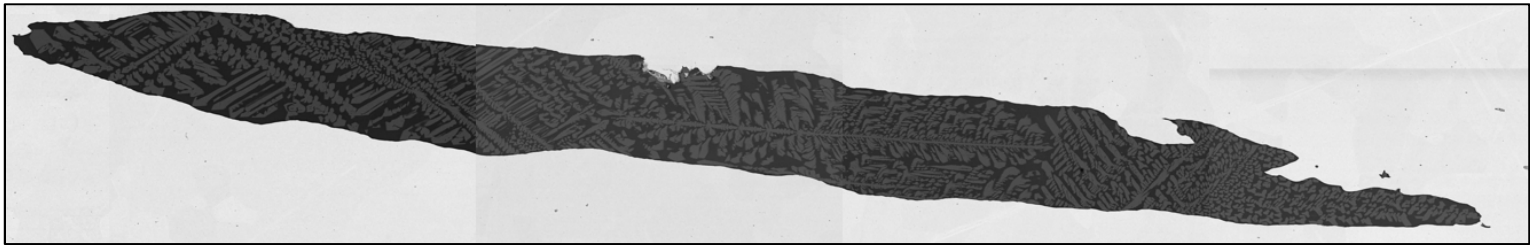


Figure 92 – BSI image of an inclusion taken from slab 7 (60% thickness reduction, rich Na/F content, low soaking time). Inclusion length of 1028 μ m. Rolling direction from left to right [9].

In the analysis of this process, however, it is once again important to consider the re-heating effect that takes place in between rolling steps, possibly partially devitrifying the already crystallized inclusions, an effect that would be especially noticeable if the melting point of the inclusion was lowered, as it is proposed.

From a processing standpoint, the ability to ascertain the phase morphology resulting from each rolling pass as a function of the different inclusion and processing parameters, as well as to predict its mechanical behaviour both in the subsequent hot-rolling stands and during the remaining operations until the final product (i.e. cold rolling) could directly help in defining the rolling schedules to be applied to the slabs based on the final product’s application.

For example, if it is determined that cuspidine dendritic structures present a less ductile behaviour (something that is usually observed in metallic dendritic structures), resulting in bulkier, less elongated inclusions, for slabs intended for in the automotive industry an effort can be made in defining a rolling schedule that promotes a higher deformation in the first stands and the crystallization of such structures later in the process. This way, the dendritic structure would be preserved, and the defect, after consequent operations where the inclusion does not break, would resemble a single dot instead of the undesirable elongated lines characteristic of the *griffe laminée*.

On the other hand, for packaging applications, where bulkier inclusions result in the split flange defect, an effort could be made to promote either glassy or globulized structures in the inclusions, by forcing an earlier crystallization and subjecting the inclusion to higher deformations later in the process, resulting in the observed phenomenon of breaking the dendritic cuspidine and allowing the evolution into a more ductile, globular structure. This would create inclusions that are more easily breakable during further operations, avoiding the bulky inclusions that could cause a split flange.

In order for these hypotheses to be validated, two main factors must be further explored. Firstly, the onset temperatures for crystallization of cuspidine, as well as the cooling rates that result in the different microstructures during hot rolling must be defined. To do so, thermo-chemical calculations based on the measured compositions and the definition of TTT/CCT diagrams for the NMI at hand is paramount. Secondly, the mechanical behaviour of the different phase morphologies must be isolated and characterized, for which a new testing methodology is proposed in future work (Section 8.2).

7 Conclusions

In the present work, artificial inclusions embedded into steel slabs were studied using optical and electron microscopy techniques after different hot-rolling schedules were applied to achieve four different thickness reductions. The preparation parameters were also varied to produce F/Na rich and poor inclusions, with low and high soaking times.

In order to help the understanding of the thermo-mechanical phenomena present in this process, a FE macro-model of the lab-scale hot rolling process used in the experimental stage was created.

When compared with the experimental results, it could be concluded that despite presenting a similar evolution in the thermal response, the rolling force predicted by the model was considerably higher than the measured one. Although force prediction is not the main objective of the model, this leads to the conclusion that further tuning of the model could be helpful.

The analysis conducted on the inclusions was divided into three main categories: inclusion shape, where the overall shape of the rolled inclusions was evaluated using different ratios; inclusion composition, where the EDS analysis results and respective variations were evaluated for the different inclusions; and phase morphology, where the microstructure of the inclusions and its evolution with the different process parameters was characterized.

Regarding the inclusion shape, the main phenomena observed regards a change in behaviour from “oval” inclusions to “drop-shaped” inclusions between the 2-pass 60% rolling reduction schedule and the 3-pass, 85% rolling schedule. When compared to the available literature, this change seems to indicate a change from a “soft” inclusion behaviour with a uniform deformation in the rolling direction to a “hard” inclusion behaviour with a different deformation in the front-end of the inclusion and the rear-end of the inclusion.

Additionally, it was concluded that not only does the aspect ratio of the inclusions decrease with the increase in thickness reduction, but it also seems to reduce its variation.

Moreover, it was observed that while a reduction in the relative plasticity index with the increase in thickness reduction (predicted in the literature) is observed up to 60% reduction, this parameter seems to stabilize for higher deformations.

For the most deformed inclusions (85% reduction), there was also the indication of an increase in aspect ratio and decrease in relative plasticity index with the increase in depth within the slab.

No discernible influence of the Na/F content or soaking time was observed in the inclusion shape.

Regarding the inclusion composition, firstly it was concluded that although the methodology used to produce F/Na variable inclusions resulted in satisfactory results for the sodium content, the difference in fluorine was not as pronounced. Nevertheless, it could be seen that, overall, the poor F/Na inclusions presented both cuspidine and wollastonite as the main crystalline

phases, while the rich F/Na inclusions resulted in cuspidine being the single crystalline phase present.

Regarding the phase morphology of the inclusions, firstly it was concluded that wollastonite was consistently found in elongated blocks in the rolling direction, whereas the cuspidine morphology changed significantly.

For the Na/F poor inclusions, cuspidine was found between the wollastonite blocks, in a globular form for the lower deformation inclusions and a quasi-dendritic form for the higher deformation inclusions, reflecting the difference in cooling rates between the different rolling schedules.

For the Na/F rich inclusions, cuspidine presented an increasingly dendritic structure with the decrease in depth within the slab, an evolution that followed the non-linearity in the temperature profile of the slab in the through-thickness direction.

Additionally, for the most deformed inclusions (85% reduction), a change in the longitudinal direction from a glassy structure, to a dendritic zone followed by a globular zone was found. It remains to be determined if this change is a cause or a consequence of the difference in deformation from the front-end and the rear end of the inclusion observed in the shape analysis.

8 Future Work

As a part of a continuous project, the work at hand lends itself to a significant quantity of ideas for further research.

Firstly, additional tuning of the developed FE model can be conducted. This might encompass further tuning of the Siciliano predictive model coefficients, possibly taking into account the metallurgical response in the lab-scale process (i.e. inter-stand phenomena) as well as a possible parameter study regarding the friction coefficient, taking into account the temperature and thickness reduction variation of this parameter. The simulation of rolling schedules equal to those found in the literature could also help in the tuning of the model. Since a variance in the initial temperature of the slabs was found in the experimental data, a FE analysis of the influence of this parameter in the overall response during rolling could be proven to be helpful in the analysis of the experimental results. Additionally, the continuation of the devised plan concerning the modelling strategy can be conducted, adapting the present model's results into the mesoscale and ultimately into the microscale.

Regarding the inclusion analysis, due to the variance in the results inherent to the testing techniques, the continued evaluation of additional inclusions, especially in the slabs in which few or no inclusions were found is detrimental to the validation of the hypothesis proposed in the present work.

The upscaling of the experimental procedure applied in the present work to the plant-scale process is also detrimental to validate the lab-scale approach, which can be further consulted in the following Section 8.1.

As previously mentioned, the exploration of thermo-chemical calculation in order to define the crystallization temperatures of the different phases could help in further understanding the results, in order to be ultimately applied in the manufacturing processes at hand.

Finally, it should be noted that several differences in the microstructure of the studied inclusions were found. Being a result of the size- and time-dependant thermal gradients during the process, it can also be concluded that these differences might be even more pronounced in the real-scale process. Therefore, the determination of the difference in mechanical behaviour resulting from the different possible microstructures might be of paramount importance for the project at hand. A proposition of an experimental procedure to evaluate this factor is presented in Section 8.2.

8.1 Plant Scale Trials

A new stage of the experimental part of the clean steel project aims at upscaling the lab scale trials to plant conditions.

To do so, new PM cylinders with artificial inclusions produced by the same methodology used in the present work will be used. These new cylinders followed the methodology developed during Pille's (2016) internship [23] and unlike the ones produced at Aachen University did not use HIP, being able to be produced at Tata Steel IJmuiden.

To do so, firstly, CIP-CC Carbonyl iron powder is mixed with a binder (4wt% of PEG 400 - polyethylene glycol) and a diluent (7wt% acetone) and pressed into a layer. The function of the acetone in this case is to lower the viscosity of the binder so as to allow a uniform dispersion with the iron powder, as well as to evaporate easily after the dispersion is complete [23]. Several layers are stacked to make each bar. The artificial inclusions are introduced in these samples, either between two layers or mixed into one of the layers.

To create a referencing system (so that the displacement of the steel matrix can be observed and the location of the inclusions retrieved), 3wt% Mo is added to every other layer, since this alloying element results in a different colour, including after etching (Figure 93) [36].

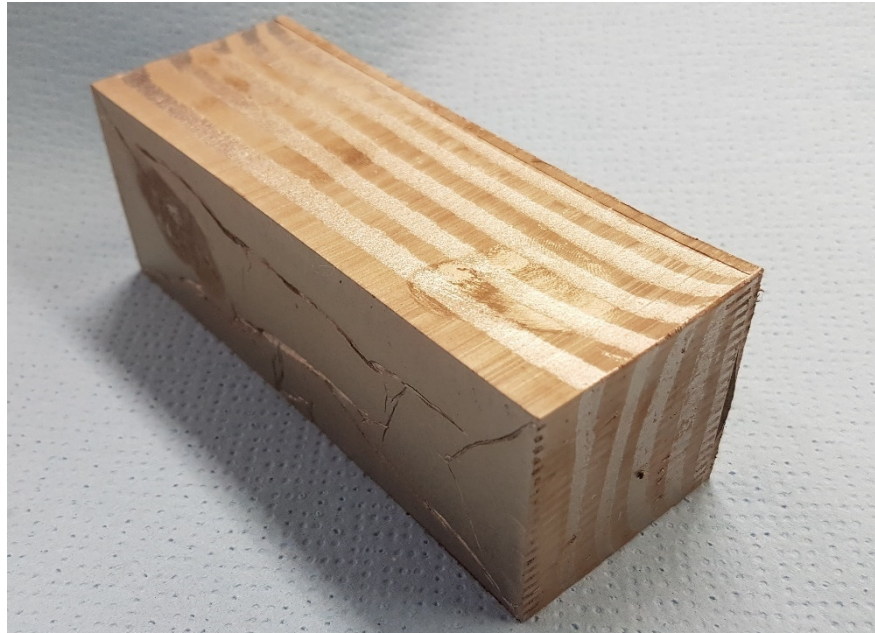


Figure 93 – Powder metallurgy bar with visible layering.

The samples are pressed and sintered, as was done in the experimental procedure of the present work.

These new cylinders, as well as some HIP cylinders remaining from the lab scale trials are then introduced in full scale steel slabs produced locally at Tata Steel IJmuiden and then rolled in the Hot Strip Mill installations on site, with its processing parameters registered for further interpretation of the results.

8.2 Slag Characterization Tests

The deformation behaviour of the inclusions during rolling could be characterized as a thermo-chemical-mechanical phenomenon, since besides the mechanical loads provided by the rolling pressure, chemical and microstructural changes occur due to the thermal variation that is imposed through the process. These complex phenomena occur at the same time for both the steel and for the inclusions, which are materials with significantly different behaviours.

In order to try to isolate the inclusion behaviour, a new test approach is proposed to characterize the mechanical behaviour at high temperatures of mould slag with different crystallinity ratios. The base idea for the tests regards the preparation and study of mould slag cylinders with different microstructures, produced using the methodology applied by Pieter Put (2012) [56].

The initial idea was to design thermal cycles for the preparation of the different samples based on different soaking times and continuous cooling rates, as can be observed in Figure 94. It should be noted that the two soaking times proposed correspond to the ones used for the slabs studied by Lennard Uittenbroek (2019) and in the present work [9].

This strategy, however, becomes problematic due to sodium and fluorine loss during the soaking times at high temperatures (above the F and Na evaporation points), unlike what happens in the rolling tests where the slag is already entrapped in the steel at the time of the soaking step.

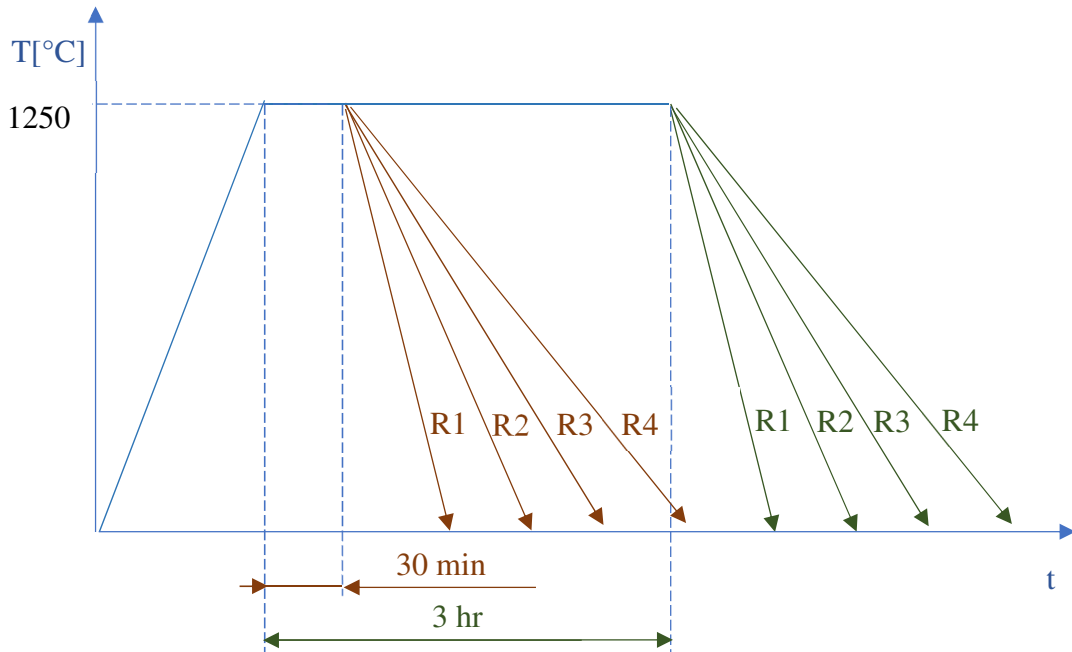


Figure 94 – Thermal cycles initially proposed for the different sample preparations.

where:

R_x , are the cooling rates applied [$^{\circ}\text{C}/\text{min}$];
 $R_1 > R_2 > R_3 > R_4$

To solve this, the concept of CCT (Continuous Cooling Transformation) vs TTT (Time Temperature Transformation, i.e. isothermal transformation) was applied. This approach, represented in Figure 95, allows the samples to achieve the different microstructures corresponding to different cooling rates, but using isothermal stages at lower temperatures followed by quick cooling, thus minimizing Na/F loss.

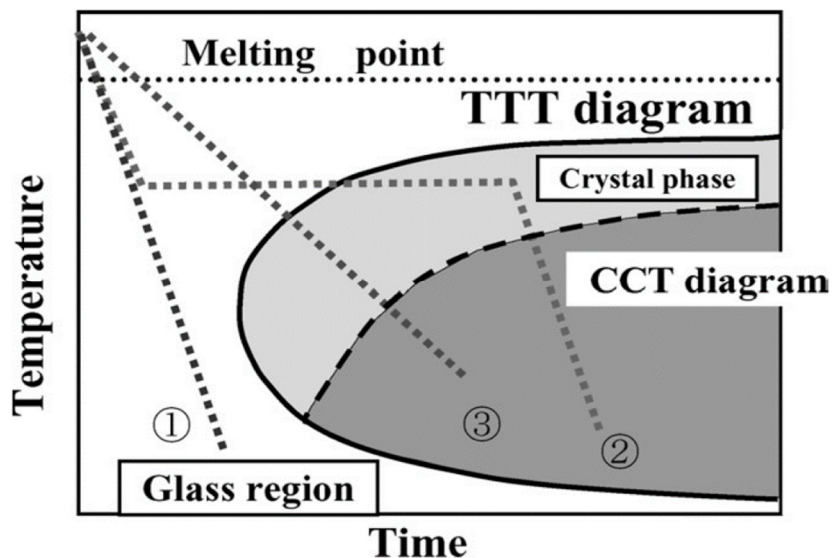


Figure 95 – Illustration of the CCT and TTT diagrams and corresponding approaches [57].

In order to define the different thermal cycles to use, a valid TTT diagram for the material at hand should be used. In this case, the material used should be the same as the one being rolled, which comes from mould powder MP-B.

The previously mentioned research conducted in the matter of the devitrification and crystallisation phenomena for mould slags by Maldonado *et al.* (2014), lead to the estimation of a TTT diagram for a mould slag presenting a similar composition to the one studied in the present thesis. The final TTT diagram can be consulted in Figure 96 [22].

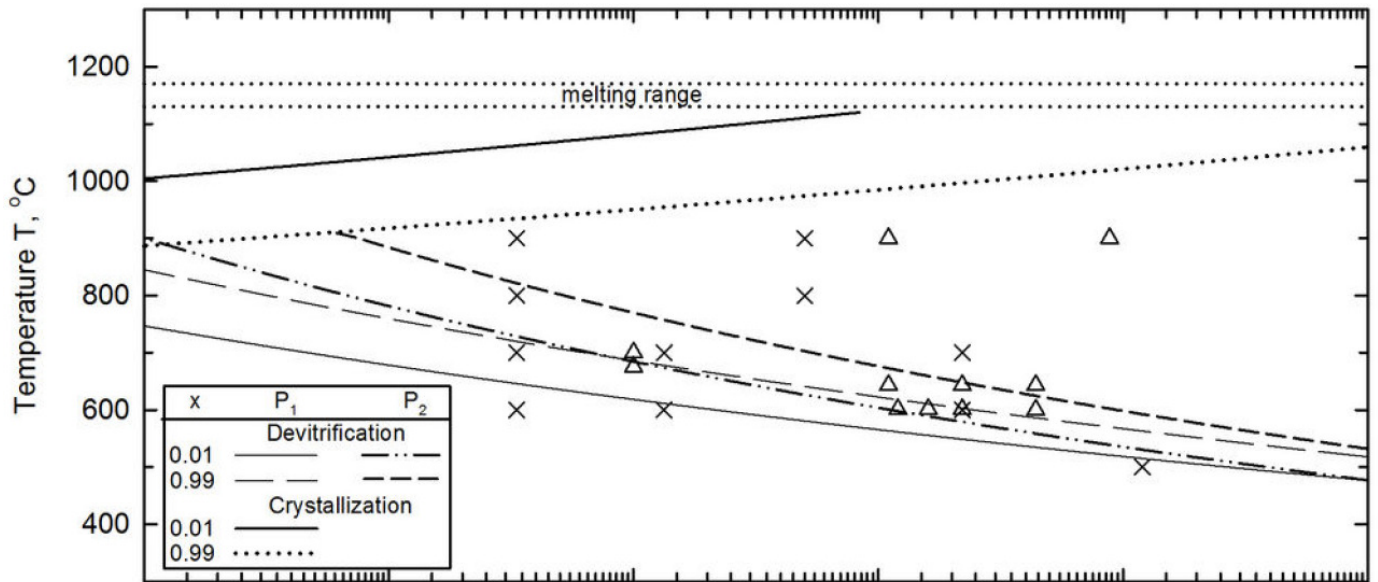


Figure 96 – TTT diagram for slag A (Maldonado *et al.*, 2014), of similar composition to the MP-B slag [22].

The main decision factors for the thermal cycles to apply in this test should be the desired number of samples and the different microstructures observed by Maldonado *et al.* (2014), as can be observed in Figure 97.

It should be noticed that the parameters used in the study corresponded to a devitrification process, since Maldonado *et al.* (2014) firstly produced a quenched solid glass structure and only then re/heated it in order to get the different microstructures.

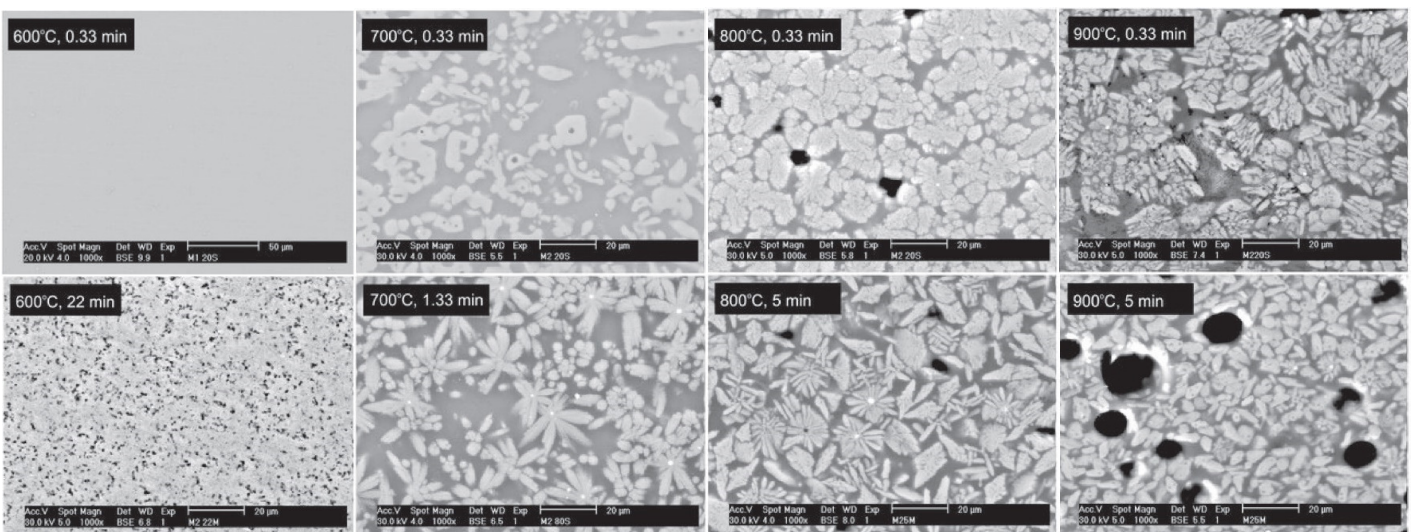


Figure 97 – Microstructures observed for different thermal cycles applied to the mould slag. BSE images [22].

For the present test, it is proposed that the same approach is taken, since the alternative (liquifying the mould powder, quickly dropping the temperature to an intermediate temperature,

holding the isothermal stage, and then quickly quenching the sample) would require a great control during the cooling from the liquid slag temperature to the intermediate temperature.

Therefore, it is proposed that the mould powder is fully liquified for a short amount of time (to minimize F and Na loss) at 1250°C, then quickly cooled in order to get a fully glassy structure, and only then re-heated to the isothermal stage temperature, held for the amount of time defined, and then quickly cooled again to preserve the microstructure achieved.

Pieter Put (2012) used an amount of approximately 100g of mould powder per sample, which resulted in big enough samples to perform the desired tests (Figure 99), so the same amount is proposed to be applied to this test. A graphite crucible similar to the one used in Pieter Put's tests is also proposed to be used, as represented in Figure 98 [56].

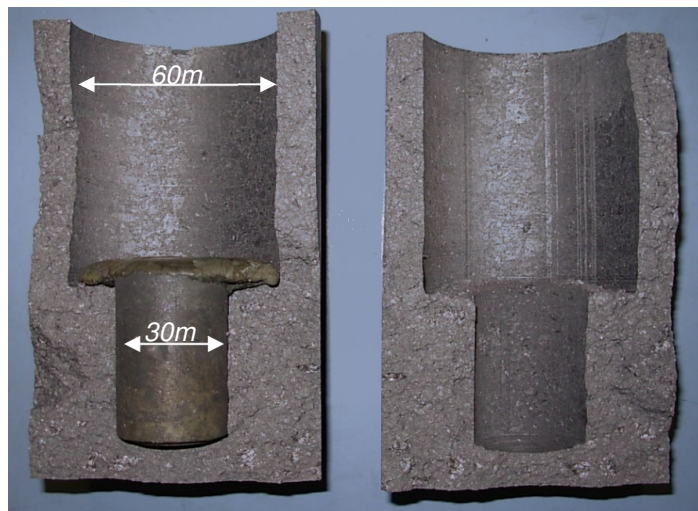


Figure 98 – Graphite crucible used by Pieter Put, 2012 [56].



Figure 99 - Example of a sample produced by Pieter Put, 2012 [56].

Concerning the testing, firstly, to evaluate the microstructure and crystallinity rate obtained, it is proposed that a cross section cut is made in the resulting samples and that the resulting slice sample is observed via optical microscopy and/or SEM.

Secondly, as used by Pieter Put [56], it is proposed that the mechanical test used is one similar to a VOD test (*Vuurvastheid Onder Druk* – Heat Resistance Under Pressure, Figure 100), where a sample under a constant load is gradually heated and the displacement (and therefore length variation) of the sample is continuously plotted against temperature. To try to approach the load

conditions during rolling, instead of the 0.02MPa used in regular VOD tests, it is proposed that 5.0MPa are applied in the Zwick Z250 pressure bench.

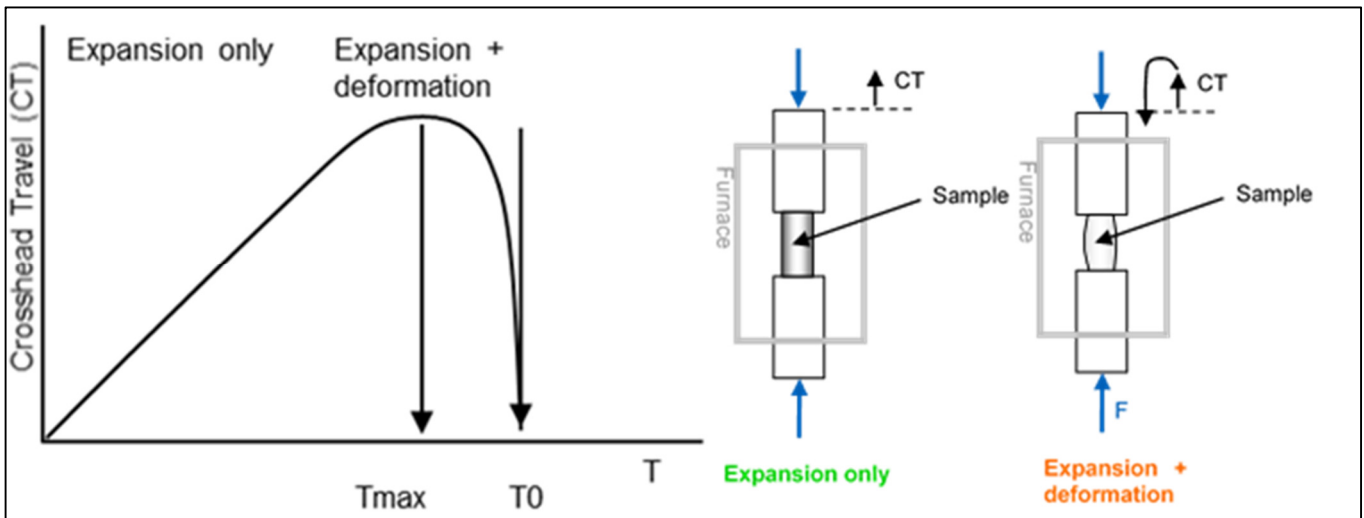


Figure 100 – Principles behind the proposed mechanical characterization test [56].

It is proposed that one preliminary sample for each microstructure is produced and analysed under the microscope. This stage can be used to define whether or not the chosen thermal cycles result in microstructures different enough to lead to relevant conclusions.

It is only after tuning the cooling parameters and verifying, via microscopy analysis, that different microstructures are indeed being obtained, that it is proposed that the mechanical testing should be conducted. The number of samples to study is dependent on the time available, but it is proposed that an average of 3 samples for each of the 8 different microstructures are prepared, resulting in a total of 24 samples.

References

1. Hansén, T. and M. Werke, *Modelling and model validation of the deformation of macro inclusions during hot deformation*, in *8th International Conference on Clean Steel*. 2012: Budapest, Hungary.
2. Le Bihan, C., et al., *Characterization (e.g. SEM, microscopy techniques) of the deformation of macro-inclusions in slabs during hot deformation pilot trials*. 2018, Tata Steel Nederland Technology BV: IJmuiden, Netherlands.
3. George, L. and S. Verdier, *Deformation Behaviour of Macro-inclusions during hot rolling*. 2015, Tata Steel Nederland Technology BV: IJmuiden, Netherlands.
4. Yang, Y., K. Raipala, and L. Holappa, *Ironmaking*, in *Treatise on Process Metallurgy*, S. Seetharaman, Editor. 2014, Elsevier: Boston. p. 2-88.
5. Jalkanen, H. and L. Holappa, *Converter Steelmaking*, in *Treatise on Process Metallurgy*, S. Seetharaman, Editor. 2014, Elsevier: Boston. p. 223-270.
6. Kromhout, J.A., *Mold powders for high speed continuous casting of steel*. 2011: Tata Steel Nederland Technology BV.
7. Louhenkilpi, S., *Continuous Casting of Steel*, in *Treatise on Process Metallurgy*, S. Seetharaman, Editor. 2014, Elsevier: Boston. p. 373-434.
8. Davies, G., *Materials for consideration and use in automotive body structures*, in *Materials for Automobile Bodies*, G. Davies, Editor. 2012, Butterworth-Heinemann: Oxford. p. 93-143.
9. Uittenbroek, L., W. Tiekink, and L.-J. Pille, *Characterization of Macro-inclusions in Steel after Deformation by Hot Rolling*. 2019, Tata Steel Nederland Technology BV: IJmuiden, Netherlands.
10. Asumadu, T.K., *Macro Inclusion Research : Detection and Evaluation of Macro Inclusions in Special Steels*. 2012. p. 52.
11. Serajzadeh, S., *Hot Rolling and Direct Cooling*, in *Comprehensive Materials Processing*, S. Hashmi, et al., Editors. 2014, Elsevier: Oxford. p. 377-396.
12. Mukerjee, K.K., *A critical review of the mechanics of metal rolling; its application to the design of hot strip mills*, in *Faculty of Engineering*. 1973, Sir George Williams University: Montreal, Canada. p. 174.
13. Munther, A., *The Effect of Material and Process Parameters on the Frictional Conditions in Hot Flat Rolling of Steels*, in *Department of Mechanical Engineering*. 1997, University of Waterloo: Waterloo, Ontario, Canada. p. 233.
14. Susa, M., et al., *Thermal conductivity and structure of alkali silicate melts containing fluorides*. *Ironmaking & Steelmaking*, 2001. **28**(5): p. 390-395.
15. Verlag, S. and E. Verein Deutscher, *Slag atlas*. 1995, Dusseldorf: Verlag Stahleisen GmbH.
16. Bale, C.W., et al., *FactSage thermochemical software and databases, 2010–2016*. *Calphad*, 2016. **54**: p. 35-53.
17. Holappa, L. and O. Wijk, *Inclusion Engineering*, in *Treatise on Process Metallurgy*, S. Seetharaman, Editor. 2014, Elsevier: Boston. p. 347-372.
18. Goharinezhad, A. and M. Abbasi, *Effect of hot rolling on non-metallic inclusions and fatigue behaviour of AISI: 1045 clean steel*. *International Journal of Microstructure and Materials Properties*, 2016. **11**: p. 487.

19. Yin, Y., et al., *Experimental Investigation on Inclusions in Hot Rolled Axle Steel by the Mold Casting*, in *Materials Science and Technology 2017 (MS&T17)*. 2017: David L. Lawrence Convention Center, Pittsburgh, Pennsylvania USA.
20. Wang, C., et al., *Influence of inclusions on matrix deformation and fracture behavior based on Gurson–Tvergaard–Needleman damage model*. *Materials Science and Engineering: A*, 2019. **756**: p. 405-416.
21. Meyneng, T., L.-J. Pille, and S. Verdier, *Characterization of the deformation of macro inclusions in slabs during hot deformation pilot trials*. 2017, Tata Steel Nederland Technology BV: IJmuiden, Netherlands.
22. Maldonado, Y., et al., *Estimation of Time–Temperature–Transformation Diagrams of Mold Powder Slags from Thermo-analysis of Non-isothermal Crystallization*. Vol. 46. 2014. 286-303.
23. Pille, L.-J., *Clean Steel Project - A study of the deformation behaviour of macro-inclusions during hot deformation at plant conditions*. 2016, Tata Steel Nederland Technology BV: IJmuiden, Netherlands.
24. Doppenberg, D. and S. Verdier, *Evolution of macro-inclusions in steel during hot deformation - Development of model material*. 2013, Tata Steel Nederland Technology BV: IJmuiden, Netherlands.
25. George, L., *Master Thesis - Deformation behavior of macro-inclusion during hot-rolling of steel*. 2015, Tata Steel Nederland Technology BV: IJmuiden, Netherlands.
26. Kanadalam, A., G. Abbel, and S. Verdier, *Modelling and Validation of Deformation Behaviour of Macro Inclusions during Hot and Cold Rolling*. 2016, Tata Steel Nederland Technology BV: IJmuiden, Netherlands.
27. Khlifi, I., *Study of the deformation behaviour of macro-inclusions during hot rolling*. 2016, Tata Steel Nederland Technology BV: IJmuiden, Netherlands.
28. Karnasiewicz, B., *Evaluation and Characterization of the In-house Produced Artificial NMI Inclusions*. 2017, Tata Steel Nederland Technology BV: IJmuiden, Netherlands.
29. Guessous, K., W. Tiekink, and S. Verdier, *Investigation on chemical composition of macro-inclusions and its influence on deformation behavior during hot rolling*. 2017, Tata Steel Nederland Technology BV: IJmuiden, Netherlands.
30. Danninger, H. and C. Gierl-Mayer, *Advanced powder metallurgy steel alloys*, in *Advances in Powder Metallurgy*, I. Chang and Y. Zhao, Editors. 2013, Woodhead Publishing. p. 149-201.
31. Akhtar, S., et al., *Recent Advancements in Powder Metallurgy: A Review*. *Materials Today: Proceedings*, 2018. **5**(9, Part 3): p. 18649-18655.
32. Tallmadge, J.A., *Powder Production by Gas and Water Atomization of Liquid Metals*, in *Powder Metallurgy Processing*, H.A. Kuhn and A. Lawley, Editors. 1978, Academic Press. p. 1-32.
33. Roll, H. and P.K. Johnson, *Iron Powder Metallurgy*. 2013: Springer US.
34. Tsukerman, S.A., *Charge Preparation and Composition*, in *Powder Metallurgy*, S.A. Tsukerman, Editor. 1965, Pergamon. p. 29-35.
35. Tsukerman, S.A., *Pressing*, in *Powder Metallurgy*, S.A. Tsukerman, Editor. 1965, Pergamon. p. 36-57.
36. Tiekink, W., *Rolling of inclusions in sintered steel*. 2018, Tata Steel IJmuiden: IJmuiden, Netherlands. p. 19.
37. Tsukerman, S.A., *Sintering*, in *Powder Metallurgy*, S.A. Tsukerman, Editor. 1965, Pergamon. p. 58-73.
38. Torralba, J.M., *Improvement of Mechanical and Physical Properties in Powder Metallurgy*, in *Comprehensive Materials Processing*, S. Hashmi, et al., Editors. 2014, Elsevier: Oxford. p. 281-294.
39. Moreira de Sá, C.P., *Microscopia Eletrónica de Varrimento - SEM e Métodos Analíticos Associados - EDS/EBSD*, in *Caraterização Morfológica, Microestrutural e Microanalítica de Materiais por Métodos Experimentais de Elevada Resolução Espacial*. 2018, CEMUP - Centro de Materiais da Universidade do Porto: Porto, Portugal.

40. Gelten, P. and H. Pattabhiraman, *Proposal for a new material & pressure hill model in IJmuiden HSM2 to predict the rolling force, rolling power, and work roll speed*, T.S.R. Development, Editor. 2019, Tata Steel IJmuiden Technology Centre: IJmuiden, Netherlands. p. 27.
41. Kirihata, A., et al., *Mathematical Modelling of Mean Flow Stress during the Hot Strip Rolling of Multiply-alloyed Medium Carbon Steels*. ISIJ International, 1998. **38**(2): p. 187-195.
42. Misaka, Y. and T. Yoshimoto, *Formularization of mean resistance to deformation of plain carbon steels at elevated temperature*. Journal of the Japan Society for Technololy of Plasticity, 1967. **8**: p. 414-422.
43. Nioi, M., et al., *Finite element modelling of surface defect evolution during hot rolling of Silicon steel*. Journal of Materials Processing Technology, 2019. **268**: p. 181-191.
44. Gillebaart, E., *Finite Element Modelling of the Temper Rolling Process*, D.T. Tata Steel Research, Editor. 2011: IJmuiden, The Netherlands.
45. Krzyzanowski, M., J.H. Beynon, and D.C.J. Farrugia, *Oxide Scale Behavior in High Temperature Metal Processing*. 2010: Wiley.
46. Lenard, J.G. and S. Kalpakjian, *An Experimental Study of Boundary Conditions in Hot and Cold Flat Rolling*. CIRP Annals, 1990. **39**(1): p. 279-282.
47. Xiong, S., et al., *Three-dimensional thermo-mechanical finite element simulation of the vertical–horizontal rolling process*. Journal of Materials Processing Technology, 2001. **110**: p. 89-97.
48. Oliveira, A., *Convecção - Convecção forçada em escoamentos externos; correlações e exemplos*, in *Transferência de Calor*. 2017, FEUP - Faculdade de Engenharia da Universidade do Porto: Porto, Portugal.
49. Konter, A., et al., *Advanced finite element contact benchmarks*. 2006, Glasgow, U.K.: NAFEMS Ltd. iv, 60 p.
50. Swart, E., Y. An, and M. Toose, *FE Analysis of Influence Material Parameters on Rolling Forces - Method to accurately determine forces and displacements for roughness transfer analysis*, D.T. Tata Steel Research, Editor. 2013, Tata Steel IJmuiden: IJmuiden, The Netherlands.
51. SIMULIA, *Abaqus Analysis User's Manual - 11.7.1 Mass scaling*. 2018, Dassault Systems: Abaqus Documentation.
52. Serajzadeh, S., A.K. Taheri, and F. Mucciardi, *Prediction of temperature distribution in the hot rolling of slabs*. Modelling and Simulation in Materials Science and Engineering, 2002. **10**(2): p. 185-203.
53. Luo, C. and U. Ståhlberg, *Deformation of inclusions during hot rolling of steels*. Journal of Materials Processing Technology, 2001. **114**(1): p. 87-97.
54. Yu, H., et al., *Deformation behavior of inclusions in stainless steel strips during multi-pass cold rolling*. Journal of Materials Processing Technology 2009. **209**: p. 455-461.
55. Malkiewicz, T. and S. Rudnik, *Deformation of non-metallic inclusions during rolling of steel*. Journal of The Iron and Steel Institute, 1963. **201**: p. 33-38.
56. Put, P., *Gietpoeder classificatie methode - Verweking Onder Druk*, T. Steel, Editor. 2012, Tata Steel Netherlands: Ijmuiden, Netherlands.
57. Kashiwaya, Y., et al., *Crystallization Behaviors Concerned with TTT and CCT Diagrams of Blast Furnace Slag Using Hot Thermocouple Technique*. ISIJ International, 2007. **47**(1): p. 44-52.

APPENDIX A: Slab Dimensions

Additional photographs of the slabs used in the lab-scale hot rolling trials examined in the present report are presented hereafter, with a scale bar to display the final dimensions.

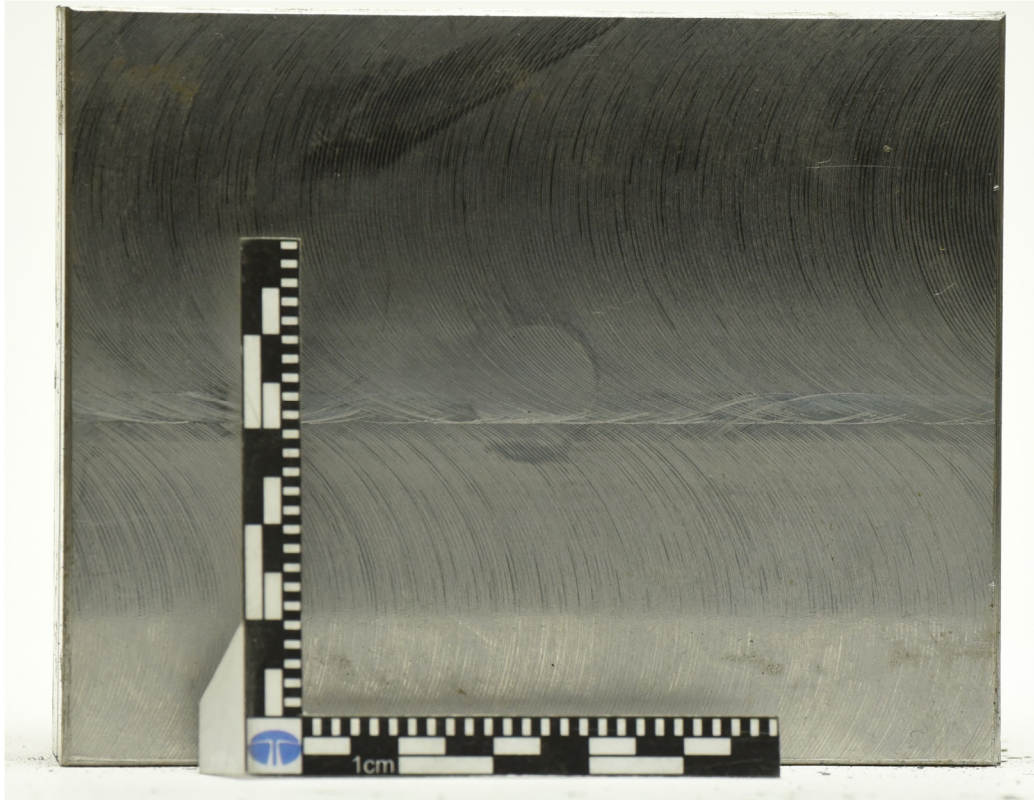


Figure A1 – Steel slab before hot rolling. PM cylinder visible in the centre of the slab.



Figure A2 – Steel slab after the 20% thickness reduction lab scale hot rolling scheme. PM cylinder visible in the centre of the slab. Example taken from slab 5.

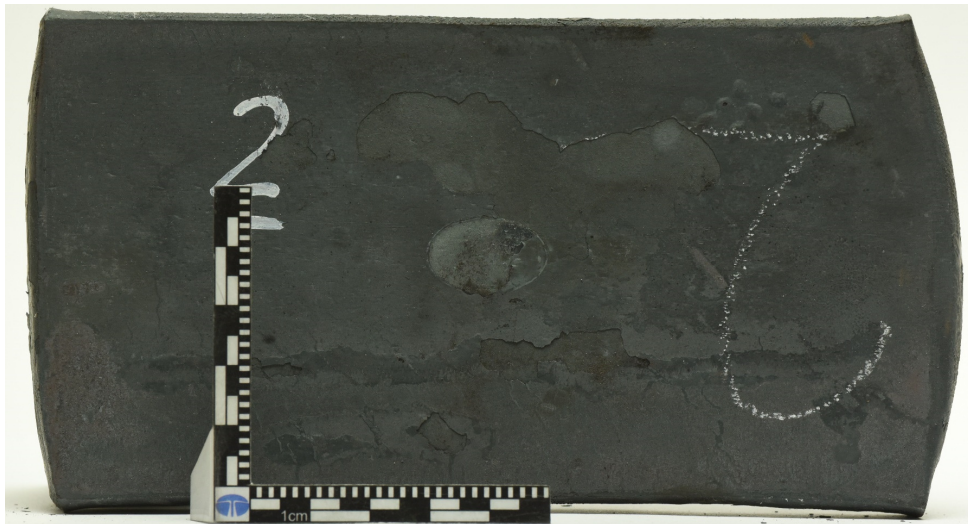


Figure A3 – Steel slab after the 40% thickness reduction lab scale hot rolling scheme. PM cylinder visible in the centre of the slab. Example taken from slab 2.



Figure A4 – Steel slab after the 60% thickness reduction lab scale hot rolling scheme. PM cylinder visible in the centre of the slab. Example taken from slab 7.



Figure A5 – Steel slab after the 85% thickness reduction lab scale hot rolling scheme. PM cylinder visible in the centre of the slab. Example taken from slab 12.

When considering the final dimensions of the slabs, it is important to notice that there is a phenomenon present in the extremities of the slab, where the width is increased in favour of the length. This phenomenon is more noticeable for higher thickness reductions, and is schematized in Figure X.

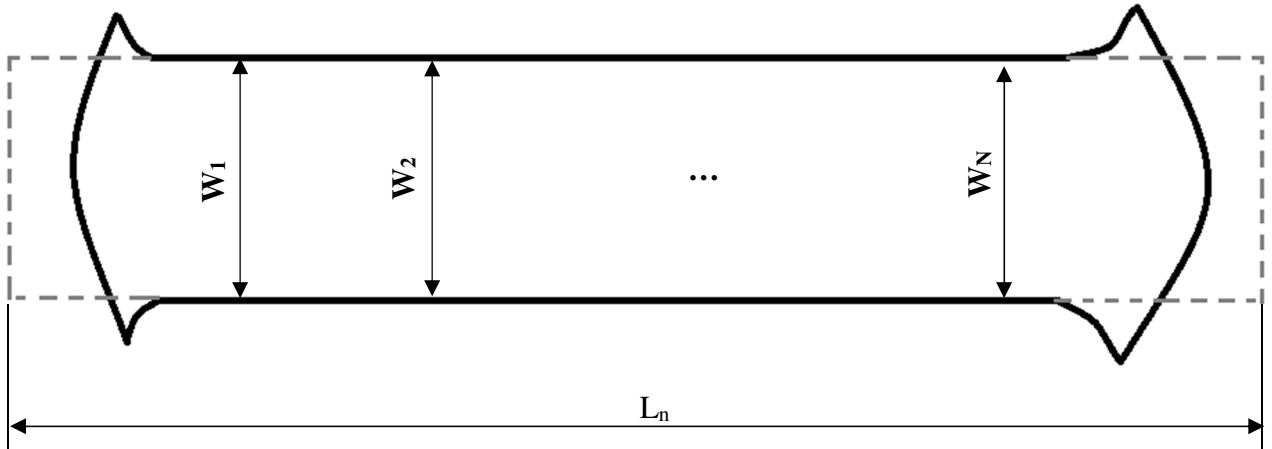


Figure A6 – Schematic representation of the final shape of the rolled slabs and the considered final dimensions.

During the present thesis, when evaluating indexes that considered the slab dimensions (e.g. the overall slab strain, used in the relative plasticity index), a normalized measure had to be created in order to compensate the different degrees at which the slabs are affected by the represented phenomenon for the different rolling schedules. Therefore, the normalized length was created, as represented in a dashed line in Figure A6, which could be calculated using the constant volume law, and considering a uniform thickness throughout the slab by Eq.(A.1):

$$L_n = \frac{L_i \cdot T_i \cdot W_i}{T_f \cdot \bar{W}_f} \quad (\text{A.1})$$

where:

L_n , is the normalized final slab length;

L_i , is the initial slab length;

T_i , is the initial slab thickness;

W_i , is the initial slab width;

T_f , is the final slab thickness;

\bar{W}_f , is the average final slab width, calculated as the average of N measurements of the width exclusively along the zone of the slab displaying a relatively constant width (as displayed in Figure A6).

APPENDIX B: Optical Microscopy Mosaics and Measurements

A compilation of the mosaics formed during optical microscopy of the prepared samples is hereafter presented.

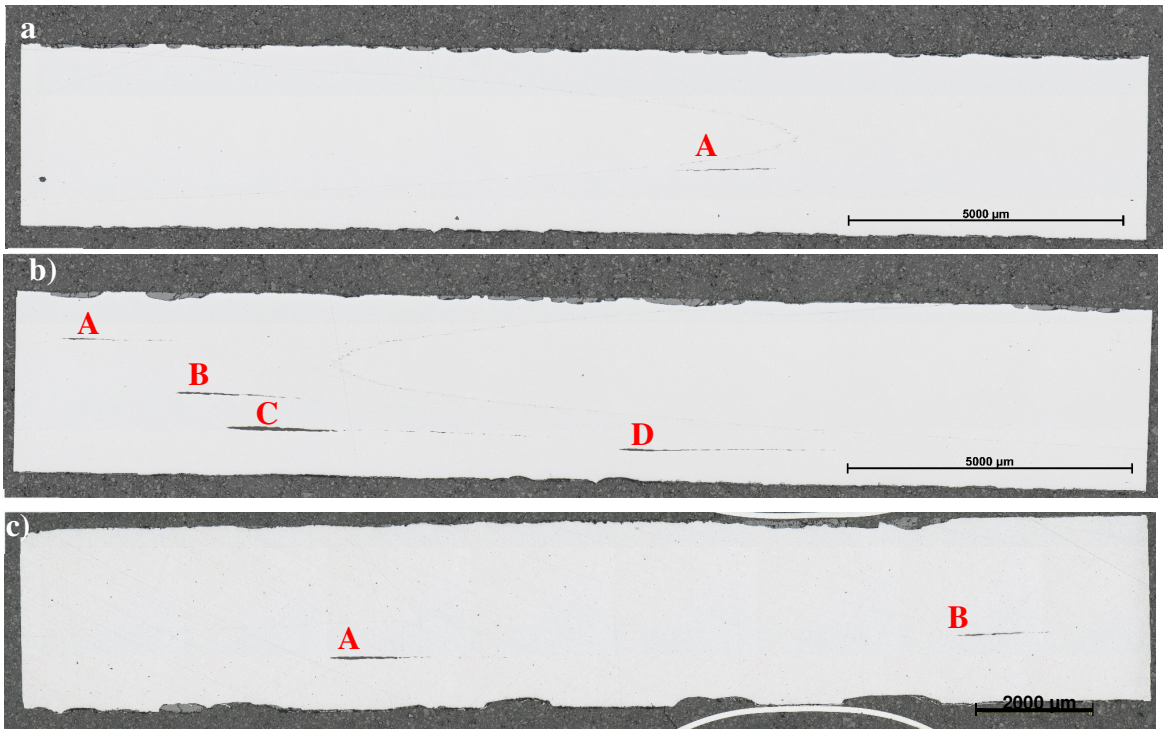


Figure B1 – Mosaic of sample from slab 4 (a), 8 (b), and 16 (c) created with 50x optical microscopy images. Inclusions identified with capital letters above.

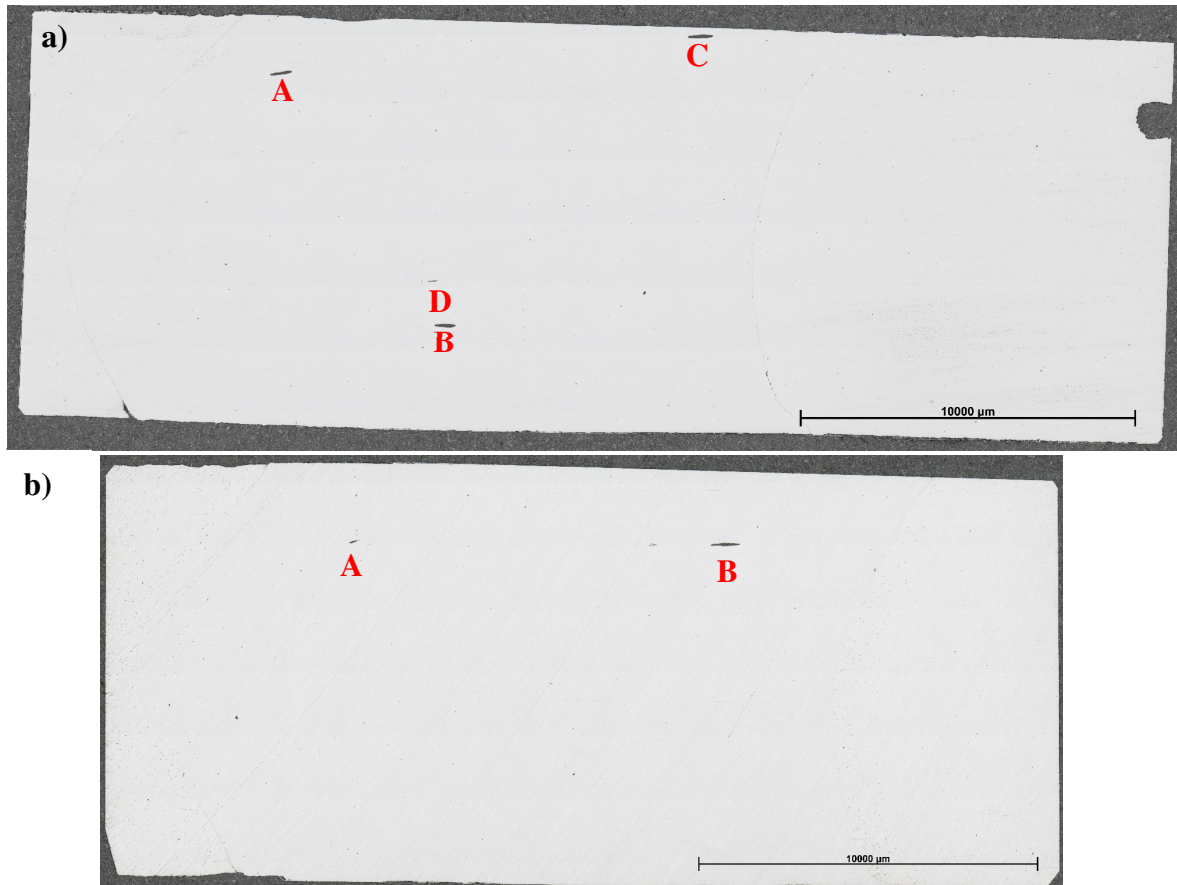


Figure B2 – Mosaic of sample from slab 2 (a) and 6 (b) created with 50x optical microscopy images. Inclusions identified with capital letters below.

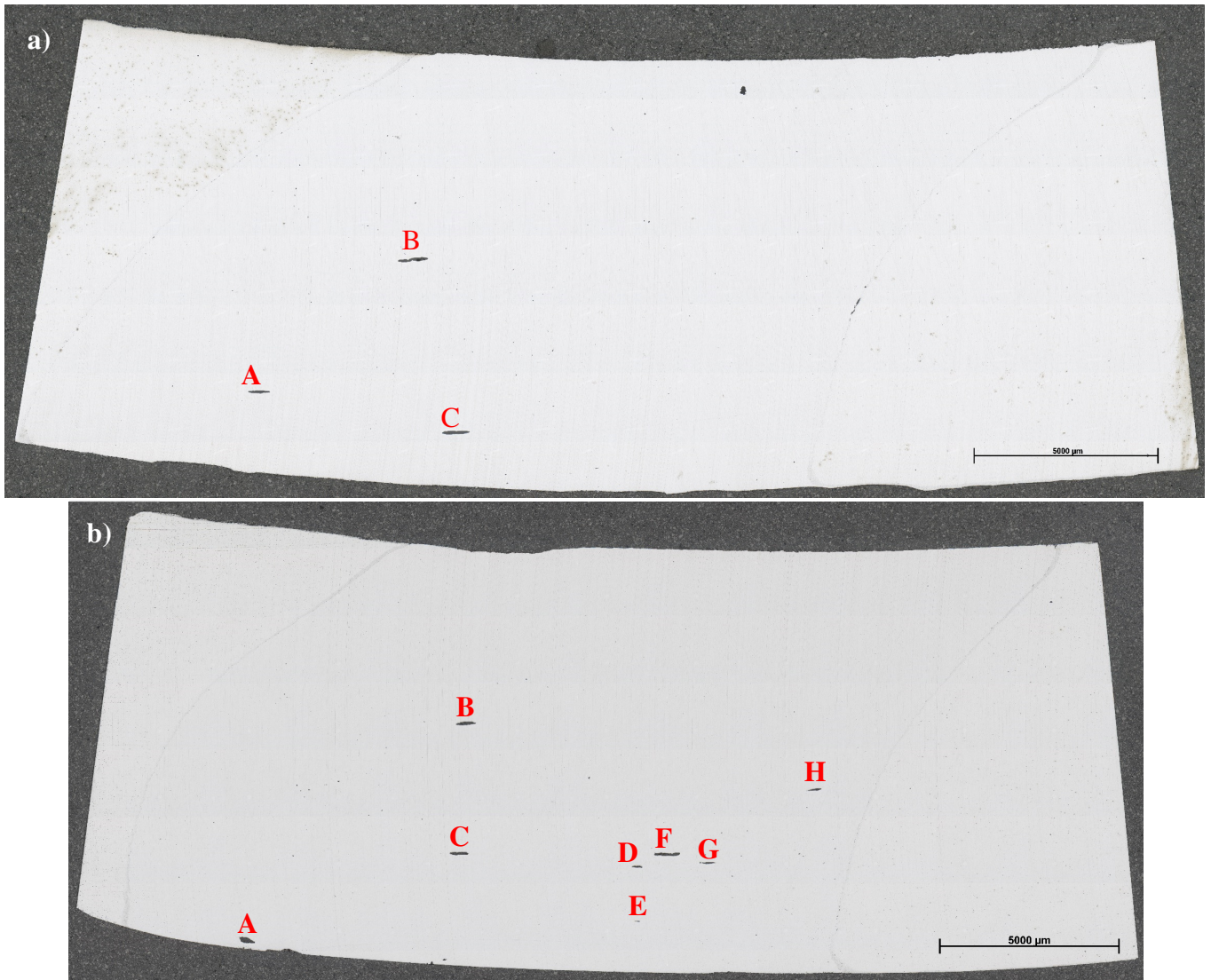


Figure B3 – Mosaic of sample from slab 10 (a) and 14 (b) created with 50x optical microscopy images. Inclusions identified with capital letters above. It can be observed that an initial angling in the beginning of the rolling procedure resulted in a curved rolled slab.

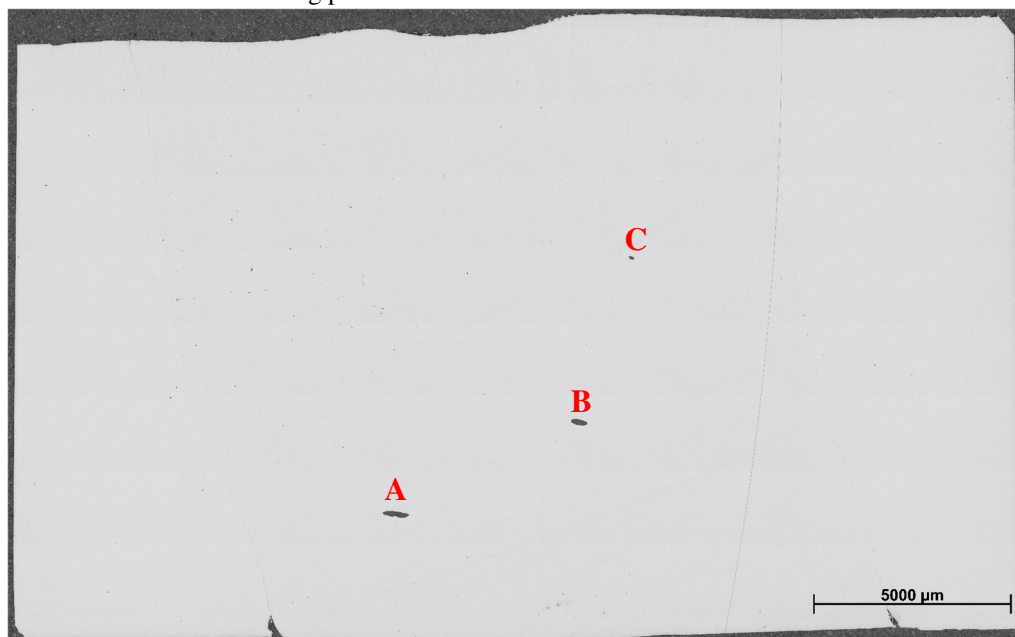


Figure B4 – Mosaic of sample from slab 1 created with 50x optical microscopy images. Inclusions identified with capital letters above.

Moreover, an explanation of the procedures used to conduct the inclusion measurements during optical microscopy testing are presented henceforth. It should be noted that the measurements were conducted on the full-resolution mosaics created, using the appropriate modules within the AxioVision software used.

The inclusion length measurements were made taking into account that some inclusions might be tilted. For the longest inclusions (found in the 85% thickness reduction slabs), this fact was relatively easy to solve, since these are also considerably thin inclusions, leaving a narrow margin of error. For the thickest inclusions however, a special care was taken to select the points in the extremities of the inclusion, since these present rounder, more oval shapes, more suitable to lead to errors. This type of measurement can be identified in yellow in Figure B5.

The thickness measurements conducted at this phase were based on the maximum thickness observed. To do so, two auxiliary lines were marked parallel to the inclusions' axis (defined by the length measurement points) as to create offset boundaries. These lines were then displaced until the extremities were found on both sides of the axis, leading to 2 points, perpendicular to the inclusion's length for which the thickness measurement was taken. For most cases, there was a clear section corresponding to the maximum thickness (i.e. both extremity points corresponded to a single section perpendicular to the axis), however, there were inclusions for which the outermost point on one side did not correspond to the outermost point on the opposite side. In these cases, a maximum thickness could not be directly defined, which lead to the measurement of several sections throughout the inclusion, from which the maximum thickness was chosen. This type of measurement can be observed in red in Figure B5.

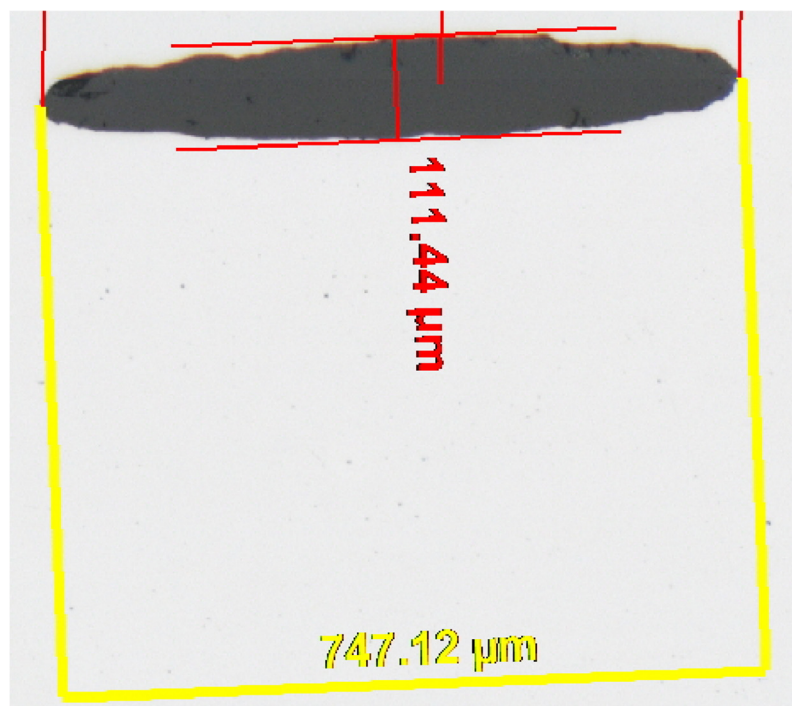


Figure B5 – Example of the length and maximum thickness measurements conducted on inclusion C of slab 2 during optical microscopy.

Finally, to measure the inclusion's depth in the slab, once again the inclusion's slope in relation to the rolling direction became a significant factor. Therefore, several measurements were conducted for each inclusion in relation to the nearest surface of the slab in order to obtain the average depth. For the inclusions for which it could not be easily determined which was the nearest slab surface, the depth in relation to both sides was calculated and the minimum value was chosen. It should be noted that these measurements were conducted perpendicularly to the rolling direction defined by the slabs' surface, where a guiding line was placed, defining the

measurement's perpendicular direction using the calliper function available in the software used, as can be observed in Figure B6.

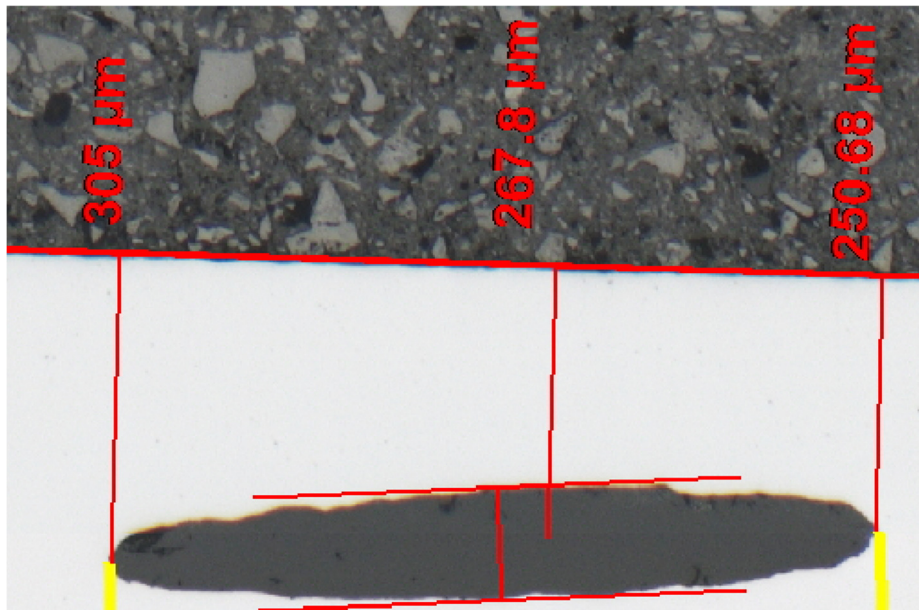


Figure B6 – Example of the depth measurements conducted on inclusion C of slab 2 during optical microscopy.

The additional measurements of the individual inclusion's area were carried out in the optical microscopy photographs of the inclusions. To do so, the image and the scale provided by the AxioVision Software were imported into Adobe Photoshop CC 2018, and the area was measured by selecting the inclusion using its distinct grey scale values from the background, with the magic wand tool, as can be observed in Figure B7.

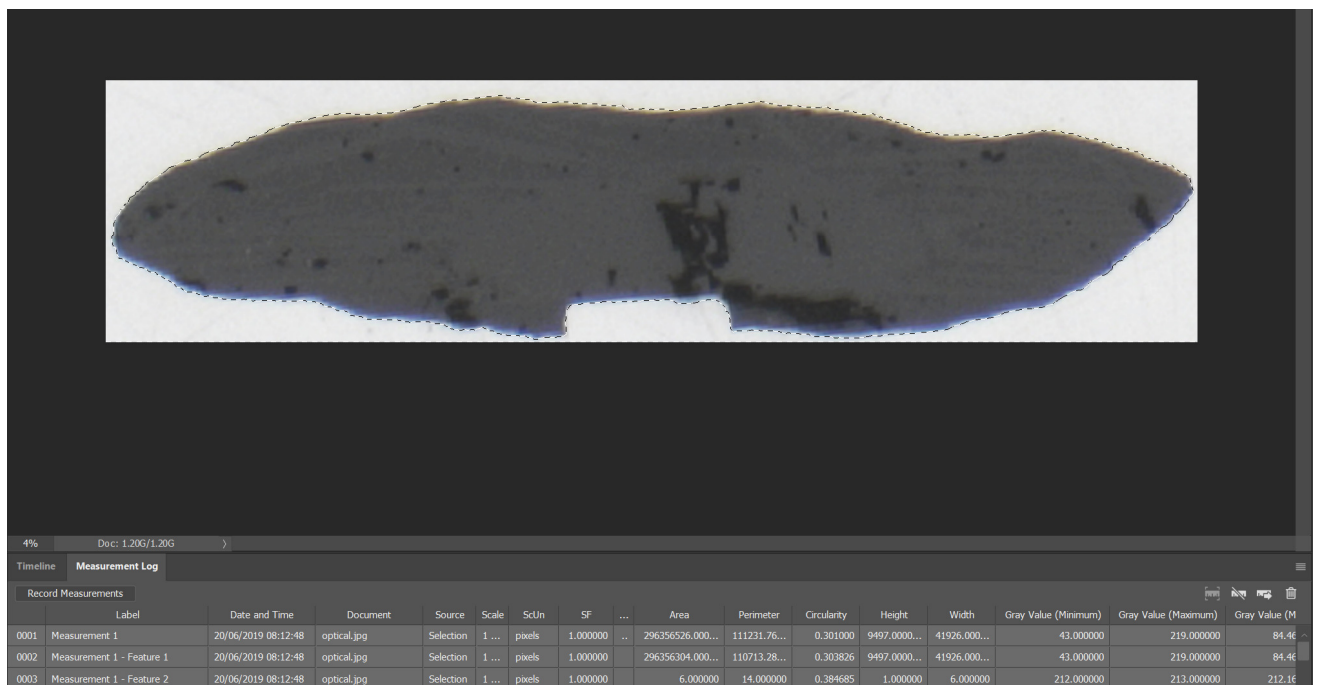


Figure B7 – Example of the area measurements conducted on inclusion A of slab 1 during optical microscopy.

APPENDIX C: Preliminary Analysis

This preliminary phase aimed at furthering the analysis of the data acquired by Uittenbroek (2019), taking into consideration the conclusions drawn in the respective report [9]. A focus was drawn into the study of the chemical evolution throughout the length of the inclusions that display the “head + tail” shape, found in the 85% thickness reduction samples as well as in the oval shaped inclusions present in the 60% reduction samples studied by Uittenbroek (2019) [9].

A compound analysis was conducted in order to understand and possibly predict the phase formation, consequent behaviour and its evolution in length. To do to, the area calculations of the wt% of compounds (direct Pathfinder results) and basicity (calculated with CaO/SiO_2) were plotted as a function of length for the first samples taken from slab 4, 8, 7, 15 and 16 (no inclusions were also found in the first sample from slab 12 and no valid area measurements were made in the lengthwise samples taken from slabs 3 and 11) and its evolution compared.

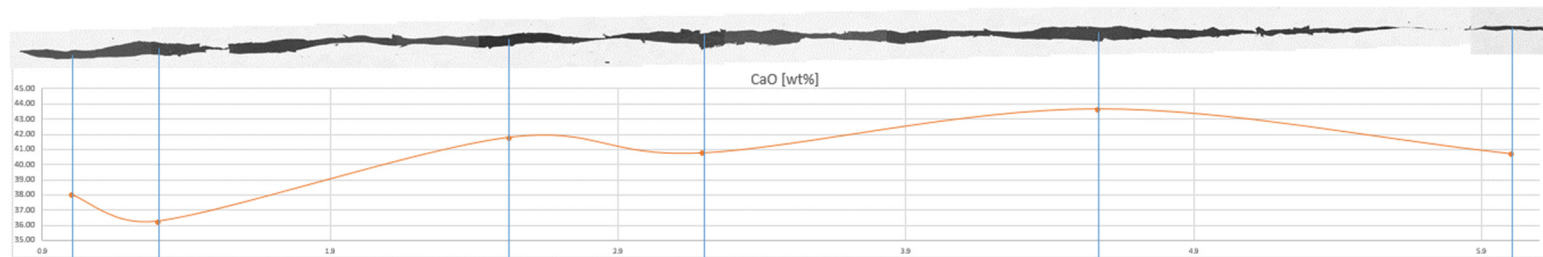


Figure C1 – Example of the analysis performed. Sample 4, Inclusion C, CaO evolution.

During this study, a correlation between the behaviour of certain compounds has been possibly identified and its explanation hypothesised. This correlation lead to a distinction between two different types of behaviour:

Behaviour A - It was observed that for some inclusions (e.g. inclusions A and B in the sample taken from slab 4 and inclusion A in the sample taken from slab 8) the evolutions of CaO and F are similar and opposite to the evolutions of Na_2O and SiO_2 , as shown in Figure C2. This behaviour might be explained by the formation of cuspidine ($\text{Ca}_4\text{Si}_2\text{F}_2\text{O}_7$), the main crystalline phase in these particular inclusions, which uses a higher Ca and F content leading to equally higher compound calculations and leaving Na and Si rich glassy zones in its boundaries. In these cases, it is clear that since SiO_2 and CaO evolutions are opposite, basicity will display a behaviour that follows the CaO trend at all times.

Behaviour B - Some other inclusions displayed a fairly different behaviour. In cases such as inclusions C and D in the sample taken from slab 4, it is SiO_2 that follows the evolution of CaO, being opposite to the behaviour of Na_2O and F (Figure C3). In these cases, it was identified that the main crystalline phase is wollastonite (CaSiO_3), which uses Ca and Si, which might lead to spikes in the respective oxide calculations, leaving a F and Na rich glassy phase where crystals cannot be found.

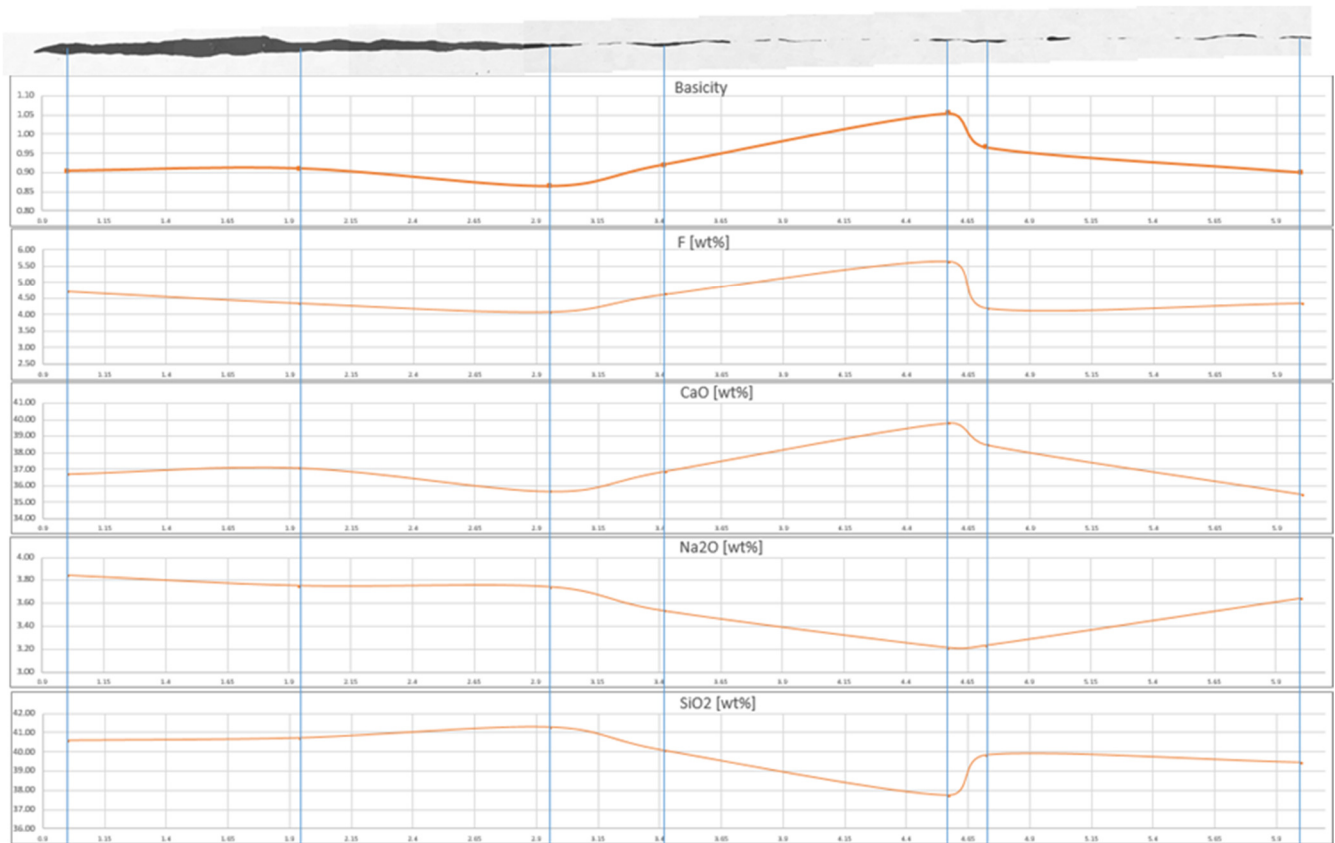


Figure C2 – Compound and basicity evolutions for inclusion A, slab 4, displaying behaviour “A”.

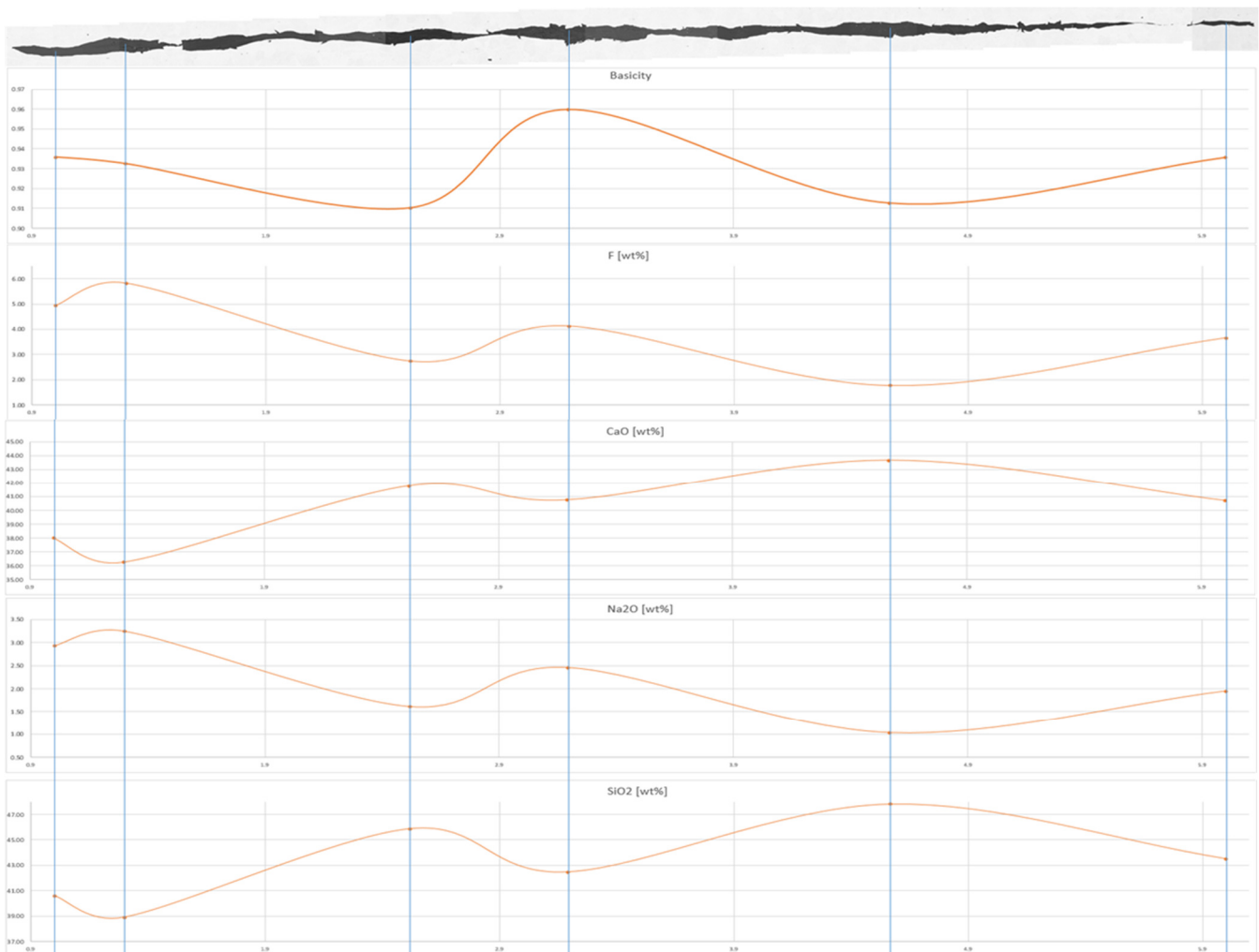


Figure C3 – Compound and basicity evolutions for inclusion C, slab 4, displaying behaviour “B”.

Other inclusions, (e.g. the ones found in the sample taken from slab 16), present either slight variation of this behaviour (e.g. CaO does not follow either F or SiO₂ trend, while all other compounds behave similarly to what is described previously) or a combination of this behaviour (e.g. the inclusion starts by displaying behaviour “A” in the “head” and changing to behaviour “B” in the “tail” in the 85% reduction samples).

Although interesting, it is important to mention that there are possible influences on these conclusions. Firstly, the studied compounds were calculated directly by Pathfinder as simple oxides, a calculation that might not be directly translatable to the real case, where more complex crystalline and glassy phases are present. Despite the hypothesized correlation between these two parameters, the study of phase evolution with length would allow to more accurately observe these phenomena. Secondly, the compound calculation was performed in discrete, relatively large areas that neither encompass the full inclusion nor allow a significant amount of points to plot the compound evolutions. An analysis with a higher number of smaller areas, equally spaced and distributed throughout each inclusion, would possibly allow a more accurate reading of the evolutions in place.

Finally, it is important to know that it is the evolution that is being primarily analysed at this stage and not the exact compound content values. The importance of this difference comes from the fact that the values are influenced by the way that the Pathfinder software calculates the oxide content. Although during EDS analysis concentration spikes for the oxygen element are found, these cannot be properly quantified. Therefore, Pathfinder operates by measuring other element contents and then considering the known simplest oxides that these elements form, leading to calculated oxygen levels, and calculated oxide levels (displayed in the evolutions). However, for the elements that are not prone to form simple oxides, as is the case of fluorine, the software presents them as single element concentrations, as can be observed with the F content throughout this stage of the analysis. This leads to a major error in the results, since F is not found in its elementary form in the inclusions, but instead primarily as calcium fluoride (CaF₂) or alternatively as stable Ca-F clusters, among other more complex phases, resulting in a necessary recalculation of the CaO content as presented:

$$CaF_2 [wt\%] = \frac{F [wt\%] \times \frac{M_{CaF_2}}{2 \times M_F}}{\Sigma C [g]} \times 100 \quad (C.1)$$

and:

$$CaO [wt\%] = \frac{\left(\frac{old\ CaO [wt\%]}{M_{CaO}} - \frac{F [wt\%]}{2 \times M_F} \right) \times M_{CaO}}{\Sigma C [g]} \times 100 \quad (C.2)$$

where:

M_{CaF_2} , is the molar mass of the CaF₂ compound, in [g/mol];

M_{CaO} , is the molar mass of the CaO compound, in [g/mol];

M_F , is the molar mass of the F element, in [g/mol];

Old CaO [wt%], is the CaO content before recalculation;

ΣC , is the summation of all compound weights, including CaF₂ and the recalculated CaO content.

During this stage of the analysis, this correction was dismissed in order to present comparable results to the original mould slag composition, which was also presented as basic oxides + F [wt%] contents. It should also be noted that similar corrections could be made for other elements (e.g. chlorine), but since the concentration of such elements is mostly insignificant in the inclusions studied, these corrections were not performed.

Additional examples of the compound evolutions with inclusion length plotted during the preliminary analysis of Lennard Uittenbroek’s samples results are presented followingly. These evolutions follow the already identified behaviours “A”, “B” and variations of these.

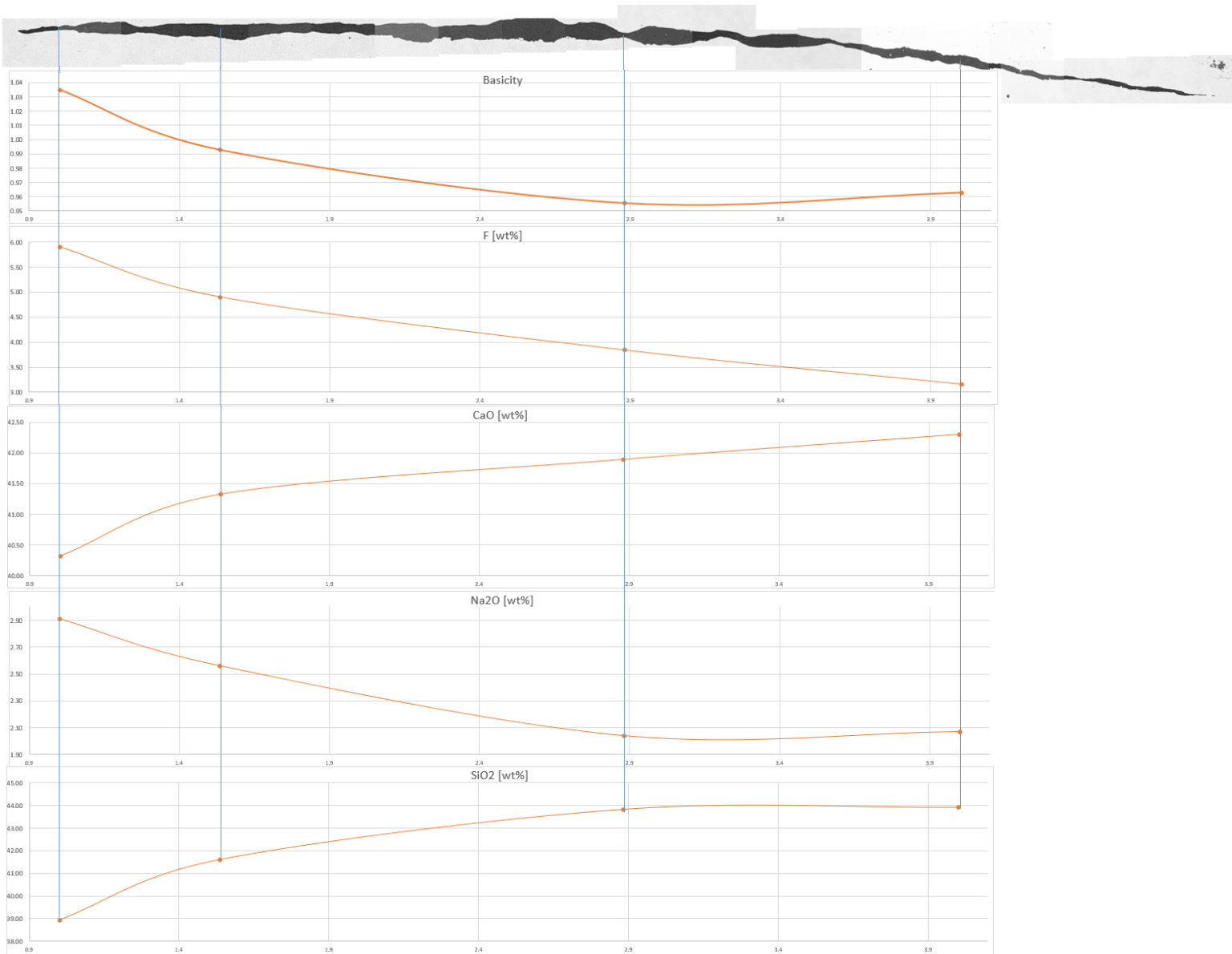


Figure C4 – Compound and basicity evolutions for inclusion D, slab 4, displaying behaviour “B”.

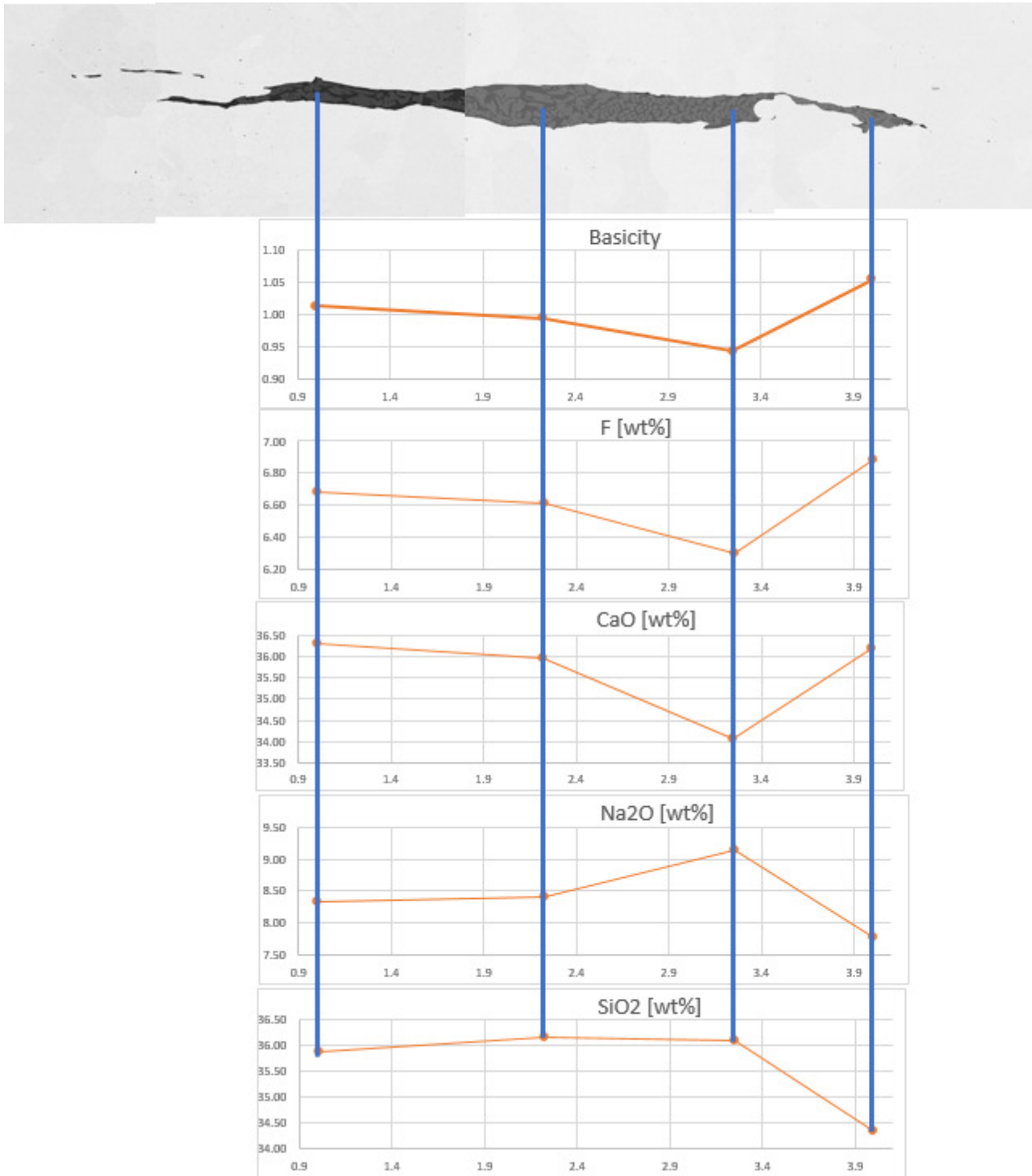


Figure C5 – Compound and basicity evolutions for inclusion D, slab 7, displaying behaviour “A”.

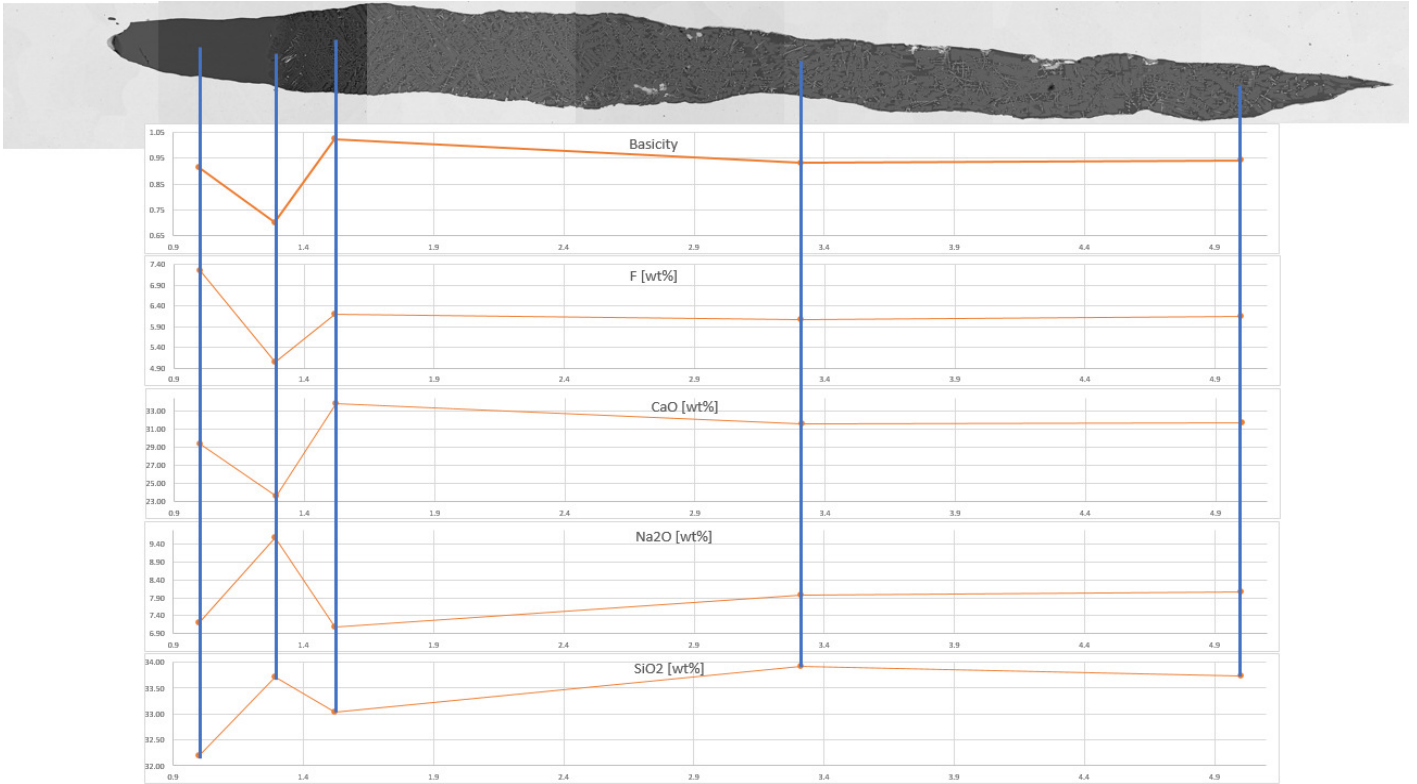


Figure C6 – Compound and basicity evolutions for inclusion B, slab 15, displaying behaviour “A”.

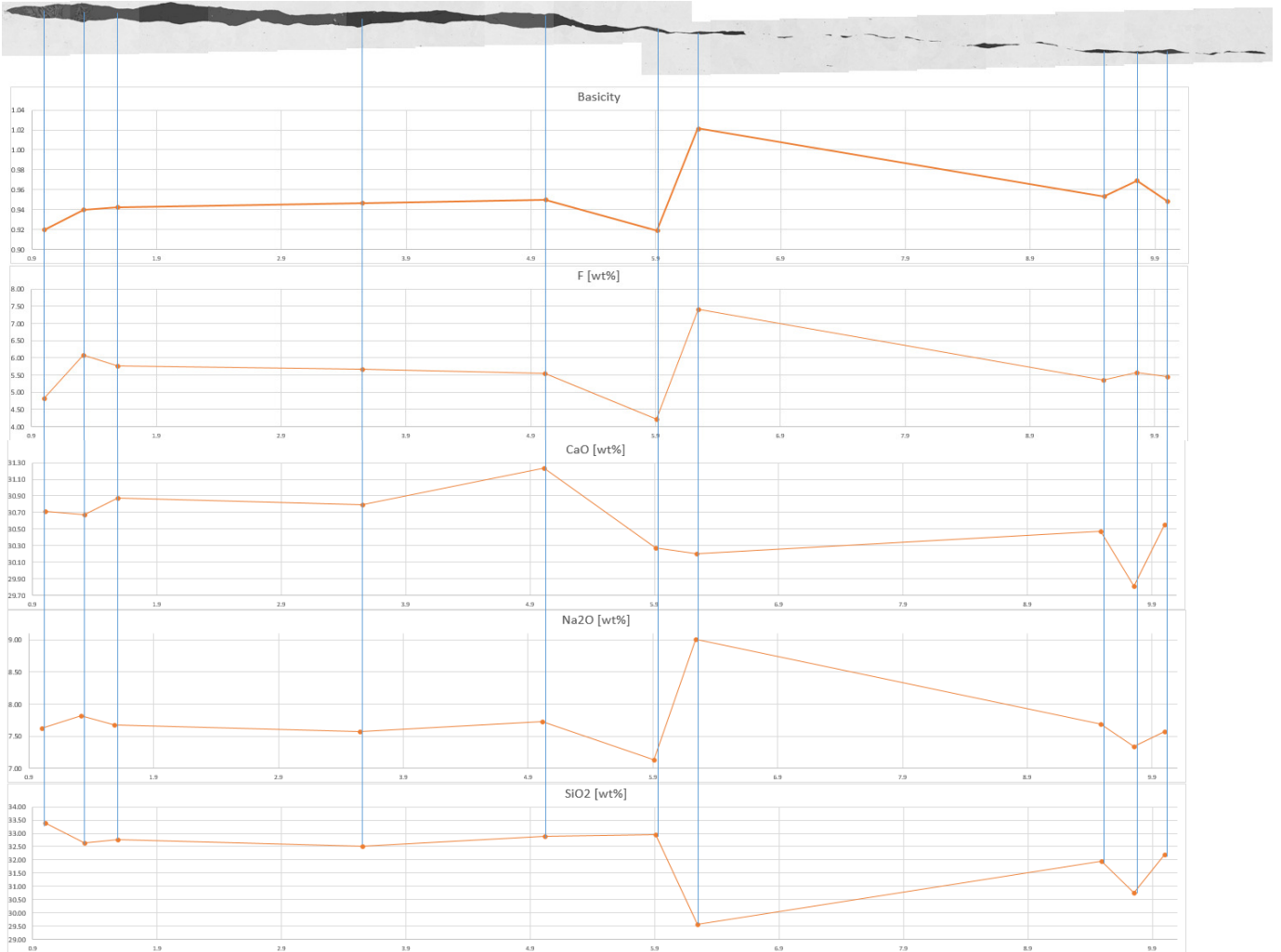


Figure C7 – Compound and basicity evolutions for inclusion C, slab 16, displaying a variation of behaviour “B” where CaO does not follow neither Na₂O nor F evolutions.

APPENDIX D: BSI Image Treatment

The inclusions' BSI images were taken in the Pathfinder automated capture mode, with a 4000x magnification. Examples of individual pictures taken with this methodology can be observed from Figure D1 to Figure D3.

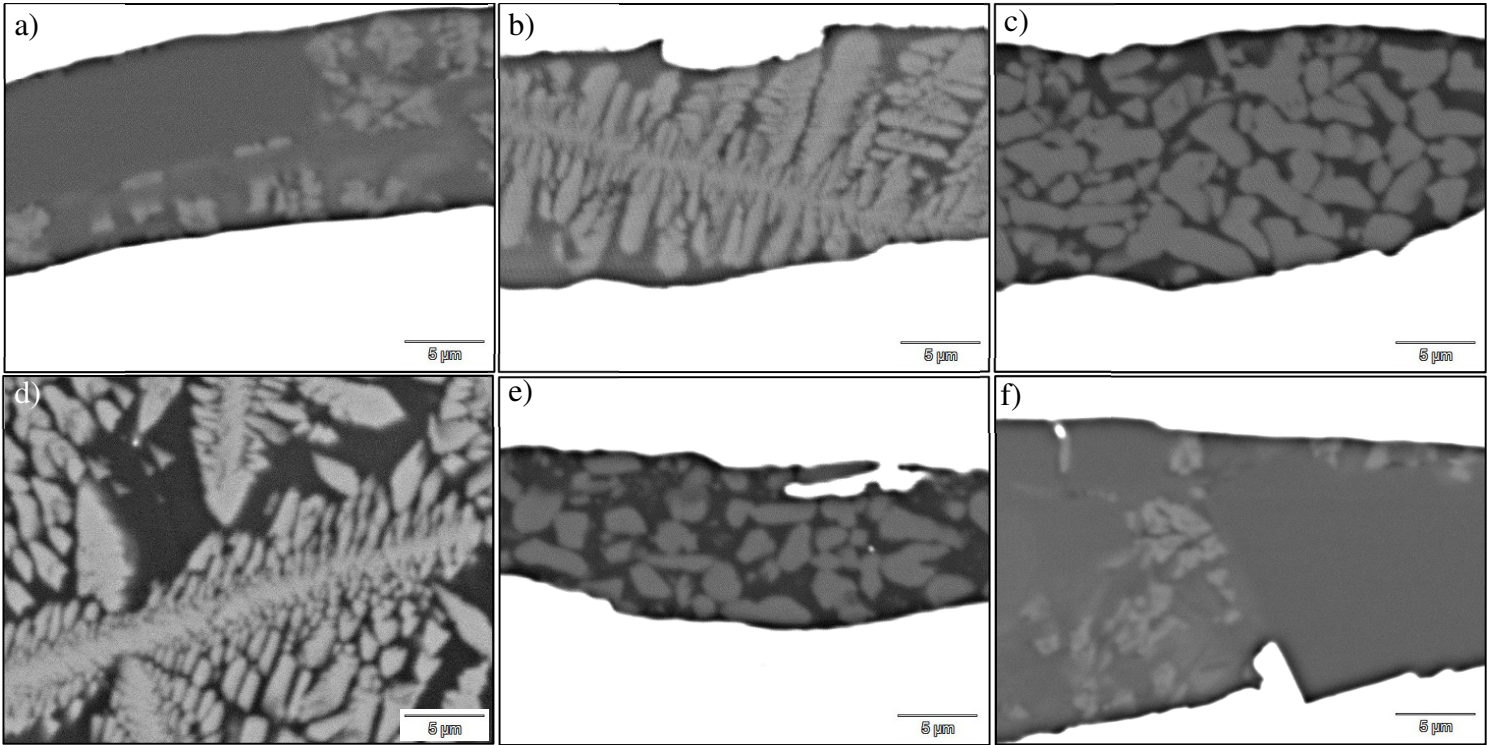


Figure D1 – Examples of individual 4000x magnification BSI images taken from the 85% thickness reduction slabs, (a) inclusion A from slab 4, (b) inclusion A from slab 8, (c) inclusion B from slab 8, (d) inclusion C from slab 8, (e) inclusion D from slab 8, (f) inclusion A from slab 4.

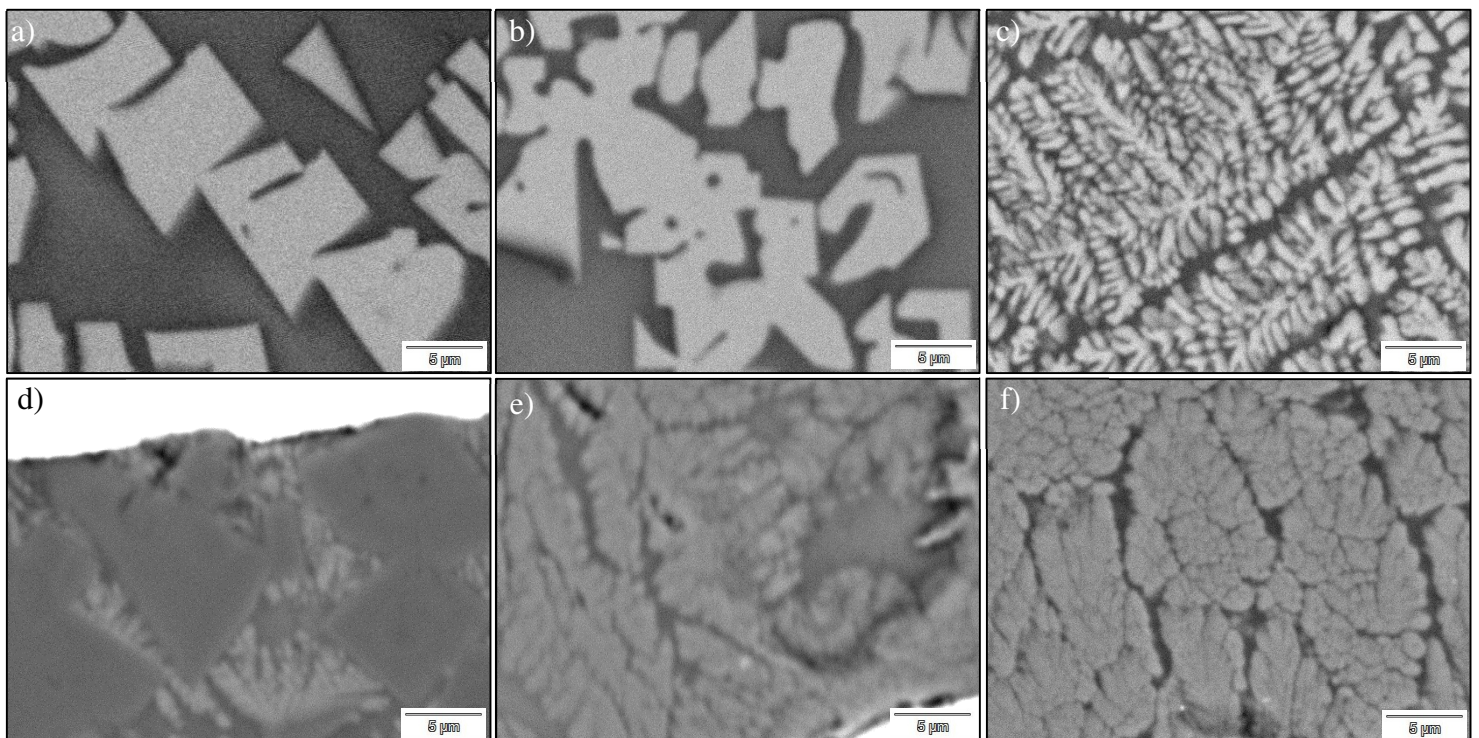


Figure D2 – Examples of individual 4000x magnification BSI images taken from the 40% thickness reduction slabs, (a) inclusion A from slab 2, (b) inclusion B from slab 2, (c) inclusion C from slab 2, (d) inclusion D from slab 2, (e) inclusion A from slab 6, (f) inclusion B from slab 6.

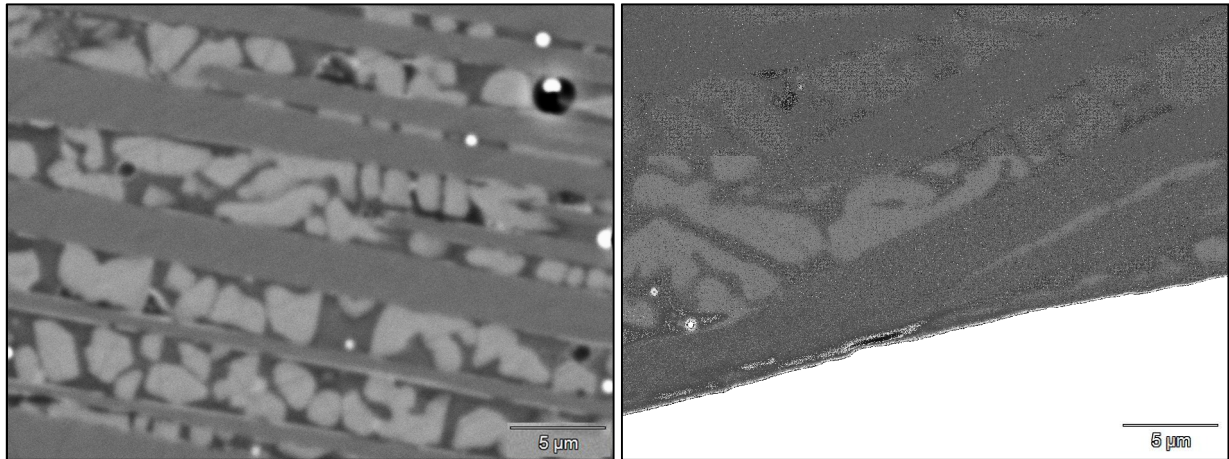


Figure D3 – Examples of individual 4000x magnification BSI images taken from the 20% thickness reduction slab 1, inclusion A.

It should be noted that the grid capture mode in Pathfinder tends to have slight misalignments that, for the selected grid, which is long enough to encompass the whole inclusion, results in a substantial difference in alignment from the first row of columns to the last one. This renders the Pathfinder stitching feature useless, since this feature uses only position data to perform the stitching, resulting in a significant error in alignment of the final picture.

Furthermore, the Pathfinder software performs an automatic brightness and contrast correction for each picture based on its greyscale levels, resulting in different combinations of these two parameters from picture to picture.

These two main factors led to the necessity for manual stitching of the BSI images, accompanied by the uniformization of the brightness and contrast settings for the pictures. This process was conducted using Adobe Photoshop CC 2018.

In order to render this process easier, a 10% overlap between pictures was selected in the image capture settings, leading to a higher number of pictures to stitch, but with a bigger area of repeated features, useful to align the adjacent images.

An example of the steps necessary to perform this process in a relatively small area of an inclusion can be observed in Figure D4.

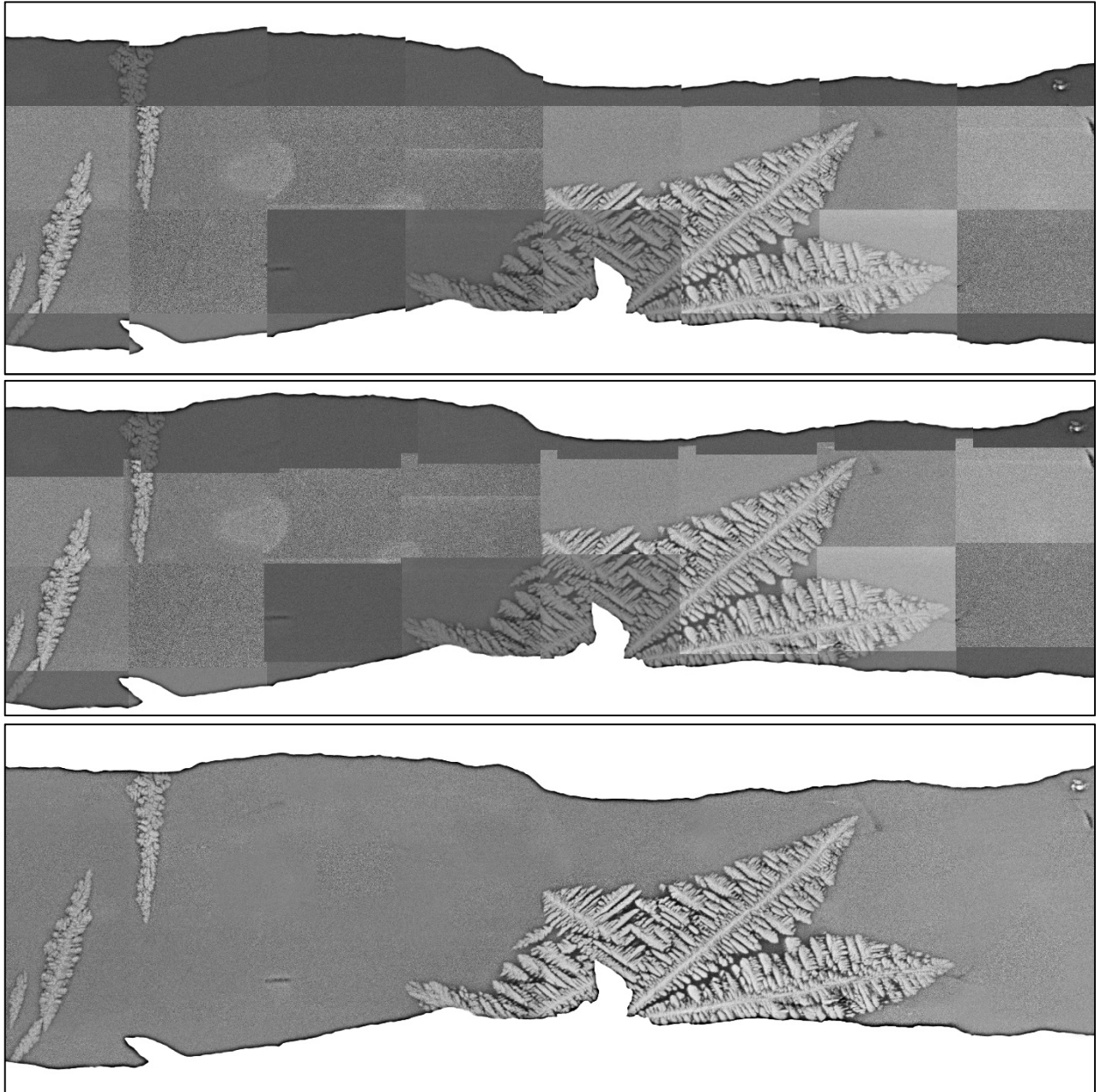


Figure D4 – BSI images taken with Pathfinder automated capture mode. (a) Inaccurate alignment performed with the Pathfinder stitching feature, (b) images aligned manually and (c) images aligned with brightness and contrast correction. Example taken from slab 8, inclusion C.

APPENDIX E: EDS Measurement and Data Treatment Procedure

The procedure used to acquire the EDS point and area measurements and results will be explained in the present section.

Firstly, the SEM, equipped with Pathfinder software, was positioned in the first position and properly focused. In order to maintain continuity with the images obtained during the BSI imaging phase, a 4000x magnification was adopted as the standard. However, for details of big dimensions, lower magnifications were selected as an exception. The selection of the zones of the inclusion to analyse was made using inclusion geometry and/or phase morphology changes as the main decision factor.

Secondly, the image was captured, and points were marked for EDS composition analysis. If two or more phases were easily identified visually, the order in which the points were selected was usually defined in order to group the points into each phase (first group of points for phase 1, second group for phase 2, etc.). This procedure significantly reduces the data treatment complexity, as will be explained afterwards. Example of the point measurements selected are presented in Figure E1.

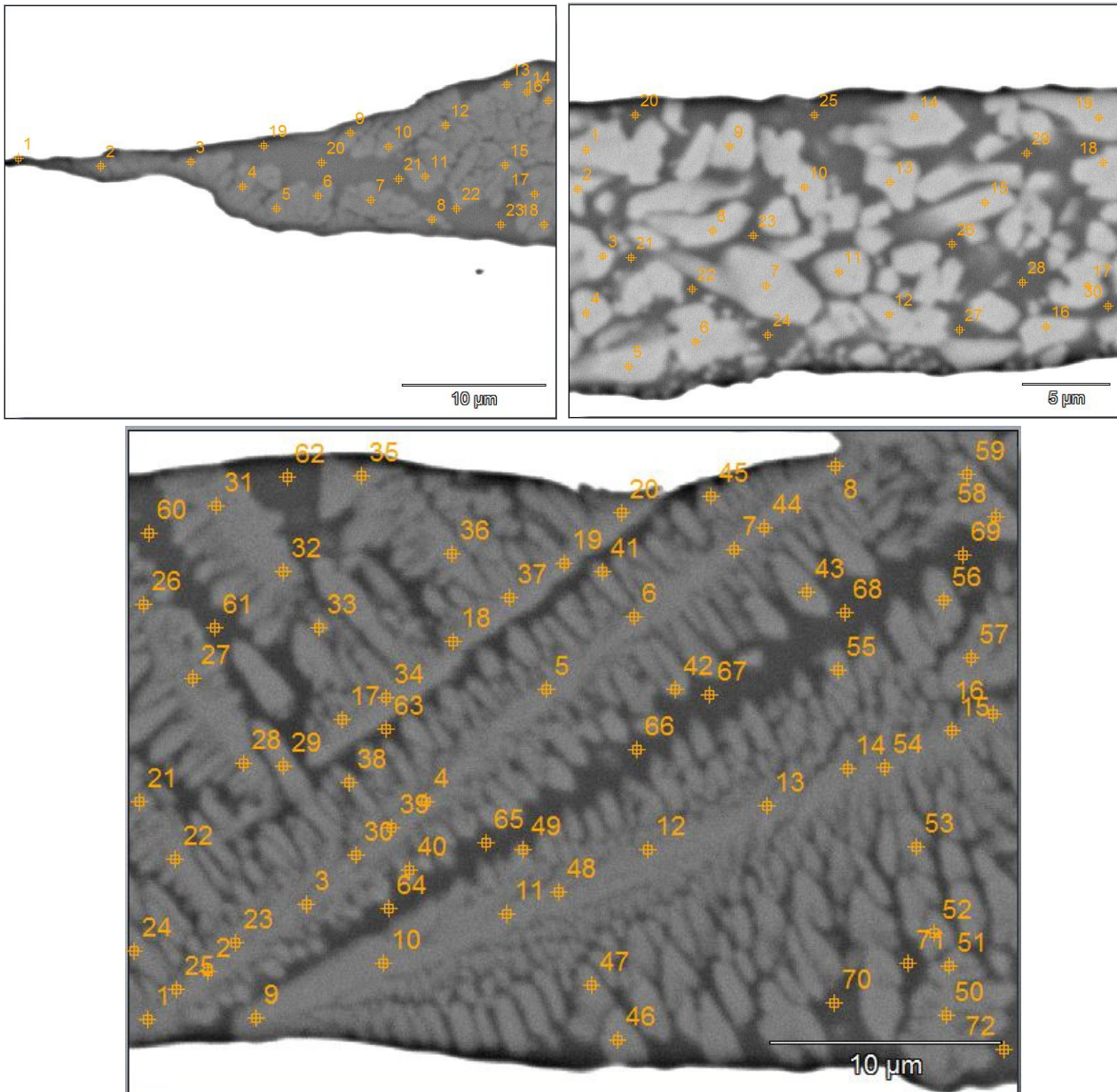


Figure E1 – Examples of the point measurements conducted. Images taken from sample 8, inclusion D.

Afterwards, the same image would be reacquired to conduct area measurements. The areas selected usually corresponded to a single phase, for which the magic wand tool with a $\approx 90\%$ greyscale tone match would be selected. For areas with simple contours, a polygonal tool was also sporadically used. For each phase, if more than one area was selected, the order of the measurements was usually chosen to follow the rolling direction (in the pictures, from left to right), in order to allow an easier treatment of the data, especially for element evolution analysis. Examples of these measurements can be observed in Figure E2.

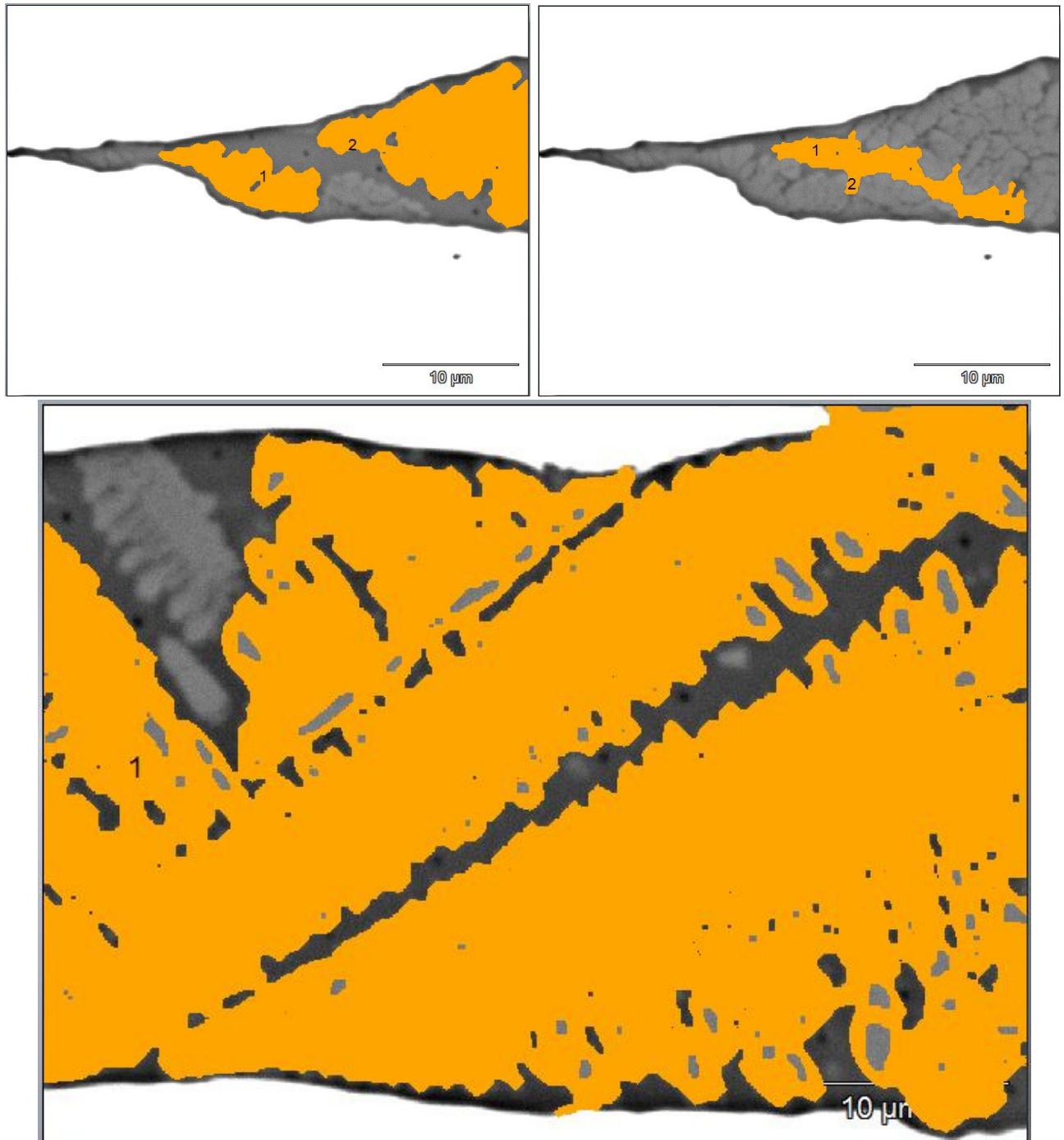


Figure E2 - Examples of the area measurements conducted. Images taken from sample 8, inclusion D.

Several overall area measurements were also performed using the polygonal area tool, as presented in Figure E3.

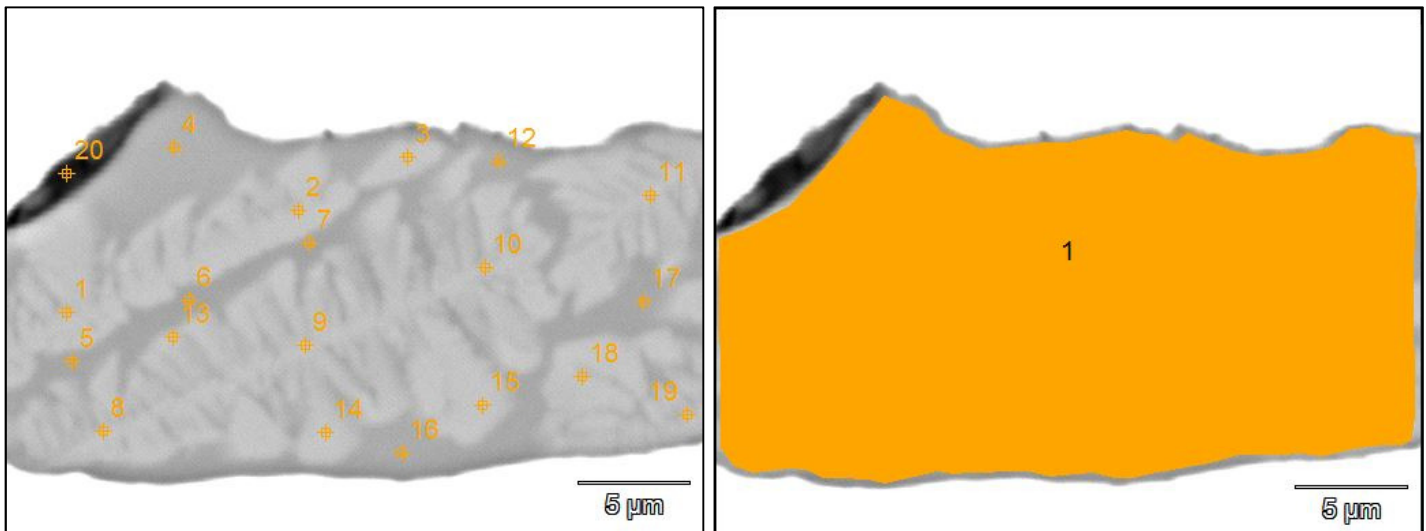


Figure E3 – Example of a point and corresponding overall area measurements (left and right respectively).
Images taken from slab 8, inclusion A.

After performing all of the measurements for each inclusion, the results were processed in batch into a Microsoft Office Excel worksheet. By this stage, these results were composed of element compositions including oxygen (in wt% and atomic%) and the respective compound compositions, for the elements for which they can be easily calculated as basic oxides (in wt%). The element results were then pre-treated in order to exclude oxygen content, since the oxygen content results provided by pathfinder might be inaccurate, and to allow to easily recognise the stoichiometric composition of the different phases expected. The compound results were also pre-treated, as explained in Appendix C, to include CaF_2 and recalculate the CaO levels accordingly.

The compound content values were then used to calculate basicity using the SiO_2 and the now corrected CaO levels. The element contents, in at%, were used to identify the phases present. Due to the significantly high amount of measurements made (an average of ≈ 330 measurements per inclusion), the phase identification process was not viable to be performed visually and individually for each point. Therefore, a simple algorithm was created within the MS Excel sheet to perform this task, using the stoichiometric compositions of each of the most common phases (Cuspidine, Rankinite, Nepheline, Wollastonite, Combeite) as well as the original slag composition as comparison terms for each measurement, with a reasonable variation margin in order to get a positive identification (Figure E4).

The algorithm was tuned with the results of each sample, and the most common variations of phases (e.g. glass with higher Fe content, interdendritic glass, etc.) identified and added to the list of expected phases with its own error margins. Sporadic, random confirmations of the results provided by the algorithm were performed using a visual inspection of the BSI images with the measured points/areas, as observed in Figure E1, Figure E2 and Figure E3, where the present phases are easily distinguishable, allowing a quick check of the algorithm.

Overall, a total of 4267 individual measurements (including only point and area measurements deemed valid) were analysed and its phases identified.

Characterization of the Deformation Behaviour of Mould Slag Inclusions During Hot Rolling

Image	Measurement	Element Atom Concentration [at%]														Phase ID	Border & Error ID	COUNT	Type		
		F	Na	Mg	Al	Si	P	S	Cl	K	Ca	Ti	Cr	Mn	Fe					Mo	Ba
1	6281-08-TD2-B1(1)_pt1	20.02	11.87	0.68	4.03	26.02	0.10	0.12	0.00	0.21	31.14	0.06	0.00	0.00	5.75	0.00	0.00	Glass Slag		1	Point
1	6281-08-TD2-B1(1)_pt2	17.78	13.42	0.90	4.54	28.63	0.08	0.10	0.02	0.17	29.47	0.06	0.06	0.19	4.58	0.00	0.00	Glass Slag		1	Point
1	6281-08-TD2-B1(1)_pt3	17.30	13.53	0.82	4.34	28.88	0.08	0.00	0.00	0.25	29.91	0.00	0.00	0.08	4.82	0.00	0.00	Glass Slag		1	Point
1	6281-08-TD2-B1(1)_pt4	19.44	11.57	0.66	3.74	25.15	0.06	0.00	0.02	0.21	31.70	0.08	0.00	0.00	7.38	0.00	0.00	Glass Slag		1	Point
1	6281-08-TD2-B1(1)_pt5	17.52	13.31	0.90	4.70	28.77	0.10	0.10	0.00	0.15	29.30	0.04	0.00	0.04	5.06	0.00	0.00	Glass Slag		1	Point
10	6281-08-TD2-B1(10)_pt1	18.48	13.45	0.79	4.50	28.77	0.08	0.00	0.00	0.21	28.93	0.02	0.00	0.12	4.64	0.00	0.00	Glass Slag		1	Glass Area
11	6281-08-TD2-B1(11)_pt1	16.95	13.63	0.86	4.52	29.22	0.06	0.11	0.02	0.23	30.17	0.15	0.00	0.11	3.97	0.00	0.00	Glass Slag		1	Point
11	6281-08-TD2-B1(11)_pt2	17.78	13.84	0.81	4.42	29.05	0.06	0.00	0.02	0.19	29.20	0.02	0.08	0.13	4.38	0.00	0.00	Glass Slag		1	Point
11	6281-08-TD2-B1(11)_pt3	17.98	13.79	0.77	4.50	28.65	0.04	0.08	0.00	0.21	29.69	0.04	0.00	0.02	4.23	0.00	0.00	Glass Slag		1	Point
11	6281-08-TD2-B1(11)_pt4	18.48	13.96	0.83	4.37	28.42	0.06	0.02	0.06	0.17	27.80	0.12	0.02	0.02	5.66	0.00	0.00	Glass Slag		1	Point
11	6281-08-TD2-B1(11)_pt5	18.33	13.90	0.79	4.39	28.57	0.10	0.12	0.00	0.17	29.13	0.04	0.00	0.00	4.45	0.00	0.00	Glass Slag		1	Point
12	6281-08-TD2-B1(12)_pt1	17.95	13.59	0.88	4.36	28.62	0.06	0.15	0.02	0.13	29.49	0.10	0.04	0.10	4.51	0.00	0.00	Glass Slag		1	Glass Area
13	6281-08-TD2-B1(13)_pt1	13.01	8.62	0.79	5.38	32.07	0.09	0.11	0.07	0.22	35.45	0.07	0.00	0.07	4.07	0.00	0.00	Glass Slag		1	Point
13	6281-08-TD2-B1(13)_pt2	21.69	6.98	0.59	3.14	27.80	0.00	0.00	0.04	0.08	37.46	0.02	0.02	0.06	2.11	0.00	0.00	Cuspidine Ca		1	Point
13	6281-08-TD2-B1(13)_pt3	22.76	4.85	0.41	3.13	27.95	0.10	0.02	0.00	0.12	38.31	0.08	0.00	0.08	2.18	0.00	0.00	Cuspidine Ca		1	Point
13	6281-08-TD2-B1(13)_pt4	23.45	4.72	0.41	3.03	27.44	0.02	0.04	0.00	0.08	38.46	0.06	0.00	0.00	2.29	0.00	0.00	Cuspidine Ca		1	Point
13	6281-08-TD2-B1(13)_pt5	24.09	4.68	0.45	2.66	26.82	0.00	0.04	0.00	0.06	39.38	0.00	0.00	0.06	1.76	0.00	0.00	Cuspidine Ca		1	Point
13	6281-08-TD2-B1(13)_pt6	23.84	4.41	0.41	2.38	27.15	0.02	0.00	0.04	0.04	39.71	0.02	0.02	0.10	1.87	0.00	0.00	Cuspidine Ca		1	Point
13	6281-08-TD2-B1(13)_pt7	23.78	4.17	0.35	2.19	26.97	0.08	0.00	0.02	0.08	40.50	0.06	0.00	0.02	1.79	0.00	0.00	Cuspidine Ca		1	Point
13	6281-08-TD2-B1(13)_pt8	19.79	6.11	0.46	4.04	28.77	0.08	0.00	0.02	0.06	37.79	0.04	0.00	0.08	2.74	0.00	0.00	Cuspidine Ca		1	Point
13	6281-08-TD2-B1(13)_pt9	22.35	6.72	0.72	2.78	27.30	0.02	0.02	0.00	0.12	37.17	0.02	0.00	0.16	2.62	0.00	0.00	Cuspidine Ca		1	Point
13	6281-08-TD2-B1(13)_pt10	22.06	7.08	0.61	2.22	26.84	0.02	0.04	0.00	0.14	37.87	0.06	0.02	0.12	2.92	0.00	0.00	Cuspidine Ca		1	Point
13	6281-08-TD2-B1(13)_pt11	24.12	4.10	0.40	1.74	26.00	0.14	0.08	0.02	0.04	41.27	0.04	0.00	0.00	2.02	0.02	0.00	Cuspidine Ca		1	Point
13	6281-08-TD2-B1(13)_pt12	22.45	7.30	0.71	2.48	26.91	0.02	0.00	0.00	0.12	37.30	0.00	0.06	0.02	2.62	0.00	0.00	Cuspidine Ca		1	Point
13	6281-08-TD2-B1(13)_pt13	23.52	4.92	0.53	1.48	26.07	0.12	0.00	0.02	0.04	41.04	0.08	0.00	0.00	2.18	0.00	0.00	Cuspidine Ca		1	Point
13	6281-08-TD2-B1(13)_pt14	24.66	5.55	0.54	1.72	25.69	0.06	0.00	0.00	0.00	39.67	0.04	0.02	0.04	2.00	0.00	0.00	Cuspidine Ca		1	Point
13	6281-08-TD2-B1(13)_pt15	26.12	4.67	0.44	1.58	24.10	0.06	0.04	0.00	0.00	40.03	0.08	0.06	0.04	2.77	0.00	0.00	Cuspidine Ca		1	Point
13	6281-08-TD2-B1(13)_pt16	24.44	4.59	0.52	1.50	25.51	0.10	0.00	0.02	0.02	41.45	0.02	0.00	0.08	1.74	0.00	0.00	Cuspidine Ca		1	Point
13	6281-08-TD2-B1(13)_pt17	23.62	4.78	0.46	1.39	25.76	0.04	0.00	0.00	0.00	41.87	0.04	0.00	0.00	2.04	0.00	0.00	Cuspidine Ca		1	Point
13	6281-08-TD2-B1(13)_pt18	23.72	5.30	0.53	1.86	26.11	0.06	0.08	0.00	0.08	39.53	0.02	0.02	0.10	2.59	0.00	0.00	Cuspidine Ca		1	Point
13	6281-08-TD2-B1(13)_pt19	25.31	4.08	0.40	1.32	25.77	0.06	0.00	0.00	0.08	41.14	0.06	0.00	0.10	1.68	0.00	0.00	Cuspidine Ca		1	Point
13	6281-08-TD2-B1(13)_pt20	24.07	5.82	0.60	1.93	25.80	0.10	0.00	0.00	0.14	39.81	0.02	0.00	0.00	1.71	0.00	0.00	Cuspidine Ca		1	Point
13	6281-08-TD2-B1(13)_pt21	3.87	21.73	2.17	9.57	39.19	0.09	0.33	0.00	0.54	10.49	0.16	0.00	0.28	11.57	0.00	0.00	Interdendritic Glass		1	Point
13	6281-08-TD2-B1(13)_pt22	4.15	21.44	2.31	10.28	40.84	0.12	0.36	0.02	0.57	6.25	0.12	0.14	0.36	13.04	0.00	0.00	Interdendritic Glass		1	Point
13	6281-08-TD2-B1(13)_pt23	3.52	22.19	2.45	9.36	40.57	0.17	0.14	0.02	0.48	7.12	0.07	0.12	0.21	13.40	0.17	0.00	Interdendritic Glass		1	Point
13	6281-08-TD2-B1(13)_pt24	4.02	21.27	1.85	9.92	37.97	0.14	0.14	0.00	0.47	13.87	0.09	0.07	0.21	9.80	0.16	0.00	Interdendritic Glass		1	Point
13	6281-08-TD2-B1(13)_pt25	4.24	21.48	2.08	9.93	38.44	0.05	0.23	0.00	0.42	12.18	0.12	0.02	0.21	10.59	0.00	0.00	Interdendritic Glass		1	Point
13	6281-08-TD2-B1(13)_pt26	4.60	22.32	1.98	10.28	40.11	0.09	0.00	0.02	0.52	7.28	0.16	0.00	0.38	12.26	0.00	0.00	Interdendritic Glass		1	Point
13	6281-08-TD2-B1(13)_pt27	5.63	18.68	2.10	9.23	38.09	0.09	0.33	0.00	0.54	10.48	0.02	0.02	0.33	14.44	0.00	0.00	Interdendritic Glass		1	Point
13	6281-08-TD2-B1(13)_pt28	7.16	16.37	1.78	8.69	37.51	0.14	0.45	0.00	0.61	12.28	0.19	0.07	0.21	14.54	0.00	0.00	Glass F Ca Fe		1	Point
13	6281-08-TD2-B1(13)_pt29	22.99	5.40	0.45	3.21	28.46	0.02	0.00	0.00	0.14	37.09	0.04	0.00	0.00	2.20	0.00	0.00	Cuspidine Ca		1	Point
13	6281-08-TD2-B1(13)_pt30	22.19	6.14	0.47	2.96	27.94	0.08	0.00	0.00	0.08	37.84	0.04	0.00	0.00	2.26	0.00	0.00	Cuspidine Ca		1	Point
13	6281-08-TD2-B1(13)_pt31	19.27	7.19	0.66	4.75	29.88	0.08	0.13	0.00	0.23	34.34	0.06	0.04	0.06	3.30	0.00	0.00	Cuspidine Ca		1	Point
13	6281-08-TD2-B1(13)_pt32	19.79	7.88	0.78	4.21	29.26	0.02	0.04	0.00	0.17	34.04	0.08	0.00	0.08	3.65	0.00	0.00	Cuspidine Ca		1	Point
13	6281-08-TD2-B1(13)_pt33	18.52	8.00	0.93	4.72	29.82	0.04	0.04	0.00	0.21	33.99	0.02	0.00	0.02	3.68	0.00	0.00	Cuspidine Ca		1	Point
13	6281-08-TD2-B1(13)_pt34	18.44	8.57	0.68	4.75	29.86	0.08	0.00	0.00	0.23	33.94	0.00	0.06	0.08	3.29	0.00	0.00	Cuspidine Ca		1	Point
14	6281-08-TD2-B1(14)_pt1	18.68	10.09	0.58	4.01	28.66	0.08	0.00	0.02	0.19	33.93	0.08	0.02	0.10	3.45	0.10	0.00	Cuspidine Ca		1	Cusp Area

Figure E4 – Example of the phase identification table created with the element composition of each measurement. Example taken from sample 8, inclusion B.